UNIVERSITY OF HAWAI‘I

FINAL TECHNICAL REPORT

U.S. Department of Energy
Grant No. DE-FG22-95PC95206
Grant Dates: 08/15/95 through 12/31/99
Project Officer: Robert P. Warzinski
COR: John R. Owen

LABORATORY EXPERIMENTS TO SIMULATE CO_2 OCEAN DISPOSAL

Submitted to:

U.S. Department of Energy
National Energy Technology Laboratory
P.O. Box 10940, MS 921-143
Pittsburgh, PA 15236-0940

Submitted by:

HAWAI‘I NATURAL ENERGY INSTITUTE
University of Hawai‘i
2540 Dole Street, Holmes Hall 246
Honolulu, Hawaii 96822

Principal Investigator:
Stephen M. Masutani

"US/DOE PATENT CLEARANCE IS NOT REQUIRED PRIOR TO THE PUBLICATION OF THIS DOCUMENT."

DISCLAIMER

ABSTRACT

This Final Technical Report summarizes the technical accomplishments of an investigation entitled "Laboratory Experiments to Simulate CO_2 Ocean Disposal," funded by the U.S. Department of Energy's University Coal Research Program. This investigation responds to the possibility that restrictions on greenhouse gas emissions may be imposed in the future to comply with the Framework Convention on Climate Change. The primary objective of the investigation was to obtain experimental data that can be applied to assess the technical feasibility and environmental impacts of oceanic containment strategies to limit release of carbon dioxide (CO_2) from coal and other fossil fuel combustion systems into the atmosphere. A number of critical technical uncertainties of ocean disposal of CO_2 were addressed by performing laboratory experiments on liquid CO_2 jet break-up into a dispersed droplet phase, and hydrate formation, under deep ocean conditions.

Major accomplishments of this study included: (1) five jet instability regimes were identified that occur in sequence as liquid CO_2 jet disintegration progresses from laminar instability to turbulent atomization; (2) linear regression to the data yielded relationships for the boundaries between the five instability regimes in dimensionless Ohnesorge Number, *Oh*, and jet Reynolds Number, *Re*, space; (3) droplet size spectra was measured over the full range of instabilities; (4) characteristic droplet diameters decrease steadily with increasing jet velocity (and increasing Weber Number), attaining an asymptotic value in instability regime 5 (full atomization); and (5) pre-breakup hydrate formation appears to affect the size distribution of the droplet phase primary by changing the effective geometry of the jet.

TABLE OF CONTENTS

LIST OF TABLES

Table Page

LIST OF FIGURES

EXECUTIVE SUMMARY

Laboratory experiments were conducted to identify the mechanisms and characteristics of liquid-liquid jet breakup into droplets under conditions relevant to CO_2 ocean disposal. Jet fluids included liquid CO_2 and silicone fluid, which served as an easily-handled analog to CO_2. For the sake of completeness, we also included information in this report on other tests conducted with high viscosity oils for an unrelated investigation of deep oil spills (Masutani & Adams, 2000). Including the oils, viscosities of the jet fluids ranged over more than three orders of magnitudes. Emphasis was placed on the largely unstudied class of transitional and turbulent jets, and measurements were conducted at different jet velocities and with various size jet discharge orifices.

The primary objectives of this study were:

- Identify the mechanisms and characteristics of liquid-liquid jet breakup into droplets under conditions relevant to CO_2 ocean disposal; provide data on breakup regimes similar to Reitz and Bracco (1986) that can be applied to the design of injection systems (i.e., injector orifice diameters and flow rates).

- Obtain data on CO_2 droplet size spectra over the entire range of jet instabilities for use with current plume models to estimate dispersion and dissolution of the discharged CO_2.

- Investigate CO_2 hydrate formation under deep ocean conditions to assess flow assurance threats and to understand the influence of this solid phase on droplet formation and dissolution.

The major results and conclusions of this study are summarized below:

1. Five instability regimes were identified by a comprehensive review of the digital video records of the 294 test runs. The five regimes which occur in sequence as liquid-liquid jet disintegration progresses from laminar instability to turbulent atomization are: (1) varicose breakup, where Rayleigh instability dominates and a symmetric surface wave forms and grows, eventually pinching off the jet; (2) sinuous wave breakup, where an asymmetric instability emerges that causes the jet to wave sinuously and generate a polydispersion of droplets; (3) filament core breakup, where the surface of the jet becomes unstable to short wavelength disturbances and disintegrates close to the orifice into fine droplets, while the core of the jet persists as a continuum fluid filament that breaks up further downstream into large droplets; (4) wave atomization, where the breakup location of the jet core filament moves closer to the orifice and the fraction of fine droplets increases; and (5) full atomization.

2. A linear regression to the data yielded relationships for the boundaries between the five instability regimes in dimensionless Ohnesorge Number, *Oh*, and jet Reynolds Number, *Re*, space. The relationships are:

   Boundary 1 between instability regions **1** and **2**:

   $$Oh = 4.9196\ Re^{-1.0459}$$

   Boundary 2 between instability regions **2** and **3**:

   $$Oh = 9.5979\ Re^{-1.0255}$$

   Boundary 3 between instability regions **3** and **4**:

   $$Oh = 15.4108\ Re^{-0.9989}$$

   Boundary 4 between instability regions **4** and **5**:

   $$Oh = 24.9548\ Re^{-1.0027}$$

3. The exponent for *Re* in the relationships for the instability regime boundaries are all very close to –1. Referring to the definitions of *Re* and *Oh*, this means that the transition between regimes is independent of jet viscosity, and the relationships for the boundaries can be rewritten as *We* ~ constant, where *We* is the Weber number. The critical transitional Weber numbers are the square of the coefficient of *Re* in the relationships for the boundaries, i.e.,

   Boundary 1 between instability regions **1** and **2**:

   $$We \sim 24$$

   Boundary 2 between instability regions **2** and **3**:

   $$We \sim 92$$

   Boundary 3 between instability regions **3** and **4**:

   $$We \sim 237$$

   Boundary 4 between instability regions **4** and **5**:

   $$We \sim 623$$

4. A method was developed to obtain a complete, composite droplet size spectra by combining size data from the PDPA and image analysis. The PDPA was not able to measure droplets larger than about 4 mm. The digital video image analysis could not measure droplets smaller than about 3 mm. The method exploits the overlap between the

two incomplete size spectra and can be applied to similar situations involving different particle size diagnostics.

5. Droplet size spectra was measured for liquid-liquid jet breakup over the full range of instabilities from regime 1 through regime 5. Characteristic average diameters and other statistics were calculated from these spectra. Over the range of conditions examined in this study, jet velocity, orifice size and geometry, and jet fluid viscosity affected droplet size. There appeared to be limited or no difference in spectra obtained for injection into tap water and sea water or for liquid CO_2 tests conducted at 52 and 62 bar.

6. Characteristic diameters decrease steadily with increasing jet velocity (and increasing *We*) in instability regimes 1 through 4, attaining an asymptotic value in regime 5. Orifice diameter appears to influence average droplet size at low *We* in regimes 1 and 2. This effect diminishes as regime 3 is approached and essentially disappears in regimes 4 and 5; the characteristic droplet diameters appeared to be the same for 2 mm, 5 mm, and 10 mm orifices, at the same value of *We*, in these regimes. This may reflect the lack of sensitivity to the transverse length scale (i.e., jet or orifice diameter) of higher order surface instabilities that have been postulated to generate small droplets. Orifice geometry (sharp edge or tube) did not seem to have a significant effect for the very low viscosity liquid CO_2, but did impact droplet size for higher viscosity jet fluids. Larger droplets and a more uniform distribution were produced when silicone fluid was injected from the tube nozzle. Finally, at low *We* in regime 1, jet viscosity seemed to have little effect on mean droplet size. In the transitional breakup regimes, droplet diameters appeared to increase slightly with viscosity.

7. For liquid CO_2 injection under deep ocean conditions, a variety of solid hydrates were observed to form, depending mainly on jet velocity, provided that temperatures and pressures were within the hydrate stability regime. At low CO_2 flow rates, in instability regime 1, thin film hydrate tubes are likely to form on the jet surface. Hydrate tubes were not evident in the transitional breakup regimes 3 and 4, but thick hydrate tubes did form for some cases (with sub-zero CO_2 temperatures) in the atomization regime 5. The streamwise growth rate of the thick hydrate tube appears to scale with CO_2 flow rate.

8. Pre-breakup hydrate formation appears to affect the size distribution of the droplet phase primary by changing the effective geometry of the jet. When a hydrate tube forms, the interface between the CO_2 and water begins at the end of the tube, which may have a different size and shape opening than the original orifice. Furthermore, flow through the tube will alter the jet inlet velocity distribution, producing more time for boundary layer growth. In the case of thick tubes, hydrate branches will divert some of the CO_2 out of the main jet flow and could produce larger droplets.

9. CO_2 droplet concentration was determined to be a critical factor which influences agglomeration. High flow rates corresponding to transitional or atomization breakup generate large numbers of droplet in close proximity near the orifice. This enhances the probability of contact and agglomeration. Aggregate droplet clusters were not observed frequently in the varicose or transitional breakup regimes where droplet concentration is

relatively low. Droplets aggregated readily on contact, but the hydrate films on their surfaces prevented coalescence.

10. Severe hydrate blockage occurred in some tests. There was some evidence that support the proposal by other researchers that certain materials (e.g., steels) are more prone to blockage since hydrates adhere well to them. Tests performed with plastic nozzles resulted in hydrate blockages that were relatively easy to expel.

1 BACKGROUND

1.1 Ocean Sequestration of Anthropogenic Carbon Dioxide

Conventional means to reduce greenhouse gas emissions include expansion of nuclear power, energy conservation, switching from coal and oil to a lower-carbon fuel such as natural gas, upgrading the efficiencies of fossil fuel energy systems and displacement of fossil fuel by renewable energy sources. Another approach is to sequester anthropogenic CO_2 captured from fossil fuel power systems away from the atmosphere, either in the deep ocean, underground, or in a stable (long-term) biological reservoir.

CO_2 may be discharged into the deep ocean as a liquid or solid as depicted in Figure 1.1 (Auerbach, 1996), where it can remain isolated from the atmosphere for centuries. The figure shows several methods that have been proposed to implement ocean sequestration including the generation of a sinking plume of CO_2 dissolved in sea water; discharge through stationary or moving conduits at intermediate depths (around 1,000 m) where the liquid CO_2 is buoyant; discharge below around 3,000 m where the CO_2 will sink and accumulate on the seafloor; and disposal as blocks of dry ice. In the near term, direct injection of liquid CO_2 at intermediate depths appears to be the most practicable alternative.

Liquid CO_2 jets discharged into the deep ocean through injectors at the end of a submerged conduit are hydrodynamically unstable and will break up into a dispersed droplet phase. Dissolution of CO_2 increases the density of the seawater in the resulting droplet plume and decreases its pH. This CO_2-enriched and acidified seawater subsequently is diluted and dispersed by ocean turbulence and currents.

Below a few hundred meters depth in the ocean, pressures and temperatures allow the formation of solid CO_2 hydrate. This phase occurs at the interface between the discharged liquid CO_2 and seawater and can, therefore, affect jet instability and break up; CO_2 droplet interactions (e.g., agglomeration) and transport; and impede the dissolution of CO_2 into the seawater. Furthermore, hydrate blockage of internal flow passages or nozzles of CO_2 injection systems pose a significant operational concern.

The viability of deep ocean CO_2 sequestration as a means to mitigate climate change depends on two primary issues: (1) the effectiveness of this strategy in reducing atmospheric CO_2 levels over time and (2) impacts on the marine environment. Models are the obvious means to determine whether discharging anthropogenic CO_2 into the deep ocean will provide any significant benefits to the global climate; laboratory experiments are of limited value. Assessing the associated impacts on the marine environment, however, involves phenomena occurring at much smaller length and time scales, some of which can be investigated in the laboratory. A major concern related to CO_2 ocean sequestration is reduction in seawater pH in the area around the discharge site and how the local benthic ecosystems respond to these changes. Since the magnitude and extent of seawater acidification depend on the initial size spectra of the dissolving dispersed CO_2 phase and its transport by buoyancy and advection, the present study focused on liquid CO_2 droplet formation and dynamics under deep ocean conditions.

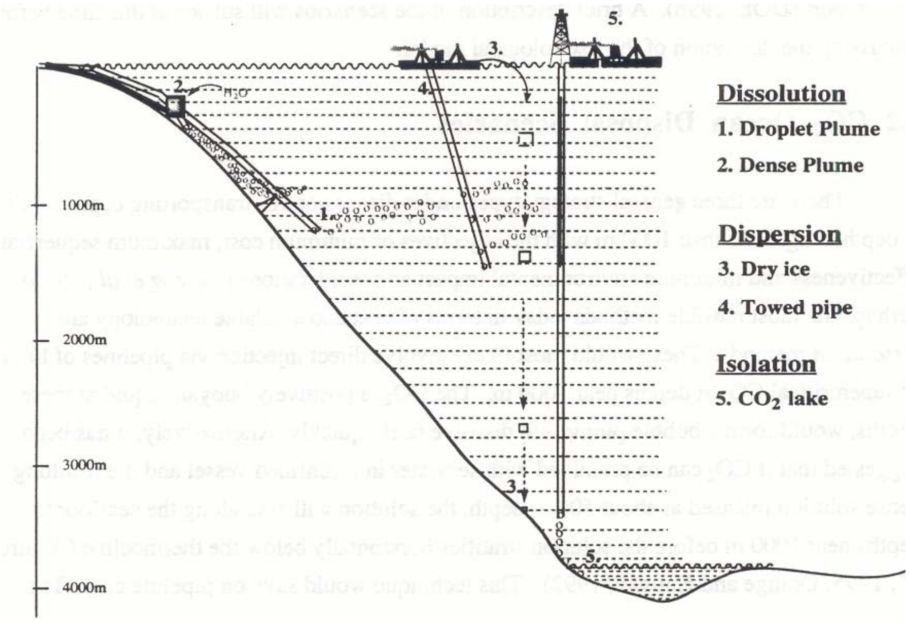

Figure 1.1 Schematic illustration of CO_2 ocean disposal scenarios (from Auerbach, 1996).

1.2 Literature Review

Hydrodynamic instabilities result in the breakup into droplets of liquid jets of CO_2 discharging into sea water. Jet instability has been studied for more than 165 years via experimental, theoretical and numerical approaches. Major investigations are summarized in Table 1.1. The majority of investigations have focused on liquid-gas systems (e.g., liquid jets discharging into air). Liquid-liquid jet instability, which is relevant to CO_2 ocean sequestration, has not been investigated as extensively as liquid-gas systems. While there are similarities between liquid-liquid and liquid-gas phenomena, there are some very important differences. For example, in liquid-gas systems, the gas can usually be treated as an inviscid fluid and pressure may be assumed to be constant on the liquid-gas interface, while in liquid-liquid systems, viscosity of both fluids are important and dynamic pressure variations exist on the interface.

Liquid jet breakup is driven by a competition between cohesive and disruptive forces. Instabilities that can lead to deformation of the jet surface may be amplified or damped. The dominant mode of instability depends on a number of factors, including jet velocity and fluid properties, and manifests itself in the appearance of the disintegrating jet. Studies have identified a number of distinct flow regimes wherein breakup apparently proceeds by different mechanisms that change the characteristics of the generated droplet ensemble. An understanding of the boundaries of these regimes is important in order to be able to anticipate the type (i.e., size; mono- or polydispersion) of droplets produced by different jet breakup scenarios.

Table 1.1 Previous studies of cylindrical liquid jet instability.

		Laminar								Transitional and Turbulent	
		Linear				Nonlinear					
		Temporal		Spatial		Temporal		Spatial			
		Liquid-Air	Liquid-Liquid	Liquid-Air	L-L	Liquid-Air	L-L	Liquid-Air	L-L		
Theory	Inviscid	Rayleigh (1878)	Tomotika (1935)	Keller (1973) Lieb(1986) Pimbely(1976) Bogy(1978)		Yuen (1968) Lafrance (1975) Chaudhary (1980)	Pimbley(977) Bogy (1978)	Pimbley&Lee (1977) Bogy(1978) Torpey (1989)			
	Viscous	Weber (1931) Ohnesorge(1936) Teng (1994)	Tyler (1934) Tomotika (1935) Meister&Scheele (1969) Kitamura (1986) Teng (1994)	Lieb (1986) Bogy (1978)		Green (1976)					
Numerical studies	Inviscid	Mansour & Lundgren(1990) Papageorgiou & Orellana (1998)									
	Viscous	Egger & Dupont (1994) Ashgriz & Mashayek (1995)			Richards (1994,1995)	Shokoohi & Elrod, 1987 Papageorgiou (1993)		Mansour & Lundgren (1990)	Homma *et al.* (2000)		
		Liquid-Air				Liquid-Liquid				L-A	L-L
Experimental studies		Halenlein (1932) Goedde & Yuen (1970) Arai & Amagai (1999)		Donnelly & Glaberson (1966) Kowalewski (1996) Lin (2003)		Hayworth & Treybal (1950) Kumar & Hartland (1984,1996) Skelland & Walker (1989) Longmire *et al.* (2001)		Kitamura *et al.* (1986) Das (1997) Milosevic & Longmire (2002)			Masutani & Adams (2000) Tang *et al* (2002, 2003)

1.2.1 Experimental Studies

Figure 1.2 from Grant and Middleman (1966) shows the typical evolution of jet breakup length observed as jet discharge velocity is increased. Breakup length is the distance from the discharge orifice to the point where discrete droplets are formed. Upstream of this point, the jet remains continuous and intact.

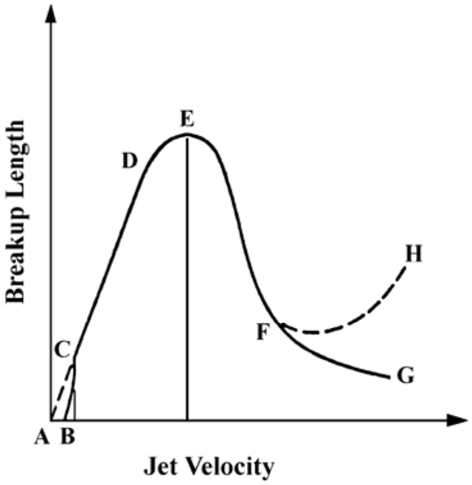

Figure 1.2 Variation of jet breakup length with velocity (from Grant & Middleman, 1966).

At very low velocities, large droplets are produced at the orifice (sometimes called drip flow). As velocity is increased, a laminar jet forms (point C) and breakup length increases linearly until it reaches a maximum. In this Rayleigh instability regime, axisymmetric disturbances grow in amplitude on the jet surface, eventually pinching off the jet column to generate a stream of essentially monodispersed droplets about 2 times of the initial jet diameter. Surface tension force is dominant over this range. The Rayleigh instability regime has been the subject of extensive theoretical analyses (Tomotika, 1935 and 1936; Weber, 1931; Teng *et al.,* 1994).

After attaining a maximum value, breakup length decreases. Droplet size remains nearly uniform and larger than the jet diameter (for liquid jets discharging into a gas). This flow regime is referred to as the "first wind-induced breakup." Hydrodynamic forces arising from the relative velocities of the jet and ambient fluid accelerate breakup. Beyond point F on the curve, the relative influence of surface tension decreases and breakup is determined by hydrodynamic forces. The term "sinuous instability" is often used to describe the process in this "second wind-induced breakup regime" and droplet size decreases and becomes irregular (polydispersed). Breakup length can increase slightly or decrease steadily before falling to zero. At higher velocities, instability begins on the jet surface and produces a polydispersed spray of fine droplets immediately downstream of the orifice; however, the core of the jet may remain intact and this filament can persist for some distance before disintegrating (Masutani & Adams, 2000). A single breakup length may not be adequate to describe the jet in this atomization regime and also during the latter stages of the second wind-induced breakup. Reitz & Bracco (1986) propose that both intact-surface and intact-core lengths be used to describe the jet.

The preceding regimes have been identified based on observations of liquid jets discharging into a gas. Figure 1.3 from Kitamura & Takahashi (1986) presents measured breakup lengths and droplet sizes for a liquid-liquid system (i.e., water injected into carbon tetrachloride). The figure also contains sketches of the jet appearance at different velocities. The general shape of the breakup curve resembles Figure 1.2; however, droplet size non-uniformities (indicated by the height of the bars around the droplet diameter data points) appear earlier and can be much more pronounced than in most liquid-gas systems. Based on the rather disorderly mode of breakup, Kitamura and Takahashi (1986) proposed that the process be designated as turbulent once jet velocity exceeds the value corresponding to the maximum jet length.

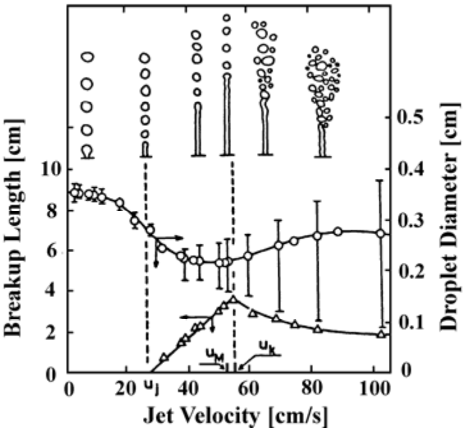

Figure 1.3 Jet breakup length and droplet size as functions of velocity for a liquid (water) jet discharging into liquid carbon tetrachloride (from Kitamura & Takahashi, 1986). Orifice diameter was 0.118 cm. The figure also shows sketches of the appearance of the jet.

In order to extend the application of case-specific data and to develop general relationships, attempts have been made to correlate experimental observations against the non-dimensional Reynolds (Re_D) and Ohnesorge (Z) numbers (Ohnesorge, 1936). Figure 1.4a provides an example of the experimentally determined boundaries of the primary instability regimes determined from liquid-gas experiments. The figure also indicates that breakup can be influenced by additional factors, such as ambient fluid density (and other properties) and the initial state of the jet, which are not accounted for by Re_D and Z. A complete characterization of the breakup process probably requires that regime boundaries be presented as surfaces rather than lines, such as in the conceptual sketch prepared by Reitz (1978) shown in Figure 1.4b.

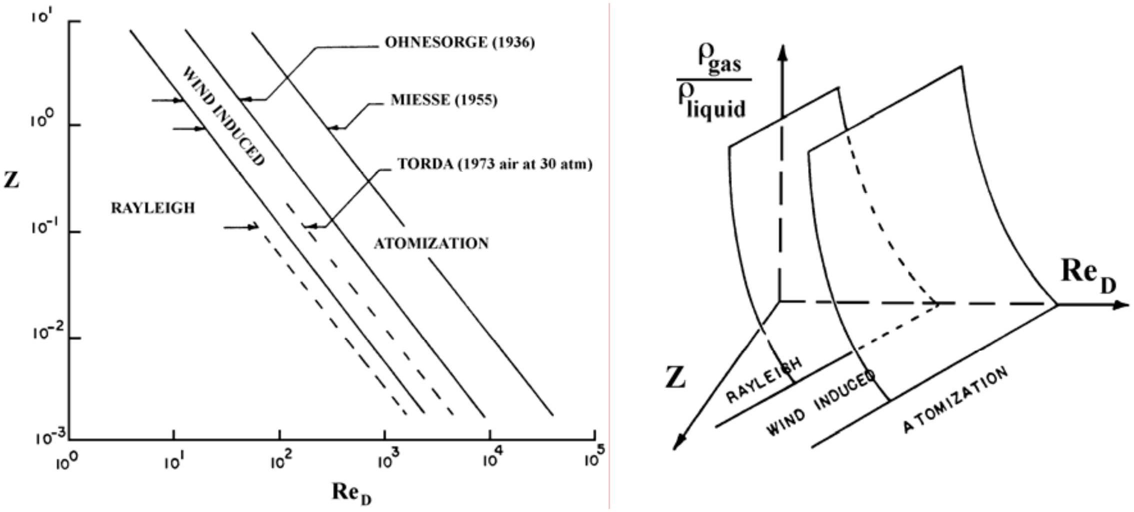

(a) (b)

Figure 1.4 (a) Instability regimes as a function of Ohnesorge (Z) and Reynolds (Re_D) numbers; the dotted lines show a shift in the boundaries due to ambient fluid density (from Reitz & Bracco, 1986); (b) conceptual sketch by Reitz (1978) showing regime boundaries as surfaces to account for the relative densities of the jet and ambient fluids.

1.2.2 Theoretical Studies

Theoretical investigations have primarily considered either perturbation-type or one-dimensional models (Mashayekhi, 1994) and have been generally restricted to the laminar flow regime. The approach taken falls into one of two categories, namely, temporal (or Lagrangian) or spatial (or Eulerian) analysis. In temporal analysis, an infinite jet, stationary relative to a moving observer, is considered and the growth rate of the disturbance amplitude is determined. In spatial analysis, the growth of a disturbance propagating along a semi-infinite jet is considered with the nozzle (i.e., inlet boundary) conditions fixed. Linear or nonlinear perturbation techniques or direct numerical methods are employed in both temporal and spatial analyses.

Perturbation analyses were applied in early investigations where a surface disturbance to the jet was imposed to produce unstable waves on the jet surface. These studies focused on deriving a viable dispersion equation (i.e., the relationship between the amplitude growth rate and the wave number) and identifying the most unstable wave that causes the jet to disintegrate.

Rayleigh (1879) used linear perturbation to derive the first analytical description of the temporal instability of both an inviscid and a viscous incompressible jet in gas (the effects of the ambient fluid on jet instability were assumed to be negligible in Rayleigh's analysis). He showed that an axisymmetric harmonic disturbance of the form

$$r = 1 + \varepsilon_0 \exp(\omega t - ikz) \tag{1.1}$$

grows in time according to

$$\omega = \left[\frac{I_1(k)}{I_2(k)} \left(1 - k^2\right) k \right]^{1/2} \tag{1.2}$$

where ω is the growth rate, ε_0 is the initial disturbance amplitude, *k* is the disturbance wave number, and I_0 and I_1 are the modified Bessel function of the first kind. Rayleigh 's result is valid only for low-velocity jets. His maximum-instability theory formed the basis for subsequent studies of instability of viscous, cylindrical liquid jets.

Weber (1931) derived a dispersion equation for liquid-gas systems that included both the influence of viscosity and hydrodynamic effects. The motion of both the jet and the ambient fluid were modeled as Stokes flows by Tomotika (1935), who extended Rayleigh's analyses for a single jet fluid phase to two phases comprising both the jet and the ambient fluid. Tomotika's dispersion equation is relatively complicated and he was only able to obtain a numerical solution to his general dispersion equation for the limiting case of a highly viscous liquid jet discharging into another highly viscous liquid with inertial effects neglected. Teng (1994) derived a general, explicit dispersion equation for the laminar instability of cylindrical liquid jets in both liquid-gas and liquid-liquid systems. Under equivalent conditions, Teng's dispersion equation reduces to the results of Rayleigh, Weber, and Bogy, and agrees with Tomotika's relationship.

The instability models described above are based on linear relationships. According to these linearized theories, surface deformation of the jet is harmonic and jet breakup produces uniformly sized droplets. Linear theory predicts well the disturbance growth rate measured by Donnelly and Glaberson (1966) and Goedde and Yuen (1970); however, linear analyses cannot explain the formation of satellite droplets (i.e., small droplets that accompany the primary train of larger droplets) that are observed in both liquid-liquid and liquid-gas systems.

Yuen (1968) was the first to analyze the formation of non-uniform-size droplets. He developed a third-order perturbation solution for a cylindrical, inviscid, liquid jet in gas, and showed that non-uniform-size droplets form as results of nonlinear effects which were neglected in Rayleigh's analysis. It is believed, however, that Yuen's analysis is flawed: errors occur at the second order solutions for both the disturbance function and the velocity potential. Lafrance (1975) and Chaudhary (1977, 1980) performed similar nonlinear analyses; however, the undisturbed surface tension pressure term is missing in Lafrance's equation and Chaudhary derived boundary conditions using Bernoulli's equation. In the analyses of Yuen, Lafrance, and Chaudhary, the original nonlinear problem was posed by directly applying Rayleigh's linearized initial condition, which is inconsistent with the assumption of finite initial disturbance. As a result, the disturbance function in the problem for each order has to be assumed arbitrarily, without regard to the constraint of the original nonlinear problem. This would likely influence the accuracy of the nonlinear analyses.

Both the linear and nonlinear methods mentioned above entail normal-mode type analyses. Berger (1988) noted that normal-mode analysis ignores the initial growth phase of the disturbances and perturbations to the ambient flow. He treated the jet instability as an initial-value problem and after linearization showed that the initial instability does not grow exponentially, as normal-mode linear analysis predicts. Teng *et al.* (1995) conducted a third order perturbation analysis to examine liquid-core instability in inverted annular flow. The shape of the liquid/vapor interface and the breakup pattern of the liquid core are found to be influenced strongly by the disturbance mode and initial disturbance amplitude. Either uniform or non-uniform surface distortions can form.

1.2.3 Numerical Studies

Schulkes (1993) and Papageorgiou & Orellana (1998) derived the complete one-dimension equations governing the motion of an axisymmetric inviscid liquid jet. Schulkes solved his newly derived equations with proper boundary conditions numerically and observed that, as disturbances grow, the characteristic axial length scales typically became of the order of the radius of the jet. This result brings into question the validity of the one-dimension approximation of the nonlinear liquid jet.

Shokoohi & Elrod (1987) used a vorticity-stream function formulation to simulate the dynamics of a liquid jet. Mansour and Lundgren (1990) used a boundary-integral method to study the instability of an inviscid jet in air. They calculated the main and satellite drop sizes as functions of the disturbance wave number. Tjahjadi *et al.* (1992) investigated the breakup of a long liquid filament in a quiescent viscous fluid by a boundary-integral calculation to study the evolution of the filament as a function of the viscosity ratio of the fluids and the initial wave numbers of the interface perturbation. Ashgriz and Mashayek (1995) studied an axisymmetric incompressible Newtonian liquid jet in vacuum and zero gravity using the volume of fluid (VOF) method. Richards *et al.* (1993, 1994, 1995) used the VOF method in liquid-liquid jet breakup for the interface reconstruction and a finite difference method to solve the Navier-Stokes equations. Instead of a boundary condition, the interfacial tension was coupled in the moment equations by a continuum surface force (CFS) model, which was first introduced by Brackbill *et al.* (1992). Homma *et al.* (2000) numerically investigate a laminar jet breakup into drops in liquid-liquid systems by a front tracking / finite difference method with cylindrical axisymmetric coordinate. For moderate Weber numbers, two sizes of the drops are observed as a result of end-pinching and capillary wave instability that both influence the drop size. The numerical method has been extended to cases where mass and/or heat transfer occurs.

1.3 Scope of Present Study

While theoretical and numerical studies performed to date provide significant insight into liquid jet instability, results have generally been limited to capillary and laminar flow situations. The aforementioned perturbation analyses and one-dimensional models apply to laminar jet flows at low velocities. Many important applications, including a number of proposed scenarios for direct injection of liquid CO_2 into the deep ocean, however, involve the breakup of transitional and turbulent jets. Jet instability theory is deficient in these flow regimes and numerical solution of the governing equations are difficult or intractable. Hence, experiments continue to remain the only way to provide information on liquid-liquid jet disintegration over the entire range spanning the laminar to turbulent flow regimes.

The deficiency in our understanding of the instability and disintegration of transitional and turbulent liquid jets warrants further investigation. Specifically, with respect to the present CO_2 ocean sequestration program, there is a critical need for information on the size spectra of droplets produced when CO_2 is discharged through submerged conduits in the deep ocean to evaluate the magnitude and extent of local changes in sea water chemistry induced by dissolution of this dispersed phase, and to design appropriate facilities and protocols to minimize these changes. Toward this end, an experimental study of liquid-liquid jet breakup phenomena was undertaken. Flow conditions (e.g., pressures, temperatures, fluids, flow rates) relevant to CO_2 ocean disposal were the focus of this investigation.

Laboratory experiments were conducted to obtain a relatively comprehensive data set on the size spectra of droplets generated by the breakup of jets of various liquids discharging into water; and to secure qualitative insight via flow visualization of the breakup phenomena. Jet fluids included liquid CO_2 and silicone fluid, which served as an easily-handled analog to CO_2. For the sake of completeness, we have also included information in this report on other tests conducted for an with high viscosity oils for an unrelated investigation of deep oil spills (Masutani & Adams, 2000). Including the oils, viscosities of the jet fluids ranged over more than three orders of magnitudes. Emphasis was placed on the largely unstudied class of transitional and turbulent jets, and measurements were conducted at different jet velocities and with various size jet discharge orifices.

As mentioned previously, the formation of solid hydrate during deep ocean disposal of CO_2 may pose an operational problem due to blockages in the transport and injection systems and could influence droplet formation and dissolution. A number of experiments were therefore conducted to investigate CO_2 hydrate blockages in internal flow passages and to determine if hydrates significantly impact jet stability.

The primary objectives of this study were:

- Identify the mechanisms and characteristics of liquid-liquid jet breakup into droplets under conditions relevant to CO_2 ocean disposal; provide data on breakup regimes similar to Reitz and Bracco (1986) that can be applied to the design of injection systems (i.e., injector orifice diameters and flow rates).
- Obtain data on CO_2 droplet size spectra over the entire range of jet instabilities for use with current plume models to estimate dispersion and dissolution of the discharged CO_2.
- Investigate CO_2 hydrate formation under deep ocean conditions to assess flow assurance threats and to understand the influence of this solid phase on droplet formation and dissolution.

2 EXPERIMENT FACILITIES

2.1 Droplet Size Measurement Techniques

For liquid droplet measurements, optical particle size methods are the general choice. Optical methods can be conveniently grouped into two categories: imaging and non-imaging techniques.

Imaging techniques include photography, holography and automatic image analysis, and high-resolution imaging and digital processing techniques. strides have been made in the use of digital image processing techniques for data acquisition in the last two decades. Technique such as fringe thinning, fringe clustering, fringe tracing, phase shifting, polarization stepping and Fourier transform methods have significantly contributed to the automation of data acquisition. A variety of electronic image sensors are available today, such as charge-coupled devices (CCD), charge injection devices (CID) and metal oxide silicon capacitors (CMOS). Of these, CCDs are probably the most widely used.

Non-imaging techniques include laser-based techniques such as single particle counter systems and Fraunhofer diffraction methods, x-ray radiography, phase Doppler particle analysis, and planar laser-included fluorescence.

In the current study, image analysis of digital video data and a non-imaging Phase Doppler Particle Analyzer (PDPA) were employed to measure droplet size. The PDPA also has the capability to perform simultaneous measurements of droplet velocity. The two different measurement techniques were needed to accommodate the full range of droplet sizes from submillimeter to more than 20 mm that were encountered in the experiments.

The PDPA optics were optimized to provide a broad measurement range extending from 0.082 to 4.056 mm. Larger droplets formed during laminar and transitional breakup were measured using digital video data collected with three 3-CCD digital camcorders, two SONY PD100s and one PD150. Results indicate that droplets with diameters greater than approximately 3 mm can be reliably sized by digital video image analysis.

2.1.1 Phase Doppler Particle Analyzer

2.1.1.1 Major Components of the PDPA

The PDPA comprises the following major components (Figure 2.1):

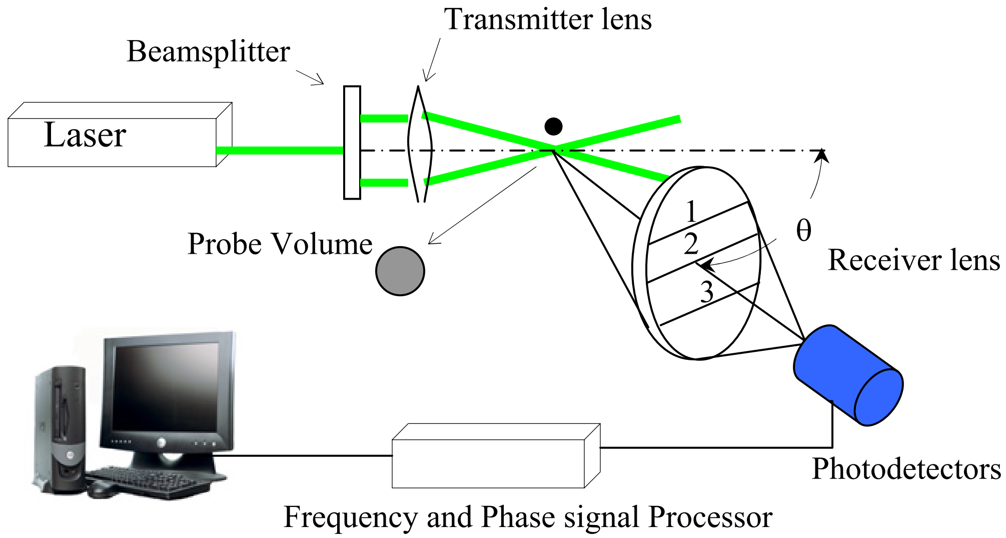

Figure 2.1 Major components of the PDPA (Replotted from http://www.tsi.com/).

(1) Air-cooled Argon-Ion laser; maximum 150mW power output (all lines).
(2) Transmitting optics including a beamsplitter, fiberoptic link, and focusing lens.
(3) Receiver Module (RCM) comprising photomultiplier tubes (PMT), tube preamplifiers and the optomechanical hardware. The RCM collects laser light scattered by droplets passing through the optical probe volume and converts it into electronic signals.
(4) Real-time Signal Analyzer (RSA) and PC that processes the phase Doppler signals using a discrete Fourier transform method to obtain size and velocity data that is stored in the PC.

2.1.1.2 PDPA Measurement Principles

Bachalo (1980) derived the basic theory for dual beam light scattering and interference that constitutes the basis of operation of the PDPA. He determined that the phase shift of light scattered by refraction or reflection from two intersecting laser beams could be used to size spherical particles. PDPA measurements are performed utilizing a small, non-intrusive optical probe volume defined by the intersection of two laser beams. The intersection of the two beams creates a fringe pattern (i.e., alternating light and dark bands) within the probe volume. As a particle passes through the standing fringe, it scatters light that is collected by a receiving lens located at an off-axis collection angle. The lens projects a portion of the scattered light onto 3 photodetectors located at slightly different angles from the probe volume. Each detector produces a Doppler burst signal with a frequency proportional to the particle velocity (Figure

2.2). The phase shift between the Doppler burst signals from two different detectors is proportional to the size of the spherical particles. Figure 2.3 provides theoretical predictions showing that the phase shift is linearly related to the diameter of the scattering particle. The figure shows the calculated phase shift between signals from three detectors (i.e., between detectors 1 and 2 ($\phi_{1\text{-}2}$) and 1 and 3 ($\phi_{1\text{-}3}$)) as a function of non-dimensional particle diameter. Two pairs of detectors are employed to eliminate ambiguities that might occur when the droplet size range is large.

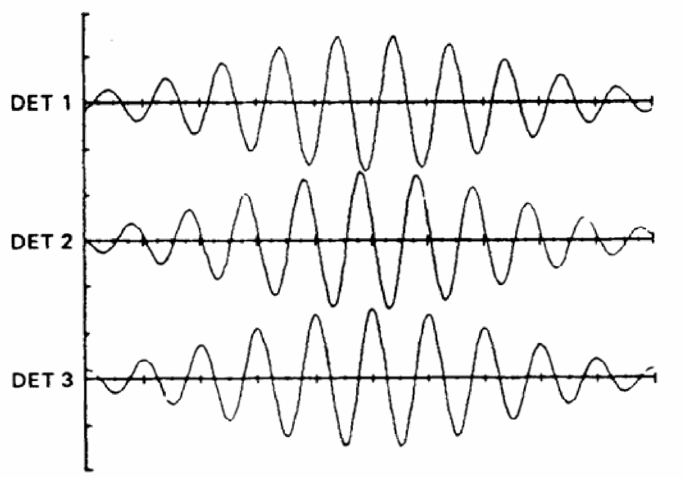

Figure 2.2 Phase shift of signals from three separate photodetectors monitoring light scattered by the same particle traversing the interference fringes at the intersection of two laser beams. The signals have been high-pass filtered to remove the Gaussian pedestal. Figure from Bachalo & Houser (1984).

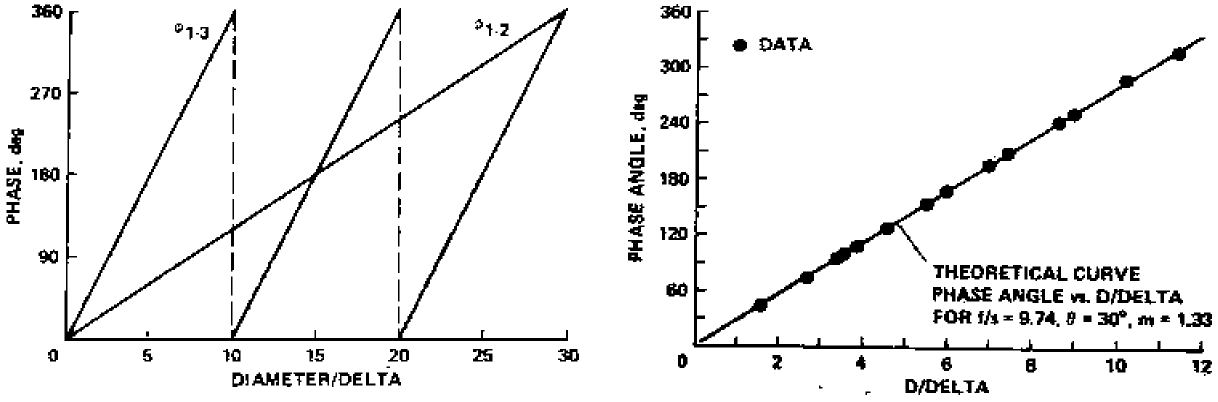

(a) (b)

Figure 2.3 Theoretical prediction showing the dependence of phase shift on dimensionless droplet size: (a) relationship for signals from three photodetectors and (b) comparison with experiment. Figures from Bachalo & Houser (1984).

2.1.1.3 PDPA Measurement Error

The theory of operation for the PDPA is based on a Mie scattering analysis that assumes the particle is spherical and its surface is smooth. Departures from this condition can result in errors. Figure 2.4 provides examples of the types of measurement errors that may occur when a non-spherical particle crosses the optical probe volume.

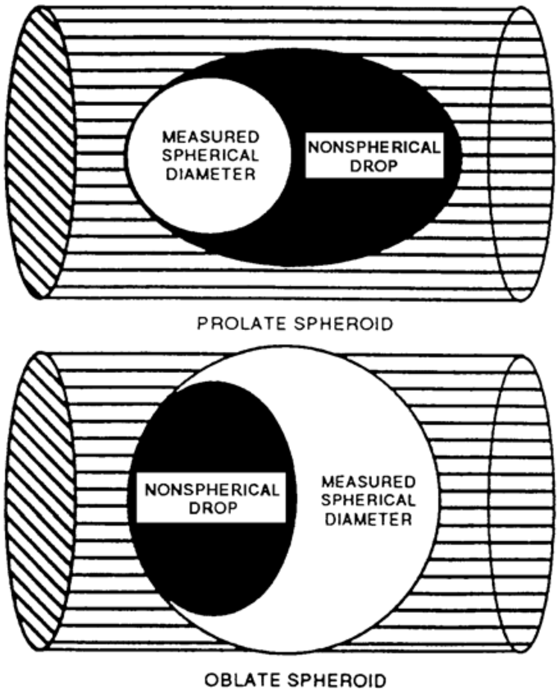

Figure 2.4 Examples of PDPA response to non-spherical droplets (Bachalo, 1994).

2.1.2 Image Analysis

Digital video image analysis was employed to estimate the size of liquid droplets that fall outside the measurement range of the PDPA (i.e., are larger than about 4 mm). Our tests suggest that, for the camera optics employed in the study, video image analysis can reliably size droplets greater than approximately 3 mm in diameter. The overlap between the measurement size ranges of the PDPA and video image analysis (i.e., 3 mm to 4 mm) is exploited to prepare composite size spectra and to provide a check of the accuracy of the data sets measured by the two techniques.

Video frames from the digital camcorder records are sampled at selected time intervals over the course of an experiment (for example, to provide enough time between frames for droplets to move out of the field of view to avoid being counted more than once). These frames are analyzed using Matlab programs including functions that we developed from the Matlab Image Processing Toolbox. Droplet size is estimated by comparing the projected area (in pixels) of a droplet with a size reference standard installed in the flow field and recorded with the video system.

2.1.2.1 Image Analysis Algorithms

Algorithms have been developed to estimate droplet size depending on image quality. For droplet images with good contrast, such as the one of a liquid CO_2 drop shown in Figure 2.5a, the Matlab Image Processing Toolbox provides standard functions to find object edges and to determine the number of pixels within these edges (Figures 2.5c and 2.5b, respectively). When image quality is poor, as in Figure 2.6a where a portion of the droplet overlaps with the viewport wall in the background, or when two or more droplets overlap in the image, the standard Matlab functions may fail to calculate the pixel count (projected area) correctly (Figure 2.6 b). An alternative algorithm was therefore developed for this situation that requires manually identifying about 8 points nearly evenly distributed around the edge of the droplet. The Matlab cubic spline interpolation function is then employed to perform a curve fit the between those points. The projected area is calculated by integration and the result is shown in Figure 2.6c. This algorithm requires significant user input and is therefore quite time-consuming.

An equivalent diameter is estimated by comparison of the calculated droplet projected area (number of pixels within the droplet edges) with the projected area of known standards such as solid spherical beads of known diameters installed in the field of view of the camcorders. The camcorder optics (i.e., depth of field and magnification) limit sizing ambiguities associated with differences in the position of imaged droplets and the reference size standards along the line of sight of the camcorder.

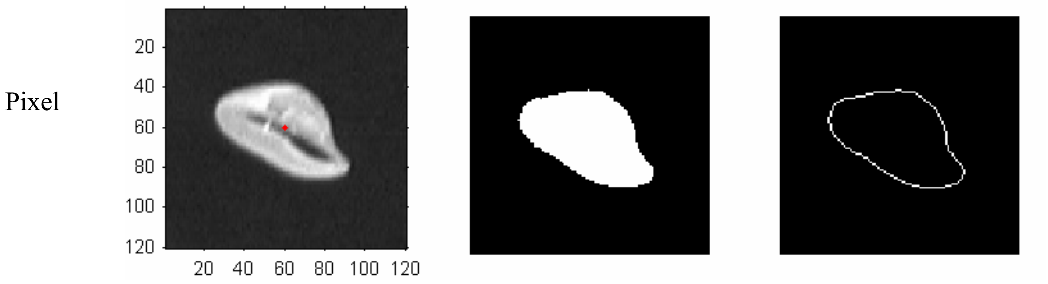

(a) (b) (c)

Figure 2.5 Algorithm to estimate droplet size by image analysis for high quality images. Figure (a) shows the video image of a liquid CO_2 droplet (units shown are in pixels). Figures (b) & (c) show, respectively, the projected area and the edges determined using standard Matlab functions.

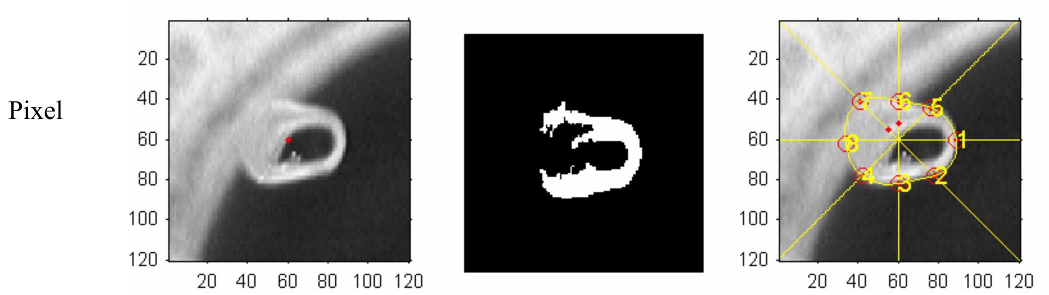

(a) (b) (c)

Figure 2.6 Algorithm to estimate droplet size by image analysis for lower quality images. Figure (a) shows the image of a liquid CO_2 droplet that overlaps with the background viewport wall. Figure (b) indicates that the standard Matlab function fails to calculate correctly the projected area (shown in white). Figure (c) shows the result obtained using the alternative algorithm.

2.1.3 Composite Size Distribution from PDPA and Video Image Analysis

The size ranges of the droplets produced in some of the experiments are relatively broad and exceed the individual measurement ranges of either the PDPA or the digital video image analysis technique. A complete droplet size spectra for such cases required combining the data from these two measurement techniques. A method to do this was developed and is described below.

As noted previously, the PDPA is capable of measuring droplets with diameters between 0.08 to 4.056 mm using the optics we have selected. Image analysis, on the other hand, can reliably size droplets greater than about 3 mm. Our experience indicates that the level of required effort and relative uncertainty associated with sizing droplets smaller than 3 mm is excessive. The effective minimum image analysis measurement size was therefore taken to be 3 mm. The overlap in the measurement size ranges of the PDPA and the image analysis technique (between 3 mm and 4 mm) can be exploited to estimate a composite droplet size spectrum from the two incomplete data sets.

We assume that a complete size spectrum, as shown in Figure 2.7, can be assembled from two partial spectra extending respectively from approximately 0 to 4 mm and ≥ 3 mm. If n is the total number of samples used to calculate the size distribution histogram, then referring to Figure 2.7:

$$n = a + b + c \tag{2.1}$$

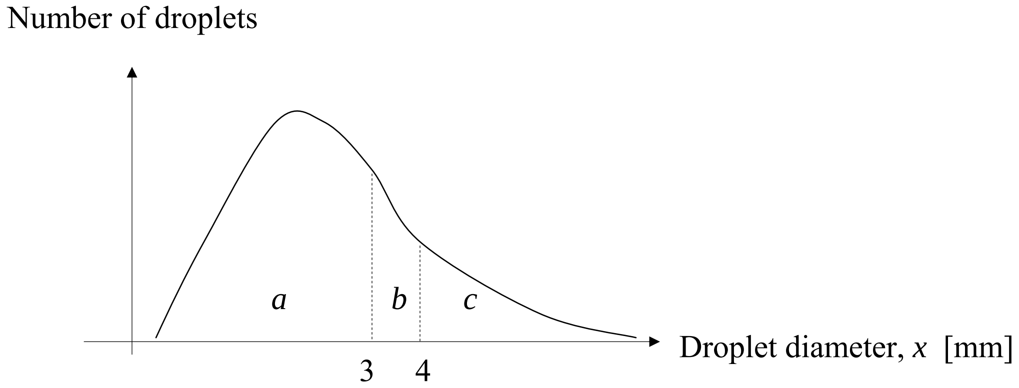

Figure 2.7 Composite droplet size distribution. *a* is the number of drops with $x < 3$ mm; *b* is the number of drops with $3 \le x \le 4$; *c* is the number of drops with $x > 4$ mm.

Consider the hypothetical case where the measurement size ranges of the PDPA and image analysis are not limited and the two techniques are used to determine the size distribution for the same test independently. For the PDPA, the relationship between the number of samples that are used to determine the probability histogram is

$$n_1 = a_1 + b_1 + c_1 \tag{2.2}$$

where, for the actual PDPA which yields an incomplete data set, a_1 and b_1 are measured and known and c_1 and n_1 are unknown (since c_1 lies outside the measurement range of the actual instrument).

For the image analysis data, we have

$$n_2 = a_2 + b_2 + c_2 \tag{2.3}$$

where, once again for the actual situation, b_1 and c_1 can be measured and a_2 and n_2 are unknown.

Since the PDPA and image analysis data are describing the same test, they must have the same Probability Density Function (PDF), *f*(*d*), and Cumulative Distribution Function (CDF), *F*(*d*). Hence,

$$\int_{0.08}^{3} f(x)dx = F(3) - F(0.08) \cong F(3)$$

same for both sets $\Rightarrow \dfrac{a_1}{n_1} = \dfrac{a_2}{n_2}$ (2.4)

$$\int_{3}^{4} f(x)dx = F(4) - F(3)$$

same for both sets $\Rightarrow \dfrac{b_1}{n_1} = \dfrac{b_2}{n_2}$ (2.5)

$$\int_4^{+\infty} f(x)dx = 1 - F(4)$$

same for both sets $\Rightarrow \dfrac{c_1}{n_1} = \dfrac{c_2}{n_2}$ (2.6)

From Equations (2.4), (2.5), and (2.6), we obtain

$$\frac{a_1}{a_2} = \frac{b_1}{b_2} = \frac{c_1}{c_2} \tag{2.7}$$

$$\Rightarrow \begin{cases} c_1 = c_2 \cdot b_1 / b_2 \\ a_2 = a_1 \cdot b_2 / b_1 \end{cases} \tag{2.8}$$

Substitution of (2.8) into (2.2) and (2.3) provides relationships for n_1 and n_2 that only employ data that can be measured (i.e., a_1, b_1, b_2, and c_2). A composite probability distribution function (PDF), $f(x)$, can then be estimated from the incomplete PDPA and image analysis data sets by

$$F(x \le x_j) = \begin{cases} \dfrac{N_{j \text{ from pdpa}}}{n_1} \dfrac{1}{\Delta D} \text{ for } x_j < 3 \\ \dfrac{N_{j \text{ from pdpa/image}}}{n_1} \dfrac{1}{\Delta D} \text{ for } 3 \le x_j \le 4 \\ \dfrac{N_{j \text{ from image}}}{n_2} \dfrac{1}{\Delta D} \text{ for } x_j > 4 \end{cases} \tag{2.9}$$

where N_j is the number of droplets in the diameter class j and ΔD is the diameter class range.

The following constraint also applies

$$\frac{a_1}{n_1} + \frac{b_1}{n_1} + \frac{c_2}{n_2} = \frac{a_1}{n_1} + \frac{b_2}{n_2} + \frac{c_2}{n_2} = 1 \tag{2.10}$$

Codes to calculate composite distributions based on the above approach have been tested using Normal and Weibull distributions. For example, as shown in Figure 2.8, two groups of normal random numbers with the same mean and variance were generated, with 2000 samples in group 1 and 200 samples in group 2. For this example, n_1 = 2000 and n_2 = 200. Samples in group 1 with values greater than 4 and samples in group 2 with values smaller than 3 were then discarded (Figure 2.8 (3) and (4)). The code was used to generate a composite distribution from these two incomplete data sets. The composite distribution should have the same statistics as the original distributions. The corresponding n_1 and n_2 of the composite distribution are 2034 and 204 for this test, which differ by 1.7% and 2.0% from the real values of $n_1 = 2000$ and $n_2 = 200$. Results are shown in the Figure 2.8 (5) and (6). For the values smaller than 3, $f(x)*\Delta D$ was calculated with numbers from group 1. Data from group 2 were used to calculate the $f(x)*\Delta D$ when $x>4$. For $3 \leq x \leq 4$, the numbers from either group 1 (Figure 2.8 (5)) or group 2 (Figure 2.8 (6)) fall in this range can be used to calculate $f(x)*\Delta D$. The application of the code to produce a composite Weibull distribution is shown in Figure 2.9. The PDF and CDF definitions of the Normal and Weibull distributions are given in section 5.3.

Tests of the above method to estimate a composite probability distribution from incomplete PDPA and image analysis size data sets suggest that the results are reasonably accurate, provided that there is no measurement bias in these incomplete data sets; i.e., that all droplets (regardless of their size) within their respective measurement size ranges are sampled equally by the PDPA and by the image analysis technique.

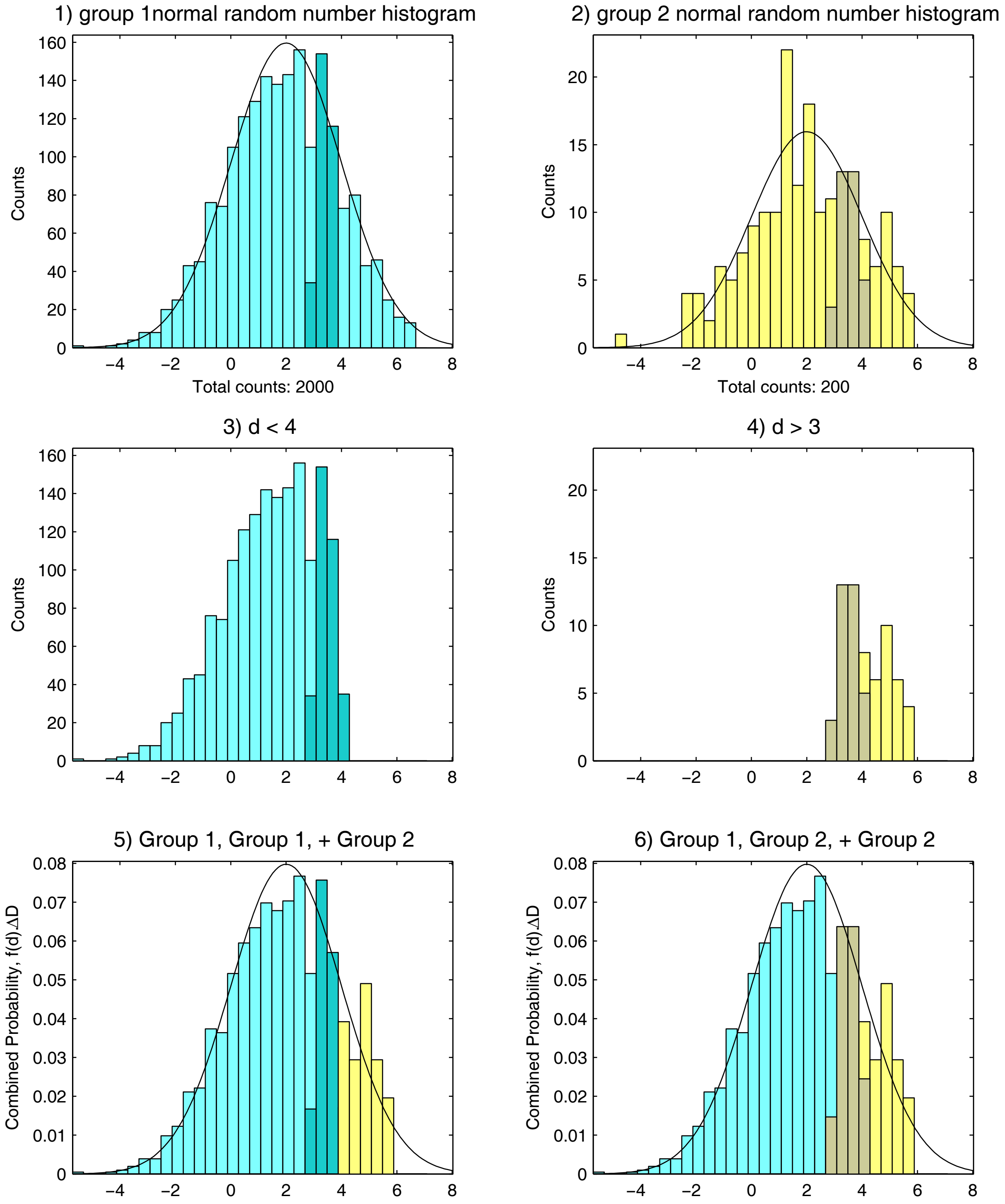
1) group 1normal random number histogram

2) group 2 normal random number histogram

3) d < 4

4) d > 3

5) Group 1, Group 1, + Group 2

6) Group 1, Group 2, + Group 2

n_1=2034; a_1= 1346; b_1=339; ε_1= 1.7%

n_2=204; b_2= 34; c_2=35; ε_2= 2.0%

Figure 2.8 Composite Normal distribution. A total of (1) 2000 and (2) 200 random numbers were generated from the Normal distribution with the same parameters. Samples in group 1 with values greater than 4 and samples with values smaller than 3 in group 2 were discarded. New composite distributions obtained from samples shown in (3) and (4) have the same statistics as the original distributions in (1) and (2). The solid line is the Normal probability density function with the same parameters as histograms (1) & (2).

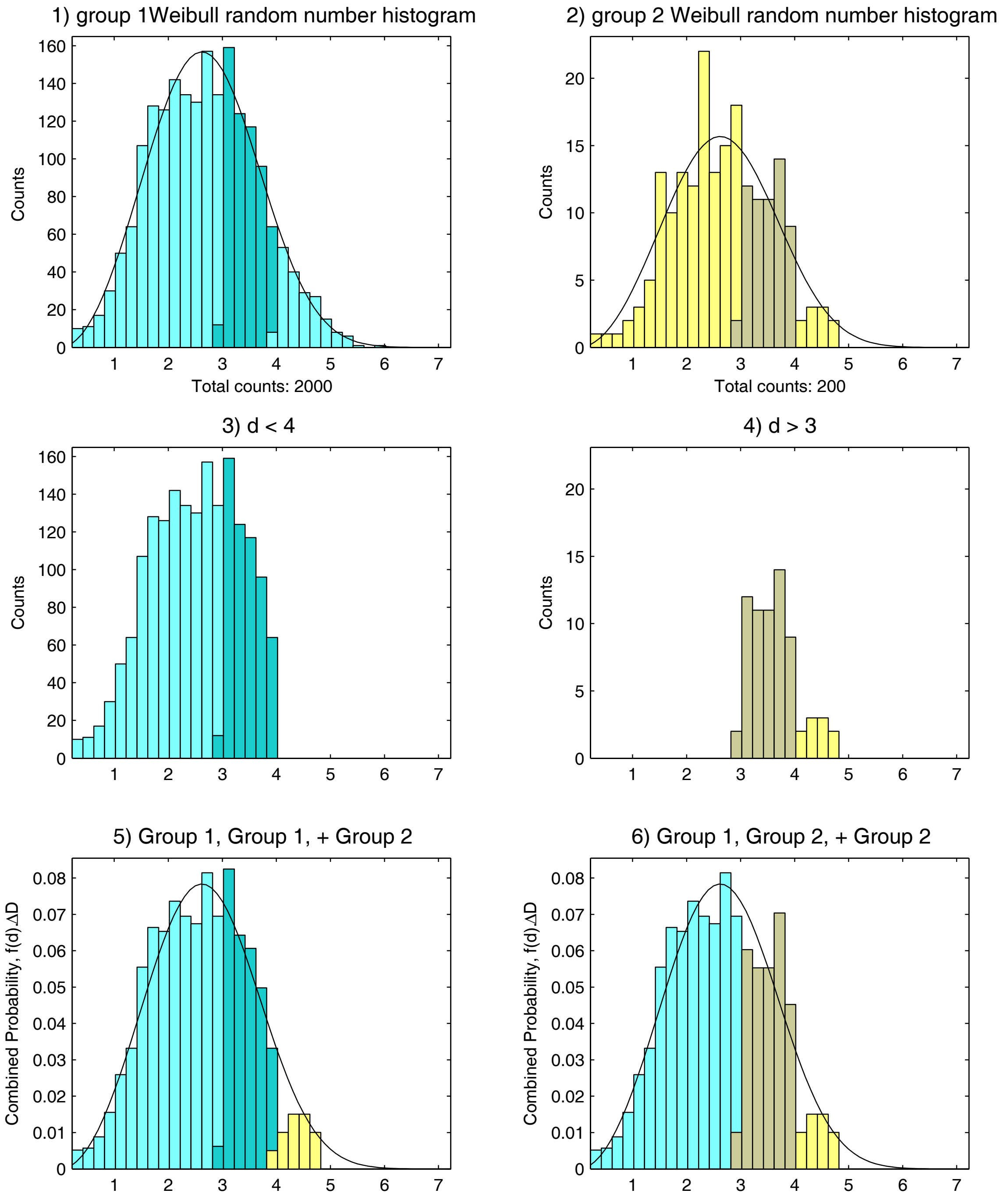

n_1=1928; a_1= 1240; b_1=572; ε_1= -3.6%

n_2=199; b_2= 59; c_2=12; ε_2= -0.5%

Figure 2.9 Composite Weibull distribution. A total of (1) 2000 and (2) 200 random numbers were generated from the Weibull distribution with the same parameters. Samples in group 1 with values greater than 4 and samples with values smaller than 3 in group 2 were discarded. New composite distributions obtained from samples shown in (3) and (4) have the same statistics as the original distributions in (1) and (2). The solid line is the Weibull probability density function with the same parameters as histograms (1) & (2).

2.2 Experimental Details

Experiments were conducted to examine the instability and breakup of jets of various fluids issuing from a number of different orifices into tap water (WT), natural surface sea water (WN,) or synthetic sea water (WS). Injection conditions were selected to span the entire range extending from laminar to turbulent jet flow. Jet fluids were chosen to: (1) accommodate specific research project objectives; i.e., to simulate CO_2 ocean sequestration; and (2) to provide a relatively wide range of jet fluid properties that would provide insight into how these properties affect breakup.

Three experimental facilities were employed to conduct the experiments. Since liquid CO_2 will boil if it is not maintained at high pressures and relatively low temperatures, injection was performed in a pressure vessel that was designed and fabricated to simulate the deep ocean environment. Two atmospheric pressure water tanks were used to conduct tests where the jet fluid does not need to be pressurized to avoid flash evaporation (e.g., silicone fluids).

2.2.1 Liquid CO_2 Injection Tests

A photograph of the Deep Ocean Simulator (DOS) is provided in Figure 2.10. Figure 2.11 shows the general experimental set up employed in the liquid CO_2 injection tests. Optical access for the PDPA and video camcorders was provided by 18 viewpoints (9.8 cm diameter clear aperture) fitted with annealed acrylic windows. To provide illumination for the digital video camcorders, three underwater lamps were installed inside the DOS. One lamp is positioned at the top and two on the bottom of the tank submerged in water. External video lamps were employed as necessary (Figure 2.12). Calibrated spherical beads were installed in the field of view of the video cameras to serve as size reference standards for the digital video image analysis (see Section 2.2.2).

During operation, the DOS is partially filled with tap or seawater chilled to a selected temperature. The water is pressurized by charging the space above the water column with an inert gas such as N_2. A single-action, positive displacement pump (CS&P Cryogenics model ICP-75) coupled with the Toshiba Tosvert VF-S9 control system is used to pressurize and transfer liquid CO_2 from a 3-ton refrigerated storage tank and inject it upward through various orifices mounted on a removable nozzle. The variable frequency drive pump is capable of providing CO_2 at flow rates up to about 12 - 18 kg/min (approximately 200 to 300 cc/s) at pressure up to 102 bar (1,500 psi). To control the CO_2 temperature, an array of counter flow, coaxial heat exchanger tubes are plumbed into the CO_2 flow system immediately downstream of a large bladder accumulator that is employed to dampen pump pressure pulses.

Electrical heating tape was wrapped around the line feeding into the heat exchanger (HX) to supplement the heat addition from the warm water flowing through the HX. The heat gained through the HX is monitored by means of thermistors inserted into the CO_2 line before and after the HX (T1 and T2 in Figure 2.11). The temperature of the CO_2 being injected is measured by a thermistor T3 located about 20 cm from the inlet into the DOS.

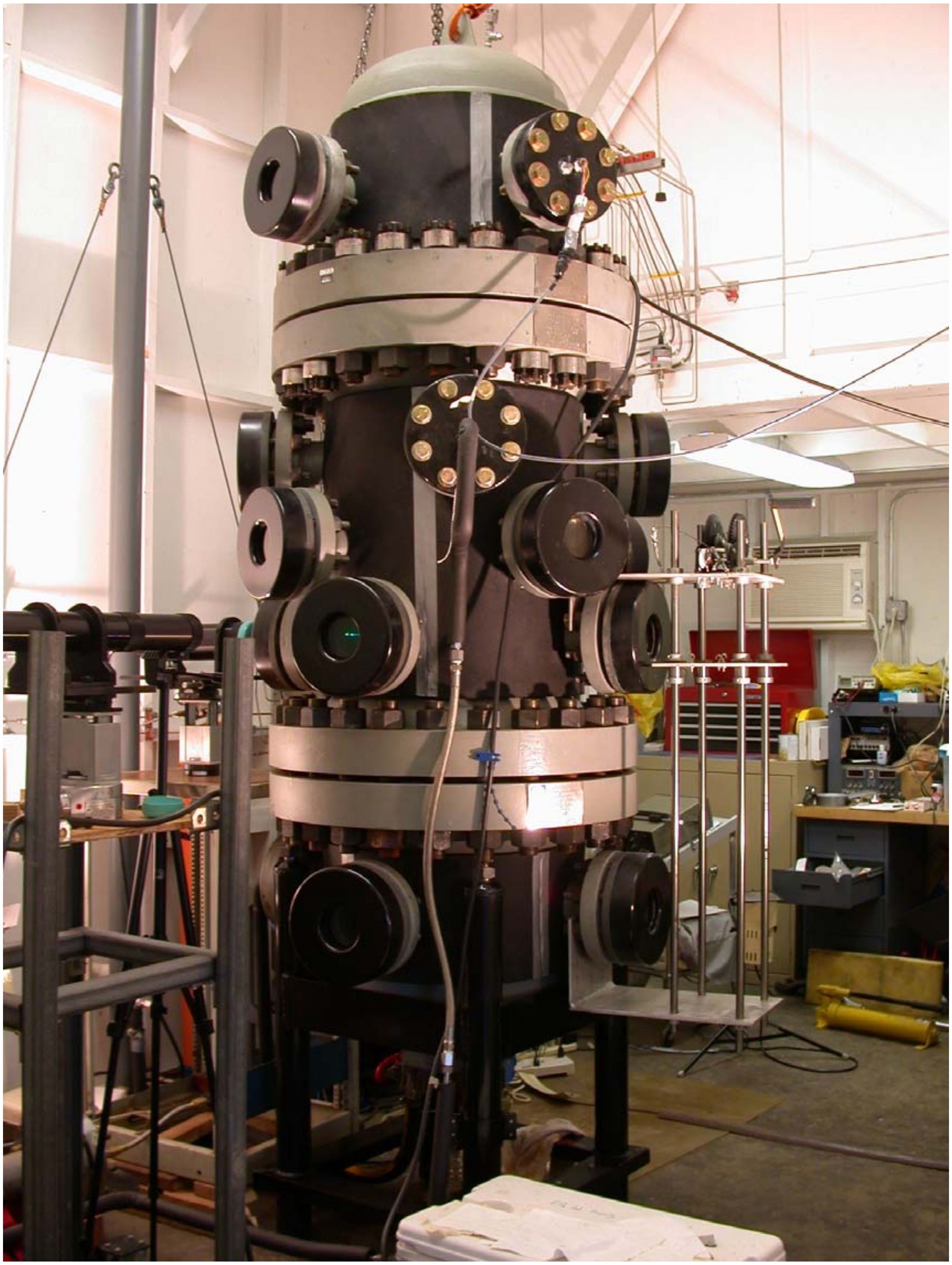

Figure 2.10 Deep Ocean Simulator

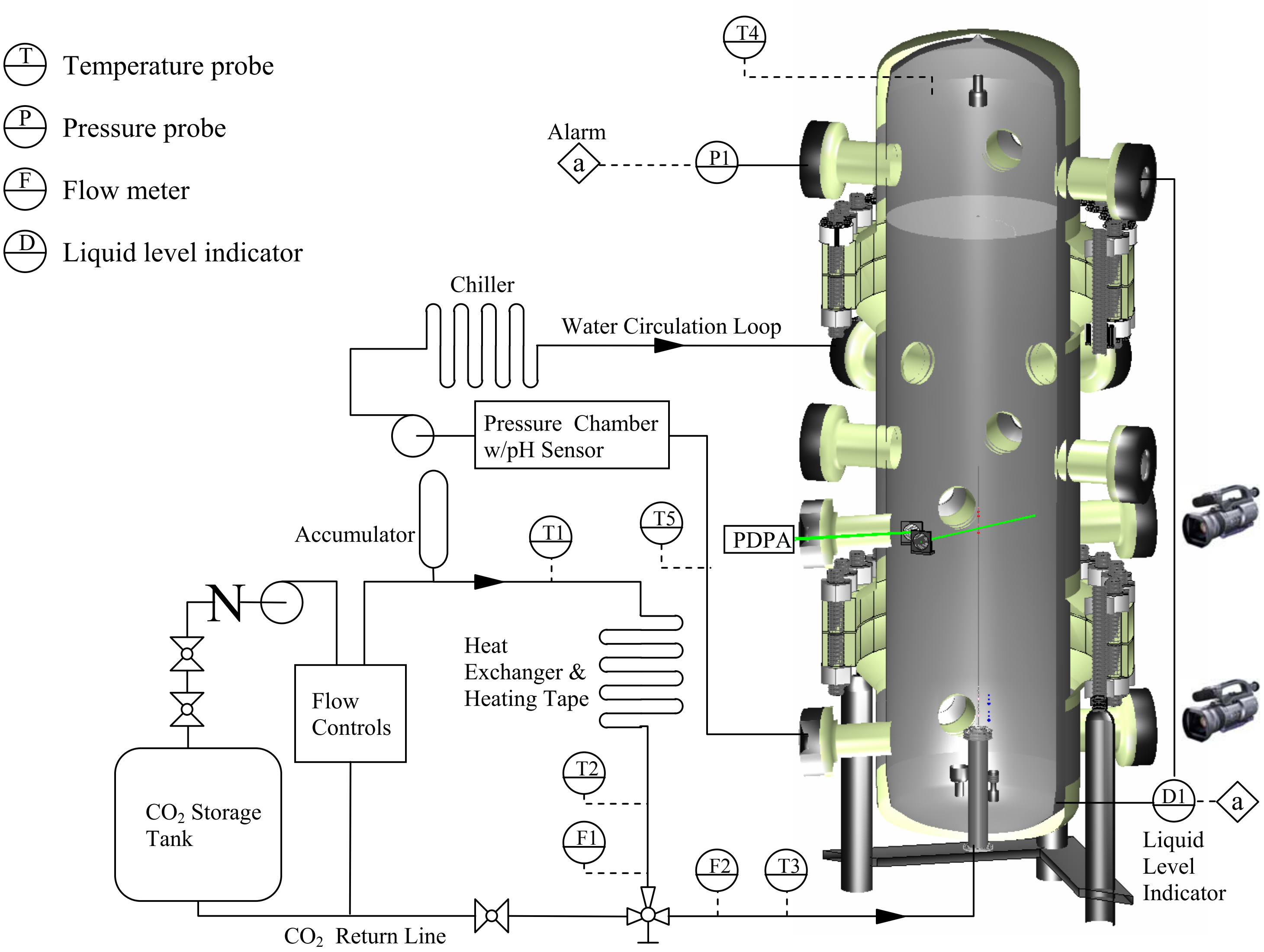

Figure 2.11 Experimental layout for the liquid CO_2 injection tests.

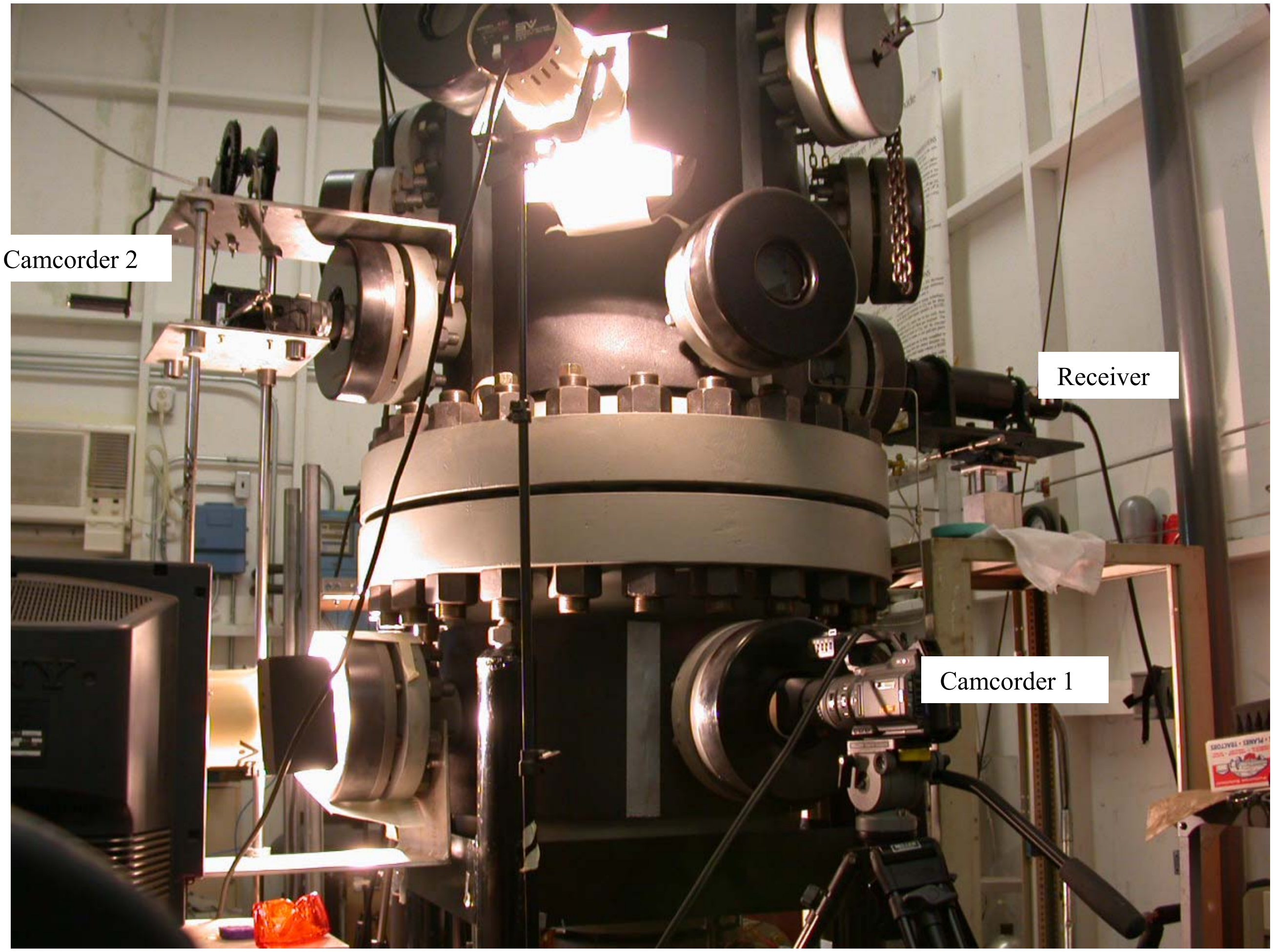

Figure 2.12 Photograph of the facility taken during CO_2 injection test.

A differential pressure transducer (D1) monitors the water level in the DOS. Temperature of the gas above the water in the DOS is measured by thermocouple T4. A pressure transducer (P1) is coupled to an electronic feedback/control device that actuates an electronic valve to vent the gas and maintain constant pressure in the DOS (< ±1%) as liquid CO_2 is injected and compresses the gas volume. To address the problem of increasing water temperature in the vessel due to heat addition from the surroundings, a water circulation loop was installed. A high pressure gear pump draws water from the vessel and passes it through chiller before returning to the pressure vessel. Water temperature in the tank is measured by thermistor T5. A Sea Bird SBE18 pH probe monitors the pH of the water upstream of the gear pump. Two flowmeters are available to measure CO_2 flow rate: a totalizer and Omega FTB9512 Precision Turbine flowmeter coupled with a FC-22 flow computer (F2).

The PDPA was positioned as shown in Figure 2.13. The CO_2 injector was aligned with the vessel centerline and the top of the injection orifice was set at the level of the lowest row of viewports. The PDPA optics were located at the second row of viewports, approximately 70 cm above the injection orifice. As indicated in Figures 2.13 and 2.14, the two 514.5 nm laser beams emerging from the transmitter are steered with a pair of dielectric mirrors inside the vessel and cross and form an interference fringe pattern directly above the injection orifice on the vessel centerline. The angle between the transmitted laser beams and the receiver optics was selected to optimize the PDPA measurements of reflective CO_2 droplets. CO_2 droplets that traverse through the PDPA optical probe volume scatter light that is collected off-axis by the receiver. Two or three digital video cameras monitor the flow through the viewports at the level of the PDPA and the injector.

2.2.2 Silicone Fluid and Oil Injection Tests

A photograph of one of the two atmospheric pressure Plexiglas tank used for the silicone fluid and oil injection experiment is provided in Figure 2.15. The square tank measures approximately 55 cm (21.5 in.) between the interior surfaces of the walls, and is about 1.3 m (51 in.) tall. It has a capacity of 400 liters (106 gallons) of water. The tank is constructed from structural aluminum angle and plate, and clear cast acrylic Plexiglas. A thermistor probe is threaded through one of the lower circular windows and a second probe can be suspended from the top to monitor water temperature. Injection nozzles were mounted on a horizontal traversing mechanism installed diagonally across the tank on two vertical shafts. The manual traverse was driven by an acetal chain and a gear-crank mechanism and was used to position the nozzle at an appropriate location relative to the PDPA optical sample volume. Silicone fluid or oil was injected vertically upward. The height of the nozzle could be changed before a test by moving and locking the traverse assembly along the vertical shafts.

Figure 2.16 presents a schematic of the experimental set up that was employed for the silicone fluid injection tests. A pulseless, magnetic drive, cavity-style gear pump (Micropump Series 2200) coupled to a Leeson variable speed 1 hp motor draws the jet fluid from a small (about 8 liter) reservoir. The reservoir is immersed in the constant temperature water bath.

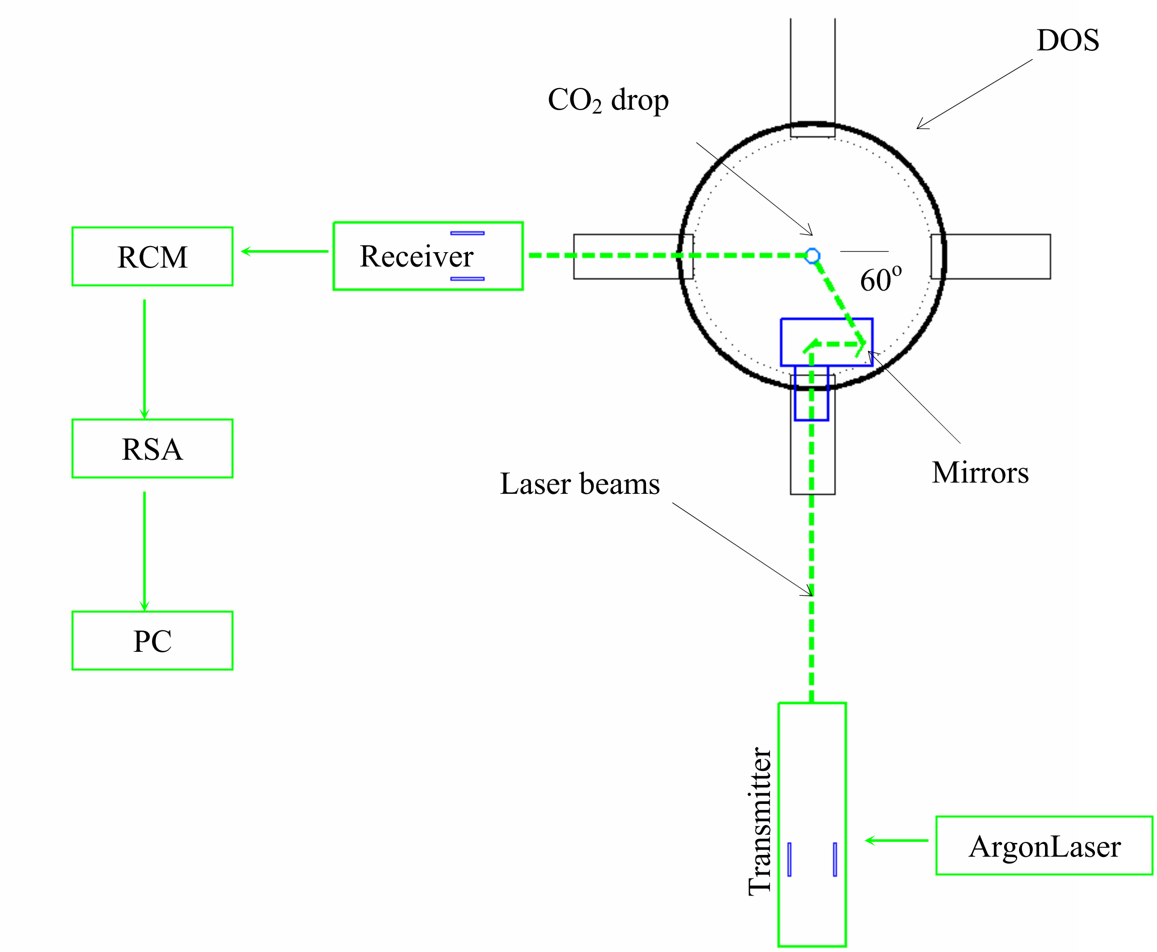

Figure 2.13 PDPA setup for liquid CO_2 injection tests.

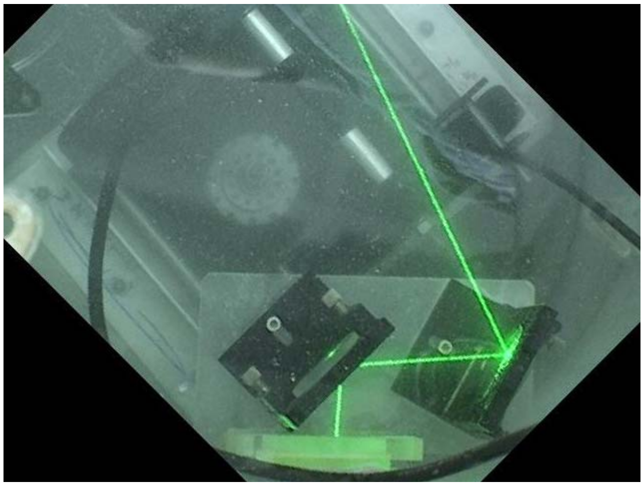

Figure 2.14 Pair of dielectric mirrors installed inside the DOS to steer the PDPA laser beam.

Flow rate (and jet velocity) is set by adjusting the pump motor speed and two needle valves dividing the flow between the injector and a bypass line back to the reservoir. A positive displacement flowmeter (Omega Engineering FTB-1002) is installed inline with the injector to measure the flow rate of silicone fluid into the tank. Fluid temperature and pressure are monitored with an inline thermistor and precision pressure gauge, respectively. The silicone enters the tank through a pipe fitting in its base and flows through a short service loop of 9.5 mm (0.375 in.) i.d. flexible tubing before entering the injection nozzle mounted on the horizontal traverse. Three nozzles were used in the experiments with circular orifice diameters of 1, 2, and 5 mm.

As in the CO_2 injection experiments, jet instability was monitored with several video cameras positioned at different heights above the injector. These video records also were employed to obtain data on the size distribution of the oil droplets that are generated by the disintegration of the jet.

Figure 2.15 Photograph of the Plexiglas water tank (Masutani & Adams, 2000).

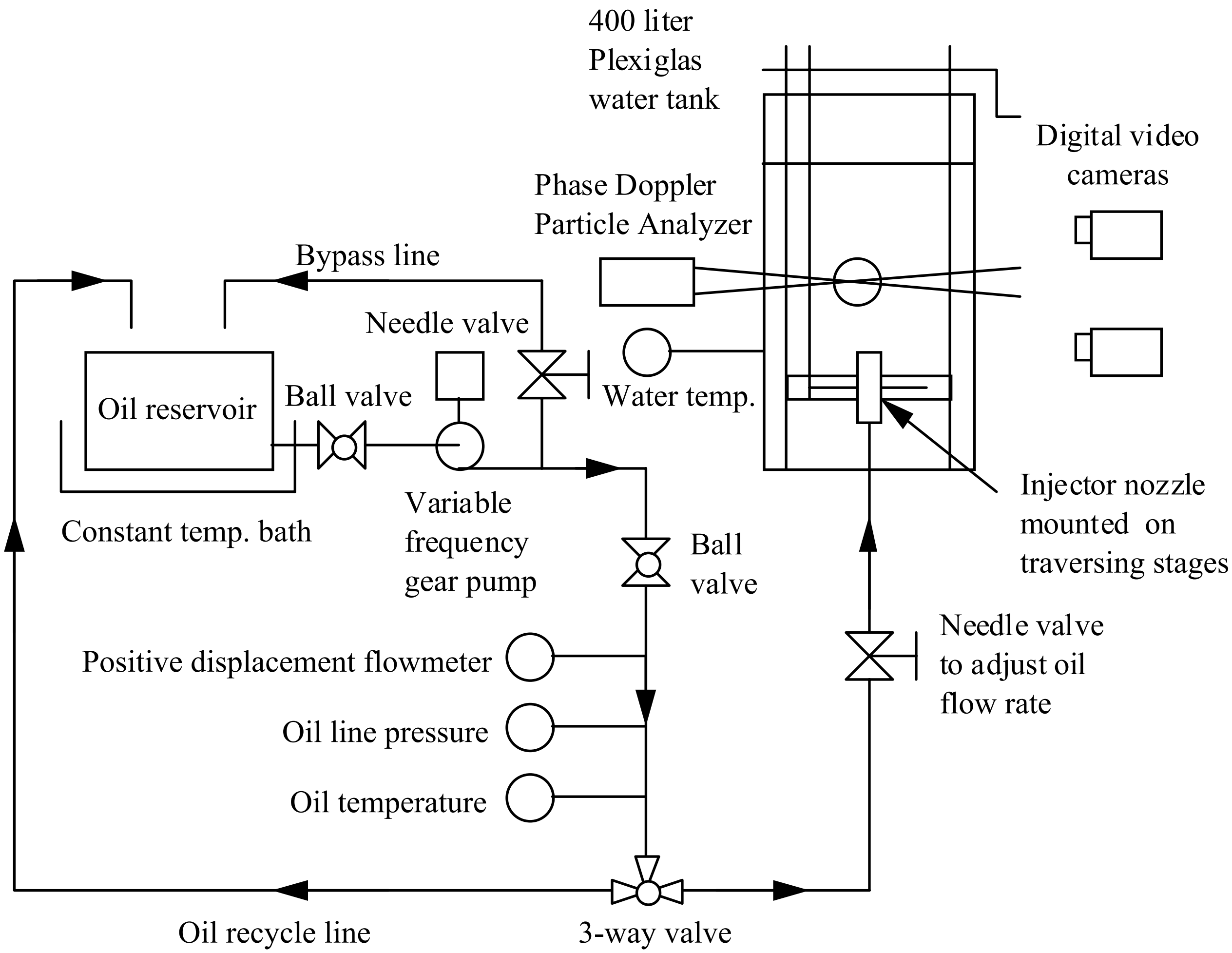

Figure 2.16 Experimental layout for the oil injection tests.

A second Plexiglas water tank, Figure 2.17, was constructed for a number of the silicone fluid injection tests. This tank was designed to optimize performance of the PDPA. The wall geometries shown in Figure 2.18 were selected to be perpendicular to the PDPA transmitter and receiver optics to minimize losses and refractive effects. The experimental set-up employed was the same as for the square tank.

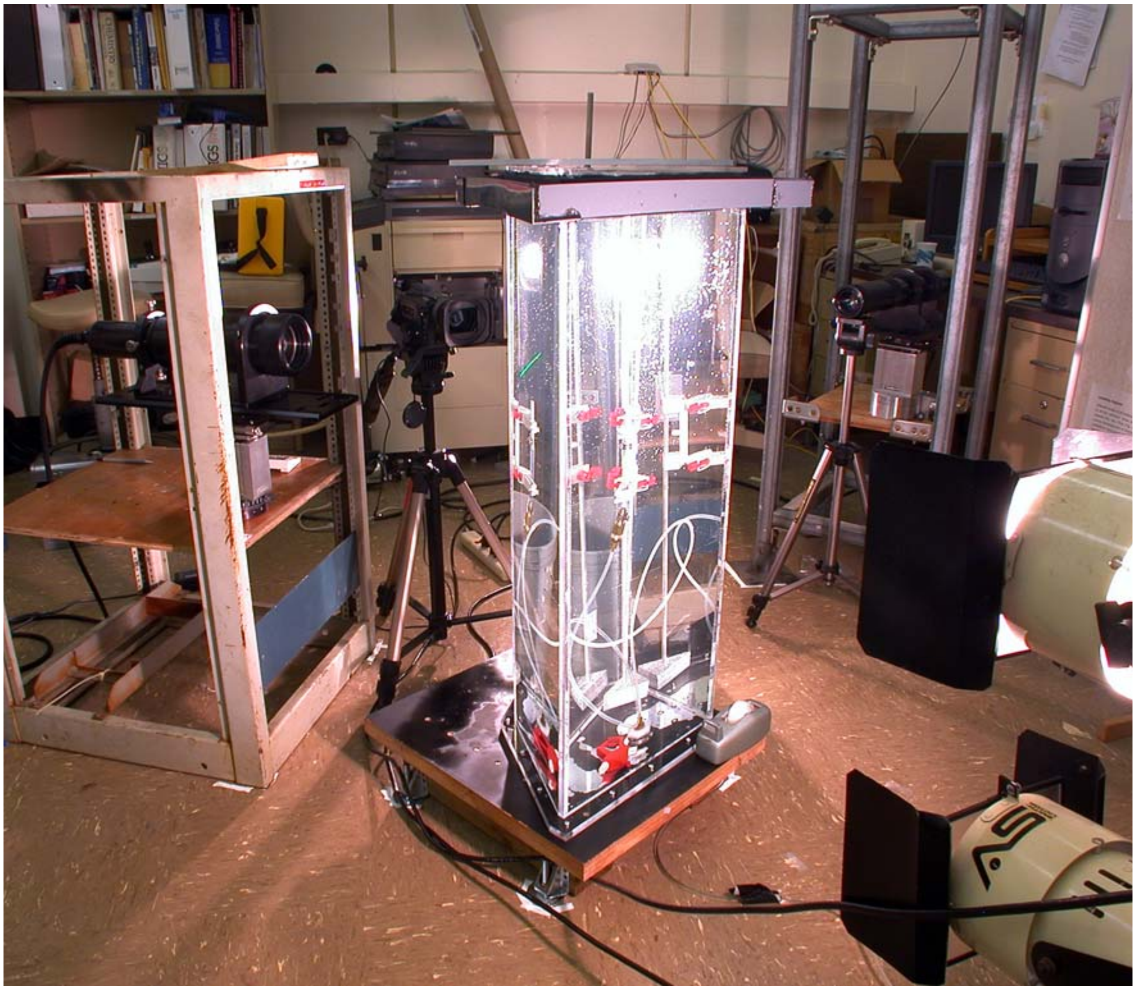

Figure 2.17 Photograph of the Plexiglas tank used for silicone fluid injection tests.

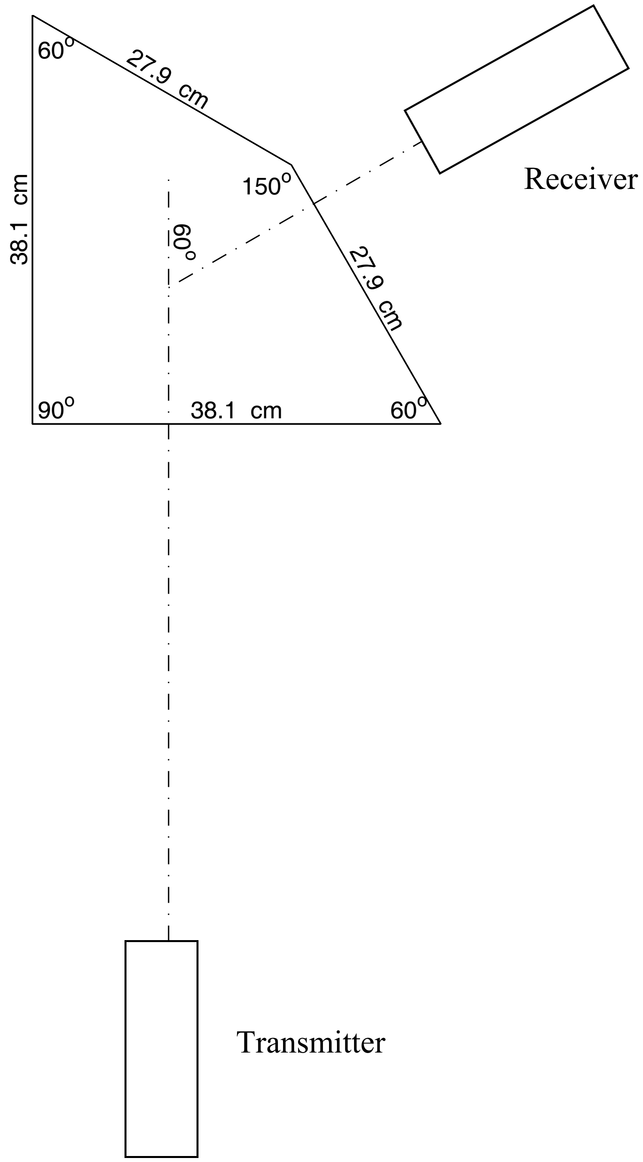

Figure 2.18 Cross section of the Plexiglas tank for silicone fluid injection tests.

2.2.3 Fluid Properties

Comparisons of properties of the liquid CO_2 and silicone fluids that were employed in the jet instability and breakup experiments are provided in Table 2.1 and Figure 2.19. The silicone fluids selected were pure polydimethylsiloxane. Information also is presented on four crude oils (Genesis, Mars TLP, Neptune Spar, and Platform Gail, Mars) that were used in similar tests for the unrelated project on deep oil spills (Masutani & Adamas, 2000) As mentioned above, the oil data are included in this report to examine the influence of jet fluid properties on instability phenomena. It should be noted that the kinematic viscosities of the various jet fluids range over three orders of magnitude.

Table 2.1 **Comparison of properties of liquid CO_2, and silicone fluids, and four deepwater crude oils at 25°C (0% evaporation); surface tension, σ, of the oils were not measured; values shown were estimated from data on σ for similar crude oils.**

Liquid Name	Symbol	Density [kg/m^3]	Kinematic Viscositiy [centistrokes]	Surface Tension [dyne/cm]
Genesis	GE	877	20.5	~25 (estimated)
Mars TLP	MA	882	27.2	~25 (estimated)
Neptune Spar	NS	861	15.1	~25 (estimated)
Platform Gail	PG	922	211	~25 (estimated)
Silicon fluid 0.65	LS	761	0.65	15.9
Silicon fluid 20	SF	977	20	21
Liquid CO_2	CD	838~986[1]	Fig 2.20	27

[1] Liquid CO_2 density range at CO_2 injection experiment conditions.

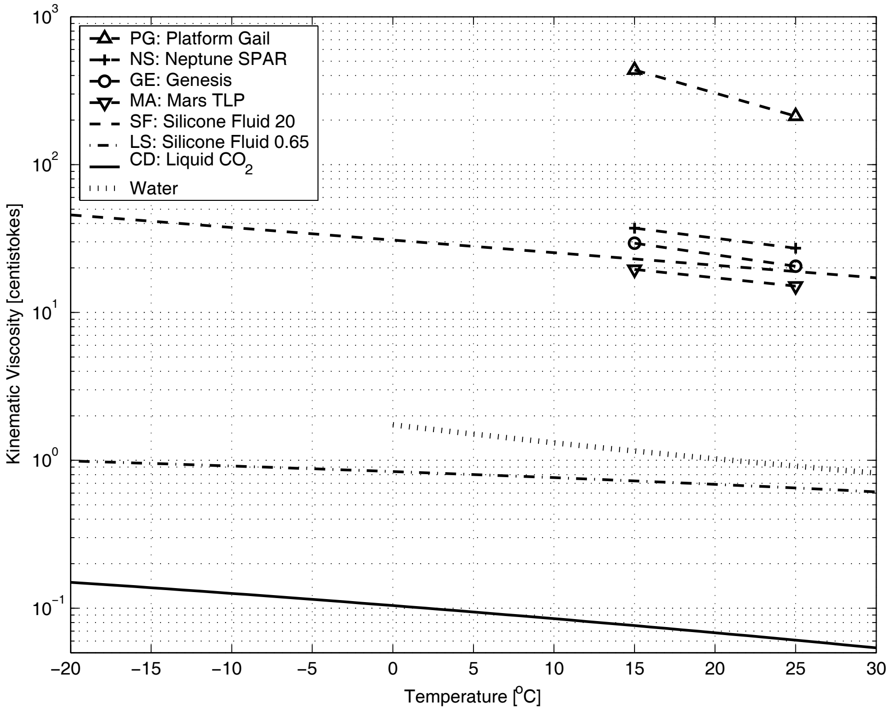

Figure 2.19 Kinematic viscosities (in centistokes) of liquid CO_2, silicone fluids, four deepwater crude oils, and water. The viscosities of silicone fluids are obtained

from the manufacturer. Crude oils viscosities are from Masutani and Adams (2000) at 15^o C and 25^o C for 0% evaporation.

2.2.4 Nozzle Characteristics

The influence of injection nozzle geometry was investigated in these experiments. To determine if boundary layer effects are significant, ASME sharp edge orifices and round tube nozzles were tested under identical flow conditions. The jet issuing from a sharp edge orifice has no separation boundary layer and typically exhibits a *vena contracta*. A boundary layer develops in a tube nozzle that may influence the jet instability and breakup. Comparisons of results for the two types of nozzles were performed.

Characteritics of the nozzles are summarized in Table 2.2. Examples of sharp edge and tube orifices that were fabricated for the liquid CO_2 injection tests are shown in Figures 2.20, 2.21, and 2.22. These nozzles bolt to the removable injector in the DOS and are positioned above a plenum and a check valve to prevent ingress of water into the liquid CO_2 line. Tube nozzles for CO_2 injection comprise lengths of plastic tubing of different inside diameter. Figure 2.21 shows multiple orifices (7 sharp edged orifice per nozzle) that were employed to investigate jet interactions.

Three nozzles with circular ASME sharp edge orifice diameters of 1 mm, 2 mm, and 5 mm were employed in the silicone fluid and crude oil experiments (Figure 2.23). The nozzles were machined from thick wall 25.4 mm (1.0 in.) diameter stainless steel tubing and marine bronze.

Figure 2.24 presents photographs of the CO_2 injector with the 5 mm tube orifice. The injector assembly is mounted on a flange that is bolted to an opening in the bottom of the DOS.

Table 2.2 Nozzle characteristics

Nozzle Symbol	Orifice Diameter D [mm]	Orifice Number	Orifice Shape	Nozzle Material	Test Jet Fluid
C02	2	1	ASME sharp edged	Stainless Steel	CO_2
C05	5	1	ASME sharp edged	Stainless Steel	CO_2
C10	10	1	ASME sharp edged	Stainless Steel	CO_2
S01	1	1	ASME sharp edged	Bronze	Oils
S02	2	1	ASME sharp edged	Bronze	Oils/ Silicone fluids
S05	5	1	ASME sharp edged	Bronze	Oils
C72	2	7	ASME sharp edged	Aluminum	CO_2
T02	2	1	Tube	Delrin	CO_2/LS

T05	5	1	Tube	Delrin	CO_2

Figure 2.20 Photograph of 2 mm (C02), 5 mm (C05) and 10 mm (C10) sharp edged, single orifice nozzles fabricated for the liquid CO_2 injection tests.

Figure 2.21 Photograph of 2 mm (C72) sharp edged, 7-orifice nozzle fabricated for the liquid CO_2 injection tests

Figure 2.22 Photograph of the 2 mm (T02) and 5 mm (T05) Delrin tube orifice nozzles.

Figure 2.23 Photograph of the 1 mm (S01), 2 mm (S02) and 5 mm (S05) sharp edged orifice nozzles.

Figure 2.24 Photographs of the CO_2 injector with the 5 (T05) mm Delrin tube orifice mounted on a flange that is bolted to an opening in the bottom of the DOS.

3 JET INSTABILITY REGIMES

Jets disintegrate into a dispersed phase as the result of the competition between cohesive forces (interfacial tension and viscous force) and disruptive forces (gravitational and hydrodynamic or aerodynamic forces). Instability regimes are used to indicate the dominant mode(s) of instability and provide general, qualitative information about droplet size spectra, jet breakup length and other flow characteristics. They are useful devices to classify disintegrating jets.

For liquid-liquid systems, information pertaining to breakup and droplet formation is largely based on experimental observations. Experiments were conducted by Hayworth and Treybal (1950), Meister and Scheele (1969), Kitamura *et al*. (1982), Kumar and Hartland (1984), Skelland and Walker (1989), Kato *et al*. (2000), Longmire *et al*. (2001) and others to study liquid-liquid jet breakup. These studies have provided useful data on droplet size and breakup length but were limited to laminar jet flow. In many practical applications involving liquid-liquid jet breakup, such as CO_2 sequestration, transitional and turbulent breakup events may occur. Neither breakup modes nor instability regimes have been clearly defined for liquid-liquid systems over the entire breakup range extended from dripping to full atomization. To address this deficiency, the extensive experimental database from this investigation and the study of deep oils spills (Masutani & Adams, 2000) was analyzed to identify the primary liquid-liquid instability modes and to define associated breakup regimes. The boundaries of these regimes were determined on the basis of certain dimensionless parameters that are discussed below.

3.1 Dimensionless Parameters

Following standard practice to develop scale-independent results, the present data were analyzed and, wherever possible, presented in non-dimensional space. It is generally agreed that the following dimensionless parameters characterize jet instability (Reitz & Bracco, 1986; Kitamura & Takahashi, 1986; Lefebvre, 1989; Teng, 1994; Masutani & Adams, 2000):

Reynolds Number, *Re*

$$Re \equiv \frac{U_j D}{\nu_j} \tag{3.1}$$

Weber Number, *We*

$$We \equiv \frac{\rho_j U_j^2 D}{\sigma} \tag{3.2}$$

Ohnesorge Number, *Oh*, and Modified Ohnesorge Number, *Oh**

$$Oh \equiv \frac{\mu_j}{\sqrt{\rho_j \sigma D}} = \frac{\sqrt{We}}{\mathrm{Re}_D} \tag{3.3a}$$

$$Oh^* \equiv \frac{3\mu_j + \mu}{\sqrt{\rho_j \sigma D}} \tag{3.3b}$$

Bond Number, *Bo*

$$Bo \equiv \frac{g \Delta\rho D^2}{\sigma} \tag{3.4}$$

The subscript j denotes properties of the jet fluid; ambient fluid properties are not subscripted. U_j is taken to be the bulk-mean inlet velocity of the jet (calculated as the volumetric flow rate of jet fluid divided by the cross sectional area of the injection orifice); D is the injection orifice diameter; g is the gravitational constant; ρ, μ, ν, and σ are, respectively, fluid density, dynamic viscosity, kinematic viscosity, and interfacial tension; and $\Delta\rho$ is the difference in the densities of the jet and ambient fluids.

Re is the ratio of inertial to viscous forces; *We* is the ratio of disruptive momentum (hydrodynamic) forces to restoring surface tension; and *Oh*, a stability index given as the ratio of viscous forces to surface tension. The modified Ohnesorge number (Teng *et al.,* 1995), *Oh**, accounts for the influence of ambient fluid viscosity on jet instability and breakup. Ambient density effects appear in the Bond number, *Bo* (sometimes called the Eötvös number; *vide* Kumar & Hartland, 1984); ambient density also is employed occasionally to calculate the Weber number. *Bo* is important for buoyancy-driven flows (e.g., gases leaking upward into a liquid; liquids falling through a gas) and is less relevant for high Weber number jets.

As mentioned previously, other factors not included in the above dimensionless groups are believed to influence jet breakup and, hence, the size distribution of the dispersed phase. The development of free shear flows, e.g., a liquid CO_2 jet, is known to depend strongly on the condition of the wall boundary layer at the point of separation and on upstream and downstream pressure fluctuations. To date, a viable approach to account for these factors in the analysis of breakup data has not been identified (furthermore, precise measurements of the jet initial and boundary conditions are not trivial) – which could explain some of the scatter encountered when data is correlated.

3.2 Liquid-liquid Jet Instability Regimes

3.2.1 Definition of the Breakup regimes

The delineation of breakup regimes has been an important focus of recent work on liquid-liquid jet instability. When a liquid jet emerges from a nozzle as a continuous body of cylindrical form, the competition between cohesive and disruptive forces gives rise to oscillations and distortions of the interface. These disturbances can grow until the liquid body disintegrates into a dispersed droplet phase. In our experiments involving different fluids, injectors, and facilities we consistently observed a progression of five breakup modes as jet velocity increased. Figure 3.1 shows a sketch of the breakup modes that define the five instability regimes. Video data frames from the numerous experiments on which the sketch was based, are provided in Figures 3.2 to 3.12. These Figures include images of liquid CO_2, crude oil, and silicone fluids being injected into water or seawater.

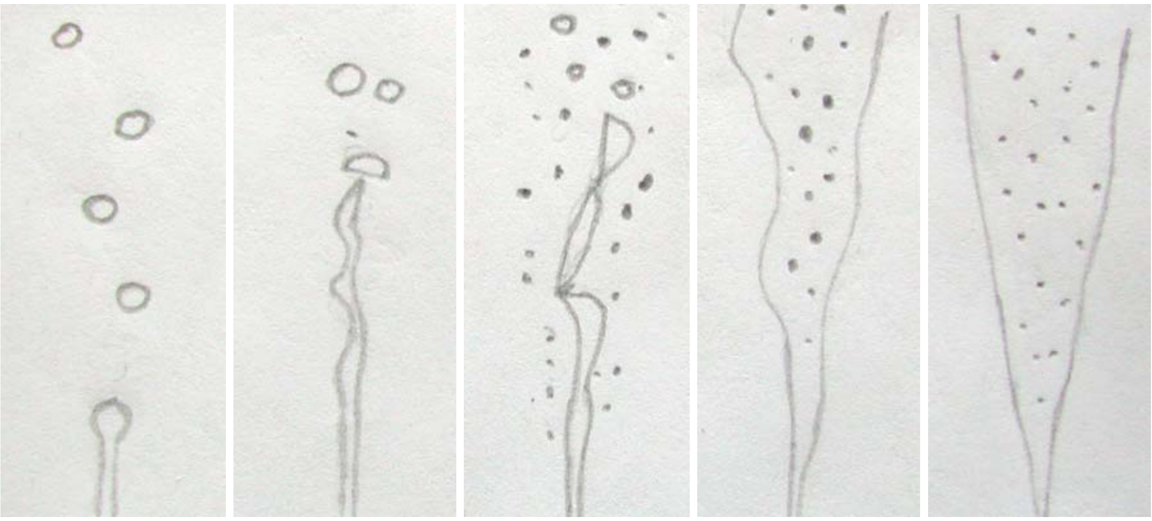

(a) (b) (c) (d) (e)

Figure 3.1 Sketch showing the general characteristics of the 5 jet breakup modes observed consistently in the liquid-liquid injection tests. Jet velocity increases from left to right. (a) Varicose breakup at instability regime 1. (b) Sinuous wave breakup at instability regime 2. (c) Filament core breakup at instability regime 3. (d) Wave shape atomization at instability regime 4. (e) Full atomization at instability regime 5.

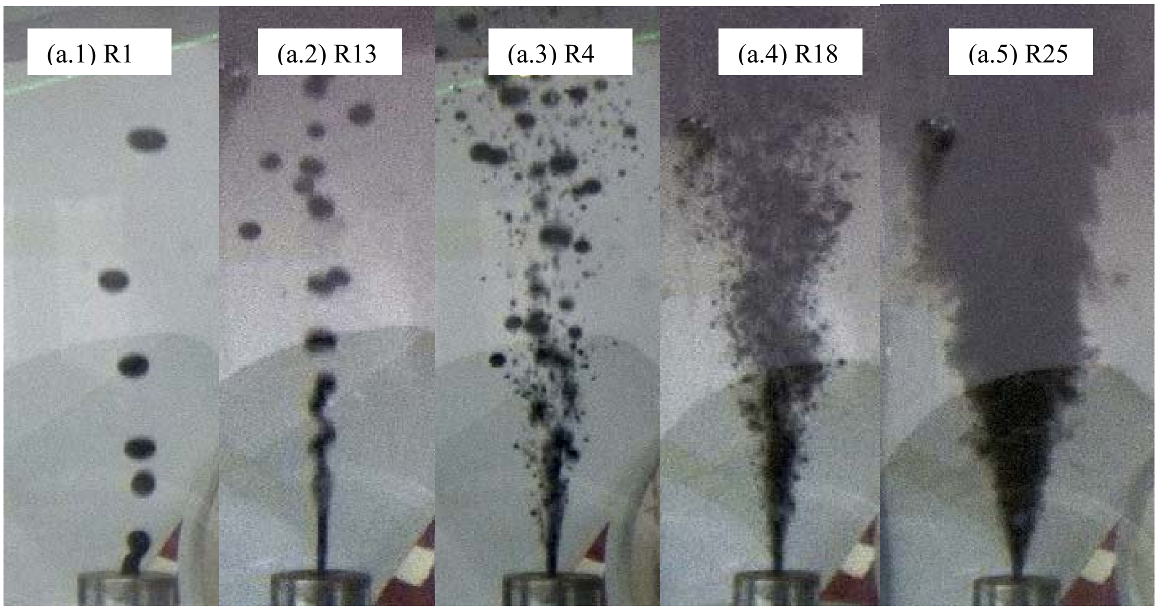

U_{jet}= 0.31 0.97 1.41 2.42 5.99 m/s

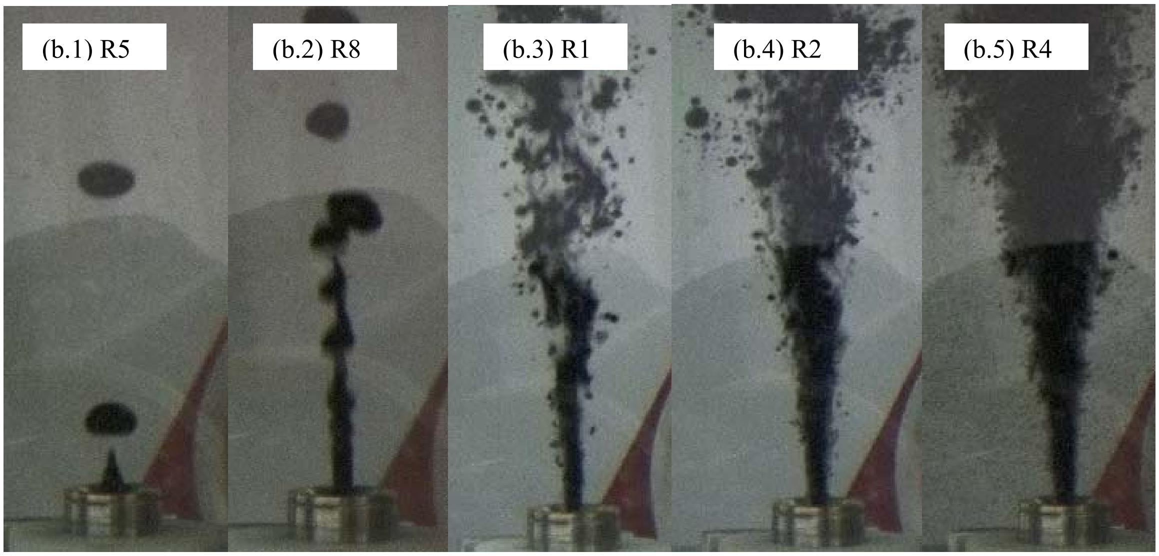

U_{jet}= 0.08 0.36 0.98 1.27 1.90 m/s

Figure 3.2 Five breakup modes of Genesis crude oil; injection into tap water. Frames a.1 to a.5 use 2 mm sharp edge nozzle; conditions given in Table 3.2 for Case GES02WTR. Frames b.1 to b.5 use 5 mm sharp edge orifice; Case GES05WTR. The outside diameter of the injection nozzles is 2.54 cm.

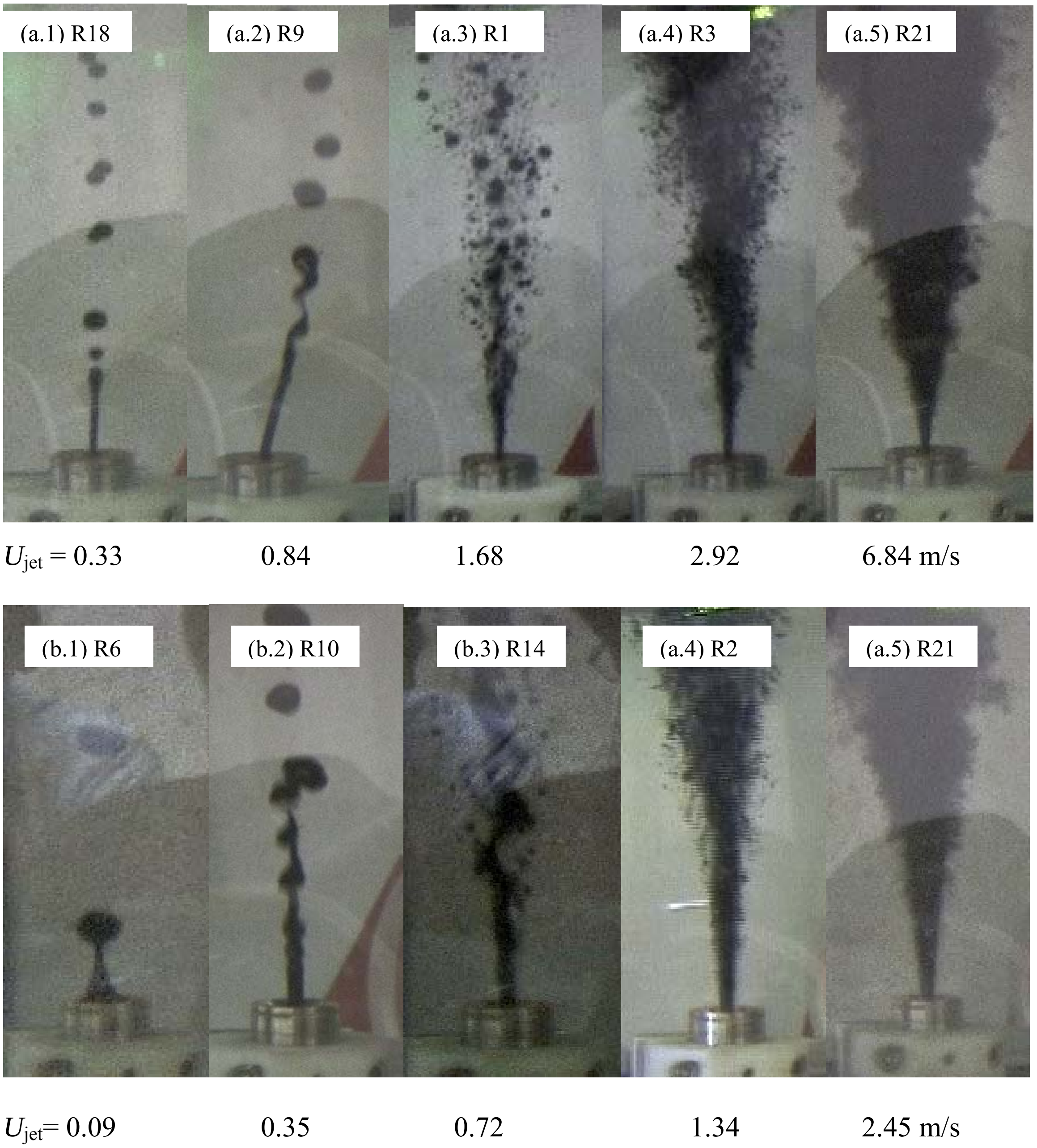

Figure 3.3 Five breakup modes of Mars TLP crude oil; injection into tap water at room temperature from 2 mm and 5 mm sharp edge orifices. Frames a.1 to a.5 correspond to Case MAS02WTR. Frames b.1 to b.5 correspond to Case MAS05WTR.

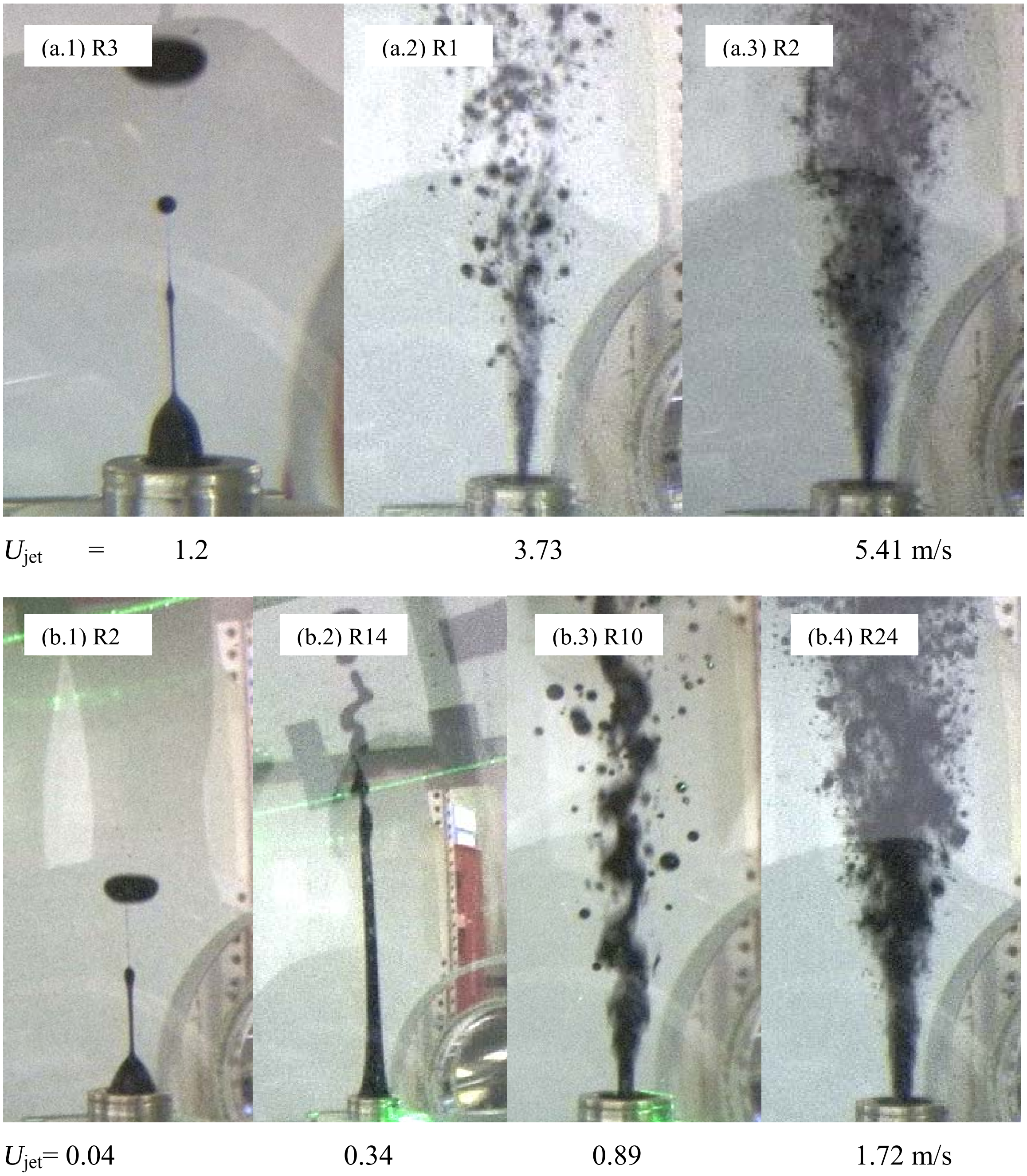

Figure 3.4 Breakup of very high viscosity Platform Gail crude oil; injection into tap water at room temperature from 1 mm and 5 mm sharp edge orifices. Frames a.1 to a.3 represent breakup modes 1, 3 and 4 for Case PGS01WTR. Frames b.1 to b.4 show breakup modes 1, 2, 3 and 4 for Case PGS05WTR.

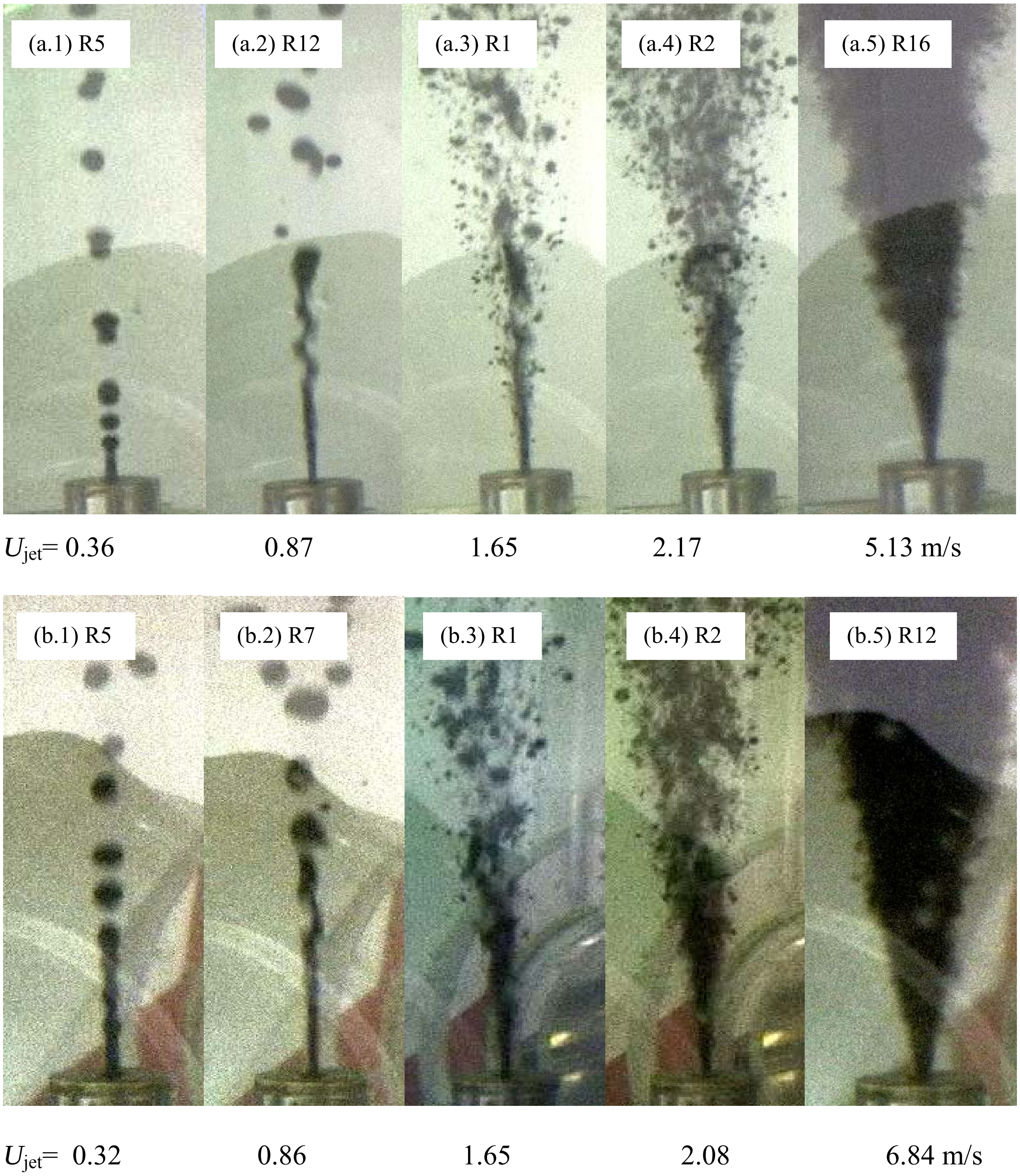

Figure 3.5 Five break-up modes of Neptune Spar crude oil; injection tests in tap water and natural surface sea water from 2 mm sharp edge orifice. Frames a.1 to a.5 correspond to Case NSS02WTR using tap water. Frames b.1 to b.5 correspond to Case NSS02WNR using sea water.

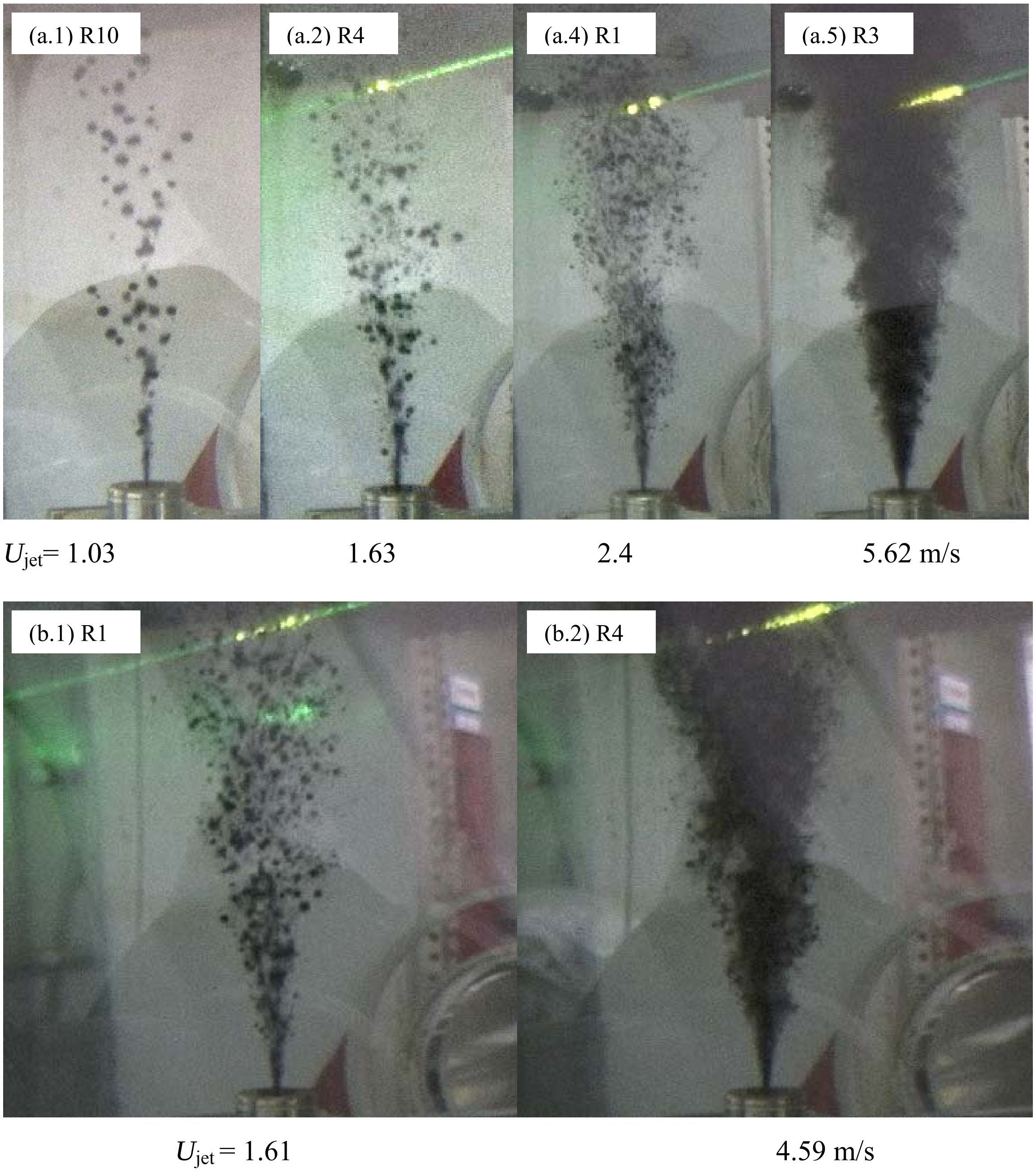

Figure 3.6 Neptune SPAR crude oil injections into tap water at different water temperatures from 1 mm sharp edge orifice (S01). Frames a.1 to a.4 represent breakup modes 2, 3, 4 and 5 at water temperature of 18.8°C for Case NSS01WTR. Frames b.1 and b.2 represent breakup modes 3 and 4 at water temperature of 8.5°C for Case NSS01WTC.

(a.1) (a.2) R2 (a.3) R3 (a.4) R7 (a.5) R9

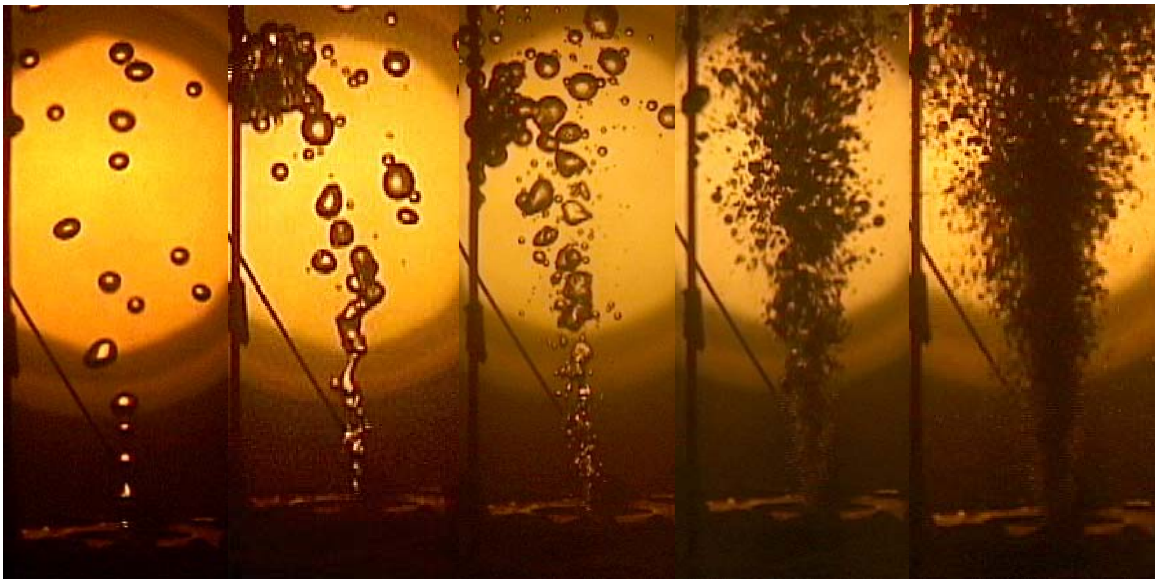

U_{jet}= <0.67 0.77 1.13 2.58 4.01 m/s

(b.1) R4 (b.2) R11 (b.3) R15 (b.4) R25 (b.5) R19

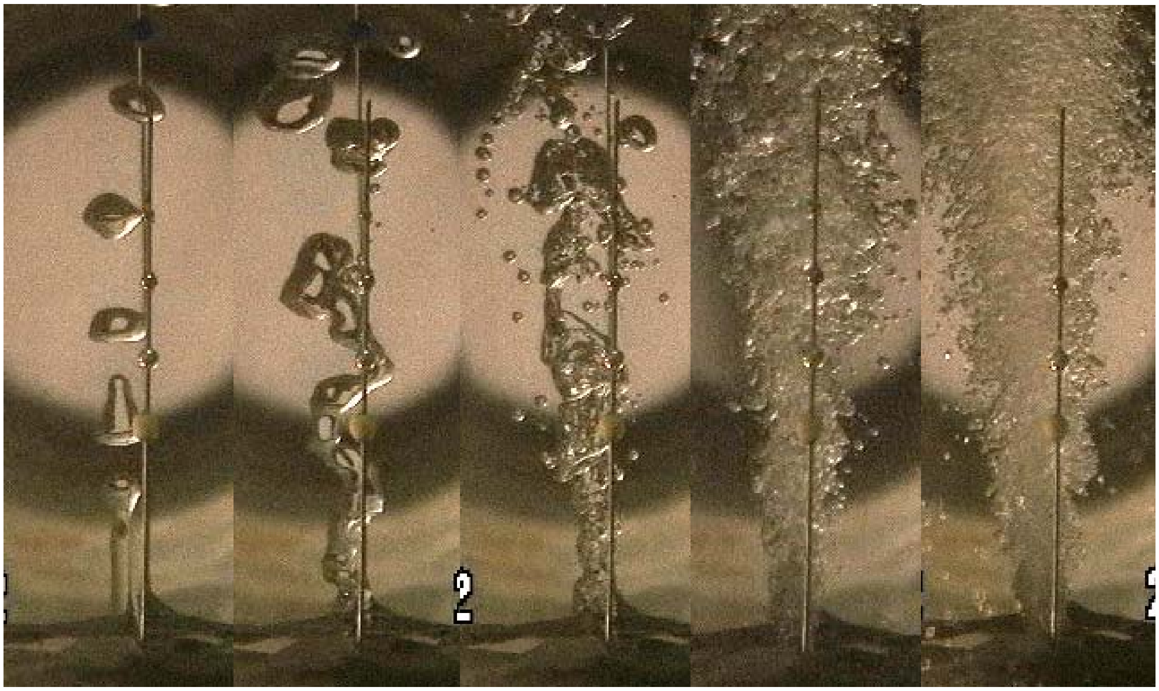

U_{jet}= 0.1 0.44 1.13 0.87 2.48 m/s

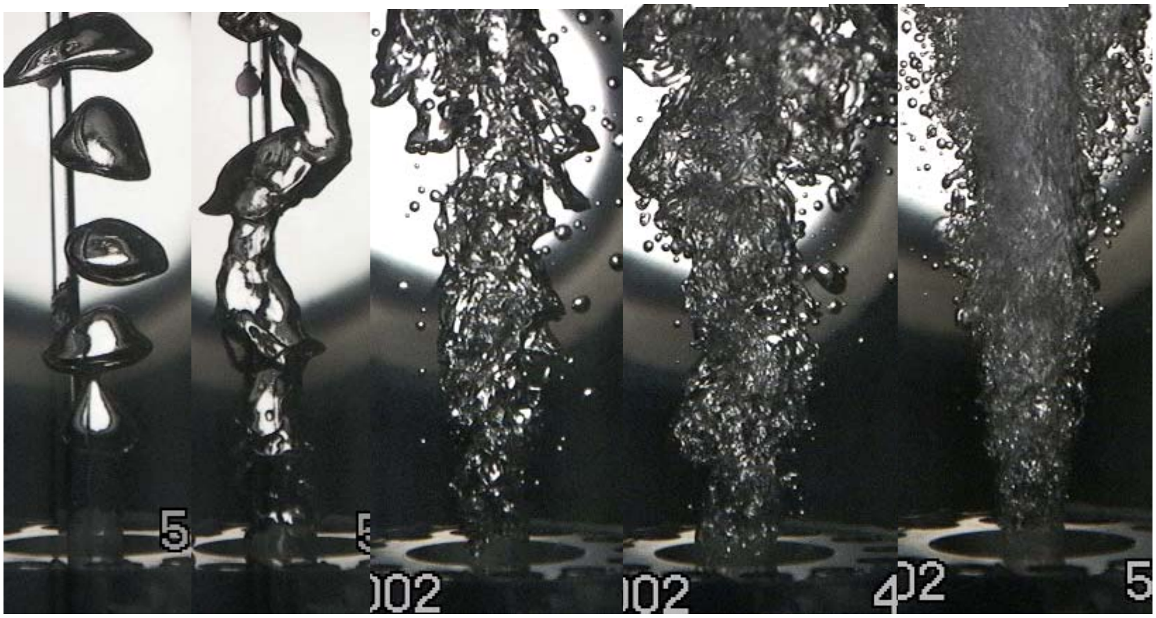

(c.1) R6 (c.2) R9 (c.3) R2 (c.4) R3 (c.5) R5

U_{jet}= 0.13 0.31 0.66 0.88 1.45 m/s

Figure 3.7 Five breakup modes observed during liquid CO_2 injection tests in tap water with the ASME sharp edge orifices of different diameters at pressure of 52 bars. Frames a.1 to a.5 show 2 mm sharp edge orifice for Case CDC02WTP52. Frames b.1 to b.5 show 5 test runs with 5 mm sharp edge orifice for Case CDC05WTP52. Frames c.1 to c.5 show 5 test runs with 10 mm sharp edge orifice for Case CDC10WTP52.

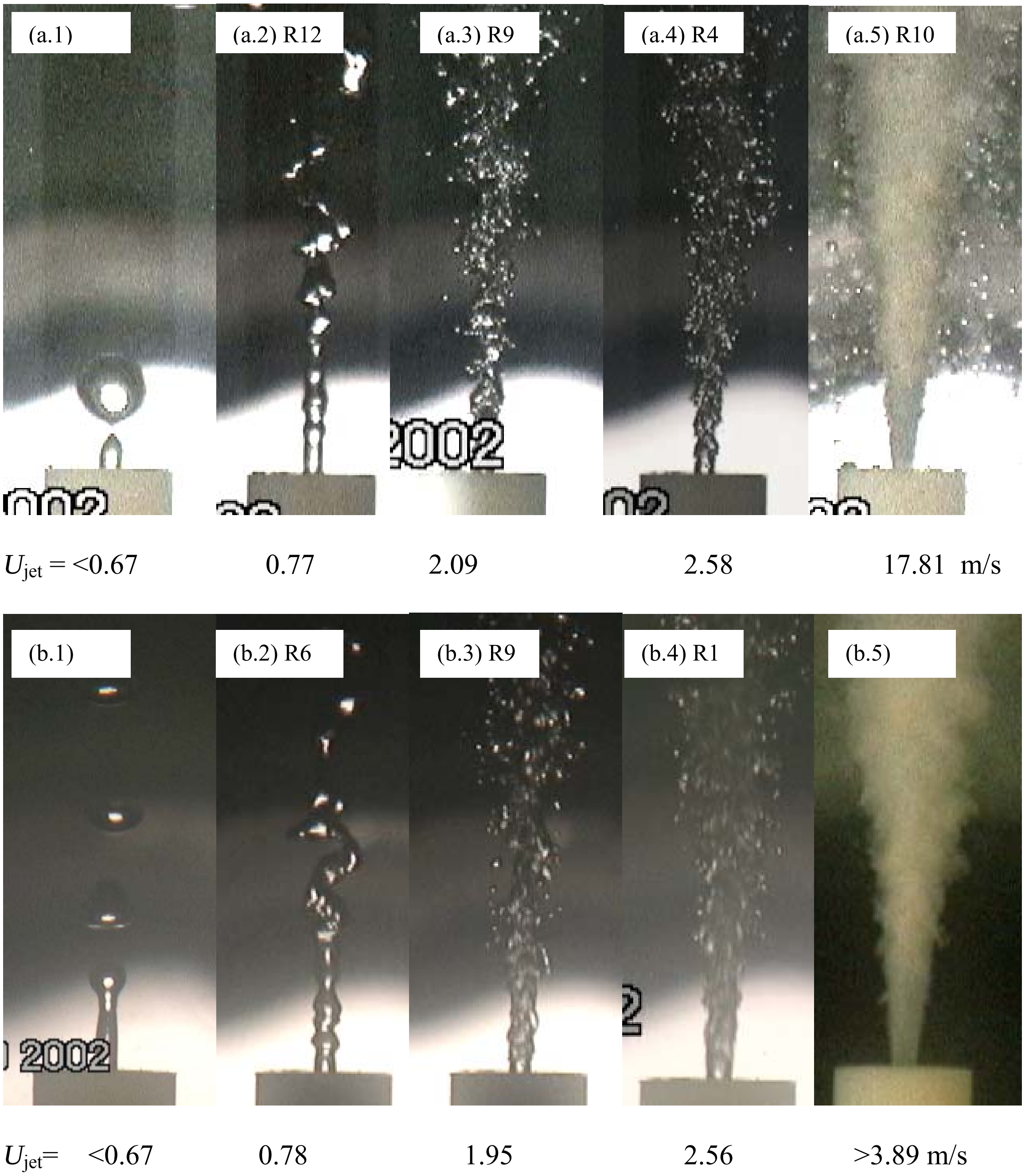

Figure 3.8 Five breakup modes observed during liquid CO_2 injection tests from a 2 mm tube orifice. Frames a.1 to a.5 employ tap water for Case CDT02WTP52. Frames b.1 to b.5 employ natural seawater for Case CDT02WNP52. Flow rates of (a.1) and (b.1) are lower than the flow meter measurement range. The outside diameter of the tube orifice is 1.27 cm (0.5 inch).

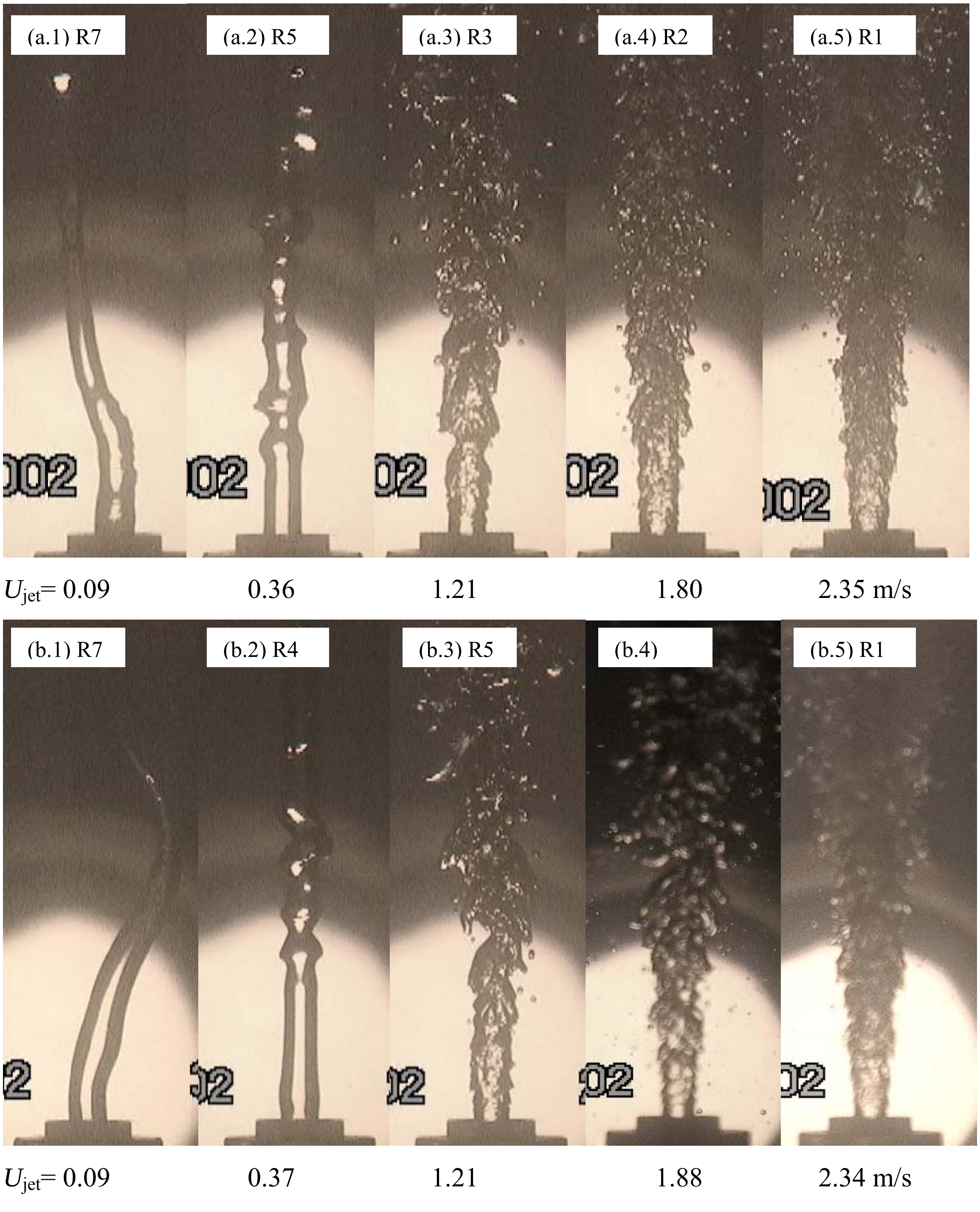

Figure 3.9 Five breakup modes observed during liquid CO_2 injection into tap water from 5 mm tube orifice at different pressures. Frames a.1 to a.5 correspond to Case CDT05WTP52 at 52 bar. Frames b.1 to b.5 correspond to Case CDT05WNP61 at 61 bar.

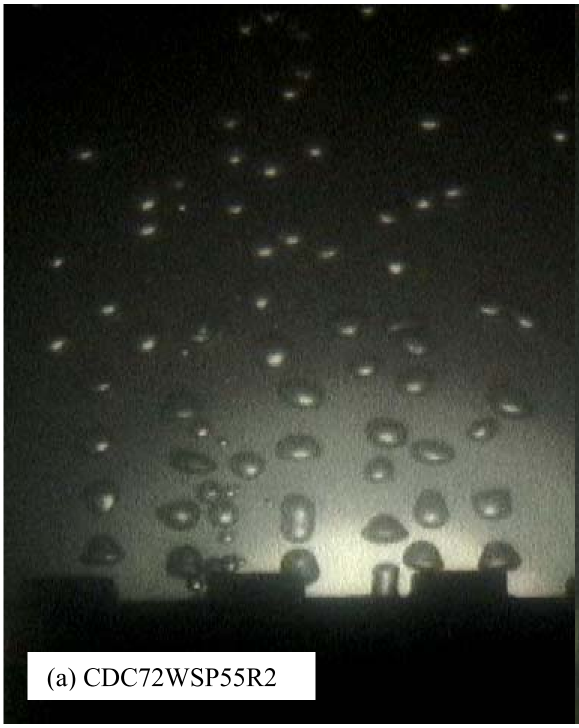

U_{jet} = 0.27 m/s

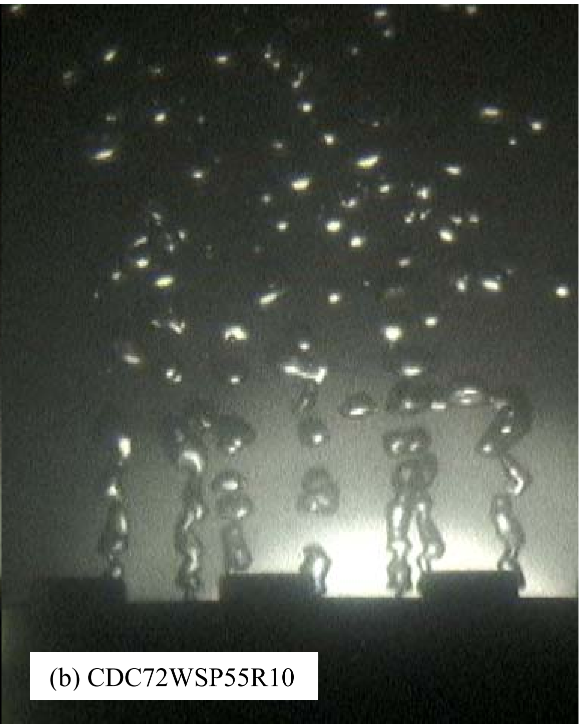

U_{jet} = 0.41 m/s

U_{jet} = 1.2 m/s

U_{jet} = 2.75 m/s

$U_{\text{jet}} = 4.69$ m/s

Figure 3.10 CO_2 injection into synthetic seawater from multi-orifice injector. Frames a, b, c, d and e show breakup modes 1, 2, 3, 4, and 5 respectively. The allen screw heads visible in silhouette in the frames are 9.5 mm (3/8 inch) in diameter.

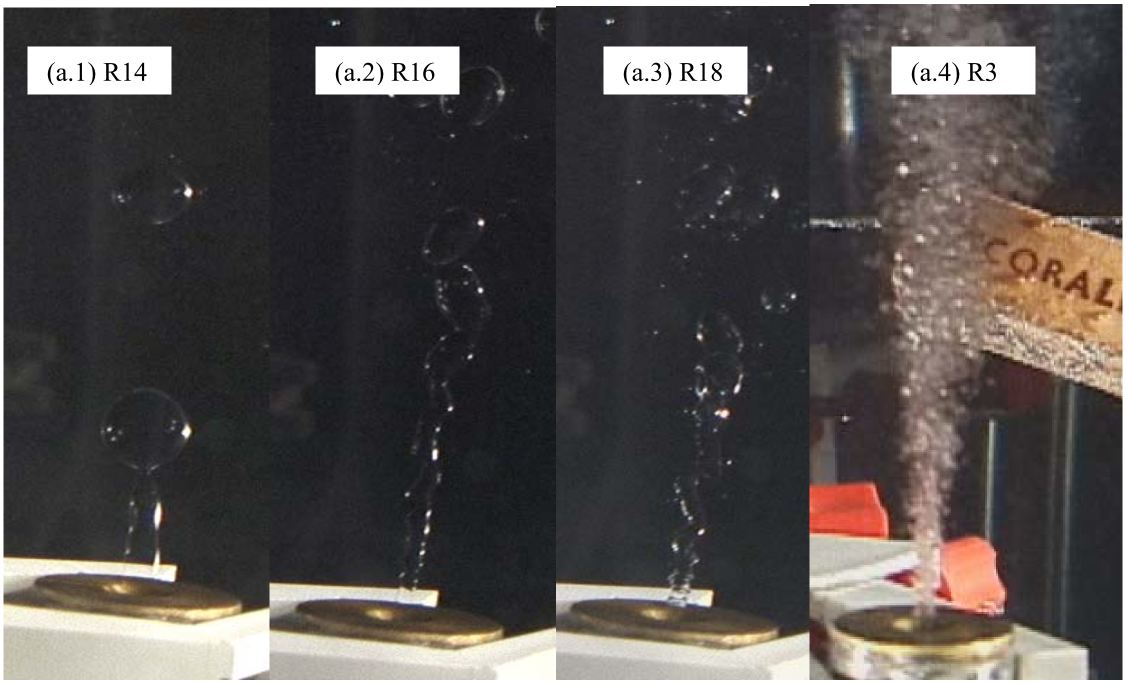

U_{jet}= 0.14 0.74 1.12 2.61 m/s

Figure 3.11 Breakup modes observed during silicone fluid injection into tap water from a 2 mm ASME sharp edge orifice. Case SFS02WTR.

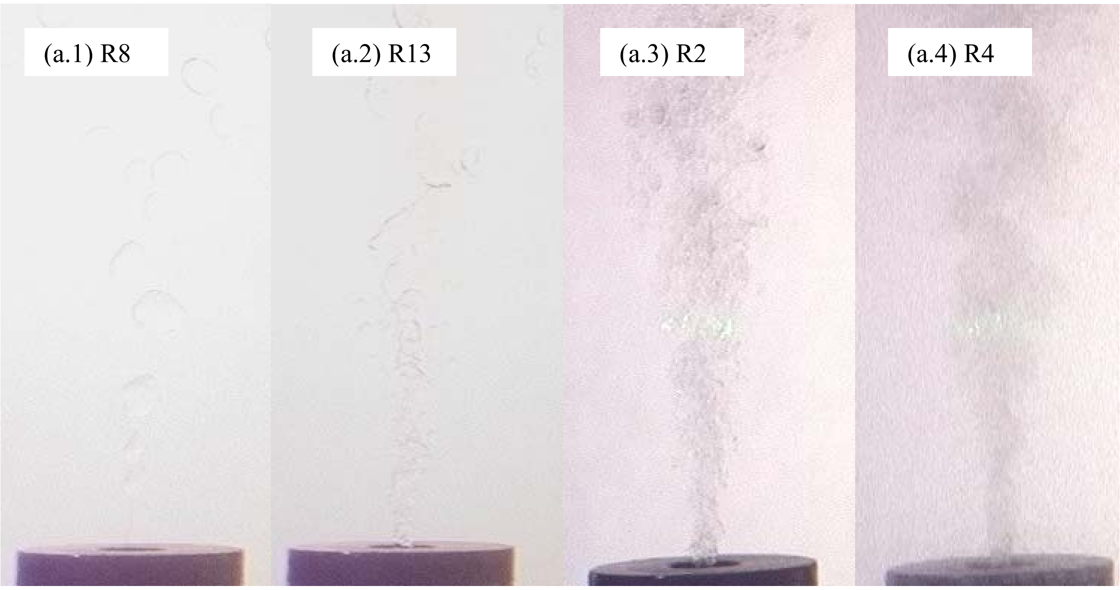

U_{jet}= 0.28 1.24 2.77 3.47 m/s

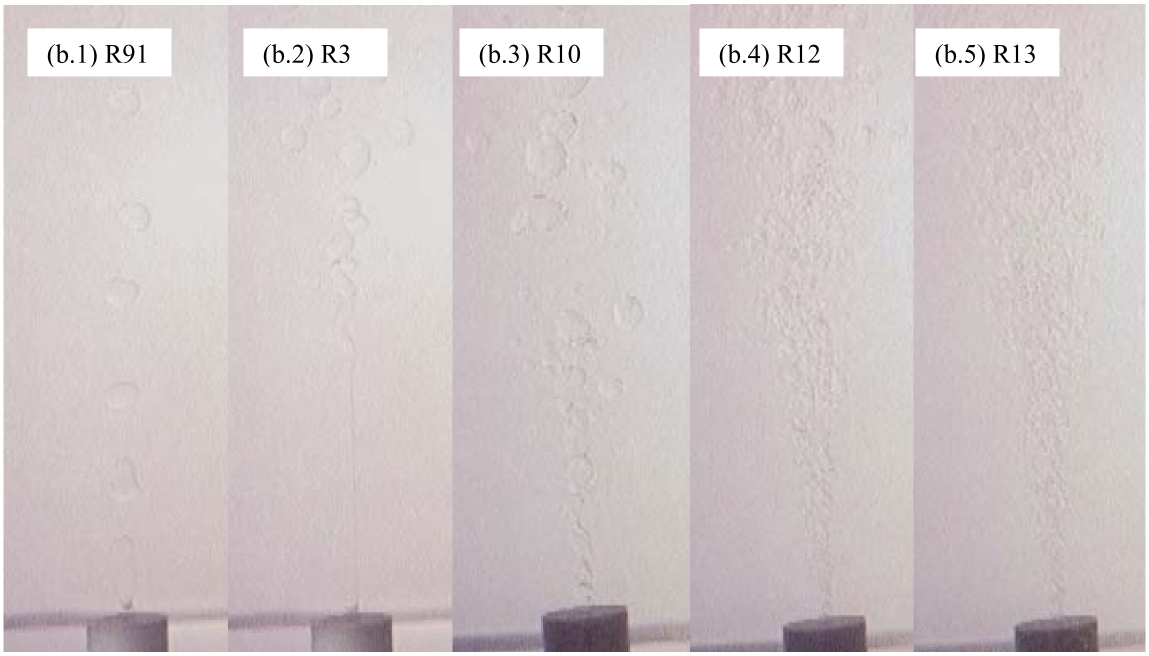

U_{jet}= <0.17 0.31 1.22 2.69 3.56 m/s

Figure 3.12 Low viscosity silicone fluid injection into tap water. Frames a.1 to a.4 show breakup modes 1, 2, 3 and 4 for Case LSS02WTR. Frames b.1 to b.5 show the 5 breakup modes for Case LST02WTR.

3.2.1.1 Instability Regime 1: Varicose Breakup

Varicose breakup has been studied extensively. At very low velocities, a symmetric surface wave forms and grows, eventually pinching off the jet and producing a train of droplets. The droplets are almost uniformly sized and their diameters exceed that of the jet.

In some situations, satellite droplets much smaller than the primary droplets, are generated between two primary droplets. Satellite droplet formation has been analyzed by Goedde and Yuen (1970), who calculated the pressure distribution in the liquid from experimentally derived wave profiles. They noted that the pressure gradient near the separation point increases as the surface contracts, and accelerates the detachment process. This results in a sharply pointed ligament whose internal pressure distribution increases to an extreme value at its point, and a droplet whose internal pressure is essentially constant. The ligament subsequently rolls up into a satellite droplet.

In our experiments, satellite droplets were observed only during injection of high viscosity crude oil (Platform Gail) into water from both 1 and 5 mm sharp edge orifices (Figures 3.13 and 3.14). The kinematic viscosity of Platform Gail crude oil is 211 centistrokes which was an order of magnitude higher than the next most viscous jet fluid. Viscosity apparently plays a critical role in the formation of satellite droplets. This is consistent with the explanation of why Rayleigh instability theory is unable to predict satellite droplets since viscous force is not considered. This deficiency is one reason why we chose to identify this instability regime as varicose breakup rather than Rayleigh instability. The principal characteristic of instability regime 1 is that the jet break-up instability is axisymmetric.

3.2.1.2 Instability Regime 2: Sinuous Wave Breakup

As jet velocity increases, the breakup length of the laminar jet increases. An asymmetric instability emerges and causes the jet to wave sinuously and generates non-uniform size droplets. This is called the first-wind induced breakup regime in liquid-gas systems. The inertial effects of the surrounding fluids can no longer be neglected.

Examples of sinuous wave breakup for various jet fluids and injection nozzles are provided in Figures 3.15 through 3.19. The data indicate that the tube nozzle (Figures 3.18 and 3.19) produced jets that were remarkably more stable than jets from a sharp edge orifice. A well-developed boundary layer that forms in the tube orifice results in a velocity profile at the orifice exit that is different from the jet exit velocity profile for a sharp edge orifice. This suggests a coupling between the initial velocity profile of the jet and the instability mechanism.

3.2.1.3 Instability Regime 3: Filament Core Breakup

At higher velocities, two instabilities mechanisms appear to operate in parallel: the surface of the jet becomes unstable to short wavelength disturbances and disintegrates close to the orifice into fine droplets, while the core of the jet persists as a continuum fluid filament that breaks up further downstream into large droplets (e.g., Figure 3.2 a.3). These two distinct instability mechanisms result in a polydispersion of droplets, initially comprising two different size groups.

3.2.1.4 Instability Regime 4: Wave atomization

Raising the velocities moves the breakup location of the jet core filament closer to the orifice and also increases the fraction of fine droplets (e.g., frames a.4 and b.4 in Figures 3.2 to 3.9). The two edges of the jet wave sinuously. In our experiments, the dense cloud of fine droplets on the perimeter of the jet obscures its interior and it could not be determined clearly whether breakup of the core filament persists and continues to produce relatively large droplets.

3.2.1.5 Instability Regime 5: Full Atomization

Finally, at high flow rates, atomization is attained. The jet breaks up into fine droplets very close to the injection orifice. As will be shown later in this report, droplet sizes in this breakup regime are relative uniform compared with those in instability regimes 3 and 4. The large droplet peaks of the multimodal distributions characteristic of regimes 3 and 4 disappear as atomization is achieved.

3.2.2 Injection Test Matrix

Tables 3.1, 3.2 and 3.3 summarize the injection tests: 97 runs with liquid CO_2; 154 runs with 4 crude oils; and 43 runs with two silicone fluids. Each run is identified by a unique alphanumeric name assigned according to following convention:

1. The first two letters indicate the jet fluid. CD stands for liquid Carbon Dioxide; GE for Genesis crude oil; MA for Mars TLP crude oil; NS for Neptune SPAR crude oil; PG for Platform Gail crude oil; SF for the Silicone Fluid with 20 cs viscosity; and LS for the low viscosity silicone fluid.
2. The next letter and two digits describe the orifice. C stands for a sharp edge orifice for liquid CO_2 tests; S for a sharp edge orifice for tests of crude oils and silicone fluids; T for a tube orifice. The digits provide the diameter of the orifice in mm: either 01, 02, 05 or 10. Multiple orifice nozzles are indicated by C72. C stands for sharp edge orifice; 7 for the number of the orifices and 2 for the diameter of the each orifice.
3. The following two letters indicate the ambient fluid: WT = tap water; WN = natural surface seawater; WS = synthetic seawater.
4. For liquid CO_2 injection tests, the next letter “P” means pressure. The two digits following “P” is the pressure of the run in bar.
5. For the crude oil and silicone fluid injection tests, the letters “R” or “C” are used instead of “P”. “R” indicates that the water is at room temperature (around 18°C) and “C” indicates that the water was chilled.
6. Finally, “R”+ digits indicates the run number for a general set of conditions. Typically, flow rate varies for different run numbers.

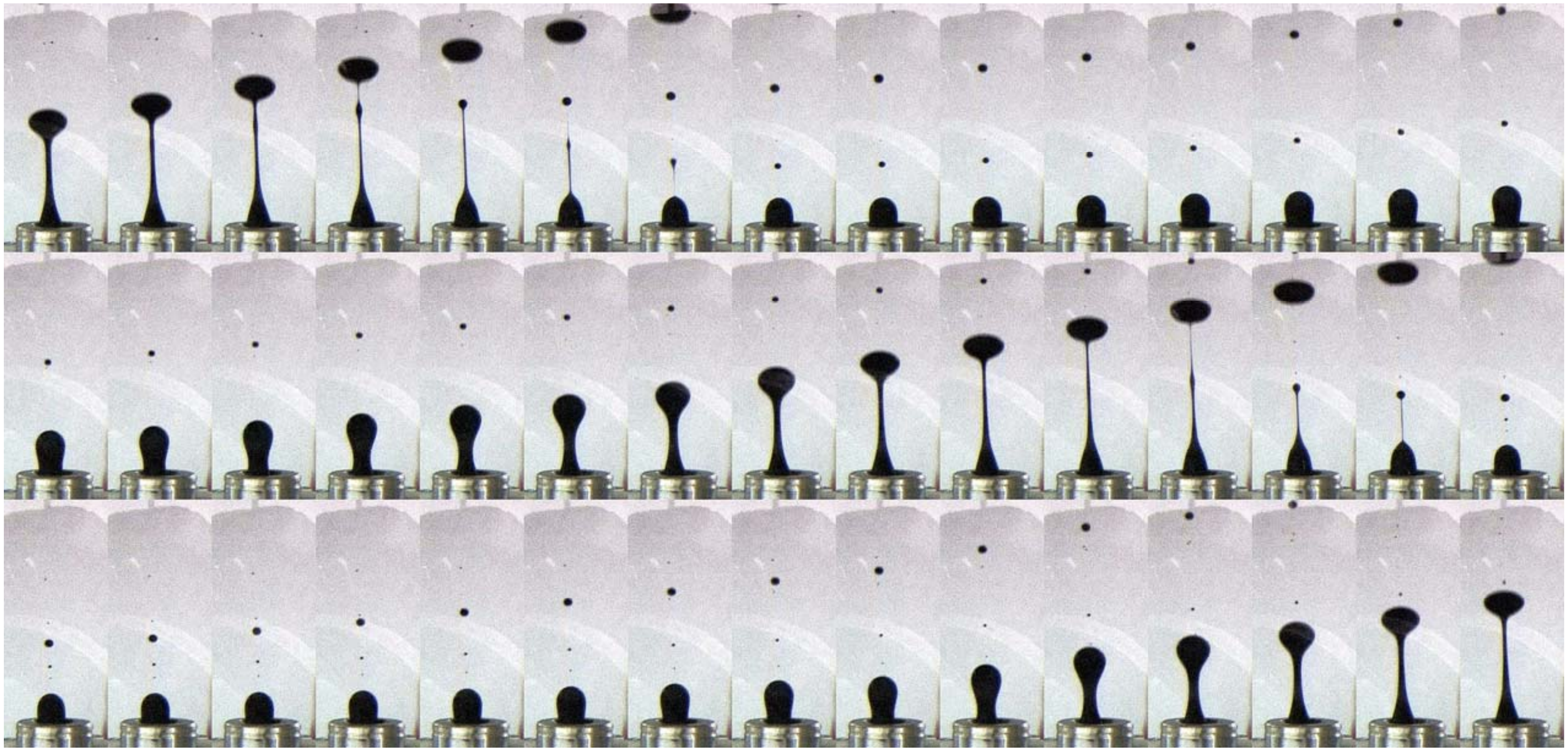

Figure 3.13 Satellite droplets observed when high viscosity Platform Gail crude oil is injected into tap water from a 1 mm sharp edge orifice at varicose breakup mode, run PGS01WTRR5. Time interval between any two adjacent frames is 1/15 second.

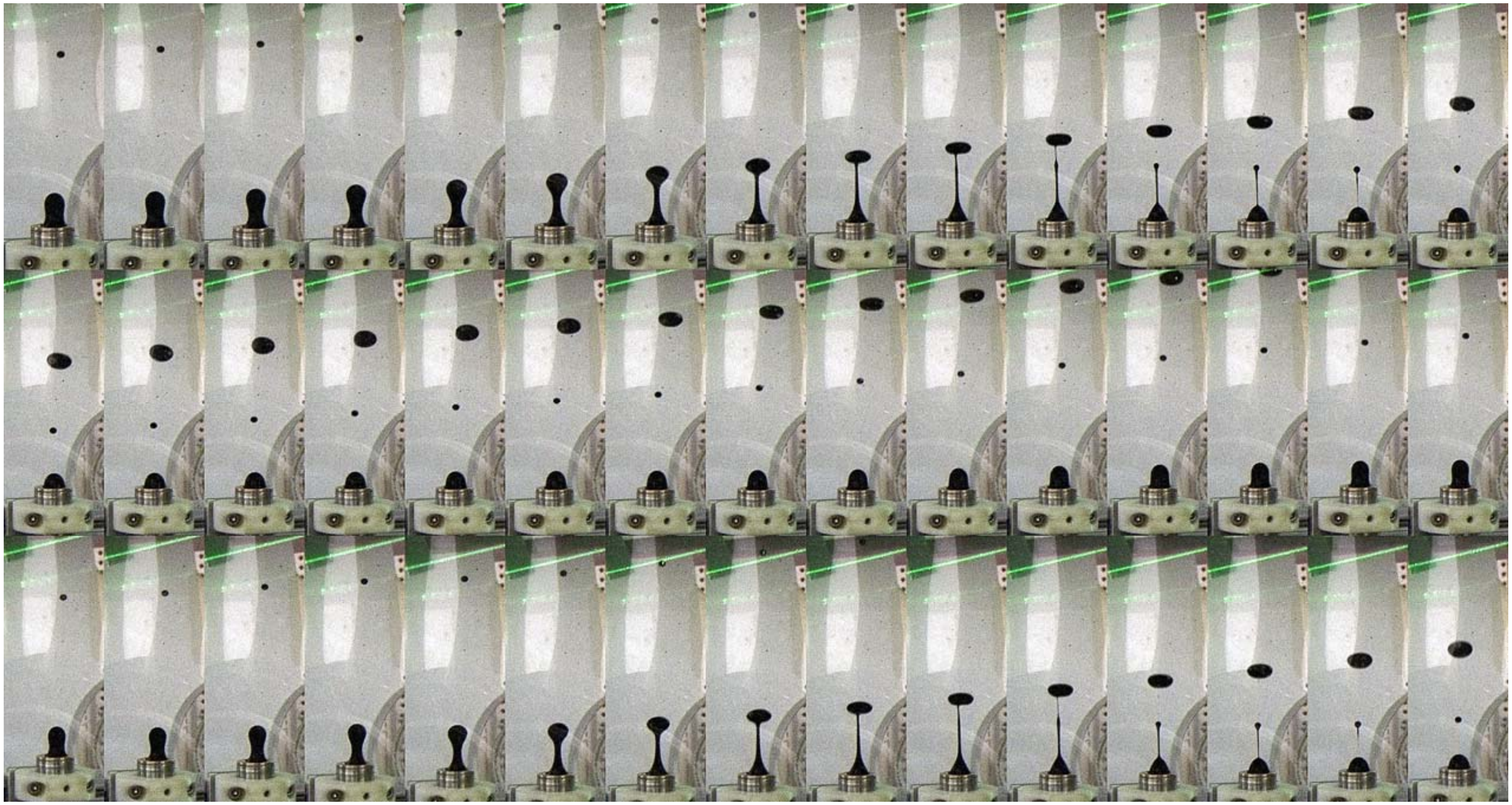

Figure 3.14 Satellite droplets observed when high viscosity Platform Gail crude oil is injected into tap water from 5 mm sharp edge orifice, run PGS05WTRR2. Time interval between any two adjacent frames is 1/15 second. $U_{jet} = 0.04$ m/s.

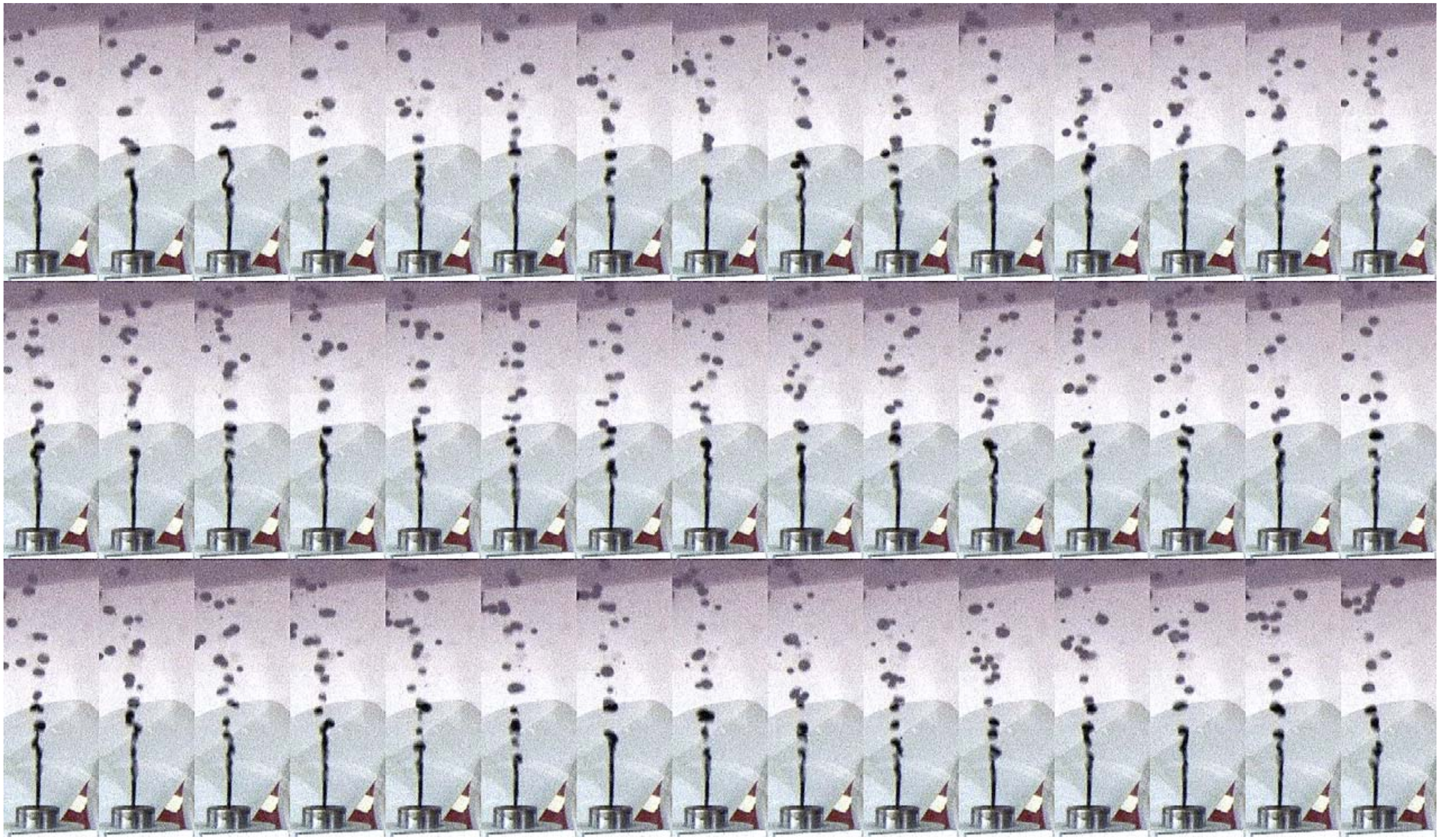

Figure 3.15 Sinuous wave breakup; instability regime 2. Frames are from test run GES02WTRR13. Genesis crude oil injected into tap water from a 2 mm sharp edge orifice. Time interval between any two adjacent frames is 1/15 second.

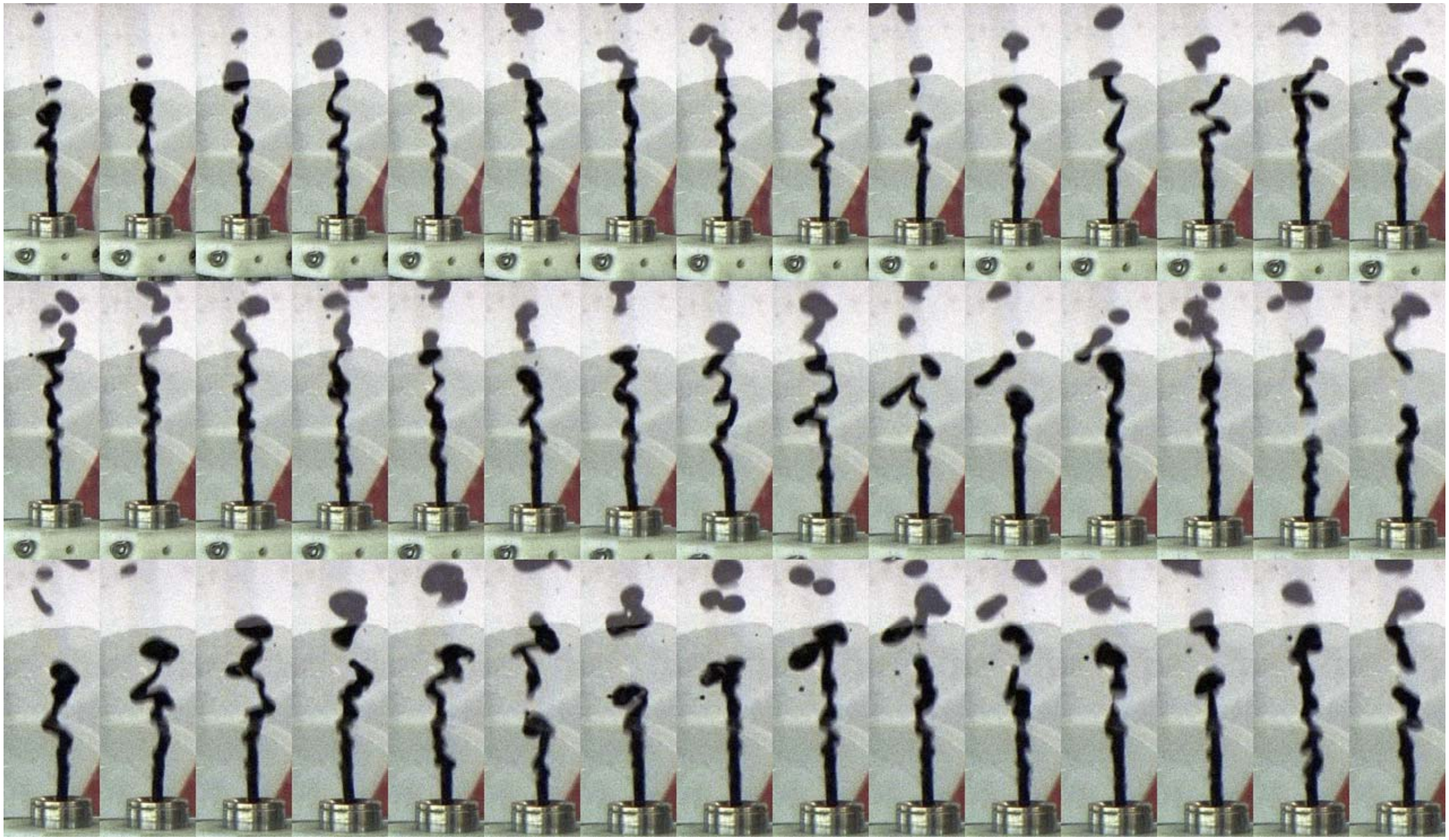

Figure 3.16 Sinuous wave breakup; instability regime 2. Frames are from test run GES05WTRR9. Genesis crude oil injected into tap water from 5 mm sharp edge orifice. Time interval between any two adjacent frames is 1/15 second.

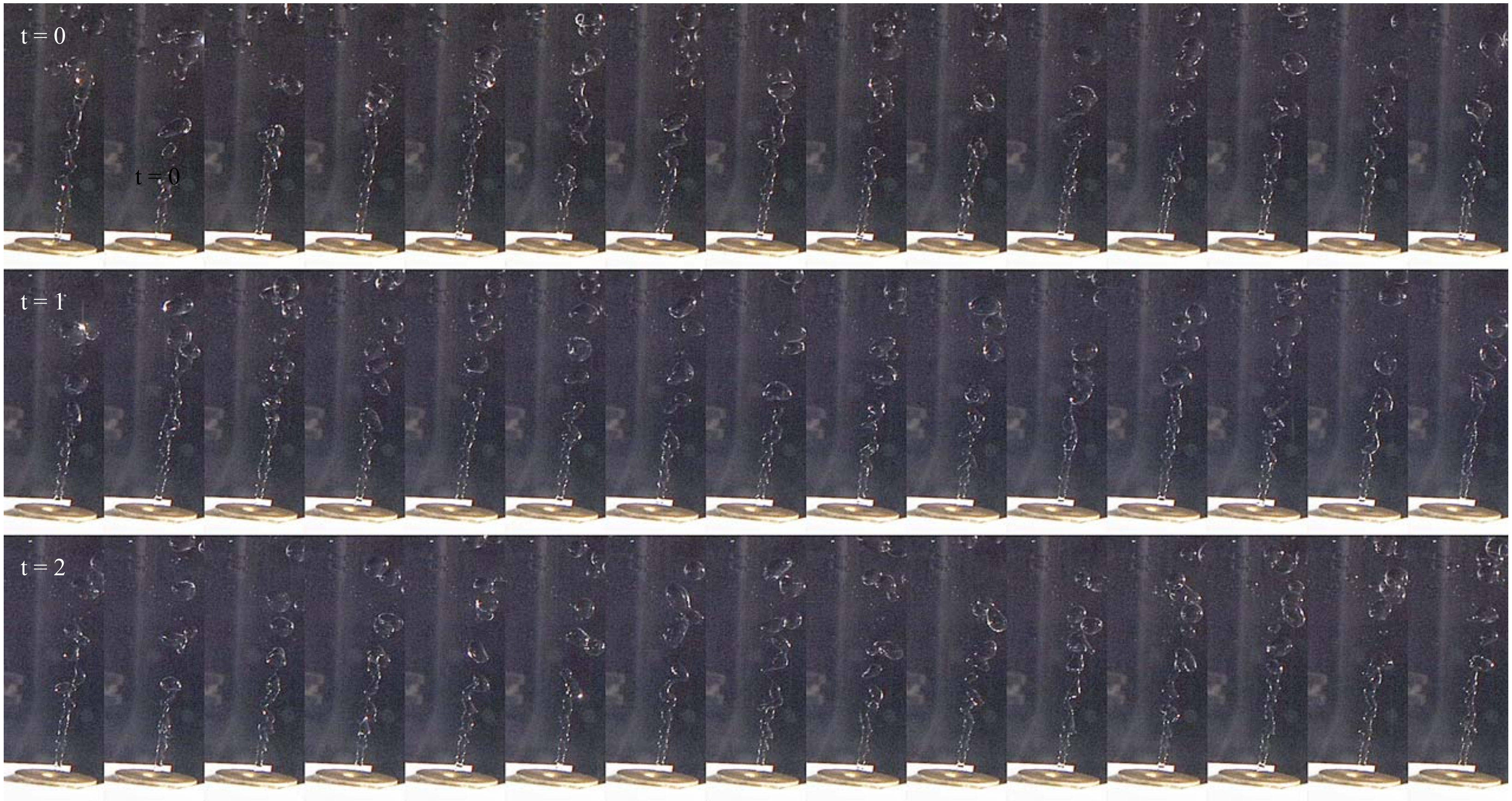

Figure 3.17 Sinuous wave breakup; instability regime 2. Frames are from test run SFS02WTRR17. Silicone fluid injected into tap water from 2 mm sharp edge orifice. Time interval between any two adjacent frames is 1/15 second.

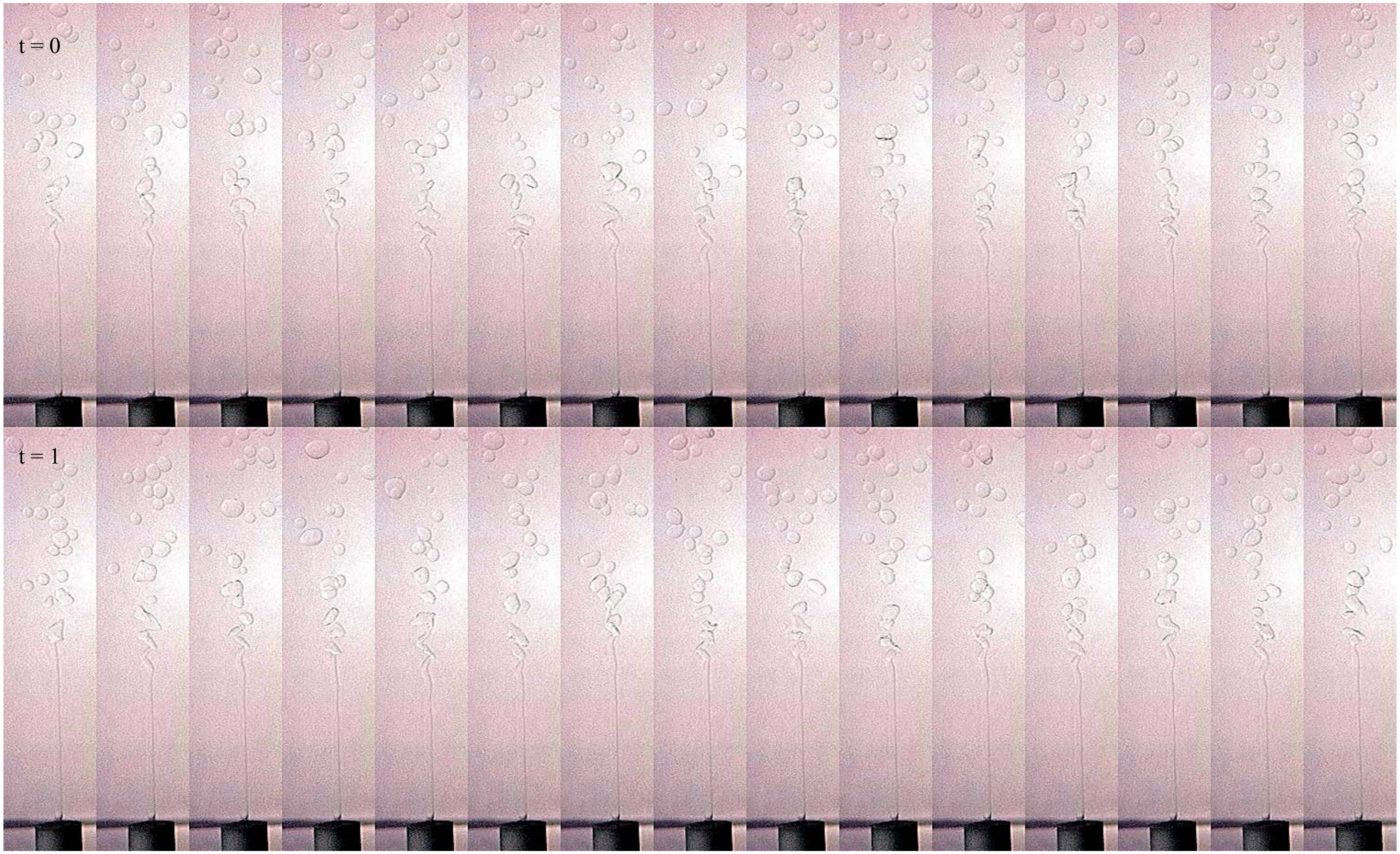

Figure 3.18 Sinuous wave breakup; instability regime 2. Test run LST02WTRR3. Low viscosity silicone fluid injected into tap water from a 2 mm i.d. tube orifice. Time interval between any two adjacent frames is 1/15 second.

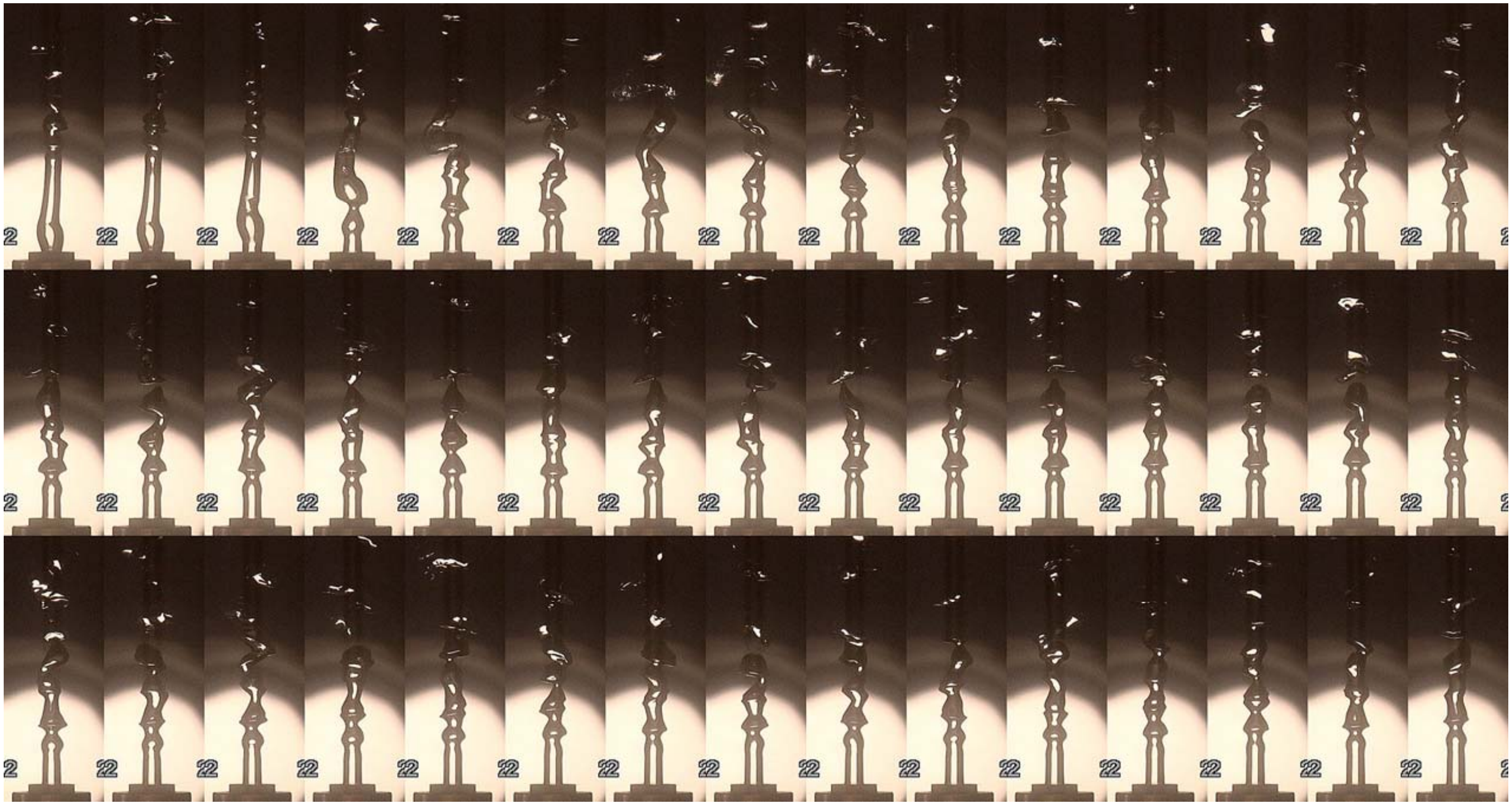

Figure 3.19 Sinuous wave breakup; instability regime 2. Test run CDT05WTP61R4. Liquid CO_2 injected into tap water from 5 mm i.d. tube orifice. Time interval between any two adjacent frames is 1/15 second.

Table 3.1 Liquid CO$_2$ Injection Test Matrix

CO$_2$ Test No.	Test Name	Orifice	Water Type	Press. *P* [bar]	Run No.	Run Time [min]	Water Temp. [°C]	CO$_2$ Temp. [°C]	CO$_2$ Mass Flowrate [kg/h]	Jet Vel. [m/s]	CO$_2$ Density [kg/m^3]	CO$_2$ Kine. Visc. [Pa s]	*IR*	*We*	*Re*	*Oh*
1	CDC02WTP52R1	C02	WT	52	1	2.92	6.88	-3.59	7.35	0.67	965.4	1.12E-04	2	3.24E+01	1.16E+04	4.89E-04
2	CDC02WTP52R2	C02	WT	52	2	2.42	6.9	0.63	8.17	0.77	940.5	1.03E-04	2	4.11E+01	1.40E+04	4.57E-04
3	CDC02WTP52R3	C02	WT	52	3	2.43	7.09	7.05	11.44	1.13	897.1	9.04E-05	2	8.45E+01	2.24E+04	4.11E-04
4	CDC02WTP52R4	C02	WT	52	4	5.73	7.31	10.74	16.62	1.69	867.5	8.36E-05	3	1.84E+02	3.51E+04	3.86E-04
5	CDC02WTP52R5	C02	WT	52	5	7.47	8.23	3.33	15.8	1.51	923.2	9.75E-05	3	1.57E+02	2.87E+04	4.37E-04
6	CDC02WTP52R6	C02	WT	52	6	6.32	8.58	9.45	19.89	2	878.4	8.59E-05	3	2.61E+02	4.09E+04	3.95E-04
7	CDC02WTP52R7	C02	WT	52	7	6.53	8.84	9.61	25.61	2.58	877.0	8.57E-05	4	4.33E+02	5.29E+04	3.94E-04
8	CDC02WTP52R8	C02	WT	52	8	7.65	9.14	9.39	31.87	3.21	878.8	8.61E-05	4	6.69E+02	6.55E+04	3.95E-04
9	CDC02WTP52R9	C02	WT	52	9	11.7	9.49	8.97	40.04	4.01	882.2	8.68E-05	5	1.05E+03	8.16E+04	3.98E-04
10	CDC02WTP52R10	C02	WT	52	10	8.42	10.12	7.82	15.8	1.57	891.3	8.89E-05	3	1.62E+02	3.14E+04	4.05E-04
11	CDC05WTP52R1	C05	WT	52	1	0.7	6.04	-5.27	2.72	0.04	974.7	1.15E-04	1	2.82E-01	1.67E+03	3.18E-04
12	CDC05WTP52R2	C05	WT	52	2	0.73	5.95	0	14.98	0.22	944.3	1.04E-04	1	8.81E-00	1.02E+04	2.92E-04
13	CDC05WTP52R3	C05	WT	52	3	1.25	6.07	-0.26	5.45	0.08	945.9	1.05E-04	1	1.16E-00	3.68E+03	2.93E-04
14	CDC05WTP52R4	C05	WT	52	4	1.15	6.4	1.42	6.81	0.1	935.5	1.01E-04	1	1.84E-00	4.75E+03	2.85E-04
15	CDC05WTP52R5	C05	WT	52	5	1	7.36	8.95	7.9	0.13	882.4	8.69E-05	1	2.62E-00	6.43E+03	2.52E-04
16	CDC05WTP52R6	C05	WT	52	6	1.02	7.55	9.39	11.17	0.18	878.8	8.61E-05	1	5.26E-00	9.18E+03	2.50E-04
17	CDC05WTP52R7	C05	WT	52	7	0.72	7.64	9.76	14.16	0.23	875.8	8.54E-05	1	8.49E-00	1.17E+04	2.48E-04
18	CDC05WTP52R8	C05	WT	52	8	0.75	7.74	10.18	17.16	0.28	872.3	8.46E-05	2	1.25E+01	1.43E+04	2.47E-04
19	CDC05WTP52R9	C05	WT	52	9	0.67	7.81	10.34	20.16	0.33	870.9	8.43E-05	2	1.73E+01	1.69E+04	2.46E-04
20	CDC05WTP52R10	C05	WT	52	10	0.65	7.91	9.96	24.24	0.39	874.1	8.50E-05	2	2.49E+01	2.02E+04	2.48E-04
21	CDC05WTP52R11	C05	WT	52	11	0.67	7.96	9.64	26.97	0.44	876.8	8.56E-05	2	3.07E+01	2.23E+04	2.49E-04
22	CDC05WTP52R12	C05	WT	52	12	0.57	8.01	9.19	34.05	0.55	880.5	8.64E-05	2	4.88E+01	2.79E+04	2.51E-04
23	CDC05WTP52R13	C05	WT	52	13	0.6	8.11	8.68	39.5	0.63	884.5	8.73E-05	3	6.54E+01	3.20E+04	2.53E-04
24	CDC05WTP52R14	C05	WT	52	14	0.58	8.12	7.48	47.13	0.75	893.8	8.96E-05	3	9.21E+01	3.72E+04	2.58E-04
25	CDC05WTP52R15	C05	WT	52	15	0.63	8.2	6.12	55.84	0.87	903.9	9.21E-05	3	1.28E+02	4.29E+04	2.64E-04

Table 3.1 (continued)

CO$_2$ Test No.	Test Name	Orifice	Water Type	Press. *P* [bar]	Run No.	Run Time [min]	Water Temp. [°C]	CO$_2$ Temp. [°C]	CO$_2$ Mass Flowrate [kg/h]	Jet Vel. [m/s]	CO$_2$ Density [kg/m^3]	CO$_2$ Kine. Visc. [Pa s]	*IR*	*We*	*Re*	*Oh*
26	CDC05WTP52R16	C05	WT	52	16	0.57	8.23	4.86	68.64	1.06	912.8	9.45E-05	3	1.91E+02	5.14E+04	2.69E-04
27	CDC05WTP52R17	C05	WT	52	17	0.52	8.38	3.25	83.9	1.28	923.7	9.77E-05	4	2.82E+02	6.08E+04	2.77E-04
28	CDC05WTP52R18	C05	WT	52	18	0.43	8.51	1.02	137.56	2.07	938.0	1.02E-04	5	7.48E+02	9.53E+04	2.87E-04
29	CDC05WTP52R19	C05	WT	52	19	0.48	8.6	-1.27	166.71	2.48	952.0	1.07E-04	5	1.08E+03	1.10E+05	2.98E-04
30	CDC05WTP52R20	C05	WT	52	20	10.2	9	4.84	38.14	0.59	913.0	9.46E-05	3	5.90E+01	2.85E+04	2.69E-04
31	CDC05WTP52R21	C05	WT	52	21	13.45	9.8	3.63	47.4	0.73	921.2	9.69E-05	3	9.04E+01	3.46E+04	2.75E-04
32	CDC05WTP52R22	C05	WT	52	22	8.65	9.88	2.23	56.39	0.86	930.4	9.97E-05	3	1.27E+02	4.00E+04	2.81E-04
33	CDC05WTP52R23	C05	WT	52	23	5.63	9.97	1.05	68.1	1.03	937.9	1.02E-04	4	1.83E+02	4.72E+04	2.87E-04
34	CDC05WTP52R24	C05	WT	52	24	4.67	10.05	0.59	82.81	1.25	940.7	1.03E-04	4	2.70E+02	5.69E+04	2.89E-04
35	CDC05WTP52R25	C05	WT	52	25	4.5	10.24	-2.45	127.21	1.88	958.9	1.09E-04	4	6.26E+02	8.23E+04	3.04E-04
36	CDC05WTP52R26	C05	WT	52	26	4.35	10.18	-4.63	165.07	2.4	971.2	1.14E-04	5	1.04E+03	1.02E+05	3.15E-04
37	CDC10WTP52R1	C10	WT	52	1	10.47	11.2	-2.82	112.5	0.41	961.0	1.10E-04	3	6.10E+01	3.62E+04	2.16E-04
38	CDC10WTP52R2	C10	WT	52	2	1.05	11.8	-4.34	179.78	0.66	969.6	1.13E-04	3	1.54E+02	5.61E+04	2.21E-04
39	CDC10WTP52R3	C10	WT	52	3	6.92	11.9	-7.18	245.7	0.88	985.0	1.20E-04	4	2.84E+02	7.27E+04	2.32E-04
40	CDC10WTP52R4	C10	WT	52	4	2.72	12.2	-9.01	330.69	1.18	994.6	1.24E-04	5	5.09E+02	9.46E+04	2.39E-04
41	CDC10WTP52R5	C10	WT	52	5	5.13	12.5	-9.75	409.69	1.45	998.4	1.25E-04	5	7.79E+02	1.16E+05	2.41E-04
42	CDC10WTP52R6	C10	WT	52	6	1.05	12.8	-2.39	34.87	0.13	958.5	1.09E-04	1	5.88E-00	1.13E+04	2.15E-04
43	CDC10WTP52R7	C10	WT	52	7	2.1	12.9	-1.63	60.75	0.23	954.1	1.08E-04	2	1.79E+01	2.00E+04	2.12E-04
44	CDC10WTP52R8	C10	WT	52	8	1.88	13	0	73.55	0.28	944.3	1.04E-04	2	2.65E+01	2.50E+04	2.06E-04
45	CDC10WTP52R9	C10	WT	52	9	1.93	13.1	-4	83.9	0.31	967.7	1.13E-04	2	3.37E+01	2.64E+04	2.20E-04
46	CDC10WTP52R10	C10	WT	52	10	1.08	13.2	-2.7	26.42	0.1	960.3	1.10E-04	1	3.37E-00	8.51E+03	2.16E-04
47	CDC10WTP52R11	C10	WT	52	11	1.15	13.2	-2	17.71	0.07	956.3	1.08E-04	1	1.52E-00	5.78E+03	2.13E-04
48	CDC10WTP52R12	C10	WT	52	12	2.98	13.3	-0.8	10.08	0.04	949.2	1.06E-04	1	4.96E-01	3.37E+03	2.09E-04
49	CDC10WTP52R13	C10	WT	52	13	1.28	13.5	2.7	5.99	0.02	927.3	9.88E-05	1	1.79E-01	2.15E+03	1.97E-04
50	CDT02WTP52R1	T02	WT	52	1	9.55	7.44	13.86	16.07	1.7	838.0	7.82E-05	3	1.79E+02	3.63E+04	3.68E-04
51	CDT02WTP52R2	T02	WT	52	2	10.23	7.91	12.85	17.16	1.79	848.1	7.99E-05	3	2.01E+02	3.80E+04	3.73E-04

Table 3.1 (continued)

CO_2 Test No.	Test Name	Orifice	Water Type	Press. *P* [bar]	Run No.	Run Time [min]	Water Temp. [°C]	CO_2 Temp. [°C]	CO_2 Mass Flowrate [kg/h]	Jet Vel. [m/s]	CO_2 Density [kg/m^3]	CO_2 Kine. Visc. [Pa s]	*IR*	*We*	*Re*	*Oh*
52	CDT02WTP52R3	T02	WT	52	3	8.82	8.32	12.2	20.16	2.09	854.3	8.11E-05	3	2.75E+02	4.40E+04	3.77E-04
53	CDT02WTP52R4	T02	WT	52	4	8.38	8.67	11.6	25.06	2.58	859.8	8.21E-05	4	4.23E+02	5.40E+04	3.81E-04
54	CDT02WTP52R5	T02	WT	52	5	7.98	8.99	10.3	31.33	3.18	871.3	8.44E-05	4	6.52E+02	6.56E+04	3.89E-04
55	CDT02WTP52R6	T02	WT	52	6	7.95	9.33	9.49	38.95	3.92	878.0	8.59E-05	5	1.00E+03	8.02E+04	3.94E-04
56	CDT02WTP52R7	T02	WT	52	7	5.63	9.61	6.59	56.39	5.54	900.5	9.12E-05	5	2.04E+03	1.09E+05	4.14E-04
57	CDT02WTP52R8	T02	WT	52	8	8.27	9.94	2.95	82.54	7.88	925.7	9.83E-05	5	4.26E+03	1.49E+05	4.39E-04
58	CDT02WTP52R9	T02	WT	52	9	4.98	10.26	1.07	136.74	12.89	937.7	1.02E-04	5	1.15E+04	2.37E+05	4.53E-04
59	CDT02WTP52R10	T02	WT	52	10	3.95	10.48	-3.11	193.95	17.81	962.7	1.11E-04	5	2.26E+04	3.10E+05	4.85E-04
60	CDT02WTP52R11	T02	WT	52	11	3	10.59	-2.55	11.17	1.03	959.5	1.09E-04	2	7.53E+01	1.80E+04	4.81E-04
61	CDT02WTP52R12	T02	WT	52	12	2.78	10.64	0.42	8.17	0.77	941.8	1.03E-04	2	4.11E+01	1.40E+04	4.58E-04
62	CDT02WTP52R13	T02	WT	52	13	1.95	10.7	2.8	7.08	0.68	926.7	9.86E-05	2	3.13E+01	1.27E+04	4.41E-04
63	CDT02WTP52R14	T02	WT	52	14	1.77	10.73	4.39	5.45	0.53	916.0	9.54E-05	2	1.88E+01	1.01E+04	4.29E-04
64	CDT02WNP52R1	T02	WN	52	1	14.12	11.89	5	26.42	2.56	911.8	9.43E-05	4	4.43E+02	4.96E+04	4.25E-04
65	CDT02WNP52R2	T02	WN	52	2	17.25	12.44	4.31	40.32	3.89	916.6	9.56E-05	5	1.03E+03	7.46E+04	4.30E-04
66	CDT02WNP52R4	T02	WN	52	4	0.1	13.43	0.83	5.45	0.51	939.2	1.03E-04	2	1.83E+01	9.40E+03	4.55E-04
67	CDT02WNP52R5	T02	WN	52	5	1.58	13.46	1.44	7.35	0.7	935.4	1.01E-04	2	3.35E+01	1.28E+04	4.51E-04
68	CDT02WNP52R6	T02	WN	52	6	0.18	13.47	2.81	8.17	0.78	926.6	9.85E-05	2	4.17E+01	1.47E+04	4.41E-04
69	CDT02WNP52R7	T02	WN	52	7	0.68	13.51	3.12	11.44	1.09	924.6	9.79E-05	3	8.20E+01	2.07E+04	4.38E-04
70	CDT02WNP52R8	T02	WN	52	8	9.22	13.54	3.92	15.53	1.49	919.2	9.64E-05	3	1.52E+02	2.85E+04	4.32E-04
71	CDT02WNP52R9	T02	WN	52	9	10.83	13.6	6.67	19.89	1.95	899.9	9.11E-05	3	2.54E+02	3.86E+04	4.13E-04
72	CDT05WTP61R1	T05	WT	61	1	8.58	7.98	-0.39	84.72	1.26	954.2	1.05E-04	3	2.79E+02	5.71E+04	2.93E-04
73	CDT05WTP61R2	T05	WT	61	2	7.62	8.36	-3.25	160.44	2.34	970.1	1.11E-04	5	9.83E+02	1.02E+05	3.07E-04
74	CDT05WTP61R3	T05	WT	61	3	2.5	8.78	0.09	46.85	0.7	951.4	1.04E-04	3	8.55E+01	3.19E+04	2.90E-04
75	CDT05WTP61R4	T05	WT	61	4	3.27	8.96	1.31	24.79	0.37	944.2	1.02E-04	2	2.41E+01	1.73E+04	2.84E-04
76	CDT05WTP61R5	T05	WT	61	5	1.83	9.1	-1.8	82.54	1.21	962.1	1.08E-04	3	2.62E+02	5.41E+04	2.99E-04
77	CDT05WTP61R6	T05	WT	61	6	2.63	9.16	-0.31	14.16	0.21	953.7	1.05E-04	1	7.80E-00	9.56E+03	2.92E-04

Table 3.1 (continued)

CO_2 Test No.	Test Name	Orifice	Water Type	Press. *P* [bar]	Run No.	Run Time [min]	Water Temp. [°C]	CO_2 Temp. [°C]	CO_2 Mass Flowrate [kg/h]	Jet Vel. [m/s]	CO_2 Density [kg/m^3]	CO_2 Kine. Visc. [Pa s]	*IR*	*We*	*Re*	*Oh*
78	CDT05WTP61R7	T05	WT	61	7	3.1	9.26	2.11	5.99	0.09	939.5	9.99E-05	1	1.42E-00	4.24E+03	2.81E-04
79	CDT05WTP52R1	T05	WT	52	1	3.85	9.45	-2.18	158.81	2.35	957.3	1.09E-04	5	9.76E+02	1.03E+05	3.02E-04
80	CDT05WTP52R2	T05	WT	52	2	6.4	9.53	-3.53	123.12	1.8	965.0	1.12E-04	4	5.82E+02	7.81E+04	3.09E-04
81	CDT05WTP52R3	T05	WT	52	3	7.6	9.62	-1.16	82.54	1.23	951.3	1.07E-04	3	2.65E+02	5.48E+04	2.97E-04
82	CDT05WTP52R4	T05	WT	52	4	2.92	9.72	0.67	47.13	0.71	940.2	1.03E-04	3	8.75E+01	3.24E+04	2.89E-04
83	CDT05WTP52R5	T05	WT	52	5	2.55	9.8	-0.89	23.97	0.36	949.7	1.06E-04	2	2.24E+01	1.60E+04	2.96E-04
84	CDT05WTP52R6	T05	WT	52	6	2.97	9.91	0.14	13.89	0.21	943.5	1.04E-04	1	7.58E-00	9.46E+03	2.91E-04
85	CDT05WTP52R7	T05	WT	52	7	2.97	10.02	0.88	5.72	0.09	938.9	1.02E-04	1	1.29E-00	3.95E+03	2.88E-04
86	CDC72WSP55R1	C72	WS	55	1	8	2	-10	1.95	0.17	1001.6	1.26E-04	1	2.19E-00	2.73E+03	5.41E-04
87	CDC72WSP55R2	C72	WS	55	2	33	2	-10	3.11	0.27	1001.6	1.26E-04	1	5.60E-00	4.37E+03	5.41E-04
88	CDC72WSP55R3	C72	WS	55	3	18	2	-10	3.89	0.34	1001.6	1.26E-04	2	8.76E-00	5.47E+03	5.41E-04
89	CDC72WSP55R4	C72	WS	55	4	27	2	-10	5.84	0.52	1001.6	1.26E-04	2	1.97E+01	8.20E+03	5.41E-04
90	CDC72WSP55R5	C72	WS	55	5	18	2	-10	7.78	0.69	1001.6	1.26E-04	3	3.50E+01	1.09E+04	5.41E-04
91	CDC72WSP55R6	C72	WS	55	6	12	2	-10	13.62	1.2	1001.6	1.26E-04	3	1.07E+02	1.91E+04	5.41E-04
92	CDC72WSP55R7	C72	WS	55	7	8	2	-10	19.46	1.72	1001.6	1.26E-04	4	2.19E+02	2.73E+04	5.41E-04
93	CDC72WSP55R8	C72	WS	55	8	8	2	-10	38.91	3.44	1001.6	1.26E-04	5	8.76E+02	5.47E+04	5.41E-04
94	CDC72WSP55R9	C72	WS	55	9	1	2	-10	53.08	4.69	1001.6	1.26E-04	5	1.63E+03	7.46E+04	5.41E-04
95	CDC72WSP55R10	C72	WS	55	10	24	2	-10	4.67	0.41	1001.6	1.26E-04	2	1.26E+01	6.56E+03	5.41E-04
96	CDC72WSP55R11	C72	WS	55	11	28	2	-10	7	0.62	1001.6	1.26E-04	3	2.84E+01	9.84E+03	5.41E-04
97	CDC72WSP55R12	C72	WS	55	12	4	2	-10	31.13	2.75	1001.6	1.26E-04	4	5.60E+02	4.37E+04	5.41E-04

Table 3.2 Crude Oil Injection Test Matrix

Oil Test No.	Test Name	Oil Type	Orifice	Water Type	Run No.	Run Time [min]	Water Temp. [°C]	Oil Temp. [°C]	Oil Flow Rate [l/h]	Jet Vel. [m/s]	Oil Density [kg/m^3]	Oil Kine. Visc. [cs]	*IR*	*We*	*Re*	*Oh*
1	GES02WTRR1	GE	S02	WT	1	0.18	18.07	27.19	3.48	0.31	884.09	16.25	1	6.70E-00	3.35E+01	7.73E-02
2	GES02WTRR2	GE	S02	WT	2	0.45	18.08	27.26	4.55	0.40	884.09	16.19	1	1.15E+01	4.40E+01	7.70E-02
3	GES02WTRR3	GE	S02	WT	3	0.53	18.11	27.28	8.52	0.75	884.09	16.18	2	4.01E+01	8.23E+01	7.69E-02
4	GES02WTRR4	GE	S02	WT	4	3.32	18.11	27.32	15.96	1.41	884.09	16.14	3	1.41E+02	1.55E+02	7.68E-02
5	GES02WTRR5	GE	S02	WT	5	0.97	18.24	27.63	24.48	2.16	884.09	15.90	3	3.31E+02	2.41E+02	7.56E-02
6	GES02WTRR6	GE	S02	WT	6	1.05	18.26	27.62	32.76	2.90	884.09	15.90	4	5.93E+02	3.22E+02	7.56E-02
7	GES02WTRR7	GE	S02	WT	7	1.83	18.21	27.72	37.89	3.35	884.09	15.82	5	7.94E+02	3.74E+02	7.53E-02
8	GES02WTRR8	GE	S02	WT	8	3.70	18.41	27.72	42.69	3.77	884.09	15.83	5	1.01E+03	4.22E+02	7.53E-02
9	GES02WTRR9	GE	S02	WT	9	0.18	18.71	27.56	3.09	0.27	884.09	15.95	1	5.28E-00	3.03E+01	7.59E-02
10	GES02WTRR10	GE	S02	WT	10	0.10	18.71	27.56	3.84	0.34	884.09	15.95	1	8.15E-00	3.76E+01	7.59E-02
11	GES02WTRR11	GE	S02	WT	11	0.27	18.71	27.56	5.00	0.44	884.09	15.95	1	1.38E+01	4.90E+01	7.59E-02
12	GES02WTRR12	GE	S02	WT	12	0.15	18.71	27.56	8.10	0.72	884.09	15.95	2	3.63E+01	7.94E+01	7.59E-02
13	GES02WTRR13	GE	S02	WT	13	0.15	18.71	27.56	10.92	0.97	884.09	15.95	2	6.59E+01	1.07E+02	7.59E-02
14	GES02WTRR14	GE	S02	WT	14	0.20	18.71	27.56	13.86	1.23	884.09	15.95	3	1.06E+02	1.36E+02	7.59E-02
15	GES02WTRR15	GE	S02	WT	15	0.07	18.71	27.56	15.24	1.35	884.09	15.95	3	1.28E+02	1.49E+02	7.59E-02
16	GES02WTRR16	GE	S02	WT	16	0.12	18.71	27.56	18.12	1.60	884.09	15.95	3	1.82E+02	1.78E+02	7.59E-02
17	GES02WTRR17	GE	S02	WT	17	0.12	18.71	27.56	21.06	1.86	884.09	15.95	3	2.45E+02	2.06E+02	7.59E-02
18	GES02WTRR18	GE	S02	WT	18	0.12	18.71	27.56	27.42	2.42	884.09	15.95	4	4.16E+02	2.69E+02	7.59E-02
19	GES02WTRR19	GE	S02	WT	19	0.22	18.71	27.56	34.32	3.03	884.09	15.95	5	6.51E+02	3.36E+02	7.59E-02
20	GES02WTRR20	GE	S02	WT	20	0.08	18.71	27.56	41.10	3.63	884.09	15.95	5	9.34E+02	4.03E+02	7.59E-02
21	GES02WTRR21	GE	S02	WT	21	0.07	18.71	27.56	42.60	3.77	884.09	15.95	5	1.00E+03	4.18E+02	7.59E-02
22	GES02WTRR22	GE	S02	WT	22	0.07	18.71	27.56	55.20	4.88	884.09	15.95	5	1.68E+03	5.41E+02	7.59E-02
23	GES02WTRR23	GE	S02	WT	23	0.12	18.71	27.56	60.30	5.33	884.09	15.95	5	2.01E+03	5.91E+02	7.59E-02
24	GES02WTRR24	GE	S02	WT	24	0.10	18.71	27.56	67.80	5.99	884.09	15.95	5	2.54E+03	6.64E+02	7.59E-02
25	GES05WTRR1	GE	S05	WT	1	1.92	18.74	27.36	69.60	0.98	884.09	16.11	4	1.71E+02	2.70E+02	4.85E-02

Table 3.2 (continued)

Oil Test No.	Test Name	Oil Type	Orifice	Water Type	Run No.	Run Time [min]	Water Temp. [°C]	Oil Temp. [°C]	Oil Flow Rate [l/h]	Jet Vel. [m/s]	Oil Density [kg/m^3]	Oil Kine. Visc. [cs]	*IR*	*We*	*Re*	*Oh*
26	GES05WTRR2	GE	S05	WT	2	1.60	18.79	27.00	90.00	1.27	884.09	16.40	4	2.87E+02	3.43E+02	4.93E-02
27	GES05WTRR3	GE	S05	WT	3	2.45	19.01	27.14	117.00	1.66	884.09	16.29	4	4.84E+02	4.49E+02	4.90E-02
28	GES05WTRR4	GE	S05	WT	4	1.92	19.09	27.30	134.40	1.90	884.09	16.16	5	6.39E+02	5.20E+02	4.86E-02
29	GES05WTRR5	GE	S05	WT	5	0.17	19.30	26.69	6.00	0.08	884.09	16.65	1	1.27E-00	2.25E+01	5.01E-02
30	GES05WTRR6	GE	S05	WT	6	0.27	19.30	26.69	11.40	0.16	884.09	16.65	1	4.60E-00	4.28E+01	5.01E-02
31	GES05WTRR7	GE	S05	WT	7	0.27	19.30	26.69	17.82	0.25	884.09	16.65	1	1.12E+01	6.69E+01	5.01E-02
32	GES05WTRR8	GE	S05	WT	8	0.13	19.30	26.69	25.20	0.36	884.09	16.65	2	2.25E+01	9.47E+01	5.01E-02
33	GES05WTRR9	GE	S05	WT	9	0.20	19.30	26.69	31.20	0.44	884.09	16.65	2	3.44E+01	1.17E+02	5.01E-02
34	GES05WTRR10	GE	S05	WT	10	0.27	19.30	26.69	45.00	0.64	884.09	16.65	2	7.17E+01	1.69E+02	5.01E-02
35	GES05WTRR11	GE	S05	WT	11	0.27	19.30	26.69	51.72	0.73	884.09	16.65	3	9.47E+01	1.94E+02	5.01E-02
36	GES05WTRR12	GE	S05	WT	12	0.40	19.30	26.69	59.82	0.85	884.09	16.65	3	1.27E+02	2.25E+02	5.01E-02
37	GES05WTRR13	GE	S05	WT	13	0.13	19.30	26.69	69.60	0.98	884.09	16.65	3	1.71E+02	2.61E+02	5.01E-02
38	GES05WTRR14	GE	S05	WT	14	0.13	19.30	26.69	75.00	1.06	884.09	16.65	4	1.99E+02	2.82E+02	5.01E-02
39	GES05WTRR15	GE	S05	WT	15	0.15	19.30	26.69	91.20	1.29	884.09	16.65	4	2.94E+02	3.43E+02	5.01E-02
40	GES05WTRR16	GE	S05	WT	16	0.30	19.30	26.69	104.10	1.47	884.09	16.65	4	3.84E+02	3.91E+02	5.01E-02
41	GES05WTRR17	GE	S05	WT	17	0.17	19.30	26.69	108.00	1.53	884.09	16.65	5	4.13E+02	4.06E+02	5.01E-02
42	MAS05WTRR1	MA	S05	WT	1	1.33	16.74	27.98	69.27	0.98	869.69	11.81	4	1.67E+02	3.61E+02	3.58E-02
43	MAS05WTRR2	MA	S05	WT	2	1.87	16.66	28.12	95.07	1.35	869.69	11.75	4	3.15E+02	4.98E+02	3.56E-02
44	MAS05WTRR3	MA	S05	WT	3	1.78	16.81	28.11	120.75	1.71	869.69	11.76	4	5.08E+02	6.32E+02	3.57E-02
45	MAS05WTRR4	MA	S05	WT	4	2.13	16.92	28.05	168.00	2.38	869.69	11.78	5	9.83E+02	8.77E+02	3.57E-02
46	MAS05WTRR5	MA	S05	WT	5	0.15	17.07	28.17	4.50	0.06	869.69	11.73	1	7.05E-01	2.36E+01	3.56E-02
47	MAS05WTRR6	MA	S05	WT	6	0.10	17.08	28.22	6.60	0.09	869.69	11.71	1	1.52E-00	3.47E+01	3.55E-02
48	MAS05WTRR7	MA	S05	WT	7	0.23	17.08	28.10	10.26	0.15	869.69	11.76	1	3.66E-00	5.37E+01	3.57E-02
49	MAS05WTRR8	MA	S05	WT	8	0.10	17.09	28.12	11.94	0.17	869.69	11.75	1	4.96E-00	6.25E+01	3.56E-02
50	MAS05WTRR9	MA	S05	WT	9	0.07	17.09	28.13	16.62	0.24	869.69	11.75	1	9.62E-00	8.70E+01	3.56E-02
51	MAS05WTRR10	MA	S05	WT	10	0.12	17.10	28.15	24.60	0.35	869.69	11.74	2	2.11E+01	1.29E+02	3.56E-02

Table 3.2 (continued)

Oil Test No.	Test Name	Oil Type	Orifice	Water Type	Run No.	Run Time [min]	Water Temp. [°C]	Oil Temp. [°C]	Oil Flow Rate [l/h]	Jet Vel. [m/s]	Oil Density [kg/m^3]	Oil Kine. Visc. [cs]	*IR*	*We*	*Re*	*Oh*
52	MAS05WTRR11	MA	S05	WT	11	0.10	17.10	28.16	31.80	0.45	869.69	11.74	2	3.52E+01	1.67E+02	3.56E-02
53	MAS05WTRR12	MA	S05	WT	12	0.18	17.11	28.18	40.80	0.58	869.69	11.73	3	5.79E+01	2.14E+02	3.56E-02
54	MAS05WTRR13	MA	S05	WT	13	0.23	17.12	28.19	45.60	0.65	869.69	11.72	3	7.24E+01	2.39E+02	3.56E-02
55	MAS05WTRR14	MA	S05	WT	14	0.17	17.12	28.20	50.76	0.72	869.69	11.72	3	8.97E+01	2.66E+02	3.55E-02
56	MAS05WTRR15	MA	S05	WT	15	0.20	17.12	28.22	61.80	0.87	869.69	11.71	3	1.33E+02	3.25E+02	3.55E-02
57	MAS05WTRR16	MA	S05	WT	16	0.35	17.12	28.23	68.40	0.97	869.69	11.71	4	1.63E+02	3.59E+02	3.55E-02
58	MAS05WTRR17	MA	S05	WT	17	0.15	17.12	28.30	97.32	1.38	869.69	11.68	4	3.30E+02	5.13E+02	3.54E-02
59	MAS05WTRR18	MA	S05	WT	18	0.30	17.13	28.37	42.60	0.60	869.69	11.65	3	6.32E+01	2.25E+02	3.53E-02
60	MAS05WTRR19	MA	S05	WT	19	0.17	17.13	28.43	30.00	0.42	869.69	11.63	2	3.13E+01	1.59E+02	3.53E-02
61	MAS05WTRR20	MA	S05	WT	20	0.23	17.14	28.50	18.00	0.25	869.69	11.60	1	1.13E+01	9.55E+01	3.52E-02
62	MAS05WTRR21	MA	S05	WT	21	2.00	17.34	28.41	173.40	2.45	869.69	11.64	5	1.05E+03	9.17E+02	3.53E-02
63	MAS02WTRR1	MA	S02	WT	1	0.95	18.27	26.76	19.02	1.68	869.69	12.30	3	1.97E+02	2.38E+02	5.90E-02
64	MAS02WTRR2	MA	S02	WT	2	0.47	18.24	26.79	24.60	2.18	869.69	12.28	4	3.29E+02	3.08E+02	5.89E-02
65	MAS02WTRR3	MA	S02	WT	3	0.63	18.25	26.82	33.00	2.92	869.69	12.27	4	5.92E+02	4.14E+02	5.89E-02
66	MAS02WTRR4	MA	S02	WT	4	1.10	18.22	26.87	38.73	3.42	869.69	12.25	5	8.16E+02	4.86E+02	5.88E-02
67	MAS02WTRR5	MA	S02	WT	5	2.10	18.23	26.93	44.94	3.97	869.69	12.23	5	1.10E+03	5.65E+02	5.86E-02
68	MAS02WTRR6	MA	S02	WT	6	0.05	18.30	26.80	3.24	0.29	869.69	12.28	1	5.71E-00	4.06E+01	5.89E-02
69	MAS02WTRR7	MA	S02	WT	7	0.10	18.32	26.88	3.76	0.33	869.69	12.25	1	7.67E-00	4.72E+01	5.87E-02
70	MAS02WTRR8	MA	S02	WT	8	0.13	18.33	26.96	7.29	0.64	869.69	12.22	1	2.89E+01	9.18E+01	5.86E-02
71	MAS02WTRR9	MA	S02	WT	9	0.18	18.35	26.98	9.48	0.84	869.69	12.21	2	4.89E+01	1.19E+02	5.85E-02
72	MAS02WTRR10	MA	S02	WT	10	0.17	18.37	26.99	12.06	1.07	869.69	12.20	3	7.91E+01	1.52E+02	5.85E-02
73	MAS02WTRR11	MA	S02	WT	11	0.18	18.39	27.01	14.46	1.28	869.69	12.20	3	1.14E+02	1.82E+02	5.85E-02
74	MAS02WTRR12	MA	S02	WT	12	0.18	18.40	27.02	17.46	1.54	869.69	12.19	3	1.66E+02	2.20E+02	5.85E-02
75	MAS02WTRR13	MA	S02	WT	13	0.12	18.42	27.02	4.11	0.36	869.69	12.19	1	9.19E-00	5.18E+01	5.85E-02
76	MAS02WTRR14	MA	S02	WT	14	0.10	18.44	27.02	4.62	0.41	869.69	12.19	1	1.16E+01	5.83E+01	5.85E-02
77	MAS02WTRR15	MA	S02	WT	15	0.17	18.46	27.02	5.91	0.52	869.69	12.19	1	1.90E+01	7.46E+01	5.85E-02

Table 3.2 (continued)

Oil Test No.	Test Name	Oil Type	Orifice	Water Type	Run No.	Run Time [min]	Water Temp. [°C]	Oil Temp. [°C]	Oil Flow Rate [l/h]	Jet Vel. [m/s]	Oil Density [kg/m^3]	Oil Kine. Visc. [cs]	*IR*	*We*	*Re*	*Oh*
78	MAS02WTRR16	MA	S02	WT	16	0.28	18.46	27.02	7.11	0.63	869.69	12.19	1	2.75E+01	8.97E+01	5.85E-02
79	MAS02WTRR17	MA	S02	WT	17	0.15	18.46	27.02	4.38	0.39	869.69	12.19	1	1.04E+01	5.53E+01	5.85E-02
80	MAS02WTRR18	MA	S02	WT	18	0.12	18.46	27.02	3.75	0.33	869.69	12.19	1	7.65E-00	4.73E+01	5.85E-02
81	MAS02WTRR19	MA	S02	WT	19	0.05	18.46	27.02	6.96	0.62	869.69	12.19	1	2.63E+01	8.78E+01	5.85E-02
82	MAS02WTRR20	MA	S02	WT	20	1.00	18.45	27.10	18.30	1.62	869.69	12.16	3	1.82E+02	2.31E+02	5.83E-02
83	MAS02WTRR21	MA	S02	WT	21	0.52	18.49	27.17	77.40	6.84	869.69	12.13	5	3.26E+03	9.81E+02	5.82E-02
84	MAS02WTRR22	MA	S02	WT	22	0.67	18.45	27.24	51.30	4.54	869.69	12.10	5	1.43E+03	6.52E+02	5.80E-02
85	PGS01WTRR1	PG	S01	WT	1	1.92	17.67	27.25	10.54	3.73	929.69	148.75	3	5.16E+02	2.33E+01	9.76E-01
86	PGS01WTRR2	PG	S01	WT	2	2.43	17.66	27.47	15.30	5.41	929.69	144.13	4	1.09E+03	3.49E+01	9.45E-01
87	PGS01WTRR3	PG	S01	WT	3	0.28	17.81	27.39	3.39	1.20	929.69	145.81	1	5.33E+01	7.63E-00	9.56E-01
88	PGS05WTRR1	PG	S05	WT	1	1.10	17.63	27.33	8.16	0.12	929.69	147.07	1	2.48E-00	3.65E-00	4.31E-01
89	PGS05WTRR2	PG	S05	WT	2	0.17	17.67	27.38	3.00	0.04	929.69	146.02	1	3.35E-01	1.35E-00	4.28E-01
90	PGS05WTRR3	PG	S05	WT	3	0.72	17.70	27.42	5.27	0.07	929.69	145.18	1	1.03E-00	2.39E-00	4.26E-01
91	PGS05WTRR4	PG	S05	WT	4	0.45	17.82	27.47	8.94	0.13	929.69	144.13	1	2.97E-00	4.08E-00	4.23E-01
92	PGS05WTRR5	PG	S05	WT	5	0.42	17.95	27.51	13.68	0.19	929.69	143.29	1	6.96E-00	6.28E-00	4.20E-01
93	PGS05WTRR6	PG	S05	WT	6	0.23	17.95	27.54	20.22	0.29	929.69	142.66	2	1.52E+01	9.32E-00	4.18E-01
94	PGS05WTRR7	PG	S05	WT	7	0.17	17.95	27.56	28.14	0.40	929.69	142.24	2	2.95E+01	1.30E+01	4.17E-01
95	PGS05WTRR8	PG	S05	WT	8	0.17	17.95	27.59	37.50	0.53	929.69	141.61	2	5.23E+01	1.74E+01	4.15E-01
96	PGS05WTRR9	PG	S05	WT	9	0.17	17.95	27.62	43.74	0.62	929.69	140.98	2	7.12E+01	2.04E+01	4.14E-01
97	PGS05WTRR10	PG	S05	WT	10	0.13	17.96	27.65	63.12	0.89	929.69	140.35	3	1.48E+02	2.96E+01	4.12E-01
98	PGS05WTRR11	PG	S05	WT	11	0.12	17.96	27.67	54.00	0.76	929.69	139.93	3	1.09E+02	2.54E+01	4.10E-01
99	PGS05WTRR12	PG	S05	WT	12	0.08	17.96	27.70	51.00	0.72	929.69	139.30	3	9.68E+01	2.41E+01	4.09E-01
100	PGS05WTRR13	PG	S05	WT	13	0.15	17.96	27.73	43.20	0.61	929.69	138.67	2	6.95E+01	2.05E+01	4.07E-01
101	PGS05WTRR14	PG	S05	WT	14	0.07	17.97	27.76	24.00	0.34	929.69	138.04	2	2.14E+01	1.14E+01	4.05E-01
102	PGS05WTRR15	PG	S05	WT	15	0.13	17.97	27.78	48.00	0.68	929.69	137.62	3	8.57E+01	2.29E+01	4.04E-01
103	PGS05WTRR16	PG	S05	WT	16	0.02	17.97	27.81	101.40	1.43	929.69	136.99	4	3.83E+02	4.87E+01	4.02E-01

Table 3.2 (continued)

Oil Test No.	Test Name	Oil Type	Orifice	Water Type	Run No.	Run Time [min]	Water Temp. [°C]	Oil Temp. [°C]	Oil Flow Rate [l/h]	Jet Vel. [m/s]	Oil Density [kg/m^3]	Oil Kine. Visc. [cs]	*IR*	*We*	*Re*	*Oh*
104	PGS05WTRR17	PG	S05	WT	17	0.02	17.97	27.84	54.00	0.76	929.69	136.36	3	1.09E+02	2.60E+01	4.00E-01
105	PGS05WTRR18	PG	S05	WT	18	0.02	17.98	27.87	88.20	1.25	929.69	135.73	4	2.89E+02	4.27E+01	3.98E-01
106	PGS05WTRR19	PG	S05	WT	19	0.05	17.98	27.89	55.80	0.79	929.69	135.31	3	1.16E+02	2.71E+01	3.97E-01
107	PGS05WTRR20	PG	S05	WT	20	0.07	17.98	27.92	49.80	0.70	929.69	134.68	3	9.23E+01	2.43E+01	3.95E-01
108	PGS05WTRR21	PG	S05	WT	21	0.07	17.98	27.95	42.00	0.59	929.69	134.05	2	6.56E+01	2.06E+01	3.93E-01
109	PGS05WTRR22	PG	S05	WT	22	0.12	17.99	27.98	31.20	0.44	929.69	133.42	2	3.62E+01	1.54E+01	3.91E-01
110	PGS05WTRR23	PG	S05	WT	23	1.08	17.99	28.00	83.16	1.18	929.69	133.00	3	2.57E+02	4.11E+01	3.90E-01
111	PGS05WTRR24	PG	S05	WT	24	2.53	17.99	28.03	121.80	1.72	929.69	132.37	4	5.52E+02	6.05E+01	3.88E-01
112	PGS05WTRR25	PG	S05	WT	25	3.00	18.17	27.82	103.77	1.47	929.69	136.78	4	4.01E+02	4.99E+01	4.01E-01
113	NSS02WTRR1	NS	S02	WT	1	1.58	17.50	28.37	18.63	1.65	888.29	20.97	3	1.93E+02	1.40E+02	9.95E-02
114	NSS02WTRR2	NS	S02	WT	2	1.18	17.50	28.65	24.54	2.17	888.29	20.72	4	3.35E+02	1.86E+02	9.83E-02
115	NSS02WTRR3	NS	S02	WT	3	1.85	17.52	28.74	32.40	2.86	888.29	20.64	4	5.83E+02	2.47E+02	9.79E-02
116	NSS02WTRR4	NS	S02	WT	4	2.30	17.53	28.87	39.81	3.52	888.29	20.52	5	8.80E+02	3.05E+02	9.74E-02
117	NSS02WTRR5	NS	S02	WT	5	0.27	17.63	28.78	4.08	0.36	888.29	20.60	1	9.25E-00	3.11E+01	9.77E-02
118	NSS02WTRR6	NS	S02	WT	6	0.23	17.66	28.69	7.26	0.64	888.29	20.68	2	2.93E+01	5.51E+01	9.81E-02
119	NSS02WTRR7	NS	S02	WT	7	0.22	17.68	28.40	8.79	0.78	888.29	20.94	2	4.29E+01	6.59E+01	9.94E-02
120	NSS02WTRR8	NS	S02	WT	8	0.23	17.69	28.10	12.30	1.09	888.29	21.21	3	8.41E+01	9.11E+01	1.01E-01
121	NSS02WTRR9	NS	S02	WT	9	0.23	17.70	28.37	15.00	1.33	888.29	20.97	3	1.25E+02	1.12E+02	9.95E-02
122	NSS02WTRR10	NS	S02	WT	10	0.08	17.70	28.64	17.10	1.51	888.29	20.72	3	1.62E+02	1.30E+02	9.83E-02
123	NSS02WTRR11	NS	S02	WT	11	0.25	17.71	28.91	11.46	1.01	888.29	20.48	2	7.30E+01	8.79E+01	9.72E-02
124	NSS02WTRR12	NS	S02	WT	12	0.25	17.71	28.93	9.84	0.87	888.29	20.46	2	5.38E+01	7.55E+01	9.71E-02
125	NSS02WTRR13	NS	S02	WT	13	0.18	17.71	28.95	6.60	0.58	888.29	20.45	2	2.42E+01	5.07E+01	9.70E-02
126	NSS02WTRR14	NS	S02	WT	14	0.23	17.72	28.96	3.90	0.34	888.29	20.44	1	8.45E-00	3.00E+01	9.70E-02
127	NSS02WTRR15	NS	S02	WT	15	0.90	17.72	28.98	45.30	4.01	888.29	20.42	5	1.14E+03	3.49E+02	9.69E-02
128	NSS02WTRR16	NS	S02	WT	16	1.57	17.73	28.88	60.00	5.31	888.29	20.51	5	2.00E+03	4.60E+02	9.73E-02
129	NSS01WTRR1	NS	S01	WT	1	0.72	18.69	26.73	6.78	2.40	888.29	22.44	4	2.04E+02	9.48E+01	1.51E-01

Table 3.2 (continued)

Oil Test No.	Test Name	Oil Type	Orifice	Water Type	Run No.	Run Time [min]	Water Temp. [°C]	Oil Temp. [°C]	Oil Flow Rate [l/h]	Jet Vel. [m/s]	Oil Density [kg/m^3]	Oil Kine. Visc. [cs]	*IR*	*We*	*Re*	*Oh*
130	NSS01WTRR2	NS	S01	WT	2	1.10	18.75	26.71	12.60	4.46	888.29	22.46	4	7.06E+02	1.76E+02	1.51E-01
131	NSS01WTRR3	NS	S01	WT	3	3.13	18.65	26.73	15.90	5.62	888.29	22.44	5	1.12E+03	2.23E+02	1.51E-01
132	NSS01WTRR4	NS	S01	WT	4	2.37	18.67	26.82	4.60	1.63	888.29	22.36	3	9.38E+01	6.46E+01	1.50E-01
133	NSS01WTRR5	NS	S01	WT	5	2.48	18.71	26.89	9.53	3.37	888.29	22.30	4	4.03E+02	1.34E+02	1.50E-01
134	NSS01WTRR6	NS	S01	WT	6	0.45	18.95	27.10	3.14	1.11	888.29	22.11	3	4.38E+01	4.46E+01	1.48E-01
135	NSS01WTRR7	NS	S01	WT	7	0.25	18.94	27.18	5.66	2.00	888.29	22.04	4	1.42E+02	8.06E+01	1.48E-01
136	NSS01WTRR8	NS	S01	WT	8	0.08	18.93	27.26	4.88	1.73	888.29	21.97	3	1.06E+02	6.98E+01	1.47E-01
137	NSS01WTRR9	NS	S01	WT	9	0.20	18.92	27.34	3.54	1.25	888.29	21.89	3	5.56E+01	5.07E+01	1.47E-01
138	NSS01WTRR10	NS	S01	WT	10	0.18	18.92	27.18	2.92	1.03	888.29	22.04	2	3.79E+01	4.16E+01	1.48E-01
139	NSS01WTCR1	NS	S01	WT	1	1.20	8.37	27.53	4.57	1.61	888.29	21.72	3	9.26E+01	6.60E+01	1.46E-01
140	NSS01WTCR2	NS	S01	WT	2	0.52	8.39	27.59	6.83	2.42	888.29	21.67	4	2.07E+02	9.90E+01	1.45E-01
141	NSS01WTCR3	NS	S01	WT	3	1.97	8.51	27.64	9.79	3.46	888.29	21.62	4	4.26E+02	1.42E+02	1.45E-01
142	NSS01WTCR4	NS	S01	WT	4	6.62	8.82	27.78	12.99	4.59	888.29	21.50	4	7.49E+02	1.90E+02	1.44E-01
143	NSS02WNRR1	NS	S02	WN	1	2.92	18.27	26.98	18.63	1.65	888.29	22.22	3	1.93E+02	1.32E+02	1.05E-01
144	NSS02WNRR2	NS	S02	WN	2	2.42	18.38	22.12	23.49	2.08	888.30	26.60	4	3.07E+02	1.39E+02	1.26E-01
145	NSS02WNRR3	NS	S02	WN	3	3.43	18.41	27.27	30.90	2.73	888.29	21.96	5	5.30E+02	2.21E+02	1.04E-01
146	NSS02WNRR4	NS	S02	WN	4	4.45	18.46	27.44	42.63	3.77	888.29	21.81	5	1.01E+03	3.07E+02	1.03E-01
147	NSS02WNRR5	NS	S02	WN	5	0.43	18.55	27.42	3.60	0.32	888.29	21.82	1	7.20E-00	2.59E+01	1.04E-01
148	NSS02WNRR6	NS	S02	WN	6	0.30	18.55	27.47	5.10	0.45	888.29	21.78	1	1.45E+01	3.68E+01	1.03E-01
149	NSS02WNRR7	NS	S02	WN	7	0.28	18.55	27.52	9.72	0.86	888.29	21.73	2	5.25E+01	7.03E+01	1.03E-01
150	NSS02WNRR8	NS	S02	WN	8	0.40	18.55	27.57	14.43	1.28	888.29	21.69	3	1.16E+02	1.05E+02	1.03E-01
151	NSS02WNRR9	NS	S02	WN	9	0.67	18.55	27.61	18.60	1.64	888.29	21.65	3	1.92E+02	1.35E+02	1.03E-01
152	NSS02WNRR10	NS	S02	WN	10	0.33	18.51	27.64	12.00	1.06	888.29	21.62	2	8.00E+01	8.72E+01	1.03E-01
153	NSS02WNRR11	NS	S02	WN	11	0.25	18.57	27.72	8.46	0.75	888.29	21.55	2	3.98E+01	6.17E+01	1.02E-01
154	NSS02WNRR12	NS	S02	WN	12	0.17	18.57	27.72	77.40	6.84	888.29	21.55	5	3.33E+03	5.64E+02	1.02E-01

Table 3.3 Silicone Fluid Injection Test Matrix

Fluid Test No.	Test Name	Fluid Type	Orifice	Water Type	Run No.	Run Time [min]	Water Temp. [°C]	Fluid Temp. [°C]	Fluid Flow Rate [l/h]	Jet Vel. [m/s]	Fluid Dens. [kg/m^3]	Fluid Kine. Visc. [cs]	*IR*	*We*	*Re*	*Oh*
1	SFS02WTRR1	SF	S02	WT	1	0.87	24.01	21.59	19.22	1.70	953	21.95	4	2.65E+02	1.55E+02	1.05E-01
2	SFS02WTRR3	SF	S02	WT	3	0.53	23.40	21.66	29.49	2.61	953	21.91	4	6.23E+02	2.38E+02	1.05E-01
3	SFS02WTRR4	SF	S02	WT	4	0.68	24.19	21.70	14.99	1.33	953	21.89	3	1.61E+02	1.21E+02	1.05E-01
4	SFS02WTRR5	SF	S02	WT	5	0.37	24.12	21.74	23.55	2.08	953	21.86	4	3.97E+02	1.90E+02	1.05E-01
5	SFS02WTRR6	SF	S02	WT	6	1.77	24.15	21.77	12.61	1.11	953	21.85	2	1.14E+02	1.02E+02	1.05E-01
6	SFS02WTRR7	SF	S02	WT	7	0.77	24.31	21.81	5.66	0.50	953	21.82	2	2.30E+01	4.59E+01	1.04E-01
7	SFS02WTRR8	SF	S02	WT	8	0.65	24.27	21.85	2.79	0.25	953	21.80	1	5.57E-00	2.26E+01	1.04E-01
8	SFS02WTRR9	SF	S02	WT	9	0.62	24.36	21.88	7.03	0.62	953	21.78	2	3.54E+01	5.71E+01	1.04E-01
9	SFS02WTRR10	SF	S02	WT	10	1.05	24.40	21.92	8.08	0.71	953	21.76	2	4.68E+01	6.57E+01	1.04E-01
10	SFS02WTRR11	SF	S02	WT	11	0.83	24.51	21.96	9.18	0.81	953	21.74	2	6.03E+01	7.47E+01	1.04E-01
11	SFS02WTRR12	SF	S02	WT	12	1.55	24.55	21.99	10.01	0.89	953	21.72	2	7.18E+01	8.15E+01	1.04E-01
12	SFS02WTRR13	SF	S02	WT	13	0.78	24.68	22.03	12.13	1.07	953	21.70	3	1.05E+02	9.89E+01	1.04E-01
13	SFS02WTRR14	SF	S02	WT	14	0.27	25.55	22.03	1.62	0.14	953	21.70	1	1.89E-00	1.32E+01	1.04E-01
14	SFS02WTRR15	SF	S02	WT	15	0.78	25.93	22.07	5.57	0.49	953	21.67	1	2.23E+01	4.55E+01	1.04E-01
15	SFS02WTRR16	SF	S02	WT	16	0.67	25.99	22.10	8.41	0.74	953	21.66	2	5.07E+01	6.87E+01	1.04E-01
16	SFS02WTRR17	SF	S02	WT	17	0.67	26.03	22.14	10.32	0.91	953	21.63	2	7.63E+01	8.44E+01	1.04E-01
17	SFS02WTRR18	SF	S02	WT	18	0.60	26.05	22.18	12.67	1.12	953	21.61	2	1.15E+02	1.04E+02	1.03E-01
18	LSS02WTRR1	LS	S02	WT	1	0.30	23.47	23.99	19.11	1.69	760	0.66	3	2.73E+02	5.14E+03	3.22E-03
19	LSS02WTRR2	LS	S02	WT	2	0.30	23.52	23.99	31.38	2.77	760	0.66	4	7.36E+02	8.44E+03	3.22E-03
20	LSS02WTRR3	LS	S02	WT	3	0.47	23.54	23.99	36.75	3.25	760	0.66	4	1.01E+03	9.88E+03	3.22E-03
21	LSS02WTRR4	LS	S02	WT	4	0.77	23.56	23.99	39.27	3.47	760	0.66	4	1.15E+03	1.06E+04	3.22E-03
22	LSS02WTRR5	LS	S02	WT	5	0.38	23.68	23.99	24.18	2.14	760	0.66	3	4.37E+02	6.50E+03	3.22E-03
23	LSS02WTRR6	LS	S02	WT	6	0.90	23.70	23.99	14.83	1.31	760	0.66	3	1.64E+02	3.99E+03	3.22E-03

Table 3.3 (continued)

Fluid Test No.	Test Name	Fluid Type	Orifice	Water Type	Run No.	Run Time [min]	Water Temp. [°C]	Fluid Temp. [°C]	Fluid Flow Rate [l/h]	Jet Vel. [m/s]	Fluid Dens. [kg/m^3]	Fluid Kine. Visc. [cs]	*IR*	*We*	*Re*	*Oh*
24	LSS02WTRR7	LS	S02	WT	7	1.60	23.77	23.99	13.22	1.17	760	0.66	3	1.31E+02	3.55E+03	3.22E-03
25	LSS02WTRR8	LS	S02	WT	8	0.67	23.17	23.99	3.12	0.28	760	0.66	1	7.27E-00	8.39E+02	3.22E-03
26	LSS02WTRR9	LS	S02	WT	9	0.52	23.48	23.99	7.34	0.65	760	0.66	2	4.02E+01	1.97E+03	3.22E-03
27	LSS02WTRR10	LS	S02	WT	10	0.58	23.59	23.99	5.97	0.53	760	0.66	2	2.66E+01	1.61E+03	3.22E-03
28	LSS02WTRR11	LS	S02	WT	11	0.58	23.63	23.99	10.32	0.91	760	0.66	2	7.95E+01	2.77E+03	3.22E-03
29	LSS02WTRR12	LS	S02	WT	12	0.58	23.60	23.99	11.76	1.04	760	0.66	3	1.03E+02	3.16E+03	3.22E-03
30	LSS02WTRR13	LS	S02	WT	13	0.60	23.61	23.99	14.03	1.24	760	0.66	3	1.47E+02	3.77E+03	3.22E-03
31	LST02WTRR1	LS	T02	WT	1	1.03	24.14	24.48	3.78	0.33	760	0.65	2	1.07E+01	1.02E+03	3.20E-03
32	LST02WTRR2	LS	T02	WT	2	0.53	24.25	24.48	1.88	0.17	760	0.65	2	2.63E-00	5.07E+02	3.20E-03
33	LST02WTRR3	LS	T02	WT	3	0.62	24.25	24.48	3.49	0.31	760	0.65	2	9.10E-00	9.44E+02	3.20E-03
34	LST02WTRR4	LS	T02	WT	4	0.60	24.32	24.48	5.88	0.52	760	0.65	2	2.58E+01	1.59E+03	3.20E-03
35	LST02WTRR5	LS	T02	WT	5	0.58	24.39	24.48	7.93	0.70	760	0.65	2	4.70E+01	2.15E+03	3.20E-03
36	LST02WTRR6	LS	T02	WT	6	0.57	24.33	24.48	9.01	0.80	760	0.65	2	6.07E+01	2.44E+03	3.20E-03
37	LST02WTRR7	LS	T02	WT	7	0.55	24.47	24.48	11.67	1.03	760	0.65	2	1.02E+02	3.16E+03	3.20E-03
38	LST02WTRR8	LS	T02	WT	8	0.58	24.44	24.48	13.77	1.22	760	0.65	3	1.42E+02	3.73E+03	3.20E-03
39	LST02WTRR9	LS	T02	WT	9	0.57	24.52	24.48	1.88	0.17	760	0.65	2	2.64E-00	5.08E+02	3.20E-03
40	LST02WTRR10	LS	T02	WT	10	4.48	24.80	24.48	16.10	1.42	760	0.65	3	1.94E+02	4.35E+03	3.20E-03
41	LST02WTRR11	LS	T02	WT	11	3.38	24.86	24.48	20.85	1.84	760	0.65	3	3.25E+02	5.64E+03	3.20E-03
42	LST02WTRR12	LS	T02	WT	12	2.20	24.92	24.48	30.44	2.69	760	0.65	4	6.92E+02	8.23E+03	3.20E-03
43	LST02WTRR13	LS	T02	WT	13	2.82	24.93	24.48	40.29	3.56	760	0.65	5	1.21E+03	1.09E+04	3.20E-03

3.2.3 Liquid-liquid Jet Instability Regime Boundaries

Digital video records of each of the 294 tests using liquid CO_2, 4 crude oils or two silicone fluids were reviewed and classified as one of the five breakup modes shown in Figure 3.1. Following convention used in previous studies of jet breakup, these data were plotted against the corresponding dimensionless Ohnesorge Number, *Oh*, and jet Reynolds Number, *Re*, to establish the boundaries of the different instability regimes. This has significant practical importance since the instability regime determines the characteristics of the droplet size distribution (i.e., monodisperse; polydisperse; coarse or fine droplets). *Re* and *Oh* can be calculated from fluid properties and known or estimated jet flow rate and orifice diameter, and can be compared with the instability diagram to predict the mode of breakup and the general characteristics of droplet size. The five instability regimes are separated by 4 boundaries, which are referred to as boundaries 1, 2, 3, and 4 in the following text.

A linear least square regression was applied to find the four best-fit boundaries between the 5 breakup regimes. Values of *Re* and *Oh* corresponding to points adjacent to the regime boundaries can be identified by examining the video records. A linear fit to these data points was performed for each boundary.

As an example, for Case GES05WTR, where Genesis crude oil was injected into tap water from a 5 mm sharp edge orifice, 17 runs were performed in which flow rate (jet velocity) was varied. The original sequences of the tests are shown on the left of Table 3.4. These entries were re-sorted in increasing value of *Re* as shown on the right of Table 3.2. Points (runs) that straddled the boundaries between regimes were selected to be included in the data set used to identify those boundaries. For example, the transition between instability regimes 1 and 2 occurred between runs 7 and 8. We selected both runs 7 and 8, the highest and lowest values of *Re* collected for regimes 1 and 2, respectively, for inclusion in the data set used to locate the boundary between regimes 1 and 2. Similarly, values of *Re* and *Oh* for runs 10 and 11, runs 1 and 14 and runs 16 and 17 were included in the data sets for the curve fits for the boundaries of regimes 2, 3, and 4, respectively.

Table 3.4 Determination of regime boundary points for case GES05WTR.

Original Order				New Order			
Run No.	Instability Regime *IR*	*Re*	*Oh*	Run No.	Instability Regime *IR*	*Re*	*Oh*
1	3	2.70E+02	4.85E-02	5	1	2.25E+01	5.01E-02
2	4	3.43E+02	4.93E-02	6	1	4.28E+01	5.01E-02
3	5	4.49E+02	4.90E-02	7	1	6.69E+01	5.01E-02
4	5	5.20E+02	4.86E-02	8	2	9.47E+01	5.01E-02
5	1	2.25E+01	5.01E-02	9	2	1.17E+02	5.01E-02
6	1	4.28E+01	5.01E-02	10	2	1.69E+02	5.01E-02
7	1	6.69E+01	5.01E-02	11	3	1.94E+02	5.01E-02
8	2	9.47E+01	5.01E-02	12	3	2.25E+02	5.01E-02
9	2	1.17E+02	5.01E-02	13	3	2.61E+02	5.01E-02
10	2	1.69E+02	5.01E-02	1	3	2.70E+02	4.85E-02
11	3	1.94E+02	5.01E-02	14	4	2.82E+02	5.01E-02
12	3	2.25E+02	5.01E-02	2	4	3.43E+02	4.93E-02
13	3	2.61E+02	5.01E-02	15	4	3.43E+02	5.01E-02
14	4	2.82E+02	5.01E-02	16	4	3.91E+02	5.01E-02
15	4	3.43E+02	5.01E-02	17	5	4.06E+02	5.01E-02
16	4	3.91E+02	5.01E-02	3	5	4.49E+02	4.90E-02
17	5	4.06E+02	5.01E-02	4	5	5.20E+02	4.86E-02

This process was repeated for each of the other 21 cases, yielding 4 sets of data points straddling the 4 regime boundaries (i.e., the boundaries between regimes 1 & 2, 2& 3, 3& 4 and 4 &5). Each data point comprises a value of *Re* and *Oh*. Linear relations for the four boundaries (*i* =1, 2, 3, and 4), are postulated:

$$\log Oh = \log a_i + b_i \log Re \qquad i = 1,2,3,4 \tag{3.5}$$

where a_i and b_i are constants to be determined by regression analysis. This least squares analysis yields:

Boundary 1 between instability regions **1** and **2**:

$$Oh = 4.9196 \; Re^{-1.0459} \tag{3.6}$$

Boundary 2 between instability regions **2** and **3**:

$$Oh = 9.5979 \; Re^{-1.0255} \tag{3.7}$$

Boundary 3 between instability regions **3** and **4**:

$$Oh = 15.4108 \ Re^{-0.9989} \tag{3.8}$$

Boundary 4 between instability regions **4** and **5**:

$$Oh = 24.9548 \ Re^{-1.0027} \tag{3.9}$$

These boundaries, identified as the four dashed lines are plotted as in Figure 3.20, along with the complete data set of 294 points. The individual data sets used to identify the four individual boundaries are plotted in Figures 3.21 to 3.24 along with the least-squares curve fit of those regime boundaries.

An important observation is that all the relationships for the boundaries have similar form:

$$Oh = a \ Re^{b}$$

where $b \cong -1$. Comparing this with equations (3.1), (3.2) and (3.3) yields the result that the transitions between regimes will occur when we attain certain critical values of We equal to a_i^2. Furthermore, viscosity does not appear in We and is not relevant with respect to transition; only the parameters ρ_j, U_j, D and σ are important.

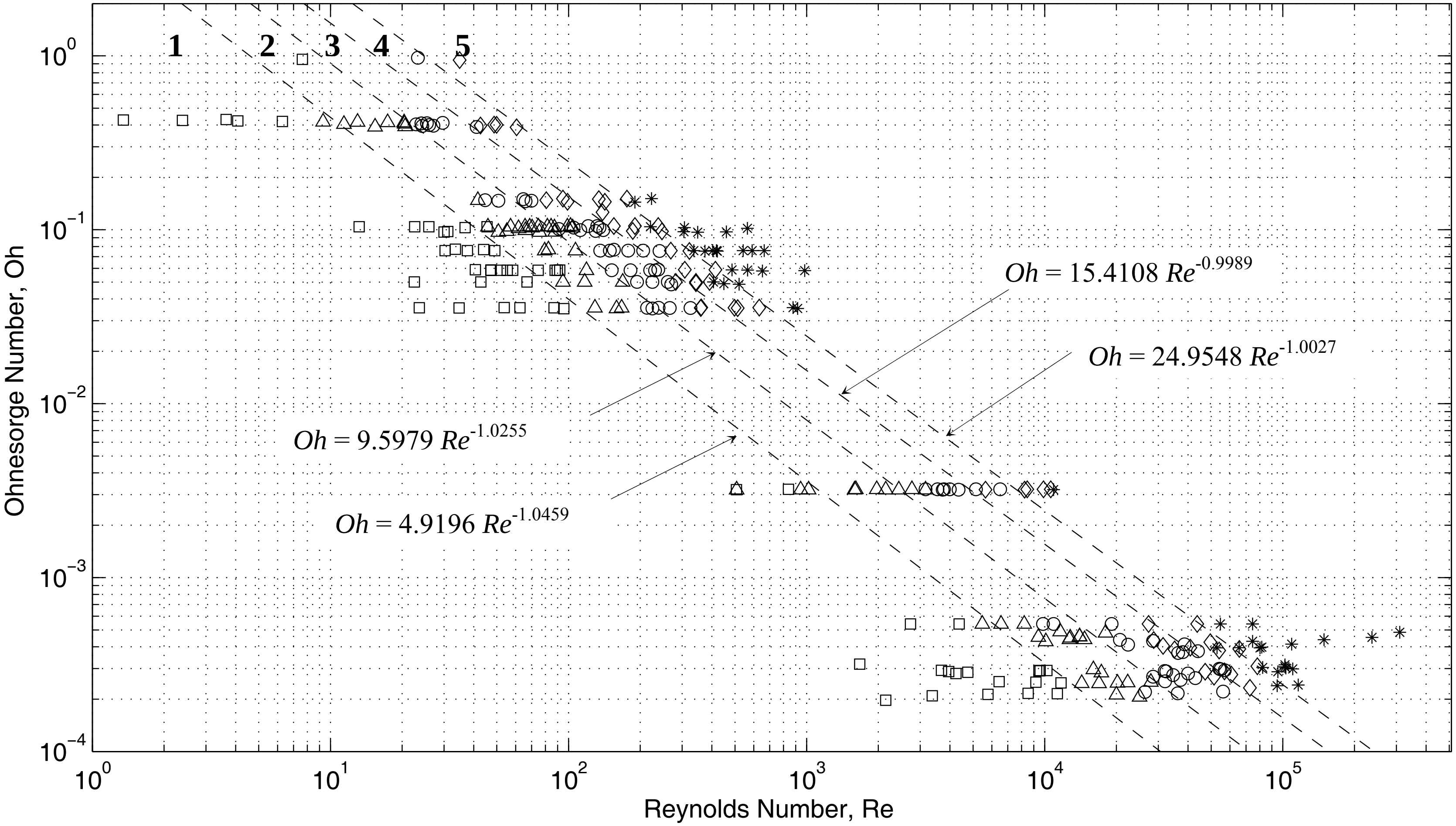

Figure 3.20 Liquid-liquid jet break-up regimes. Data points correspond to 154 oil and 43 silicone fluid injection tests (upper two sets), and 97 liquid CO_2 injection tests (lower right hand corner). □, varicose breakup; Δ, sinuous wave breakup; o, filament breakup; ◊, wave atomization; *, full atomization.

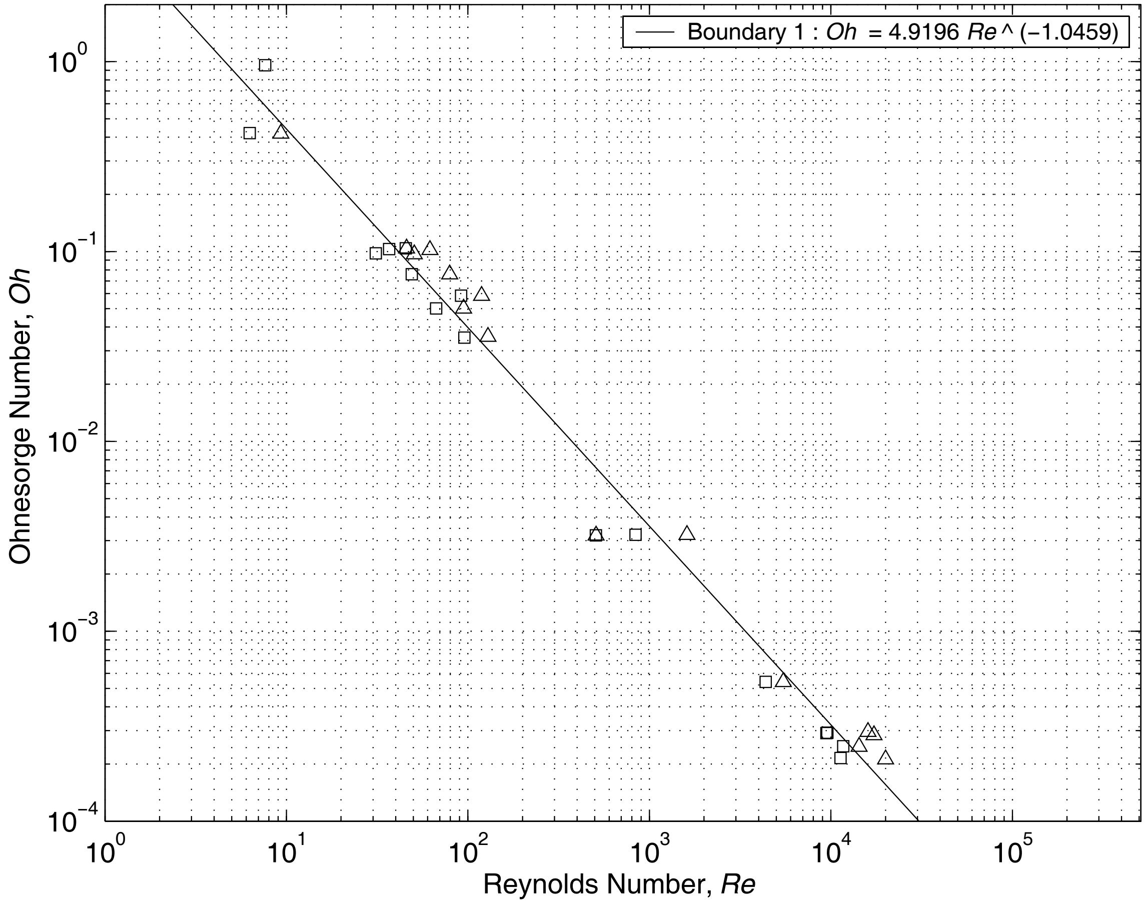

Figure 3.21 Boundary 1 between instability regimes 1 and 2. □, varicose breakup at instability regime 1; Δ, sinuous wave breakup at instability regime 2.

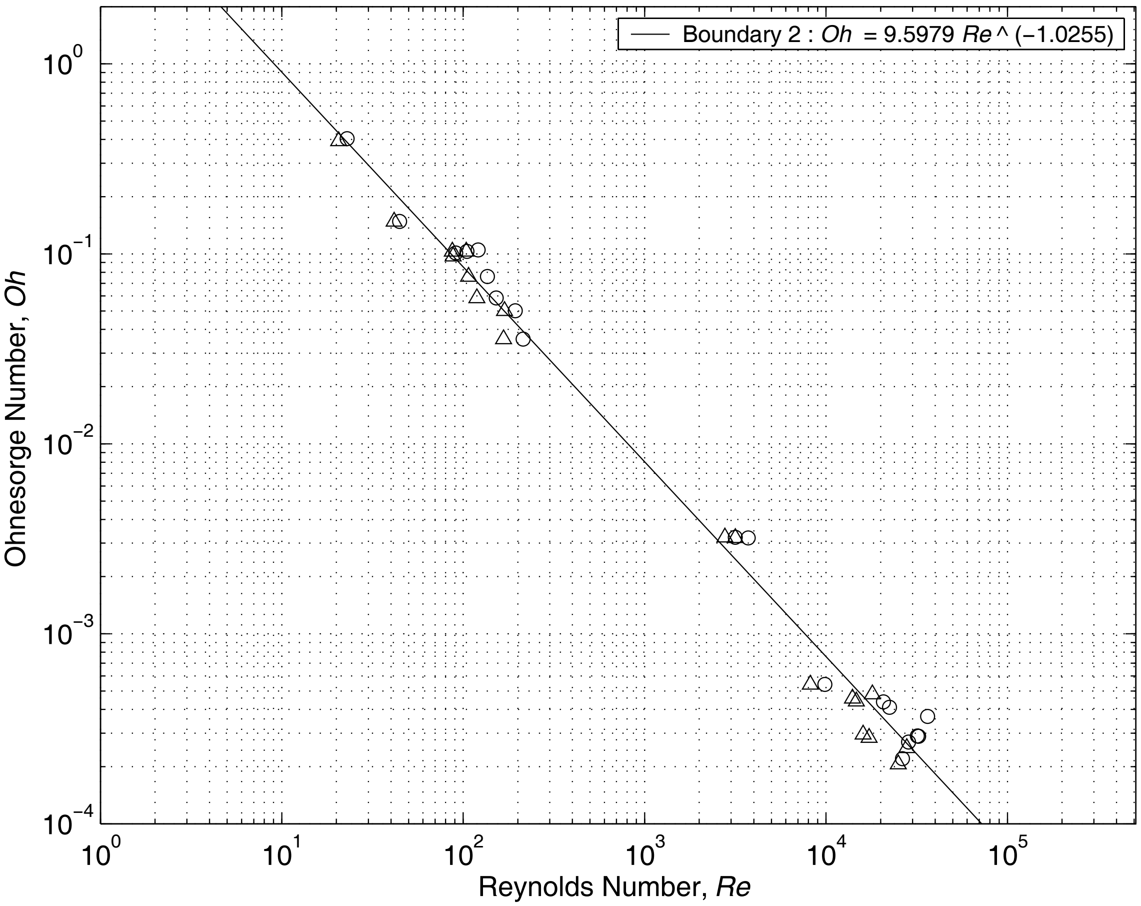

Figure 3.22 Boundary 2 between instability regimes 2 and 3. Δ, sinuous wave breakup at instability regime 2. o, filament core breakup at instability regime 3.

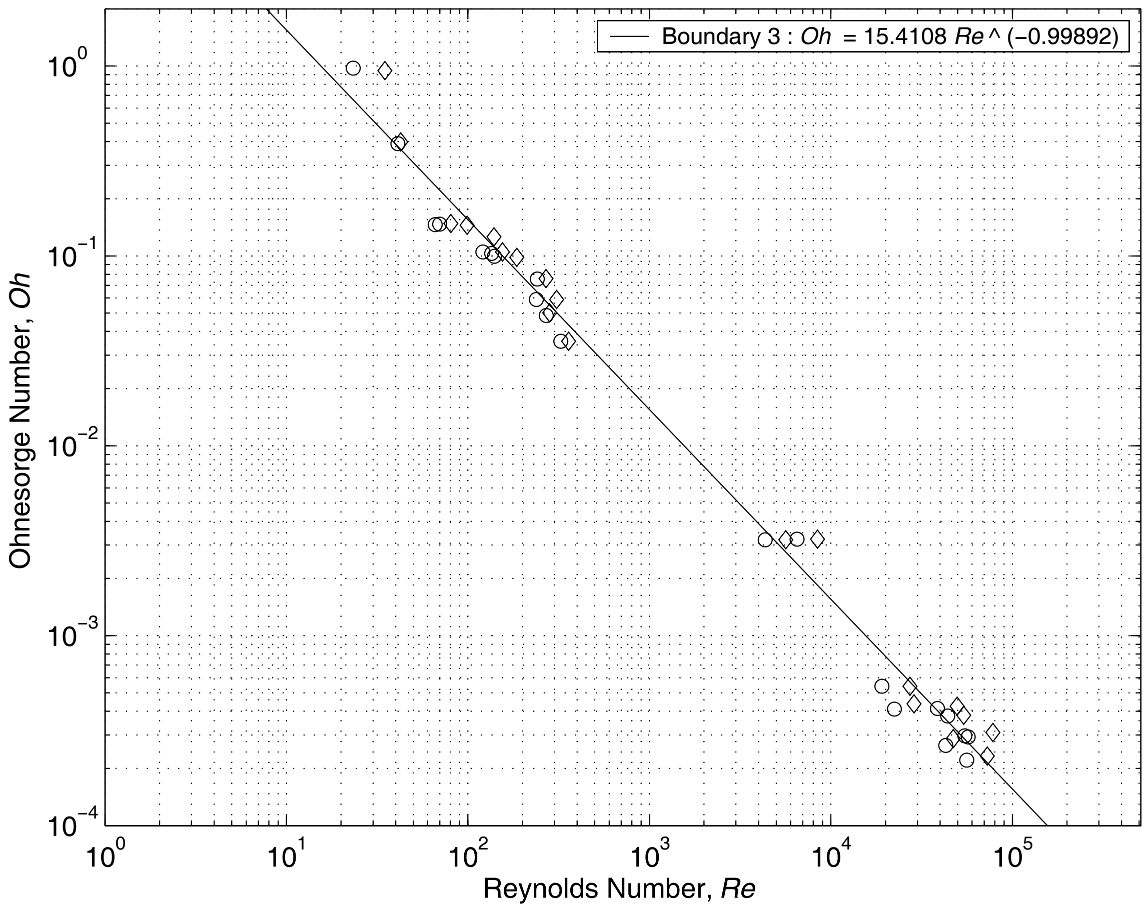

Figure 3.23 Boundary 3 between instability regimes 3 and 4. o, filament core breakup at instability regime 3; ◊, wave atomization at instability regime 4.

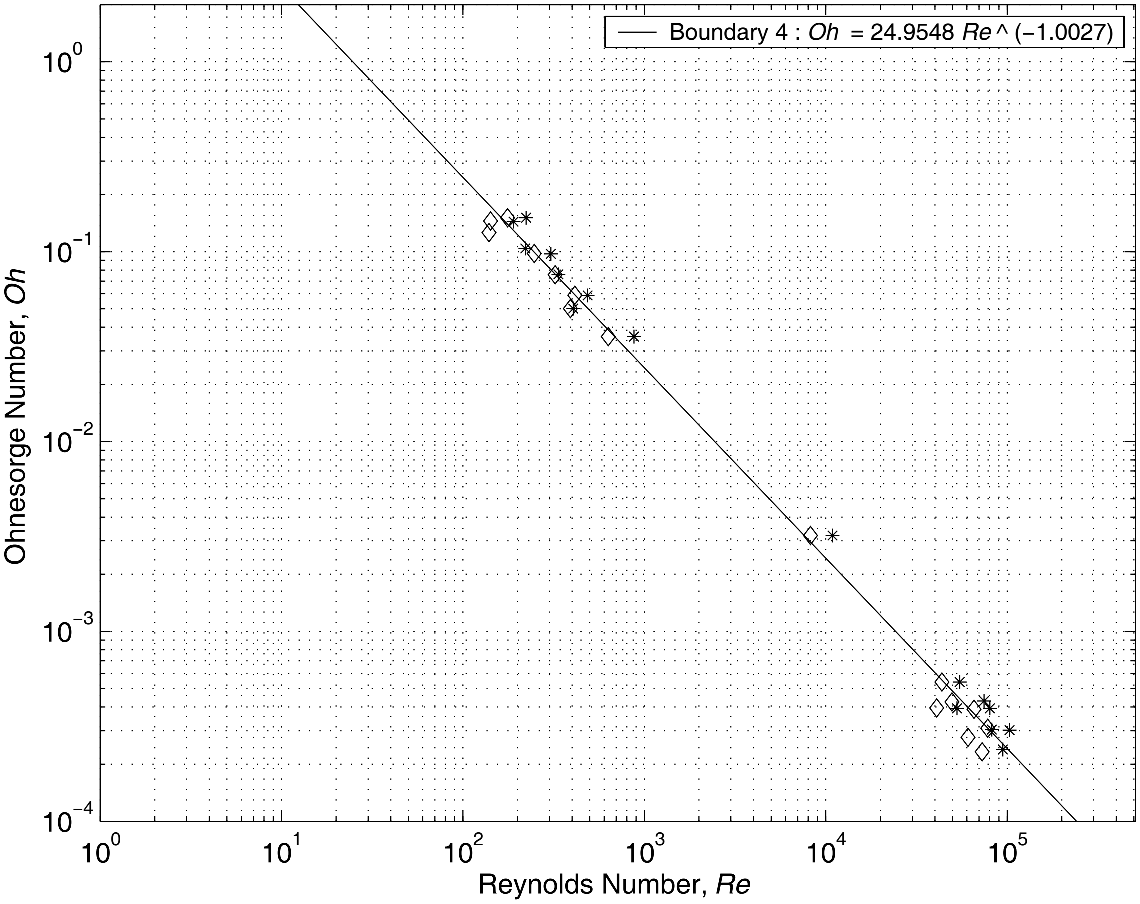

Figure 3.24 Boundary 4 between instability regimes 4 and 5. ◊, wave atomization at instability regime 4. *, full atomization at instability regime 5.

4 DROPLET SIZE SPECTRA

4.1 Characteristic Diameters of Measured Droplet Size Data

4.1.1 Definitions of Characteristic Diameters

The diameter of an “average” droplet in an ensemble of polydispersed droplets can be represented by several statistically-determined quantities. Characteristic diameters conventionally employed in multi-phase flow studies that were applied in this investigation are (Masutani & Adams, 2000; Lefebvre, 1989):

Arithmetic Mean Diameter, x_{10}

$$x_{10} \equiv \int_0^{+\infty} x f(x) dx \tag{4.1}$$

For a complete (i.e., non-truncated due to limited instrument measurement range) droplet data set consisting of *n* droplets, Equation (4.1) can be approximated by the discrete sum:

$$x_{10} = \frac{\sum_{i=1}^{n} x_i}{n} \tag{4.2a}$$

where x_i is the diameter of *i*th droplet. For a composite data set obtained from two incomplete data sets by the method described in section 2.2.3, Equation (4.1) can be expressed as:

$$x_{10} = \int_0^{\alpha} x f(x) dx + \int_{\alpha}^{+\infty} x f(x) dx = \frac{\sum_{i=1}^{a_1} x_i}{n_1} + \frac{\sum_{j=1}^{b_2+c_2} x_j}{n_2} \tag{4.2b}$$

where α is the limiting diameter that divides the two data sets, in this case 3 mm; a_1 is the total number of droplets measured with the PDPA with $x_i < 3$ mm; b_2+c_2 is the total number of droplets determined by image analysis with $x_j \geq 3$ mm; and n_1 and n_2 are the size of the composite ensembles defined by Equations (2.2) and (2.3), respectively.

Surface Mean Diameter, x_{20}

$$x_{20} \equiv \left[\int_0^{+\infty} x^2 f(x) dx \right]^{1/2} \tag{4.3}$$

For a complete droplet data set consisting of *n* droplets, Equation (4.3) can be approximated by the discrete sum:

$$x_{20} = \sqrt{\frac{\sum_{i=1}^{n} x_i^2}{n}} \tag{4.4a}$$

For a composite data set obtained from two incomplete data sets, Equation (4.3) becomes:

$$x_{20} = \sqrt{\frac{\sum_{i=1}^{a_1} x_i^2}{n_1} + \frac{\sum_{j=1}^{b_2+c_2} x_j^2}{n_2}} \tag{4.4b}$$

Volume Mean Diameter, x_{30}

$$x_{30} \equiv \left[\int_0^{+\infty} x^3 f(x)dx\right]^{1/3} \tag{4.5}$$

For a complete droplet data set consisting of *n* droplets, Equation (4.5) can be approximated by the discrete sum:

$$x_{30} = \left[\frac{\sum_{i=1}^{n} x_i^3}{n}\right]^{1/3} \tag{4.6a}$$

For a composite data set obtained from two incomplete data sets, Equation (4.5) becomes:

$$x_{30} = \left[\frac{\sum_{i=1}^{a_1} x_i^3}{n_1} + \frac{\sum_{j=1}^{b_2+c_2} x_j^3}{n_2}\right]^{1/3} \tag{4.6b}$$

Sauter Mean Diameter, x_{32}

$$x_{32} \equiv \frac{x_{30}^3}{x_{20}^2} \tag{4.7}$$

In the preceding definitions, x_{10} is the ensemble mean diameter. x_{20} and x_{30} are the diameters that correspond to the calculated average droplet surface area and volume, respectively. The Sauter mean diameter, x_{32}, is the diameter of a droplet that has the same ratio of volume to surface area as the entire ensemble. It is particularly relevant to analyses of droplet mass transfer (e.g., dissolution; evaporation) and chemical reaction (e.g., spray combustion; hydrate formation), while x_{20} applies to studies of surface phenomena, such as hydrodynamic drag and heat transfer, and x_{30} to areas such as momentum transfer and buoyancy. In addition to characteristic diameters, the variance, s^2, also provides information about the droplet size distribution. The definition of the variance is:

$$s^2 \equiv \int_0^{+\infty} f(x)(x-\mu)^2 dx \tag{4.8}$$

where μ is the expectation value, typically the ensemble mean, x_{10}. The variance therefore measures the expected square of the deviation of droplet diameter from its expectation value. For a complete droplet data set consisting of n droplets, Equation (4.8) can be approximated by the discrete sum:

$$s^2 = \frac{1}{n}\sum_{i=1}^{n}(x_i - x_{10})^2 \tag{4.9a}$$

For a composite data set obtained from two incomplete data sets, Equation (4.8) becomes:

$$s^2 = \frac{\sum_{i=1}^{a_1}(x_i - x_{10})^2}{n_1} + \frac{\sum_{j=1}^{b_2+c_2}(x_j - x_{10})^2}{n_2} \tag{4.9b}$$

The variance is an indicator of the spread of the size distribution, $f(x)$. Large values of s^2 suggest a broad polydispersion, while monodispersions are characterized by small values of s^2.

4.1.2 Summaries of Measured Droplet Size Data

4.1.2.1 Characteristic Diameters and Standard Deviation of CO_2 Droplets

CO_2 droplet size data were collected at 72 different tests conditions. Table 4.1 summarizes the tests results. Test runs are listed in order of increasing jet velocity. The table includes the instability regime (*IR*); Weber (*We*), Reynolds (*Re*), and Ohnesorge (*Oh*) numbers; range of measured droplet diameters; characteristic diameters; and the standard deviation (square root of the variance) for each test condition.

4.1.2.2 Characteristic Diameters and Standard Deviation of Crude Oil Droplets

Characteristic diameters and standard deviations of crude oil droplets formed in instability regimes 1 and 2 are provided in Table 4.2. These size data were obtained by digital video analysis. The opacity of the crude oil droplets mde it impossible to perform accurate droplet size measurements with the PDPA (Masutani & Adams, 2000); hence, the PDPA data are not reported nor used to calculate droplet size statistics.

4.1.2.3 Size Histograms of Silicone Fluid Droplets from PDPA Measurements

Unlike crude oil, droplets of clear silicone fluid in water could be measured accurately with the PDPA; however, as noted in Chapter 3, silicone fluid is difficult to visualize (unless it is mixed with dye or other colorants–which was not pursued in this study). The refractive indices of silicone fluid and water are nearly the same: 1.40 and 1.33, respectively. The inability to identify clearly the edges of silicone fluid droplets in the digital video images precluded the use of this sizing technique. Since the PDPA measurement range of 0.08 to 4.056 mm excluded large droplets, it was not possible accurately to calculate characteristic diameters and standard deviations. Although incomplete, the PDPA silicone droplet size histograms provide useful insight into the evolution of the spectra at different flow conditions. Representative results corresponding to instability regimes 3, 4 and 5 are presented in Figures 4.1, 4.2 and 4.3. Figure 4.1 corresponds to silicone fluid 20 injection into tap water through a 2 mm sharp edge orifice. Figure 4.2 presents size histograms for low viscosity silicone fluid injected into tap water through a 2 mm sharp edge orifice. In Figure 4.3, the low viscosity silicone fluid was discharged into tap water through a 2 mm tube orifice. Additional information is provided to the right of the histograms: We is Weber number; IR is instability regime; $x_{10,\mathrm{PDPA}}$ and s_{PDPA} are, respectively, ensemble average droplet diameter and standard deviation calculated using the incomplete PDPA data ensemble; n is the size of the ensemble measured with the PDPA.

Table 4.1 Summary of CO_2 Droplet Size Measurements

No.	Test Name	Table 3.1 No.	*IR*	Jet Vel. [m/s]	*We*	*Re*	*Oh*	Size Range						Standard Deviation [mm]
								min [mm]	max [mm]	x_{10} [mm]	x_{20} [mm]	x_{30} [mm]	x_{32} [mm]	
1	CDC02WTP52R1	1	2	0.674	3.25E+01	1.16E+04	4.89E-04	1.44	10.95	4.54	4.76	5.01	5.56	1.45
2	CDC02WTP52R2	2	2	0.768	4.11E+01	1.40E+04	4.57E-04	1.13	5.89	3.66	3.84	3.98	4.28	1.17
3	CDC02WTP52R3	3	2	1.128	8.45E+01	2.24E+04	4.11E-04	0.83	6.75	3.00	3.26	3.48	3.97	1.28
4	CDC02WTP52R5	5	3	1.513	1.57E+02	2.87E+04	4.37E-04	0.01	4.86	1.37	1.64	1.88	2.44	0.91
5	CDC02WTP52R10	10	3	1.567	1.62E+02	3.14E+04	4.05E-04	0.01	6.21	1.31	1.46	1.60	1.93	0.63
6	CDC02WTP52R4	4	3	1.694	1.84E+02	3.51E+04	3.86E-04	0.05	3.79	1.25	1.42	1.56	1.88	0.68
7	CDC02WTP52R6	6	3	2.002	2.61E+02	4.09E+04	3.95E-04	0.01	3.96	1.31	1.51	1.67	2.05	0.75
8	CDC02WTP52R7	7	4	2.581	4.33E+02	5.29E+04	3.94E-04	0.02	3.99	1.30	1.43	1.55	1.82	0.60
9	CDC02WTP52R8	8	4	3.207	6.69E+02	6.55E+04	3.95E-04	0.01	3.98	1.22	1.38	1.53	1.88	0.64
10	CDC02WTP52R9	9	5	4.013	1.05E+03	8.16E+04	3.98E-04	0.02	4.03	1.00	1.08	1.16	1.35	0.40
11	CDC05WTP52R1	11	1	0.04	2.82E-01	1.67E+03	3.18E-04	3.29	8.74	5.71	5.86	5.99	6.26	1.28
12	CDC05WTP52R3	13	1	0.081	1.16E+00	3.68E+03	2.93E-04	3.22	10.71	6.71	6.83	6.95	7.21	1.28
13	CDC05WTP52R4	14	1	0.103	1.84E+00	4.76E+03	2.85E-04	4.08	10.14	6.65	6.76	6.87	7.08	1.21
14	CDC05WTP52R5	15	1	0.127	2.62E+00	6.43E+03	2.52E-04	3.80	23.55	6.77	7.23	7.97	9.67	2.55
15	CDC05WTP52R6	16	1	0.18	5.26E+00	9.18E+03	2.50E-04	2.33	10.16	6.74	6.92	7.07	7.38	1.55
16	CDC05WTP52R7	17	1	0.229	8.49E+00	1.17E+04	2.48E-04	1.09	9.97	6.48	6.70	6.88	7.24	1.70
17	CDC05WTP52R8	18	2	0.278	1.25E+01	1.43E+04	2.47E-04	0.78	11.25	6.55	6.79	6.98	7.37	1.79
18	CDC05WTP52R9	19	2	0.327	1.73E+01	1.69E+04	2.46E-04	1.63	10.94	6.20	6.53	6.81	7.40	2.05
19	CDC05WTP52R10	20	2	0.392	2.49E+01	2.02E+04	2.48E-04	1.01	15.71	6.43	6.99	7.50	8.62	2.73
20	CDC05WTP52R11	21	2	0.435	3.07E+01	2.23E+04	2.49E-04	1.80	13.44	6.97	7.49	7.95	8.96	2.75
21	CDC05WTP52R12	22	2	0.547	4.88E+01	2.79E+04	2.51E-04	1.20	14.37	6.32	6.98	7.52	8.74	2.96
22	CDC05WTP52R20	30	3	0.591	5.90E+01	2.85E+04	2.69E-04	0.04	10.80	1.75	2.54	3.34	5.78	1.85
23	CDC05WTP52R21	31	3	0.728	9.04E+01	3.46E+04	2.75E-04	0.01	11.61	4.09	4.85	5.44	6.85	2.61
24	CDC05WTP52R22	32	3	0.857	1.27E+02	4.00E+04	2.81E-04	0.02	12.23	2.73	3.92	4.86	7.48	2.80
25	CDC05WTP52R23	33	4	1.027	1.83E+02	4.72E+04	2.87E-04	0.01	11.13	2.03	2.86	3.62	5.77	2.02
26	CDC05WTP52R24	34	4	1.245	2.70E+02	5.69E+04	2.89E-04	0.01	8.78	2.01	2.74	3.30	4.82	1.85

Table 4.1 (Continued)

No.	Test Name	Table 3.1 No.	*IR*	Jet Vel. [m/s]	*We*	*Re*	*Oh*	Size Range min [mm]	Size Range max [mm]	x_{10} [mm]	x_{20} [mm]	x_{30} [mm]	x_{32} [mm]	Standard Deviation [mm]
27	CDC05WTP52R25	35	4	1.877	6.26E+02	8.23E+04	3.04E-04	0.02	4.05	1.24	1.52	1.78	2.44	0.89
28	CDC05WTP52R26	36	5	2.405	1.04E+03	1.03E+05	3.15E-04	0.02	7.76	1.62	2.39	2.98	4.64	1.76
29	CDC10WTP52R13	49	1	0.023	1.79E-01	2.15E+03	1.97E-04	7.69	10.17	9.10	9.11	9.13	9.17	0.57
30	CDC10WTP52R12	48	1	0.038	4.96E-01	3.37E+03	2.09E-04	2.71	10.78	8.16	8.33	8.47	8.75	1.69
31	CDC10WTP52R10	46	1	0.097	3.37E+00	8.51E+03	2.16E-04	1.89	13.38	8.96	9.46	9.80	10.53	3.05
32	CDC10WTP52R6	42	1	0.129	5.88E+00	1.13E+04	2.15E-04	2.32	16.06	7.75	8.55	9.25	10.81	3.61
33	CDC10WTP52R7	43	2	0.225	1.79E+01	2.00E+04	2.12E-04	0.96	20.53	6.75	7.96	8.96	11.35	4.23
34	CDC10WTP52R8	44	2	0.275	2.65E+01	2.50E+04	2.06E-04	1.36	14.29	5.31	6.29	7.14	9.21	3.36
35	CDC10WTP52R9	45	2	0.307	3.37E+01	2.64E+04	2.20E-04	0.97	18.11	6.98	8.06	8.97	11.11	4.02
36	CDC10WTP52R1	37	3	0.414	6.10E+01	3.62E+04	2.16E-04	0.01	13.73	2.67	3.79	4.73	7.34	2.70
37	CDC10WTP52R2	38	3	0.656	1.54E+02	5.61E+04	2.22E-04	0.02	13.78	1.17	2.16	3.18	6.90	1.82
38	CDC10WTP52R3	39	4	0.882	2.84E+02	7.27E+04	2.32E-04	0.01	11.01	2.23	3.35	4.29	7.02	2.50
39	CDC10WTP52R4	40	5	1.176	5.09E+02	9.46E+04	2.39E-04	0.02	4.04	1.14	1.47	1.75	2.49	0.93
40	CDC10WTP52R5	41	5	1.451	7.79E+02	1.16E+05	2.41E-04	0.01	1.51	0.51	0.54	0.57	0.65	0.18
41	CDT02WTP52R14	63	2	0.526	1.88E+01	1.01E+04	4.29E-04	1.27	6.80	4.15	4.27	4.36	4.55	0.98
42	CDT02WTP52R13	62	2	0.676	3.14E+01	1.27E+04	4.41E-04	1.17	7.01	4.54	4.71	4.83	5.09	1.23
43	CDT02WTP52R12	61	2	0.767	4.11E+01	1.40E+04	4.58E-04	1.00	7.77	3.90	4.24	4.50	5.07	1.67
44	CDT02WTP52R11	60	2	1.029	7.53E+01	1.80E+04	4.81E-04	1.38	8.36	4.35	4.61	4.82	5.28	1.51
45	CDT02WTP52R1	50	3	1.696	1.79E+02	3.64E+04	3.68E-04	0.04	7.53	0.85	1.18	1.70	3.55	0.82
46	CDT02WTP52R2	51	3	1.789	2.01E+02	3.80E+04	3.74E-04	0.03	7.48	1.67	2.42	3.06	4.93	1.75
47	CDT02WTP52R3	52	3	2.086	2.75E+02	4.40E+04	3.77E-04	0.01	6.54	2.58	3.04	3.35	4.06	1.61
48	CDT02WTP52R4	53	4	2.577	4.23E+02	5.40E+04	3.81E-04	0.01	6.84	1.37	1.97	2.49	4.00	1.41
49	CDT02WTP52R5	54	4	3.179	6.52E+02	6.56E+04	3.89E-04	0.01	5.78	1.40	1.87	2.24	3.20	1.25
50	CDT02WTP52R6	55	5	3.923	1.00E+03	8.02E+04	3.94E-04	0.01	4.95	0.94	1.30	1.63	2.54	0.90
51	CDT02WTP52R7	56	5	5.537	2.05E+03	1.09E+05	4.14E-04	0.01	5.58	1.03	1.37	1.65	2.40	0.90
52	CDT02WTP52R8	57	5	7.884	4.26E+03	1.49E+05	4.40E-04	0.01	5.86	1.06	1.50	1.88	2.95	1.06
53	CDT02WTP52R9	58	5	12.894	1.16E+04	2.37E+05	4.53E-04	0.02	5.88	0.89	1.21	1.57	2.64	0.81

Table 4.1 (Continued)

No.	Test Name	Table 3.1 No.	*IR*	Jet Vel. [m/s]	*We*	*Re*	*Oh*	Size Range		x_{10} [mm]	x_{20} [mm]	x_{30} [mm]	x_{32} [mm]	Standard Deviation [mm]
								min [mm]	max [mm]					
54	CDT02WTP52R10	59	5	17.814	2.26E+04	3.10E+05	4.85E-04	0.01	4.06	1.01	1.32	1.63	2.46	0.85
55	CDT02WNP52R4	66	2	0.513	1.83E+01	9.40E+03	4.55E-04	0.81	5.59	3.56	3.69	3.79	4.01	0.98
56	CDT02WNP52R5	67	2	0.695	3.35E+01	1.28E+04	4.51E-04	0.86	6.44	3.94	4.09	4.22	4.47	1.12
57	CDT02WNP52R6	68	2	0.78	4.17E+01	1.47E+04	4.41E-04	0.83	7.08	3.73	4.01	4.23	4.70	1.47
58	CDT02WNP52R8	70	3	1.493	1.52E+02	2.85E+04	4.33E-04	0.03	6.38	1.53	1.79	2.11	2.93	0.92
59	CDT02WNP52R9	71	3	1.954	2.55E+02	3.86E+04	4.13E-04	0.04	3.76	1.35	1.46	1.56	1.78	0.55
60	CDT02WNP52R1	64	4	2.562	4.43E+02	4.96E+04	4.25E-04	0.03	3.95	1.56	1.67	1.76	1.97	0.59
61	CDT02WNP52R2	65	5	3.889	1.03E+03	7.46E+04	4.30E-04	0.04	3.99	1.57	1.66	1.75	1.92	0.55
62	CDT05WTP61R7	78	1	0.09	1.42E+00	4.24E+03	2.81E-04	1.62	8.09	5.08	5.19	5.28	5.46	1.04
63	CDT05WTP61R6	77	1	0.21	7.80E+00	9.56E+03	2.92E-04	1.37	10.83	6.86	7.19	7.44	7.96	2.15
64	CDT05WTP61R4	75	2	0.371	2.41E+01	1.73E+04	2.84E-04	1.01	12.63	7.01	7.43	7.77	8.50	2.47
65	CDT05WTP61R1	72	3	1.256	2.79E+02	5.71E+04	2.93E-04	0.01	4.03	0.83	1.21	1.57	2.65	0.88
66	CDT05WTP61R2	73	5	2.34	9.84E+02	1.02E+05	3.07E-04	0.01	4.04	0.86	1.10	1.40	2.28	0.68
67	CDT05WTP52R7	85	1	0.086	1.29E+00	3.95E+03	2.88E-04	0.83	7.73	5.68	5.89	6.02	6.30	1.53
68	CDT05WTP52R6	84	1	0.208	7.58E+00	9.46E+03	2.91E-04	0.85	9.98	5.74	6.08	6.31	6.81	2.01
69	CDT05WTP52R5	83	2	0.357	2.24E+01	1.60E+04	2.96E-04	0.82	14.55	6.72	7.35	7.86	9.01	2.98
70	CDT05WTP52R3	81	3	1.227	2.65E+02	5.48E+04	2.97E-04	0.01	12.14	2.72	3.67	4.41	6.37	2.47
71	CDT05WTP52R2	80	4	1.805	5.82E+02	7.81E+04	3.09E-04	0.01	4.05	0.90	1.22	1.56	2.52	0.82
72	CDT05WTP52R1	79	5	2.347	9.76E+02	1.03E+05	3.02E-04	0.01	4.06	0.79	1.05	1.34	2.18	0.70

Table 4.2 Summary of Crude Oil Droplet Size Measurements

No.	Test Name	Table 3.2 No.	*IR*	Jet Velocity [m/s]	*We*	*Re*	*Oh*	Ensemble Size	Size Range min [mm]	Size Range max [mm]	x_{10} [mm]	x_{20} [mm]	x_{30} [mm]	x_{32} [mm]	Standard Deviation [mm]
1	GES02WTRR9	9	1	0.273	5.28E-00	3.03E+01	7.59E-02	28	6.81	9.32	8.24	8.26	8.29	8.34	0.67
2	GES02WTRR1	1	1	0.308	6.70E-00	3.35E+01	7.73E-02	39	5.52	8.66	7.09	7.14	7.20	7.31	0.91
3	GES02WTRR2	2	1	0.403	1.15E+01	4.40E+01	7.70E-02	225	1.17	9.51	5.91	6.00	6.09	6.27	1.06
4	GES02WTRR11	11	1	0.442	1.38E+01	4.90E+01	7.59E-02	134	3.62	8.29	5.44	5.54	5.65	5.86	1.06
5	GES02WTRR12	12	2	0.716	3.63E+01	7.94E+01	7.59E-02	48	3.68	7.29	5.50	5.61	5.70	5.91	1.09
6	GES02WTRR3	3	2	0.753	4.01E+01	8.23E+01	7.69E-02	600	0.92	8.30	4.90	5.06	5.20	5.49	1.24
7	GES02WTRR13	13	2	0.966	6.59E+01	1.07E+02	7.59E-02	68	2.95	8.02	5.83	5.93	6.03	6.23	1.11
8	GES05WTRR6	30	1	0.161	4.60E-00	4.28E+01	5.01E-02	74	5.65	14.31	9.79	9.95	10.11	10.43	1.82
9	GES05WTRR7	31	1	0.252	1.12E+01	6.69E+01	5.01E-02	112	2.82	13.45	8.78	9.12	9.40	9.99	2.49
10	GES05WTRR8	32	2	0.357	2.25E+01	9.47E+01	5.01E-02	37	4.18	13.02	9.24	9.49	9.70	10.15	2.16
11	GES05WTRR9	33	2	0.441	3.44E+01	1.17E+02	5.01E-02	86	3.39	15.18	9.11	9.42	9.69	10.28	2.40
12	GES05WTRR10	34	2	0.637	7.17E+01	1.69E+02	5.01E-02	86	3.88	15.10	7.95	8.36	8.76	9.62	2.59
13	MAS05WTRR7	48	1	0.145	3.66E-00	5.37E+01	3.57E-02	30	5.99	10.78	8.12	8.21	8.29	8.45	1.19
14	MAS05WTRR20	61	1	0.255	1.13E+01	9.55E+01	3.52E-02	59	6.61	12.80	9.74	9.82	9.89	10.05	1.25
15	MAS05WTRR10	51	2	0.348	2.11E+01	1.29E+02	3.56E-02	29	3.34	14.70	10.84	11.15	11.38	11.86	2.65
16	MAS05WTRR19	60	2	0.424	3.13E+01	1.59E+02	3.53E-02	49	7.76	20.29	12.91	13.25	13.59	14.28	3.02
17	MAS05WTRR11	52	2	0.45	3.52E+01	1.67E+02	3.56E-02	25	6.01	16.75	11.95	12.22	12.44	12.91	2.59
18	MAS02WTRR18	80	1	0.332	7.65E-00	4.73E+01	5.85E-02	46	4.23	8.69	5.84	5.93	6.03	6.23	1.04
19	MAS02WTRR13	75	1	0.363	9.19E-00	5.18E+01	5.85E-02	35	3.12	8.47	5.81	5.93	6.04	6.26	1.18
20	MAS02WTRR17	79	1	0.387	1.04E+01	5.53E+01	5.85E-02	45	3.65	8.44	5.68	5.78	5.88	6.09	1.08
21	MAS02WTRR14	76	1	0.408	1.16E+01	5.83E+01	5.85E-02	24	3.62	8.77	6.03	6.11	6.19	6.36	1.04
22	MAS02WTRR15	77	1	0.523	1.90E+01	7.46E+01	5.85E-02	79	3.19	10.99	6.07	6.24	6.40	6.75	1.44
23	MAS02WTRR19	81	1	0.615	2.63E+01	8.78E+01	5.85E-02	21	5.48	9.37	7.37	7.44	7.50	7.63	1.00
24	MAS02WTRR16	78	1	0.629	2.75E+01	8.97E+01	5.85E-02	139	2.57	9.50	5.67	5.88	6.07	6.46	1.57
25	MAS02WTRR8	70	1	0.645	2.89E+01	9.18E+01	5.86E-02	50	5.79	9.73	7.88	7.94	7.99	8.10	0.96

Table 4.2 (Continued)

No.	Test Name	Table 3.2 No.	*IR*	Jet Velocity [m/s]	*We*	*Re*	*Oh*	Ensemble Size	Size Range		x_{10}	x_{20}	x_{30}	x_{32}	Standard Deviation
									min [mm]	max [mm]	[mm]	[mm]	[mm]	[mm]	[mm]
26	MAS02WTRR9	71	2	0.838	4.89E+01	1.19E+02	5.85E-02	67	3.93	10.58	7.21	7.35	7.48	7.75	1.45
27	PGS01WTRR3	87	1	1.197	5.33E+01	7.63E-00	9.56E-01	21	2.66	10.96	6.97	7.93	8.58	10.06	3.87
28	PGS05WTRR3	90	1	0.075	1.03E-00	2.39E-00	4.26E-01	139	3.14	9.89	6.54	6.67	6.81	7.08	1.34
29	PGS05WTRR1	88	1	0.115	2.48E-00	3.65E-00	4.31E-01	227	4.70	13.10	8.17	8.32	8.48	8.79	1.58
30	PGS05WTRR4	91	1	0.126	2.97E-00	4.08E-00	4.23E-01	133	5.03	10.65	7.94	8.02	8.11	8.27	1.15
31	PGS05WTRR5	92	1	0.194	6.96E-00	6.28E-00	4.20E-01	113	6.22	14.61	9.58	9.73	9.87	10.16	1.69
32	PGS05WTRR6	93	2	0.286	1.52E+01	9.32E-00	4.18E-01	51	7.40	16.19	11.29	11.49	11.68	12.08	2.17
33	PGS05WTRR14	101	2	0.34	2.14E+01	1.14E+01	4.05E-01	24	6.82	14.28	10.08	10.27	10.47	10.87	2.03
34	PGS05WTRR7	94	2	0.398	2.95E+01	1.30E+01	4.17E-01	24	8.76	19.29	12.83	13.10	13.35	13.89	2.65
35	PGS05WTRR13	100	2	0.611	6.95E+01	2.05E+01	4.07E-01	47	3.55	17.64	12.01	12.52	12.93	13.80	3.58
36	PGS05WTRR9	96	2	0.619	7.12E+01	2.04E+01	4.14E-01	28	9.13	18.17	13.36	13.54	13.72	14.08	2.23
37	NSS02WTRR14	126	1	0.345	8.45E-00	3.00E+01	9.70E-02	162	2.78	6.57	4.38	4.46	4.54	4.71	0.85
38	NSS02WTRR5	117	1	0.361	9.25E-00	3.11E+01	9.77E-02	78	4.25	9.54	6.75	6.85	6.94	7.13	1.16
39	NSS02WTRR13	125	2	0.584	2.42E+01	5.07E+01	9.70E-02	144	2.67	7.57	4.89	4.99	5.09	5.30	1.02
40	NSS02WTRR6	118	2	0.642	2.93E+01	5.51E+01	9.81E-02	131	2.92	9.49	5.67	5.83	5.98	6.29	1.33
41	NSS02WTRR7	119	2	0.777	4.29E+01	6.59E+01	9.94E-02	144	2.59	8.69	5.56	5.70	5.83	6.11	1.26
42	NSS02WTRR12	124	2	0.87	5.38E+01	7.55E+01	9.71E-02	98	2.68	7.71	5.12	5.27	5.40	5.68	1.25
43	NSS02WTRR11	123	2	1.013	7.30E+01	8.79E+01	9.72E-02	183	1.90	8.91	5.39	5.57	5.73	6.07	1.40
44	NSS01WTRR10	138	2	1.033	3.79E+01	4.16E+01	1.48E-01	78	2.52	5.26	3.47	3.52	3.56	3.65	0.55
45	NSS02WNRR5	147	1	0.318	7.20E-00	2.59E+01	1.04E-01	177	4.08	8.00	5.82	5.86	5.90	5.98	0.67
46	NSS02WNRR6	148	1	0.451	1.45E+01	3.68E+01	1.03E-01	149	2.91	8.49	5.76	5.84	5.92	6.08	0.98
47	NSS02WNRR7	149	2	0.859	5.25E+01	7.03E+01	1.03E-01	186	1.71	10.08	5.98	6.18	6.35	6.70	1.53

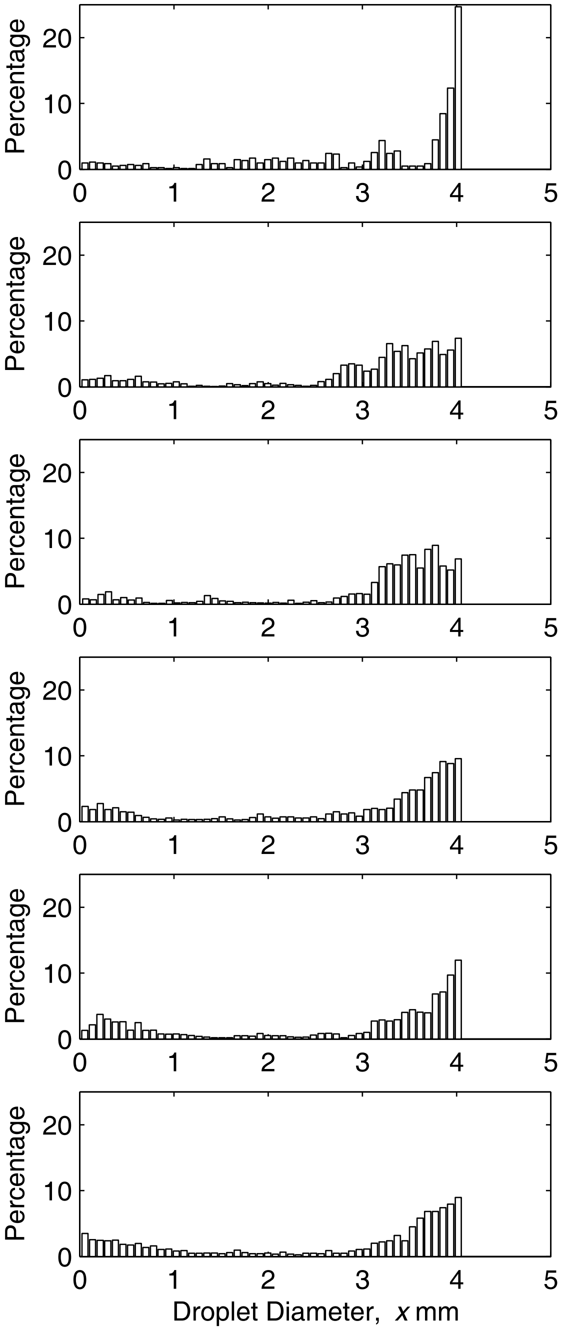

(1) SFS02WTRR6

We = 113.86 IR = 2

U_{jet} = 1.11 m/s n = 827

x_{pdpa} = 3.08 mm s_{pdpa} = 1.13

(2) SFS02WTRR4

We = 160.97 IR = 3

U_{jet} = 1.33 m/s n = 2242

x_{pdpa} = 2.98 mm s_{pdpa} = 1.10

(3) SFS02WTRR1

We = 264.64 IR = 4

U_{jet} = 1.70 m/s n = 2681

x_{pdpa} = 3.12 mm s_{pdpa} = 1.03

(4) SFS02WTRR5

We = 397.32 IR = 4

U_{jet} = 2.08 m/s n = 1953

x_{pdpa} = 2.90 mm s_{pdpa} = 1.30

(5) SFS02WTRR2

We = 400.36 IR = 4

U_{jet} = 2.09 m/s n = 2091

x_{pdpa} = 2.73 mm s_{pdpa} = 1.42

(6) SFS02WTRR3

We = 623.02 IR = 4

U_{jet} = 2.61 m/s n = 1685

x_{pdpa} = 2.66 mm s_{pdpa} = 1.43

Figure 4.1 Silicone fluid droplet size histograms measured with the PDPA. The kinematic viscosity of the silicone fluid was ν = 20 cs; injection into tap water through a 2 mm sharp edge orifice.

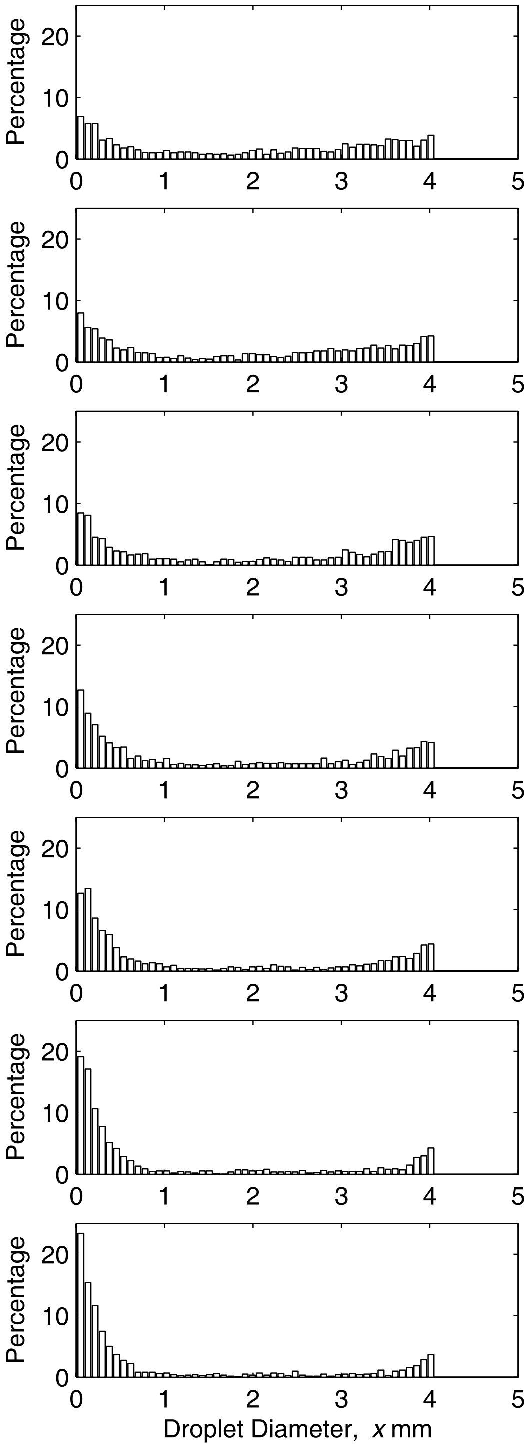

(1) LSS02WTRR7

$We = 130.56$ $IR = 3$

$U_{jet} = 1.17$ m/s $n = 1299$

$x_{pdpa} = 1.98$ mm $s_{pdpa} = 1.42$

(2) LSS02WTRR6

$We = 164.46$ $IR = 3$

$U_{jet} = 1.31$ m/s $n = 1281$

$x_{pdpa} = 1.97$ mm $s_{pdpa} = 1.45$

(3) LSS02WTRR1

$We = 272.94$ $IR = 3$

$U_{jet} = 1.69$ m/s $n = 1348$

$x_{pdpa} = 1.98$ mm $s_{pdpa} = 1.52$

(4) LSS02WTRR5

$We = 436.97$ $IR = 3$

$U_{jet} = 2.14$ m/s $n = 1176$

$x_{pdpa} = 1.62$ mm $s_{pdpa} = 1.53$

(5) LSS02WTRR2

$We = 736.07$ $IR = 4$

$U_{jet} = 2.77$ m/s $n = 1184$

$x_{pdpa} = 1.40$ mm $s_{pdpa} = 1.51$

(6) LSS02WTRR3

$We = 1009.57$ $IR = 4$

$U_{jet} = 3.25$ m/s $n = 1147$

$x_{pdpa} = 1.04$ mm $s_{pdpa} = 1.39$

(7) LSS02WTRR4

$We = 1152.84$ $IR = 4$

$U_{jet} = 3.47$ m/s $n = 1236$

$x_{pdpa} = 0.95$ mm $s_{pdpa} = 1.34$

Figure 4.2 Silicone fluid droplet size histograms measured with the PDPA. Low viscosity silicone fluid ($\nu = 0.65$ cs) injected into tap water through a 2 mm sharp edge orifice.

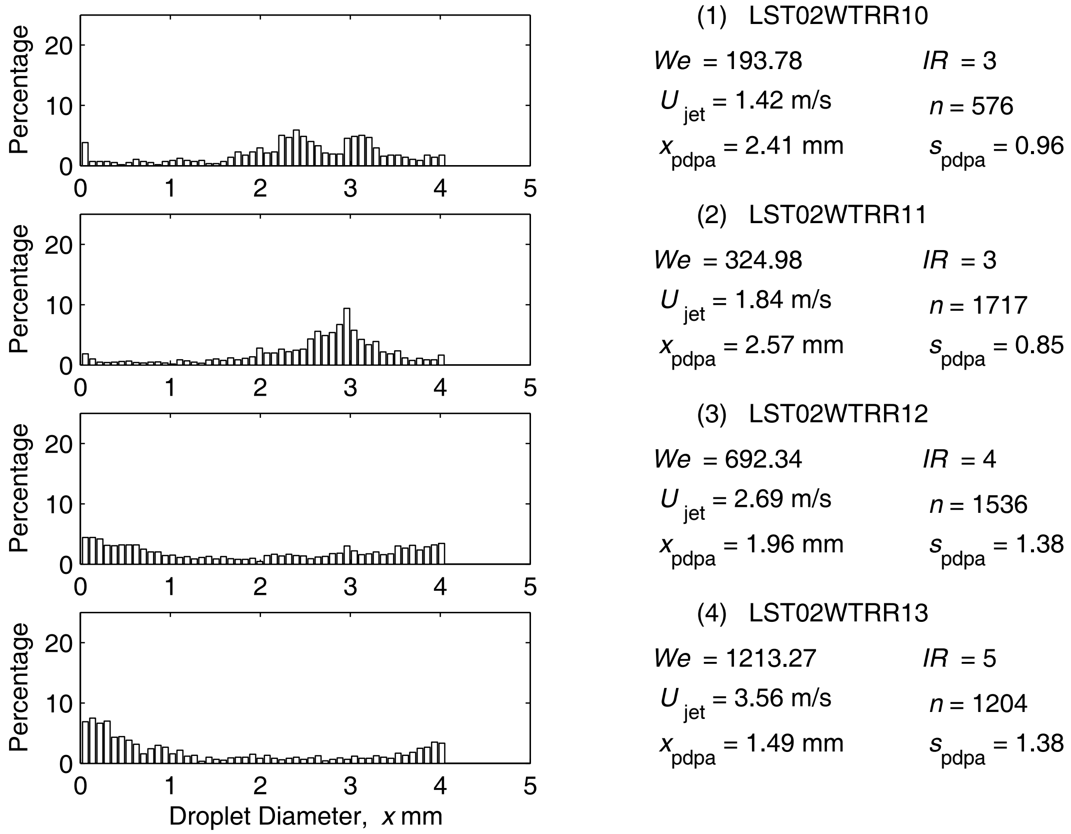

Figure 4.3 Silicone fluid droplet size histograms measured with the PDPA. Low viscosity silicone fluid (ν = 0.65 cs) injected into tap water through a 2 mm tube orifice.

4.1.3 Effects of Jet Flow Rate, Orifice Properties, Ambient Fluid, Pressure and Viscosity on Droplet Size

4.1.3.1 Flow Rate Effect

The characteristic diameters, x_{10}, x_{20}, x_{30} and x_{32} are plotted against corresponding Weber numbers in Figures 4.4a to 4.4d for the 72 liquid CO_2 injection tests. The characteristic diameters decrease as *We* increases in regimes 1 through 4. In instability regime 5, the characteristic diameters remain essentially constant, exhibiting only a small degree of variation. The standard deviations of the size distributions for the 72 tests are plotted in Figure 4.5 as a function of *We*. In regimes 1 and 5, droplets formed by jet breakup are relatively uniform in size, resulting in small values of the standard deviation. On the other hand, in transitional regimes 2, 3 and 4, breakup generates a wide polydispersion of droplets which is reflected in the large values of *s*. Figures 4.6, 4.7, and 4.8 present the composite droplet size histograms for the 7 different liquid CO_2 injection cases. The data are plotted against non-dimensionalized droplet diameter (*x*/*D*; where *D* is the injection orifice diameter) and *We*.

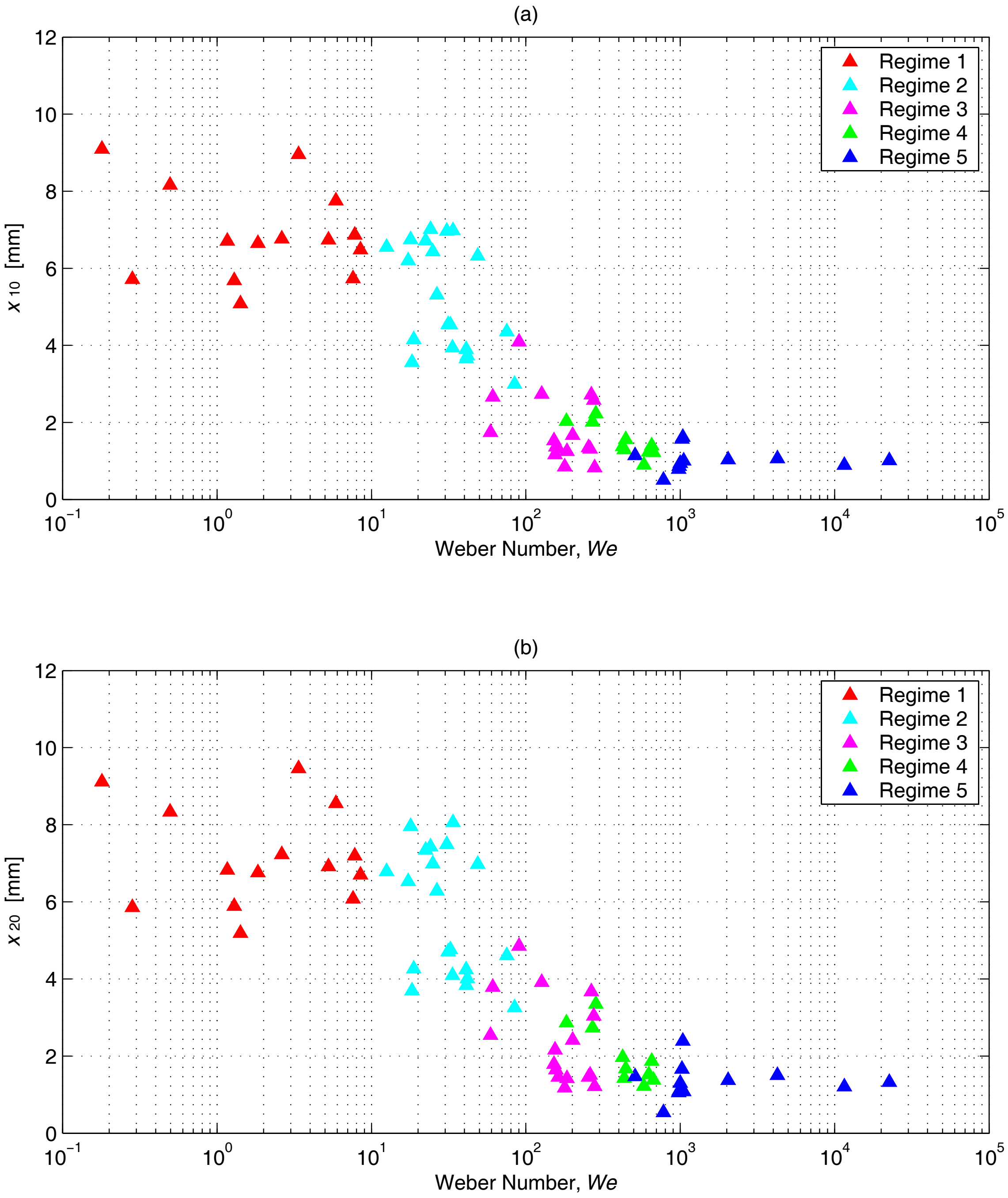
(a)
12
10
8
6
4
2
0
x_{10} [mm]
Regime 1
Regime 2
Regime 3
Regime 4
Regime 5
10^{-1}
10^{0}
10^{1}
10^{2}
10^{3}
10^{4}
10^{5}
Weber Number, *We*
(b)
12
10
8
6
4
2
0
x_{20} [mm]
Regime 1
Regime 2
Regime 3
Regime 4
Regime 5
10^{-1}
10^{0}
10^{1}
10^{2}
10^{3}
10^{4}
10^{5}
Weber Number, *We*

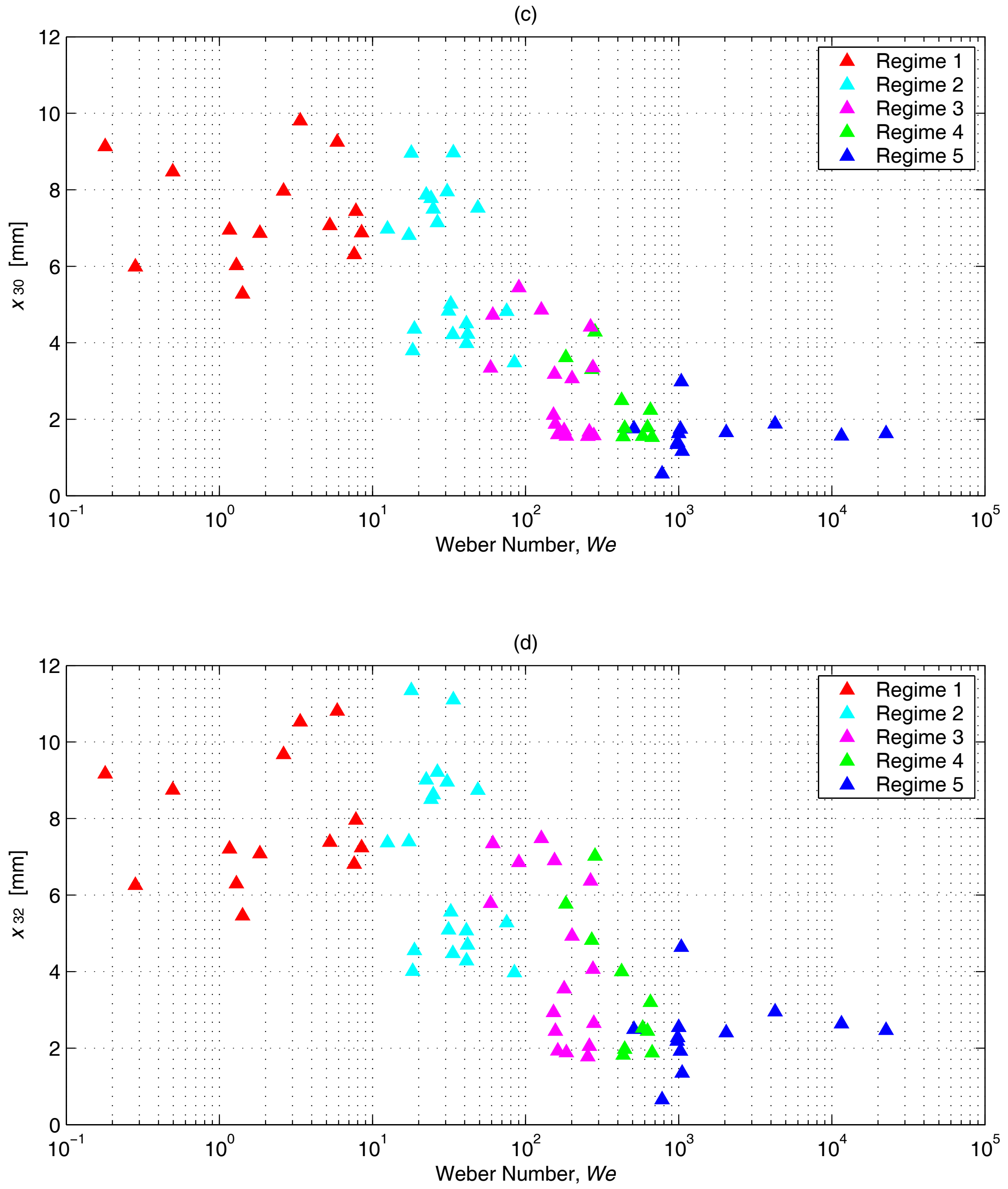

Figure 4.4 Characteristic diameters of CO_2 droplets vs. We from 72 tests. (a) x_{10}; (b)x_{20}; (c) x_{30}; (d) x_{32}.

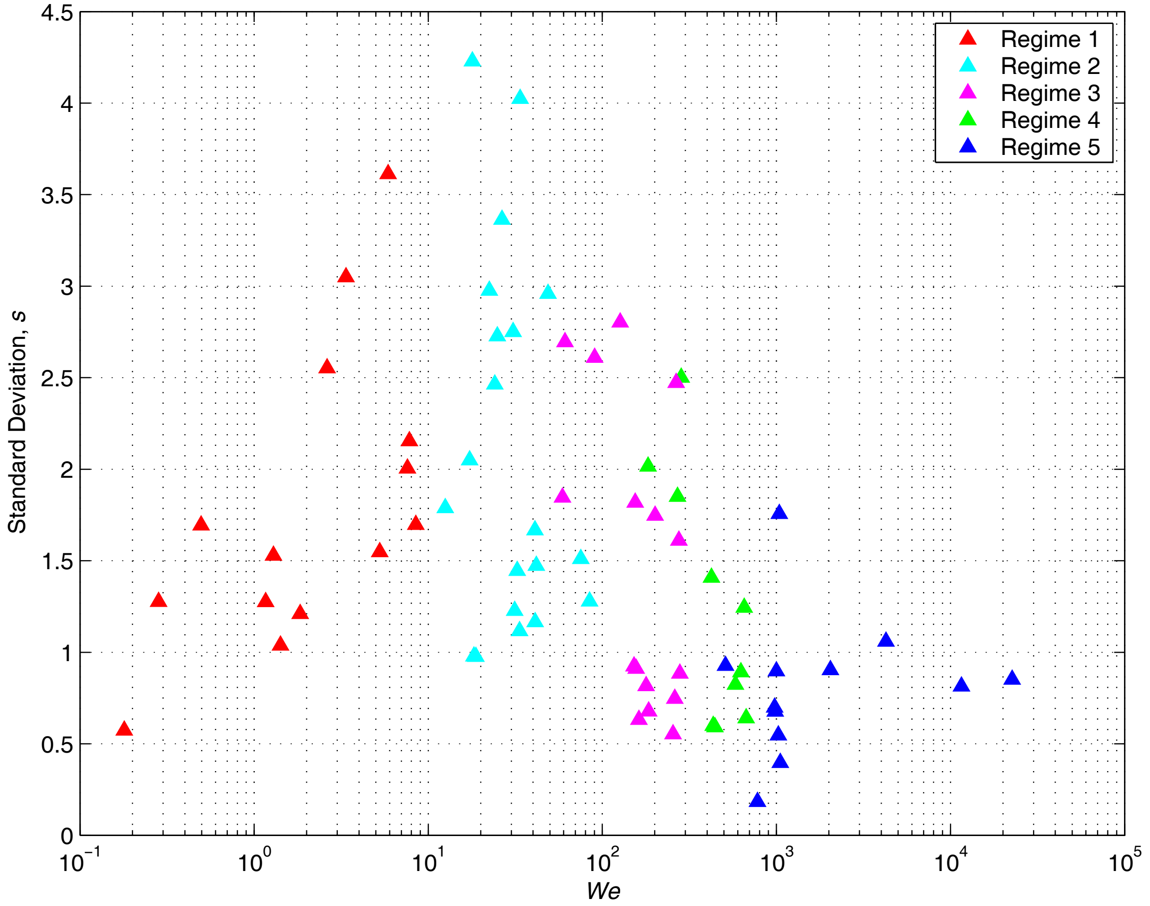

Figure 4.5 Standard deviations of CO_2 droplets vs. We from 72 tests.

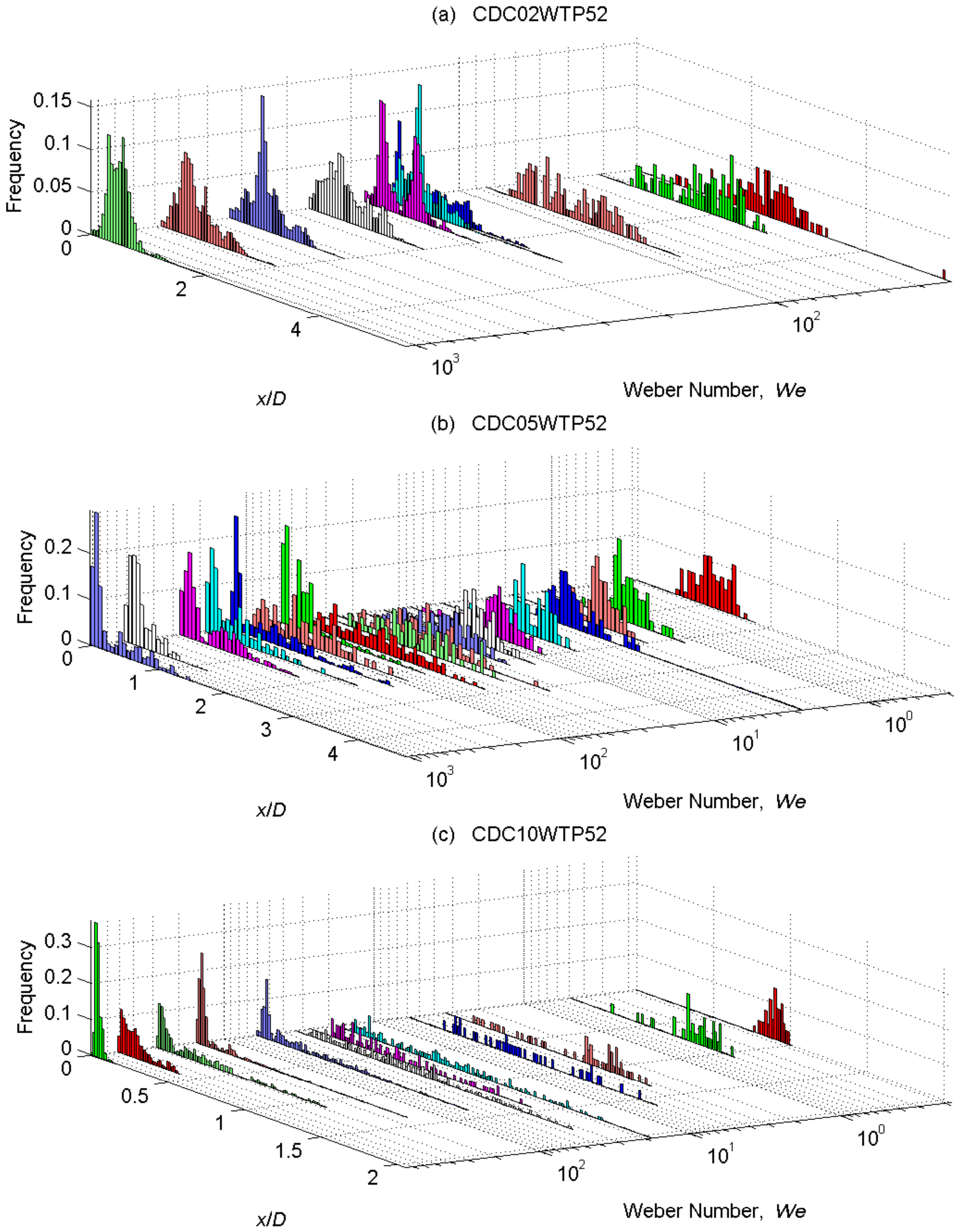

Figure 4.6 CO_2 droplet size histograms. Data are for liquid CO_2 injection into tap water from (a) 2 mm, (b) 5 mm and (c) 10 mm sharp edge orifices. x/D is droplet diameter non-dimensionalized with the orifice diameter.

(a) CDT02WTP52

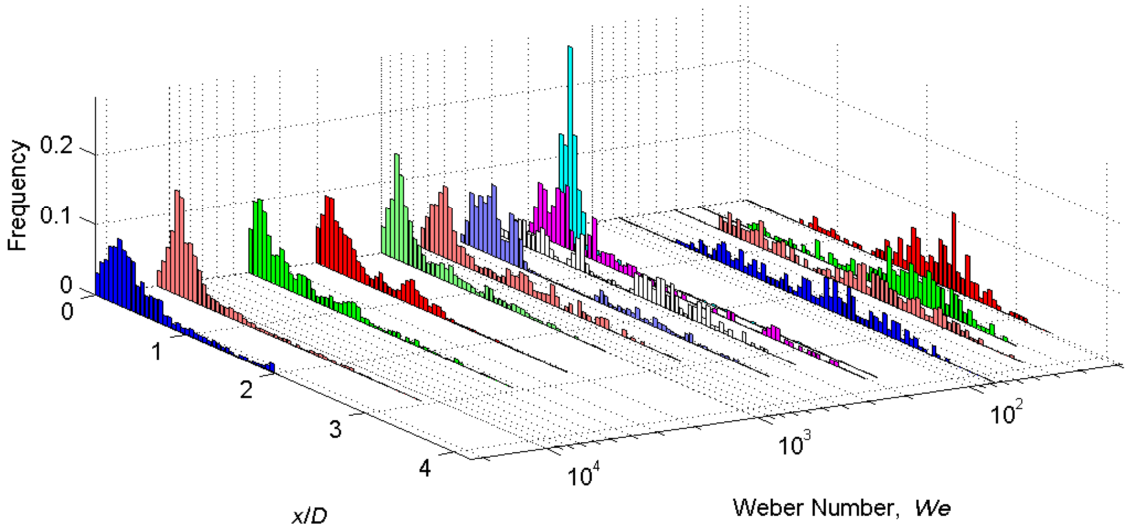

(b) CDT02WNP52

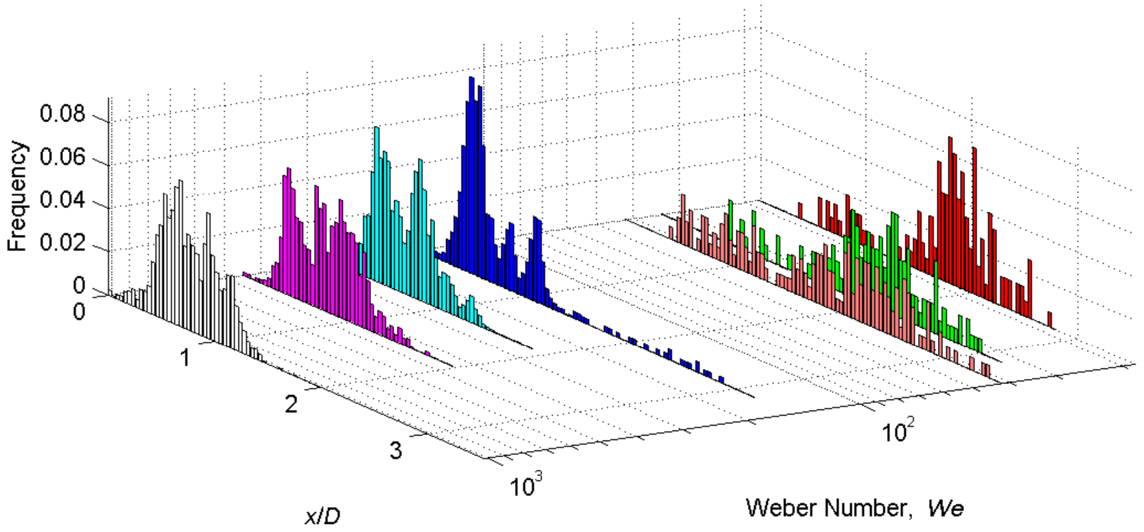

Figure 4.7 CO_2 droplet size histograms. Data are for liquid CO_2 injection through a 2 mm tube orifice into (a) tap water and (b) natural sea water. x/D is droplet diameter non-dimensionalized with the orifice diameter.

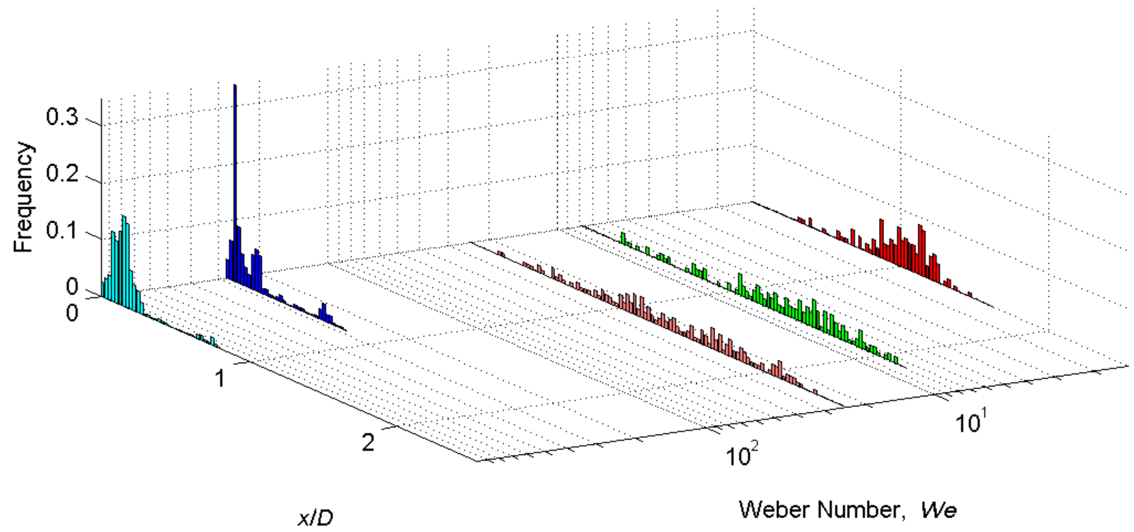

(a) CDT05WTP61

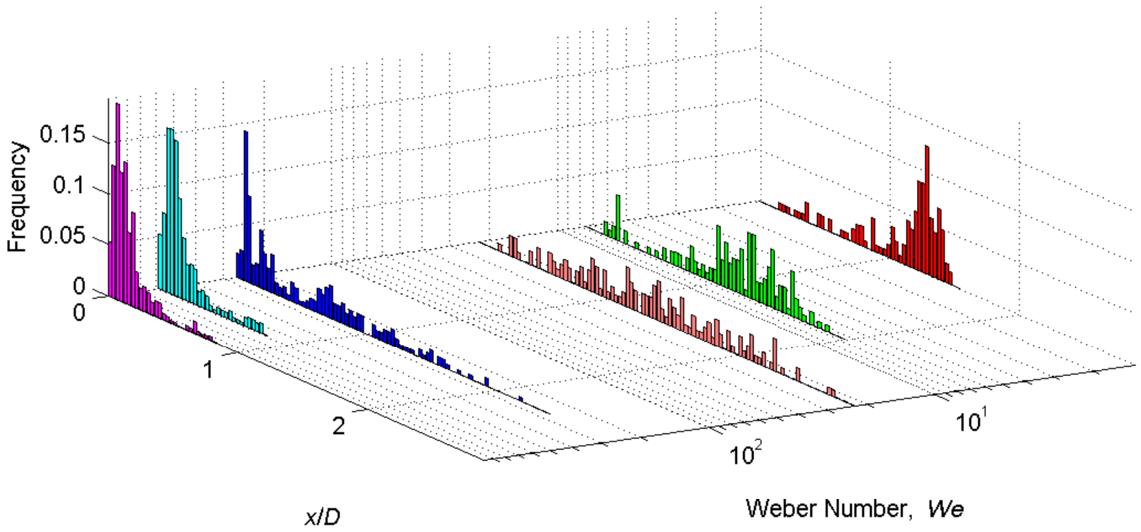

(b) CDT05WTP52

Figure 4.8 CO_2 droplet size histograms. Data are for liquid CO_2 injection through a 5 mm tube orifice into tap water at (a) P = 61 bar and (b) P = 52 bar. x/D is droplet diameter non-dimensionalized with the orifice diameter.

4.1.3.2 Orifice Effect

The effects of orifice diameter on x_{10}/D and x_{10}, are examined in Figure 4.9. These data are for liquid CO_2 injection into tap water through sharp edge orifices with $D = 2$ mm, 5 mm, and 10 mm, at a pressure of 52 bars. When the ensemble mean diameter is non-dimensionalized with the orifice diameter, x_{10}/D is larger for smaller D at the same value of We (Figure 4.9a). When x_{10} is plotted vs. We in Figure 4.9b, however, it becomes clear that a larger orifice produces modestly bigger droplets at low We in instability regime 1, but this effect diminishes as the transition to regime 3 is approached. Eventually, in regimes 4 and 5, orifice diameter appears to have little influence on the mean droplet diameter. Similar results were obtained for liquid CO_2 injection into tap water from 2 mm and 5 mm tube orifices at a pressure of 52 bars (Figures 4.10a and b). This behavior is consistent with the postulated evolution of instabilities, wherein higher order surface instabilities begin to dominate in regimes 4 and 5. Provided that the curvature of jet surface is not too great, these surface instabilities may not be sensitive to the initial jet diameter (which is determined by the orifice diameter).

The variation of the standard deviation with *We* observed in the CO_2 injection tests is plotted in Figure 4.11. In instability regimes 2 and 3, the standard deviation of the size distributions increases with orifice diameter, indicating a wider spread of droplets from the expectation value. Similar results were obtained for injection of Genesis (Figure 4.12) and Mars TLP (Figure 4.13) crude oils into tap water from 2 mm and 5 mm sharp edge orifices.

The effects of nozzle geometry on droplet size statistics are presented in Figures 4.14 and 4.15. These data correspond to liquid CO_2 injection into tap water at 52 bar through tube nozzles and sharp edge orifices. As seen in Figure 4.14, there is no obvious difference in the ensemble mean diameter of droplets generated by the tube nozzle and sharp edge orifice (for the same orifice diameter). Figure 4.15 suggests that the size distribution of droplets produced by the 2 mm tube nozzle may have larger standard deviations than the 2 mm sharp edge orifice at higher values of Weber number, but this effect is not observed for the 5 mm nozzle.

For low viscosity silicone fluid injection (where the kinematic viscosity of the jet fluid is about six times larger than liquid CO_2), nozzle geometry does appear to have an effect on droplet size. Figure 4.16 compares ensemble mean diameters and standard deviations, calculated using the incomplete PDPA size ensemble, for a 2 mm tube nozzle and a 2 mm sharp edge orifice. The tube nozzle produces larger x_{pdpa} and has a more uniform droplet size distribution than the sharp edge orifice. The reason for the difference in behavior from the CO_2 injection results is not clear, but might reflect the influence of jet fluid viscosity on the tube nozzle boundary layer development.

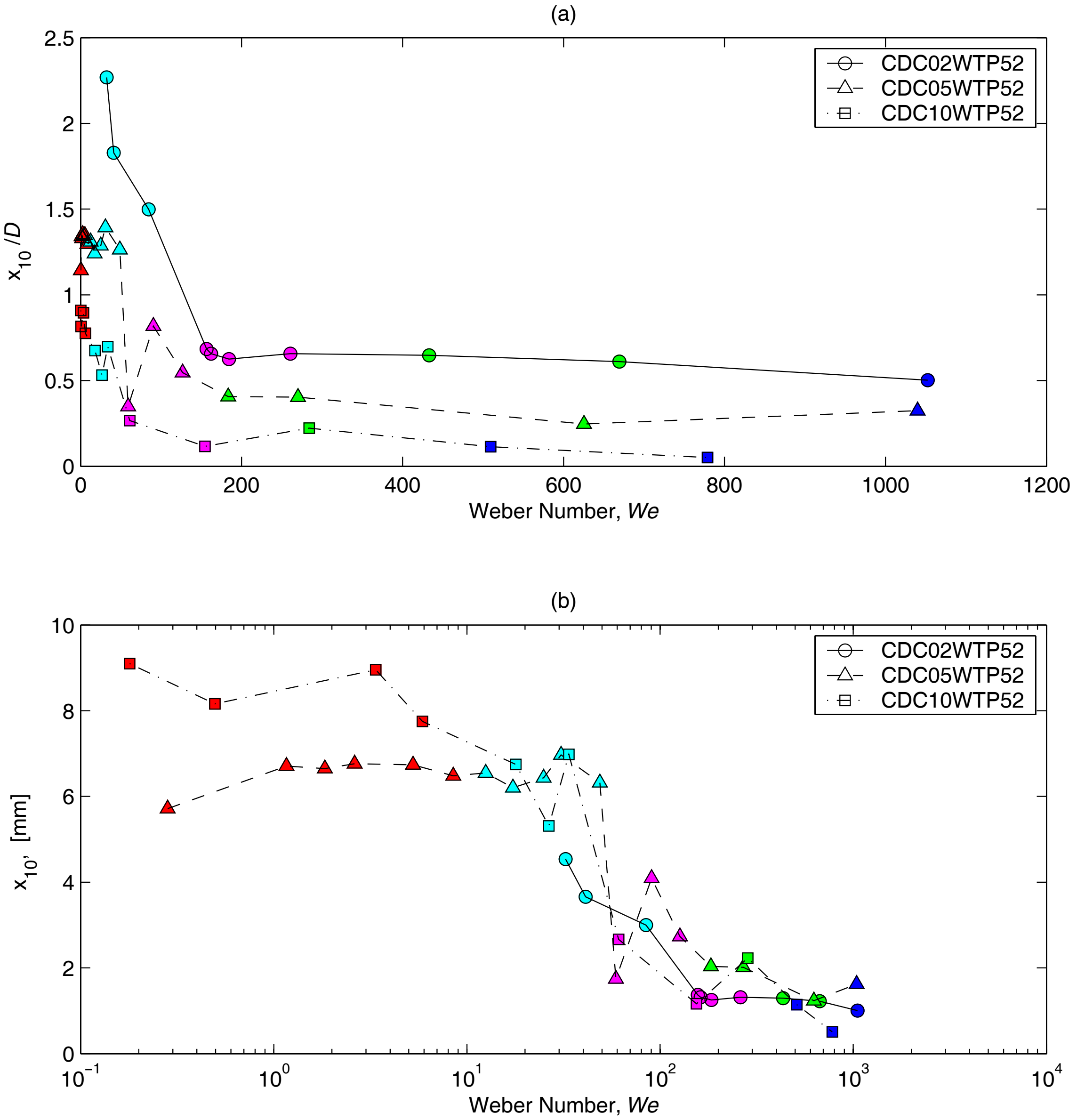

Figure 4.9 Effect of orifice diameter on (a) non-dimensional and (b) dimensional mean droplet diameter. Data are for liquid CO_2 injection into tap water from 2 mm, 5 mm, and 10 mm sharp edge orifices. Red, cyan, magenta, green and blue data points correspond to instability regimes 1, 2, 3, 4, and 5, respectively.

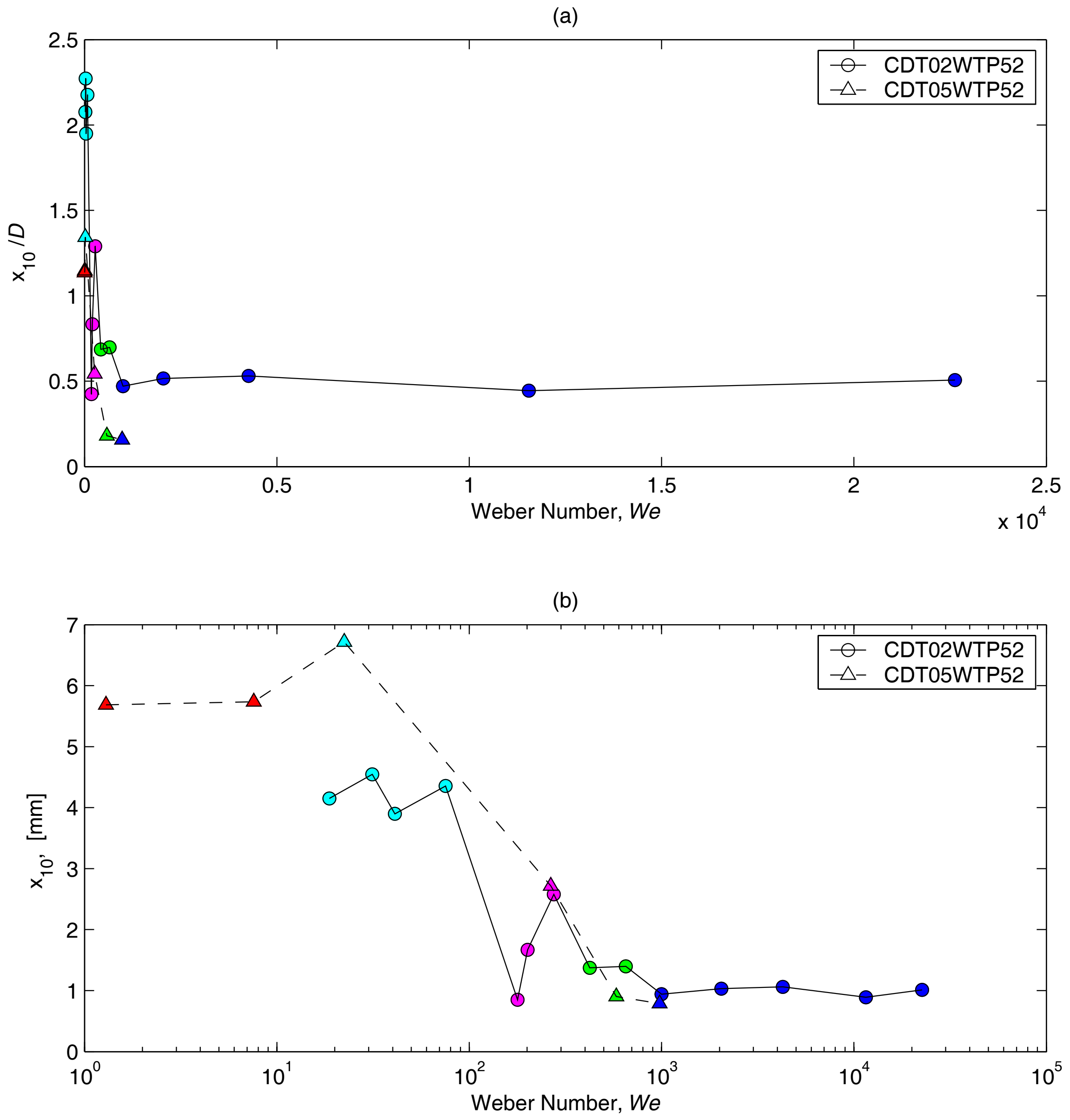

Figure 4.10 Effect of orifice diameter on (a) non-dimensional and (b) dimensional mean droplet diameter. Data are for liquid CO_2 injection into tap water from 2 mm and 5 mm tube orifices at P = 52 bar. Red, cyan, magenta, green and blue data points correspond to instability regimes 1, 2, 3, 4, and 5, respectively.

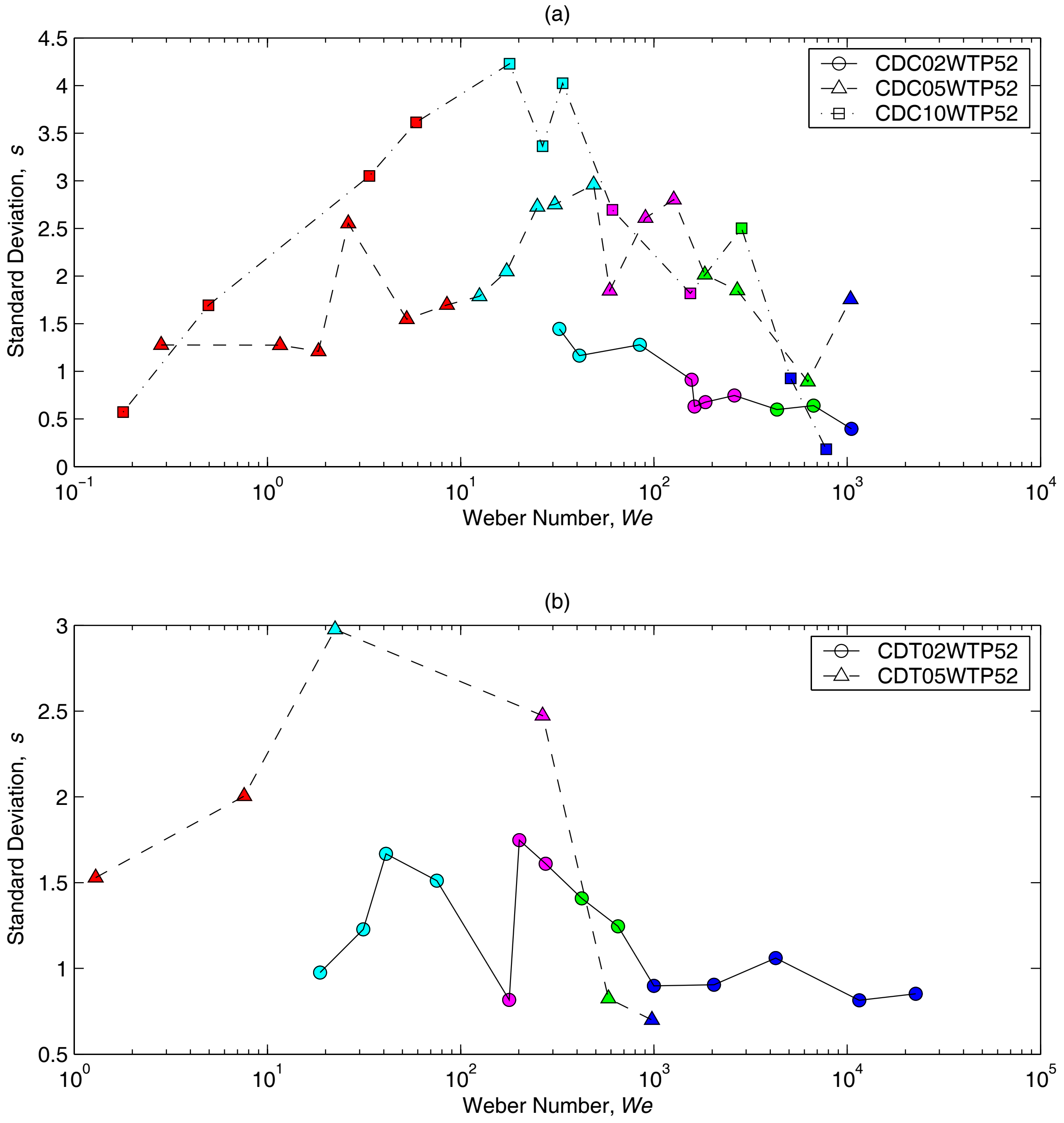

Figure 4.11 Effect of orifice diameter on standard deviation. Data are for liquid CO_2 injection into tap water at 52 bar from (a) sharp edge orifices with 2 mm, 5 mm and 10 mm inside diameters, and (b) tube orifices with 2 mm and 5 mm inside diameters. Red, cyan, magenta, green and blue correspond to instability regimes 1, 2, 3, 4, and 5, respectively.

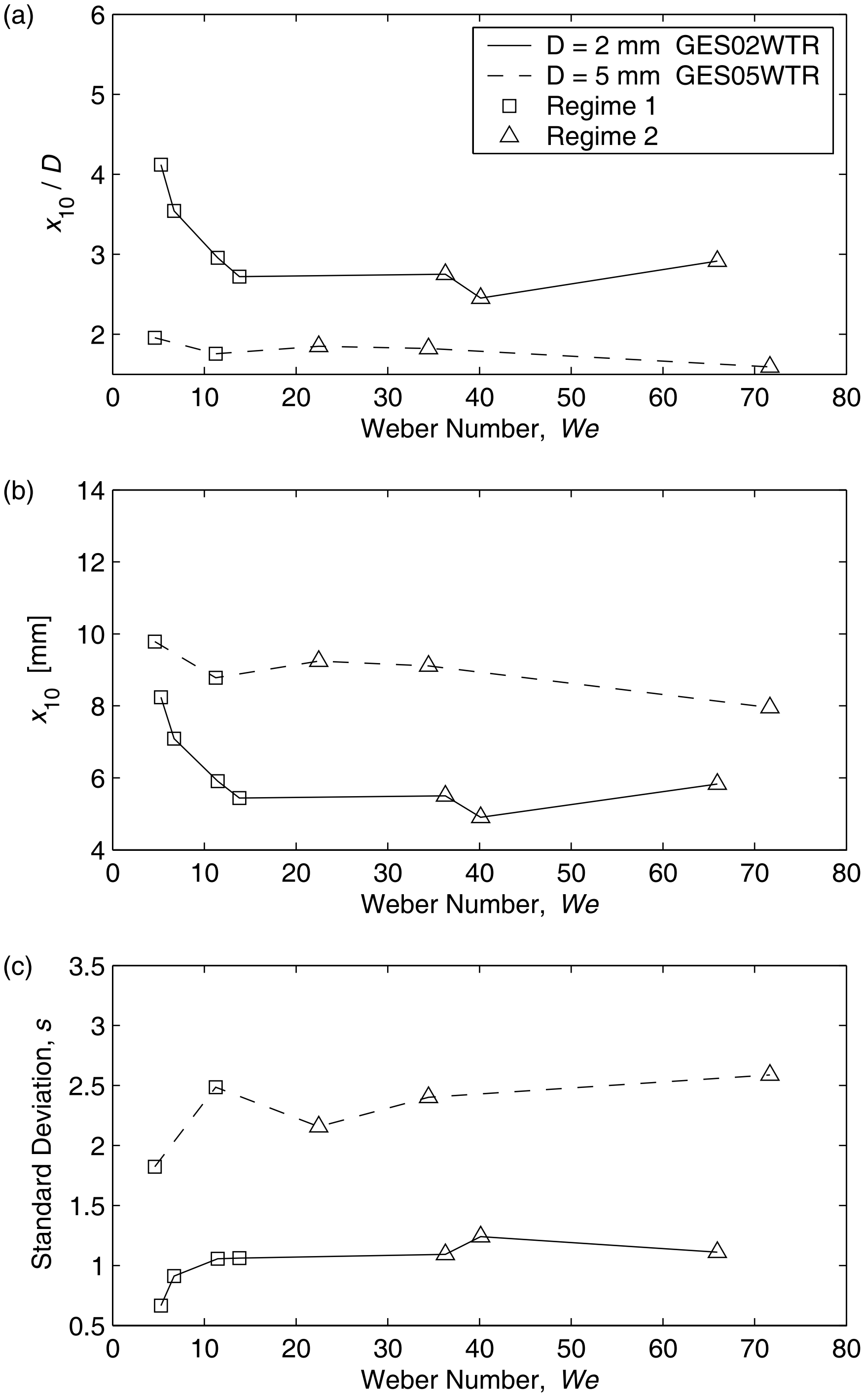

Figure 4.12 Effect of orifice diameter on (a) non-dimensional mean droplet diameter, x_{10}/D, (b) mean diameter x_{10} and (c) standard deviation, s. Data are for Genesis crude oil injection into tap water through sharp edge orifices with 2 mm and 5 mm inside diameters.

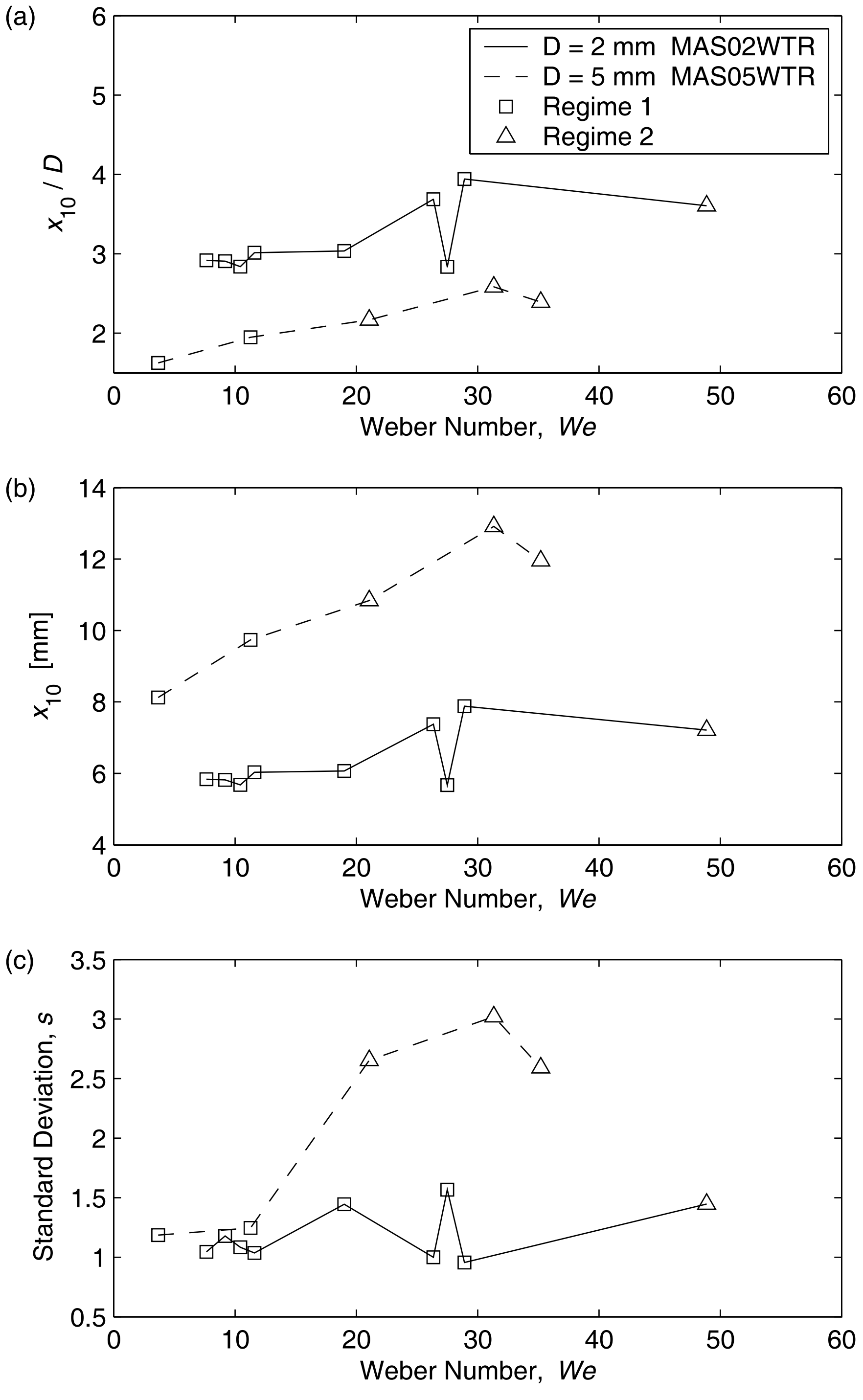

Figure 4.13 Effect of orifice diameter on (a) non-dimensional mean droplet diameter, x_{10}/D, (b) mean diameter x_{10} and (c) standard deviation, s. Data are for Mars TLP crude oil injection into tap water through sharp edge orifices with 2 mm and 5 mm diameters.

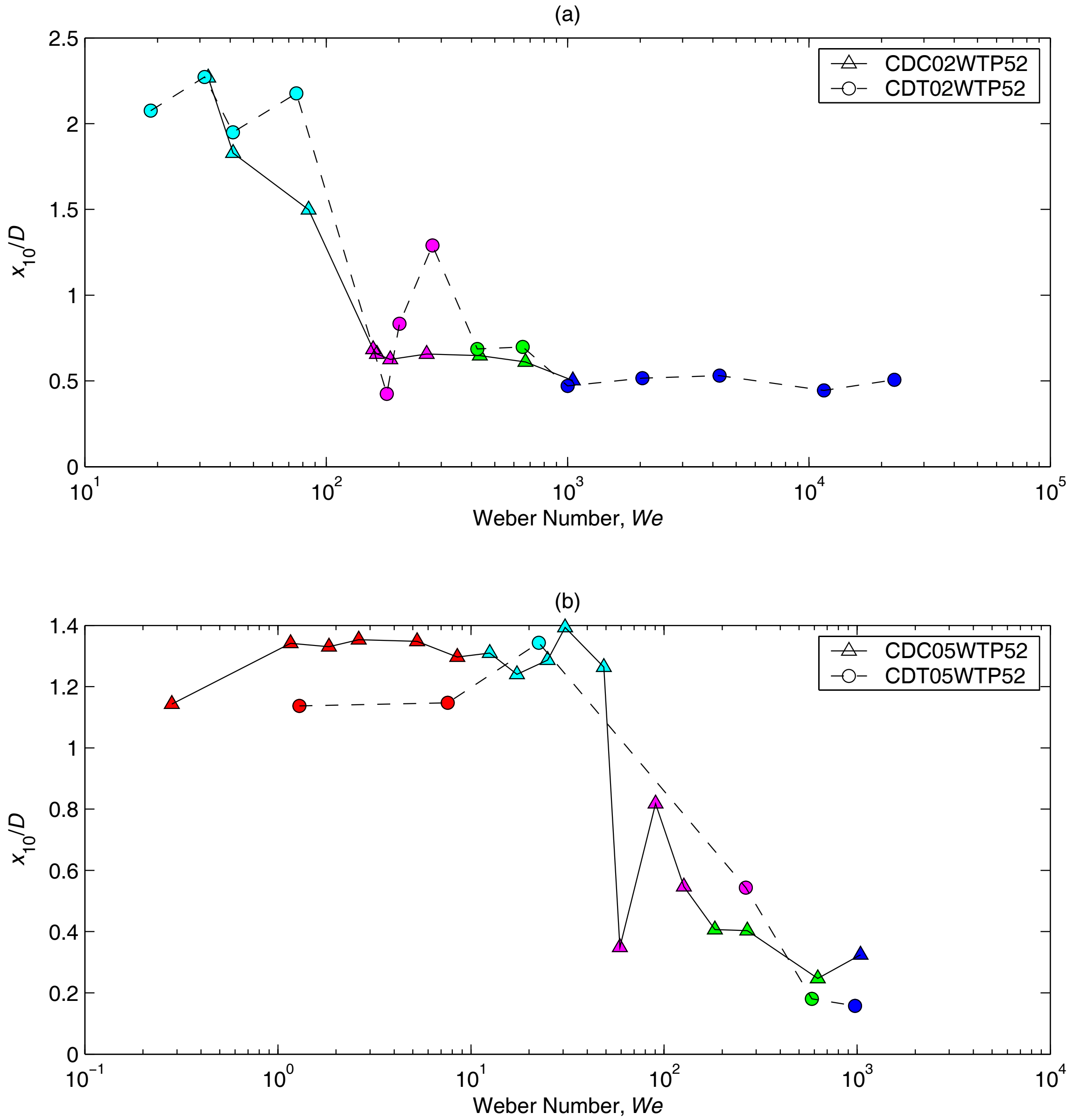

Figure 4.14 Effect of orifice geometry on non-dimensional mean droplet diameter. Data are for liquid CO_2 injection into tap water through sharp edge orifices and tube nozzles with inside diameters of (a) D = 2 mm and (b) D = 5 mm. Red, cyan, magenta, green and blue correspond to instability regimes 1, 2, 3, 4, and 5, respectively.

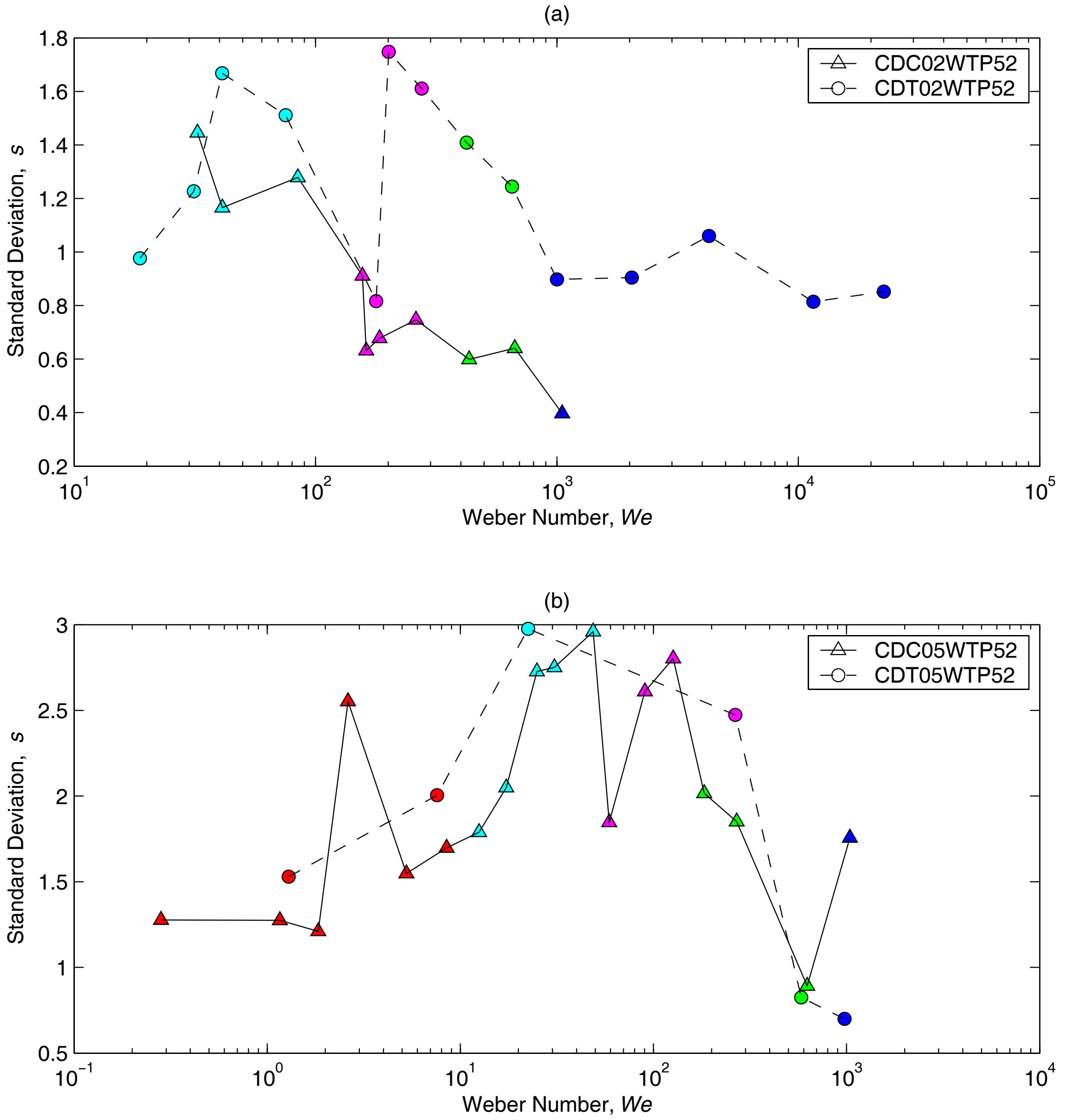

Figure 4.15 Effect of orifice geometry on standard deviation. Data are for liquid CO_2 injection into tap water through sharp edge orifices and tube nozzles with (a) D = 2 mm and (b) D = 5 mm. Red, cyan, magenta, green and blue correspond to instability regimes 1, 2, 3, 4, and 5, respectively.

4.1.3.3 Ambient Fluid Effect

The results of this investigation did not provide any clear evidence that the droplet size distribution of the tested jet fluids was significantly different in tap or sea water. Figure 4.17, plots mean diameters and standard deviations for Neptune Spar crude oil injection into tap water and sea water from a 2 mm sharp edge orifice. These data correspond to instability regimes 1 and 2. In Figure 4.18, results from the CO_2 injection tests employing a 2 mm tube orifice and tap water and sea water at $P = 52$ bar are compared. x_{10} are similar over the entire range of instability regimes. There is some indication that the droplet size distribution has a greater spread (i.e., larger standard deviation) in tap water than sea water at higher values of We.

4.1.3.4 Pressure Effect

Figure 4.19 compares the results from liquid CO_2 injection through a 5 mm tube orifice into tap water at 52 and 62 bar. In this range, pressure does not appear to exercise any significant influence on the droplet size statistics.

4.1.3.5 Viscosity Effect

Data corresponding to four jet fluids with kinematic viscosities ranging over three orders of magnitude are plotted in Figure 4.20. These data are for injection through 5 mm sharp edge orifices into tap water. At low We in regime 1, jet viscosity seems to have little effect on mean droplet size. As We increases, mean droplet size appears to increase slightly with jet fluid viscosity. Additional insight is provided by Figure 4.21 that compares PDPA data from the injection of two silicone fluids and liquid CO_2 into tap water through 2 mm sharp edge orifices. x_{pdpa} is larger for the higher viscosity fluids in the transitional breakup regimes.

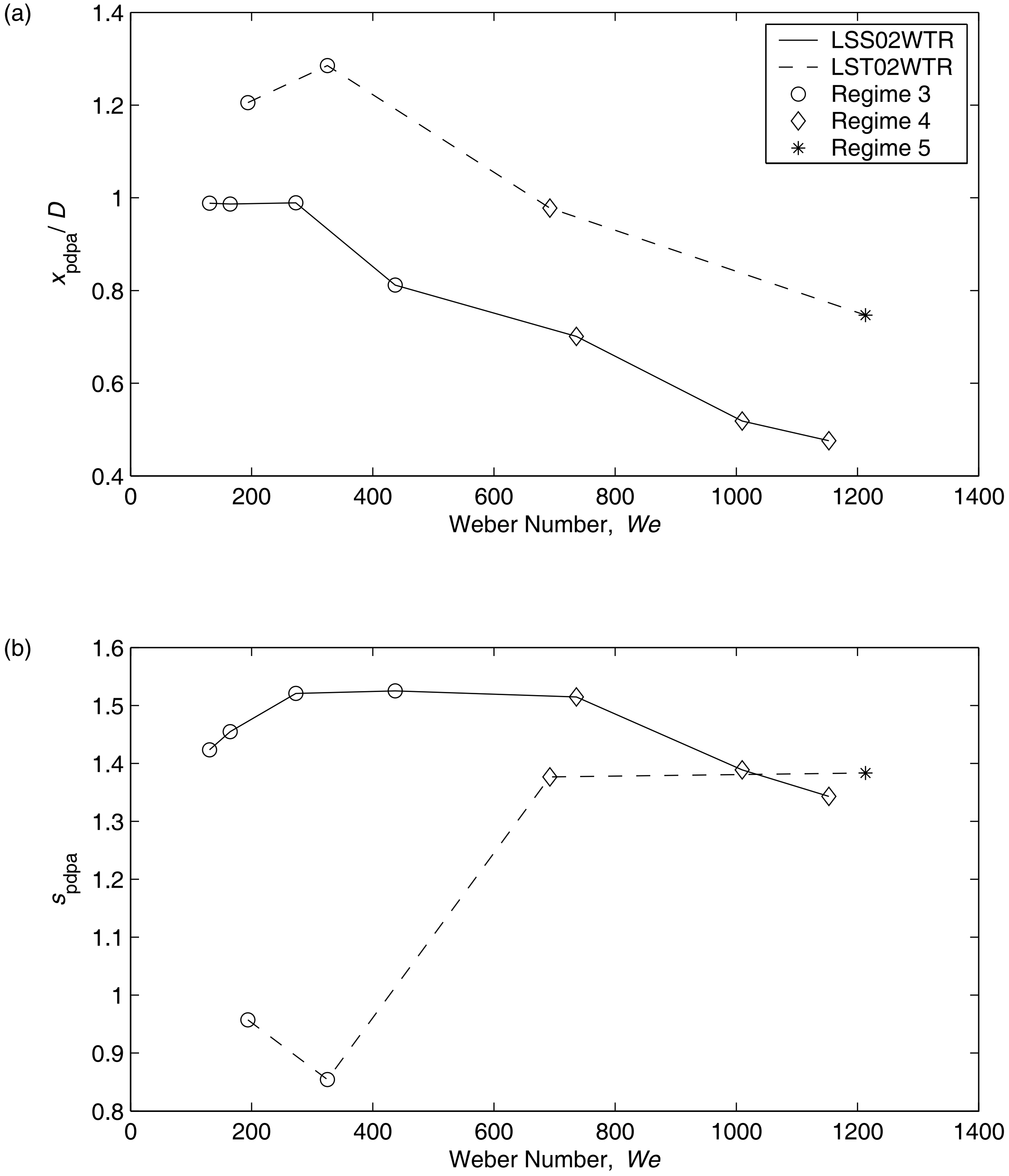

Figure 4.16 Effects of orifice geometry on (a) x_{pdpa} and (b) s_{pdpa}. Data are calculated from incomplete size spectra obtained from PDPA measurements of low viscosity silicone fluid injection into tap water from 2 mm sharp edge orifices and tube nozzles.

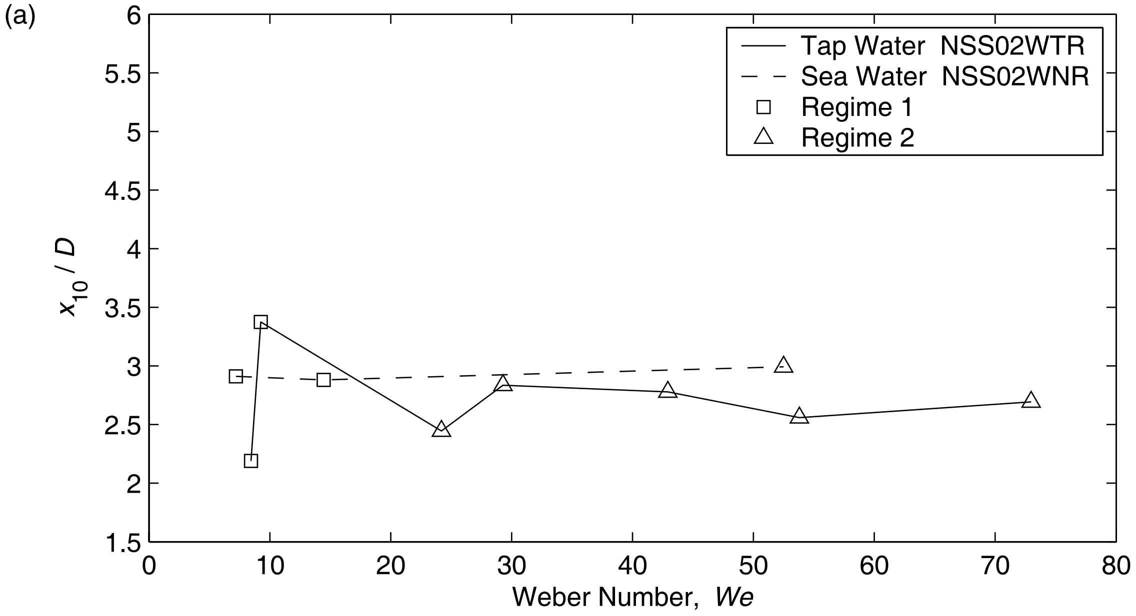

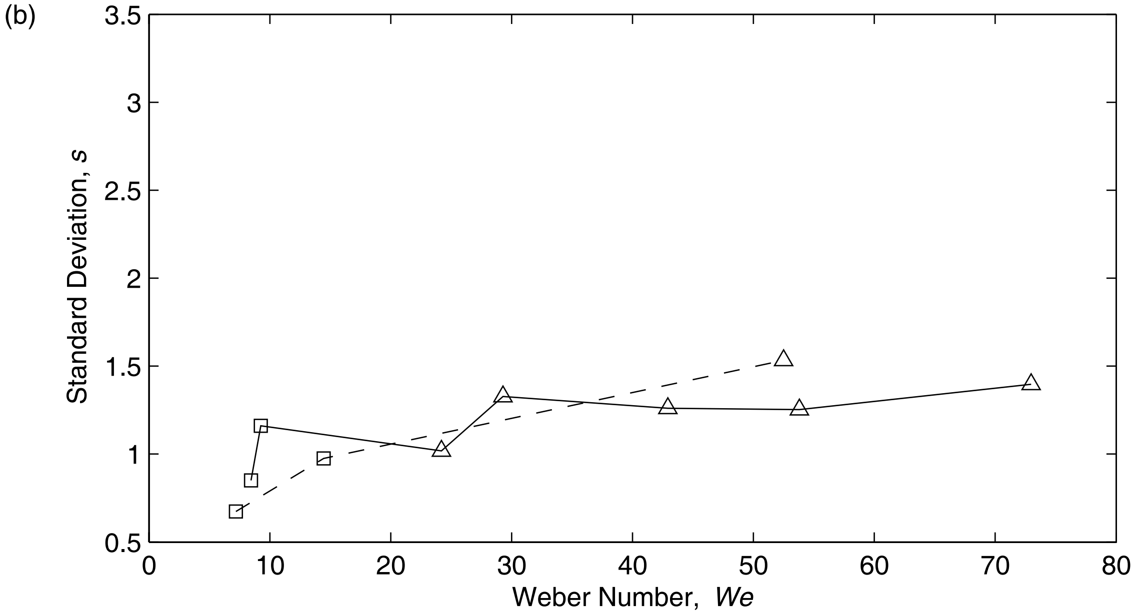

Figure 4.17 Effect of ambient fluid to (a) non-dimensional mean droplet diameter and (b) standard deviation. Data are for Neptune Spar crude oil injection into tap water and natural sea water from a 2 mm sharp edge orifice.

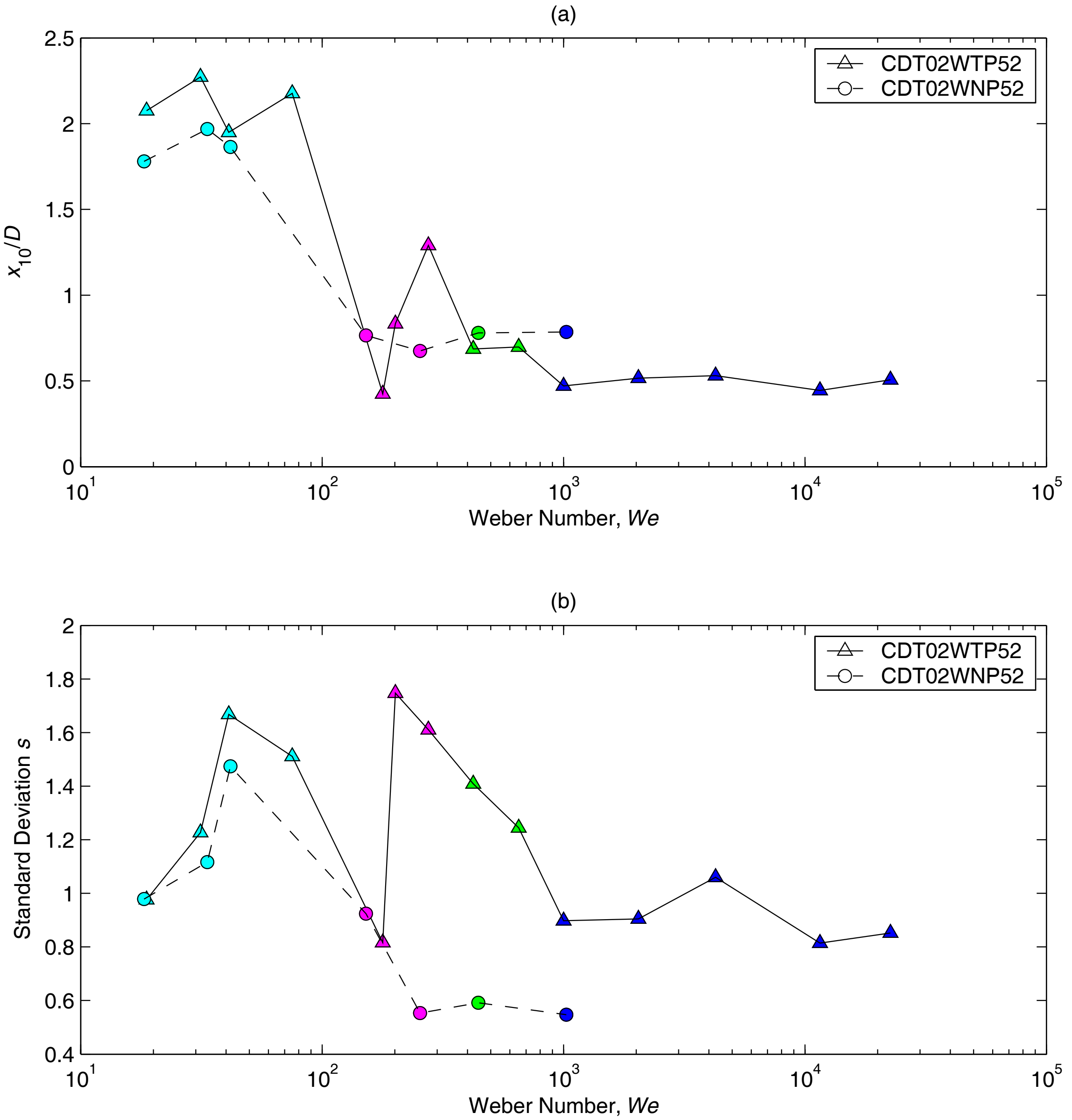

Figure 4.18 Effects of ambient fluid on non-dimensional mean droplet diameter and standard deviation. Data are for liquid CO_2 injection into tap water and natural sea water from a 2 mm tube nozzle. Red, cyan, magenta, green and blue correspond to instability regimes 1, 2, 3, 4, and 5, respectively.

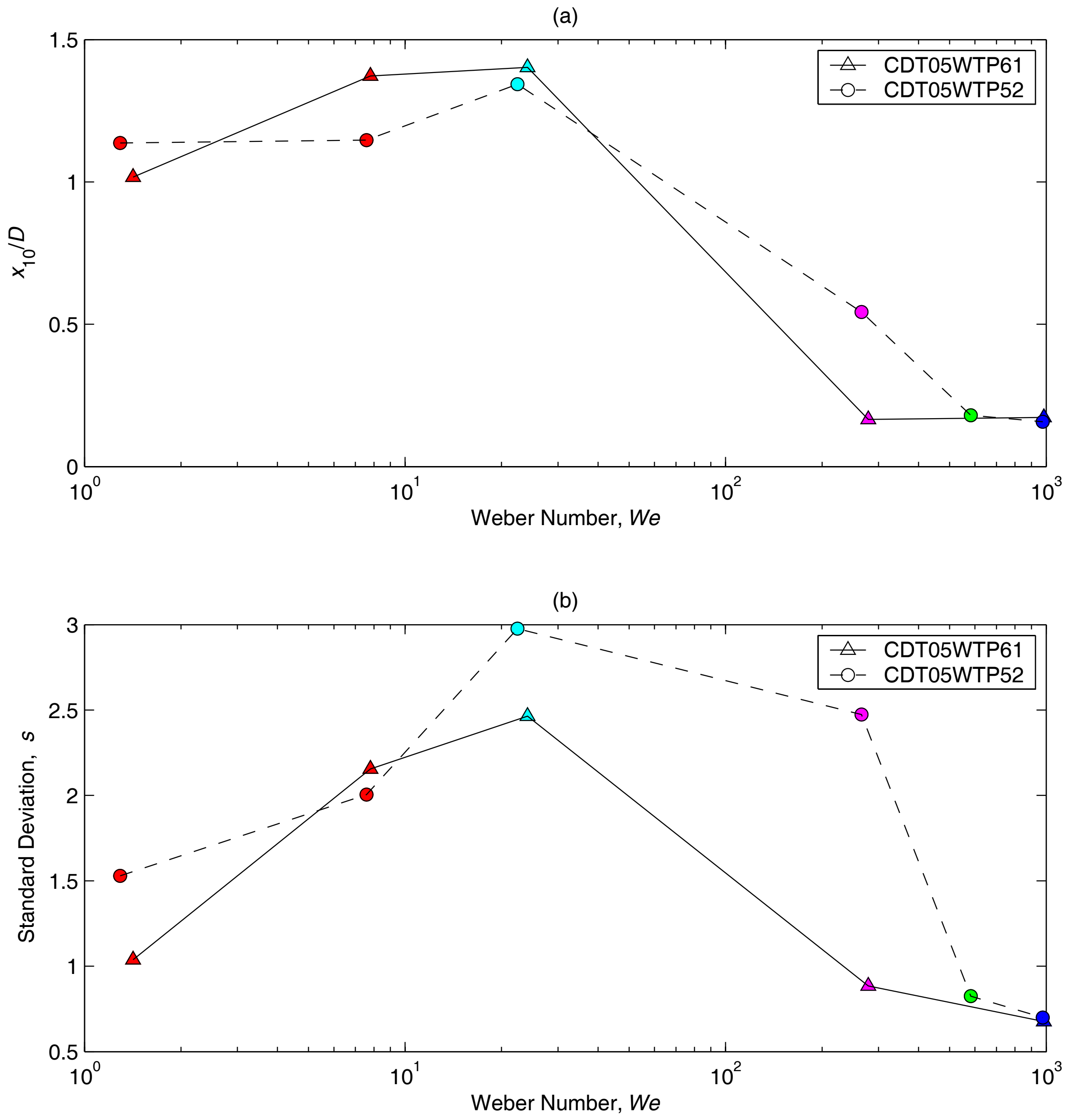

Figure 4.19 Effect of pressure on (a) non-dimensional mean droplet diameter and (b) standard deviation. Data are for liquid CO_2 injection into tap water from a 5 mm tube nozzle at 61 (triangles) and 52 (circles) bar. Red, cyan, magenta, green and blue correspond to instability regimes 1, 2, 3, 4, and 5, respectively.

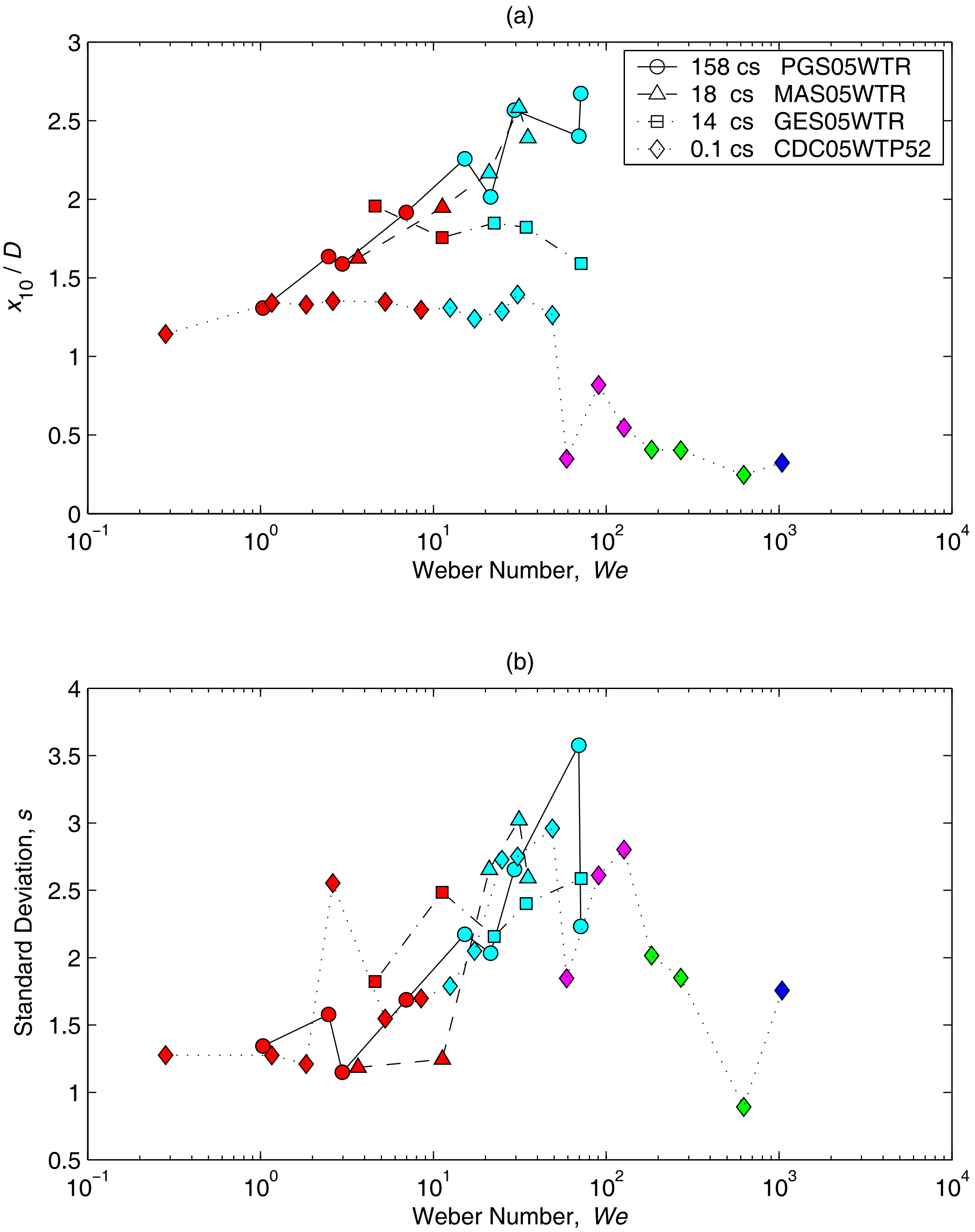

Figure 4.20 Effect of jet fluid viscosity on (a) non-dimensional mean droplet diameter and (b) standard deviation. Data are for injection of 3 crude oils and liquid CO_2 into tap water through 5 mm sharp edge orifices. Red, cyan, magenta, green and blue correspond to instability regimes 1, 2, 3, 4, and 5, respectively.

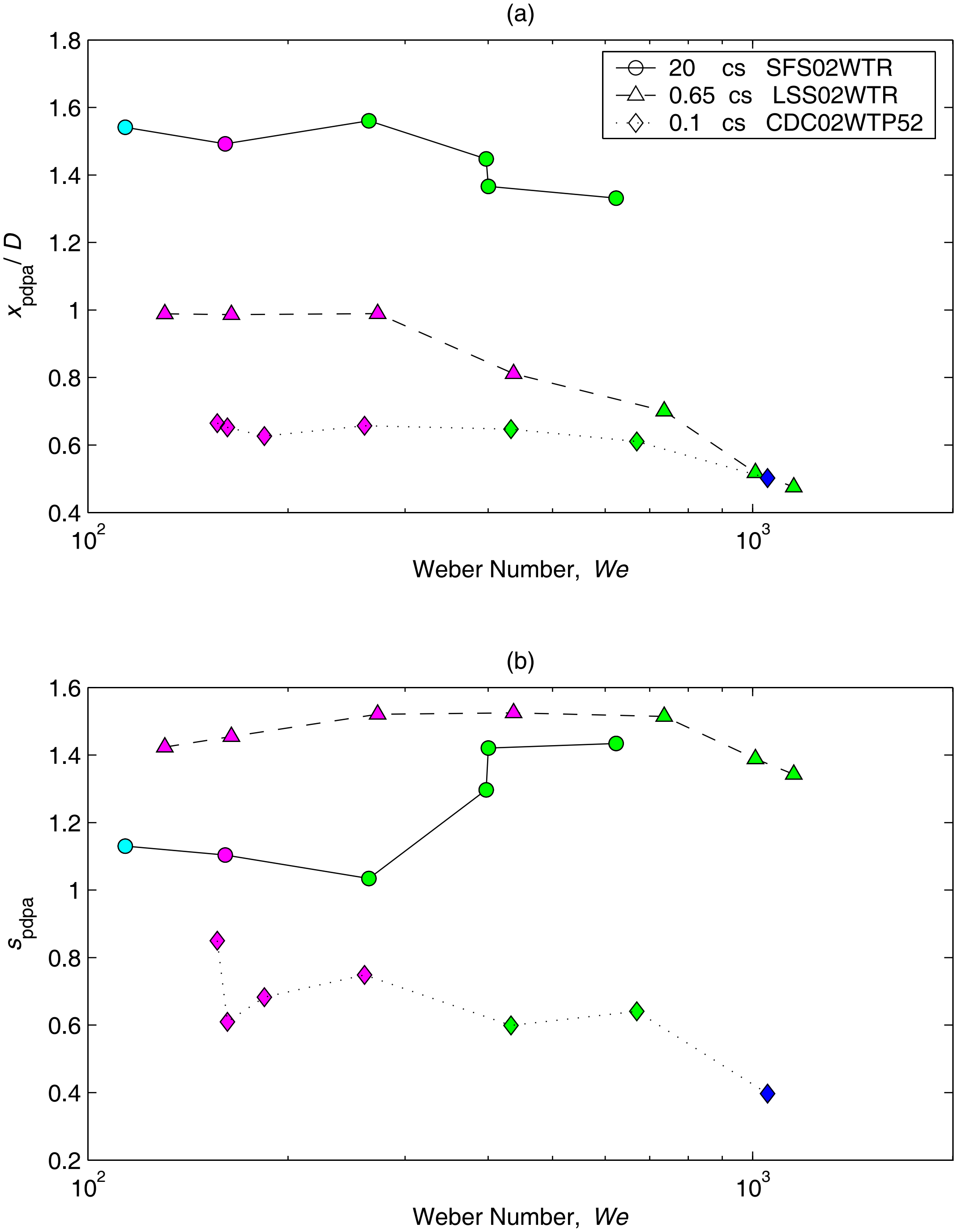

Figure 4.21 Effect of viscosity on (a) x_{pdpa} and (b) s_{pdpa} based on incomplete size spectra obtained from PDPA measurements. Data are for injection of 2 silicone fluids and liquid CO_2 into tap water from 2 mm sharp edge orifices. Cyan, magenta, green and blue correspond to instability regimes 2, 3, 4, and 5, respectively.

5 EXPERIMENTAL RESULTS: CO_2 HYDRATE

During the injection of liquid CO_2 into fresh water or seawater, CO_2 hydrate may form(Aya *et a*l., 1992, 1997; Hirai, *et al*., 1997): (1) prior to the jet breakup on injector internal passages and on the jet surface; and (2) after jet breakup on the surfaces of liquid CO_2 droplets. A number of studies (Teng & Yamasaki, 1999; Uchida *et al*., 2000) have examined hydrate formation on the surface of CO_2 droplets; however little work has been done to understand CO_2 hydrate formation prior to jet break up. In this section, from the present results from the liquid CO_2 injection experiments are reviewed and analyzed to investigate the effects of hydrate formation on jet instability and potential practical operational problems due to fouling of orifices and internal flow passages.

5.1 CO_2 Hydrate

When CO_2 is injected under deep ocean conditions (i.e., high pressure and low temperature), a solid hydrate phase will form at the CO_2-water interface. The hydrate stability regime is presented in the CO_2-H_2O phase equilibrium diagram shown in Figure 5.1.

The solid hydrate comprises a crystalline lattice of hydrogen-bonded water molecules. The interstitial spaces are occupied by “guest” molecules, in this case, CO_2. Hydrate formation is described by

$$CO_2 + n\ H_2O \Leftrightarrow CO_2 \cdot nH_2O + \Delta H \tag{5.1}$$

where ΔH = 60.4 kJ/mole (at 277 K). *n* is the hydration number with a value of 5.75 at stoichiometric conditions (Teng *et al*., 1996). A value of 7.3 has been experimentally determined by Chen (1972), who suggested that the hydration number is probably sensitive to ambient conditions (Wong & Hirai, 1997). The density of the hydrate is about 1.13 g/cm^3. This value was determined from X-ray crystallography (Wadesley, 1995), while Bozzeo *et al.* (1975) have reported a density of 1.1 g/cm^3.

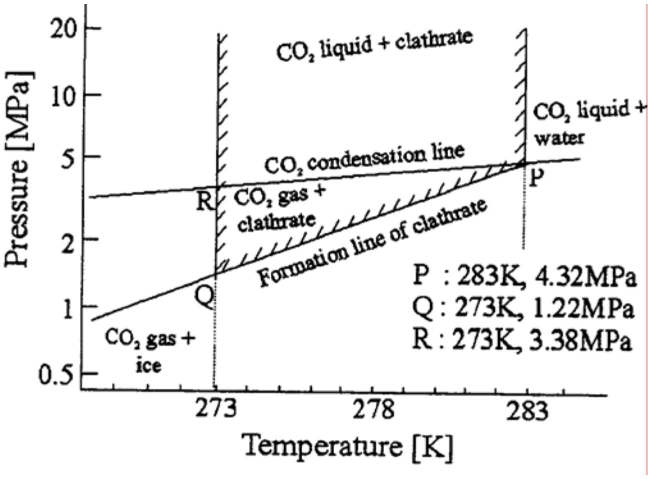

Figure 5.1 CO_2-H_2O equilibria (from Wong & Hirai, 1997).

CO_2 hydrate that forms on CO_2 droplet surfaces in the deep ocean following jet breakup restricts the dissolution of the injected CO_2 (Aya *et al.*, 1992; Nishikawa *et al*., 1995; Wong & Hirai, 1997; Hirai *et al*., 1997). This impacts the level and extent of acidification of seawater near the discharge location and, potentially, the effectiveness of this CO_2 sequestration technique.

Hydrate formation that occurs prior to breakup may affect the jet instability mechanism and alter the size of droplets or result in flow blockage in submerged conduits, valves and injectors used to transport and inject liquid CO_2 into the deep ocean. Pre-breakup hydrate formation has not been studied extensively. Hence, the present CO_2 injection experimental results were reviewed: (1) to investigate the influence of hydrate formation on the breakup of jets of liquid CO_2 injected into water; and (2) to investigate CO_2 hydrate formation phenomena in flow in internal passages.

Jet break-up is a consequence of the growth of instabilities at the interface between the jet and ambient fluid. Hydrate formation is also a surface phenomenon. If the formation of a solid hydrate film on the surface of the CO_2 jet occurs faster than the growth of the surface fluid instability, then the instability may be damped and break-up of the jet into droplets may be affected (Teng *et al*., 1996). Since the size of the droplets is an important parameter in the subsequent dissolution and dispersion of the CO_2 into the ocean water column, it is important to understand how and under what circumstances hydrate formation will impact break-up. The analysis of Teng *et al*. (1996) suggested that the time scale of hydrate formation depends primarily on CO_2 and water temperatures and water chemistry (e.g., solubility of CO_2 in water). The characteristic time for instability growth depends on the flow regime (i.e., the dominant mode of instability, such as Rayleigh, asymmetric,etc.). For example, if Rayleigh's maximum-instability theory applies, it can be shown that the characteristic time for jet breakup depends primarily on jet velocity, jet orifice diameter, and interfacial tension (Teng, 1994).

The present CO_2 injection experiments were conducted over a range of jet injection velocities at different CO_2 and water temperatures using a variety of injection orifices . As a consequence, the data represent flow scenarios corresponding to different characteristic times for hydrate formation and jet instability.

5.2 Hydrate Formation on the Surface of the Jet

Digital video results from the CO_2 injection experiments were reviewed and analyzed to identify conditions that promote pre-breakup hydrate formation and to gain insight into this phenomenon.

5.2.1 Hydrate Tubes

In a number of experiments, hydrate or hydrate and ice tubes were observed to form around the perimeter of the CO_2 jet adjacent to the injector. Figure 5.2 presents images of CO_2 hydrate and ice tubes that formed in the wave breakup and full atomization flow regimes during 3 different runs using the 10mm sharp edge orifice (C10) and tap water. The corresponding flow conditions are described in Table 5.1. The liquid CO_2 jet continued to flow through upon the hydrate tube and droplets formed above the tube.

The formation process of hydrate tube 3 is demonstrated in Figure 5.3. The dissolved CO_2 concentration in the water increases rapidly at high CO_2 injection rates. When the temperature and pressure at the jet-water interface are within the hydrate stability regime, hydrate starts to form at the jet surface on the injector (Figure 5.3a). Since the temperature of CO_2 is lower than the freezing point of water at the experimental pressure level, the solid phase may also include ice crystals mixed with the hydrate. The hydrate ring advances upward along the jet, forming a solid tube around it while the liquid CO_2 continues flowing through the center of the tube (Figures 5.3b to 5.3i). The thickness of the hydrate tube is increased by the extrusion of liquid CO_2 from small holes on the tube surface or from weak portions of the tube. Smaller hydrate branches grow around the liquid CO_2 extrusions. Eventually, a hydrate web may connect all the branches and the primary hydrate tube (Figure 5.3j). Note that the slow flow of CO_2 through the branches can generate large droplets that are not anticipated at the total jet flow rate that corresponds to atomization. This is another means by which pre-breakup hydrate formation can alter the size spectra of the droplet phase.

The digital video data were analyzed to estimate the rate that the hydrate tube advanced upward along the jet. In Figure 5.4, tube height is plotted as a function of time for tubes 2 and 3. The data suggests a constant growth rate. A linear regression yields a growth rate of 0.71 mm/s for tube 1 and 0.52 mm/s for tube 2. For these two cases, growth rate appears to scale directly with CO_2 flow rate.

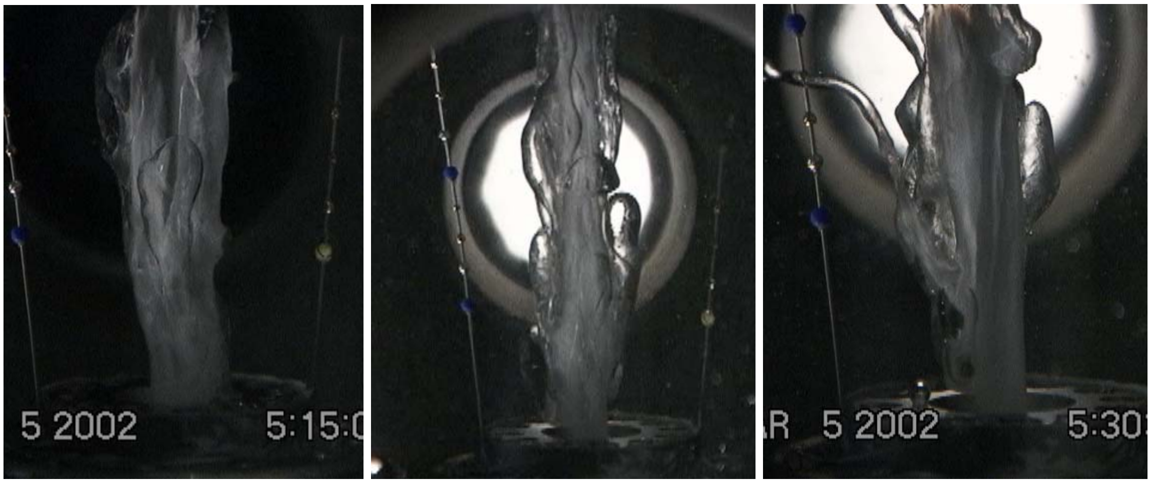

(a) Hydrate tube 1 (b) Hydrate tube 2 (c) Hydrate tube 3

Figure 5.2 CO_2 hydrate tubes with 10 mm sharp edge orifice (C10) in tap water at pressure of 52 bars with different CO2 flow rates.

Table 5.1 Flow conditions for hydrate tube formation shown in Figure 5.2 in tap water at pressure of 52 bars.

CO_2 hydrate tube No.	Conditions at start of formation			Hydrate growth rate [mm/s]
	CO_2 Temperature [°C]	Ave. Jet velocity [m/s]	Ave. water Temp. [°C]	
1	-9.44[2]	0.89	11.9	N/A[1]
2	-9.15	1.17	12.2	0.52
3	-9.08	1.47	12.5	0.71

1: Data not available since the camcorders weren't recording.
2: CO_2 temperature when the camcorder was turned on after the hydrate tube 1 had already formed (Figure 5.2 a).

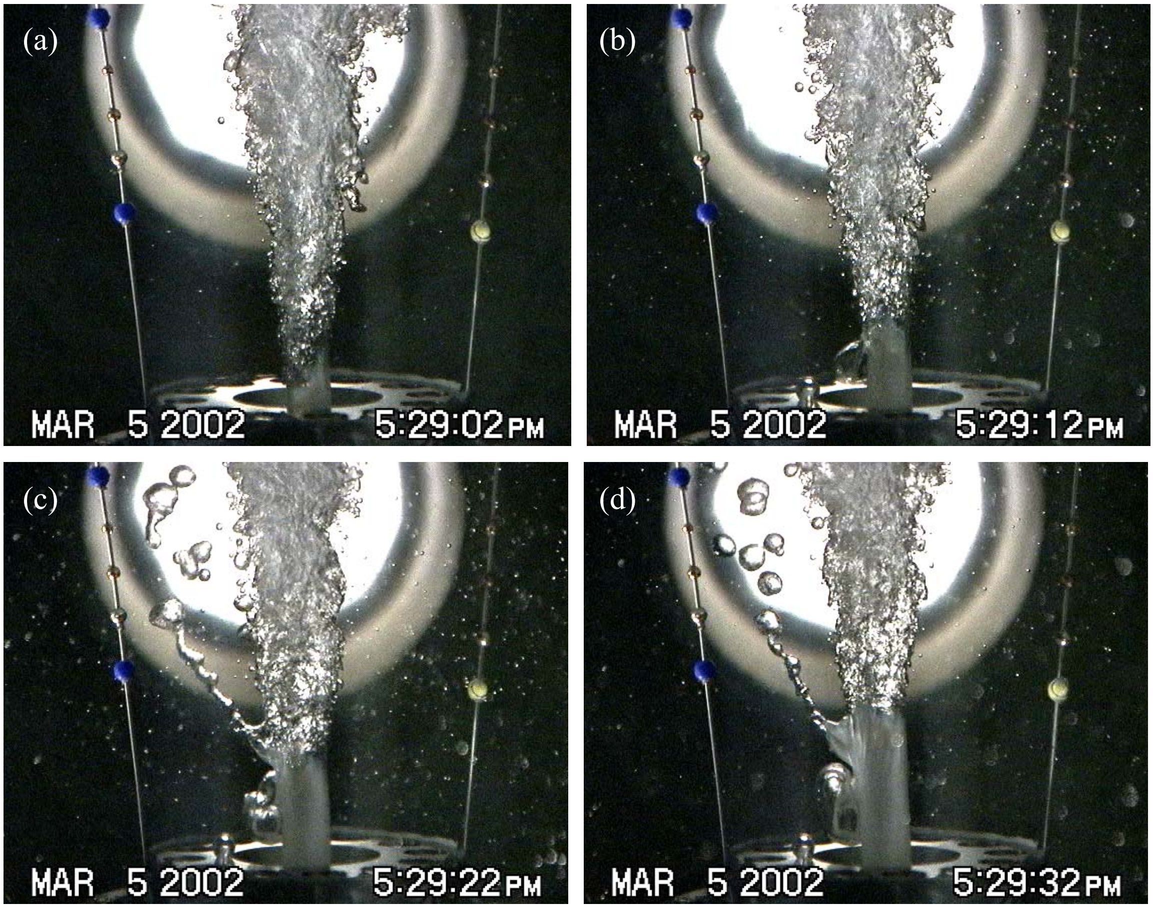

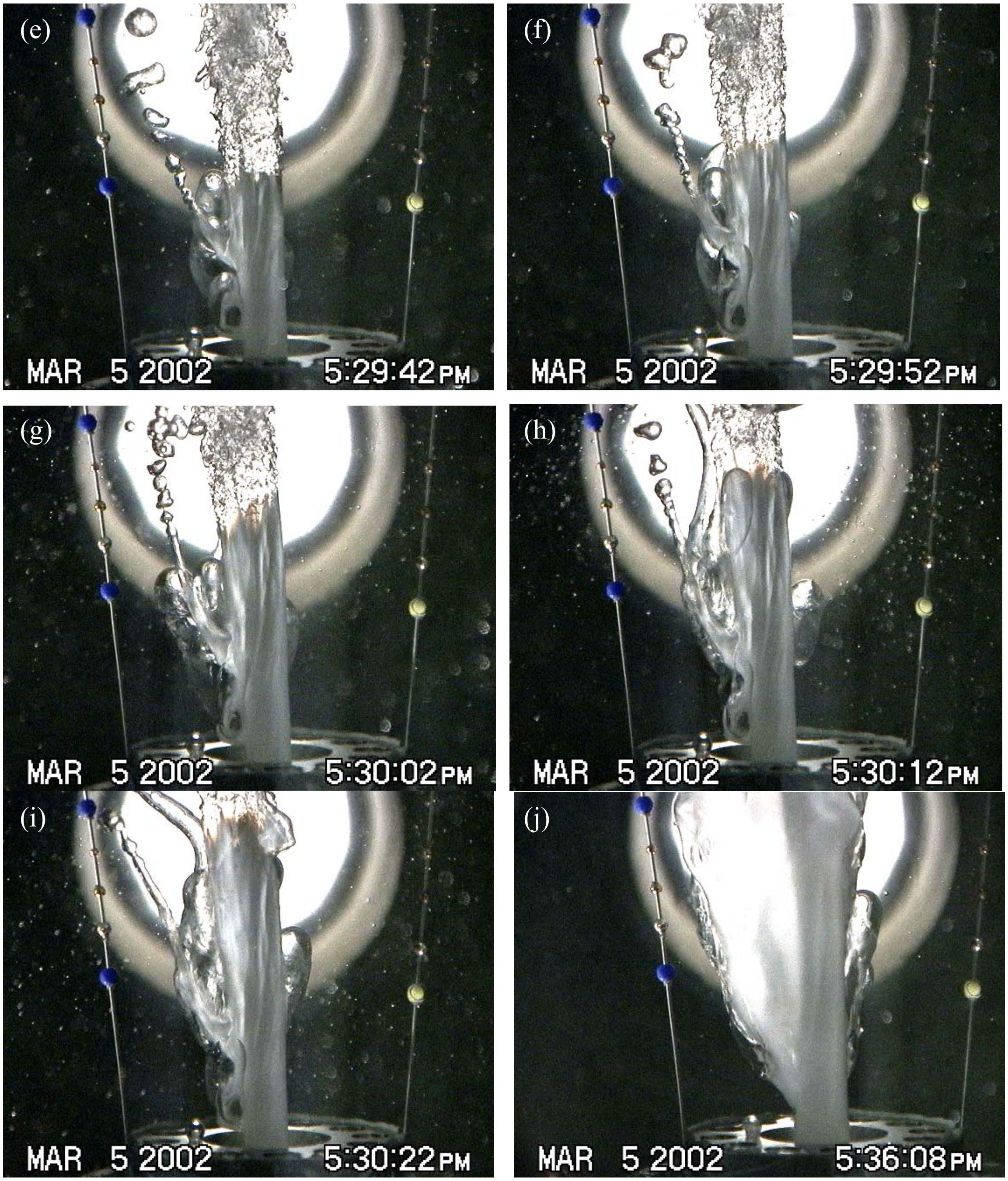

Figure 5.3 Formation process of hydrate tube 3.

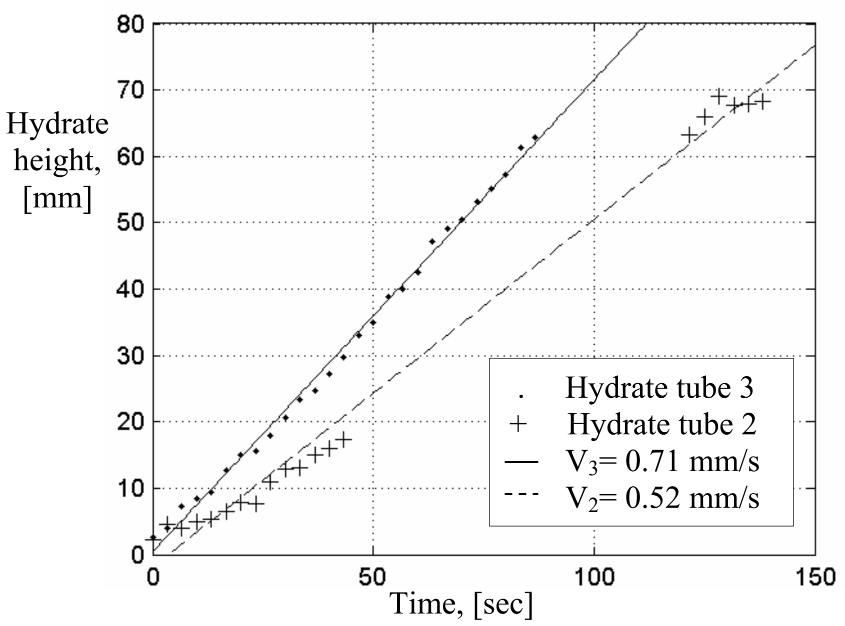

Figure 5.4 Hydrate tube height as a function of time. Solid and dashed lines are linear curve fits to the data.

5.2.2 Thin Film Hydrate Tubes

Thin film hydrate tubes were observed in tests conducted in the varicose breakup regime with low CO_2 flow rates. Examples are shown in Figure 5.5 for different injector orifices. The corresponding test conditions are given in Table 5.2. The thin film tubes appeared to be unstable. As shown in Figures 5.6 and 5.7, the thin film tubes typically persisted for about 10 to 20 seconds before detaching from the orifice. A new tube forms immediately after the old one detaches. This process repeats itself as the flow conditions, such as CO_2 flow rate, temperature and pressure, etc., remain the same.

The thin film tube appeared to be moderately ductile and would deform slightly; they were not perfectly rigid. In many of these tests, CO_2 temperatures were only slightly below or above the freezing point of water. Moreover, the CO_2 flow rates were very low and the ambient water temperature were relatively high, suggesting that the cooling effect of the CO_2 jet would probably not be sufficient to produce much or any ice. The thin film tubes were believed to comprise primarily or entirely hydrates and no ice.

The video records indicate that CO_2 droplet form by breakup of the jet issuing from the end of the thin film hydrate tube. The opening at the end of these tubes may be different in size and shape from the injector orifice and geometry. Since orifice diameter affects droplet size, hydrate formation can alter the spectra of the droplet phase through changes in effective jet diameter and shape.

(a) 5 mm sharp edge orifice (C05) (b) 5 mm tube orifice (T05)

(c) 10 mm sharp edge orifice (C10) (d) 2 mm tube orifice (T02)

Figure 5.5 Thin film CO_2 hydrate tubes observed in the varicose breakup regime with different orifice diameters and shapes. All photos correspond to liquid CO_2 injection tests into tap water.

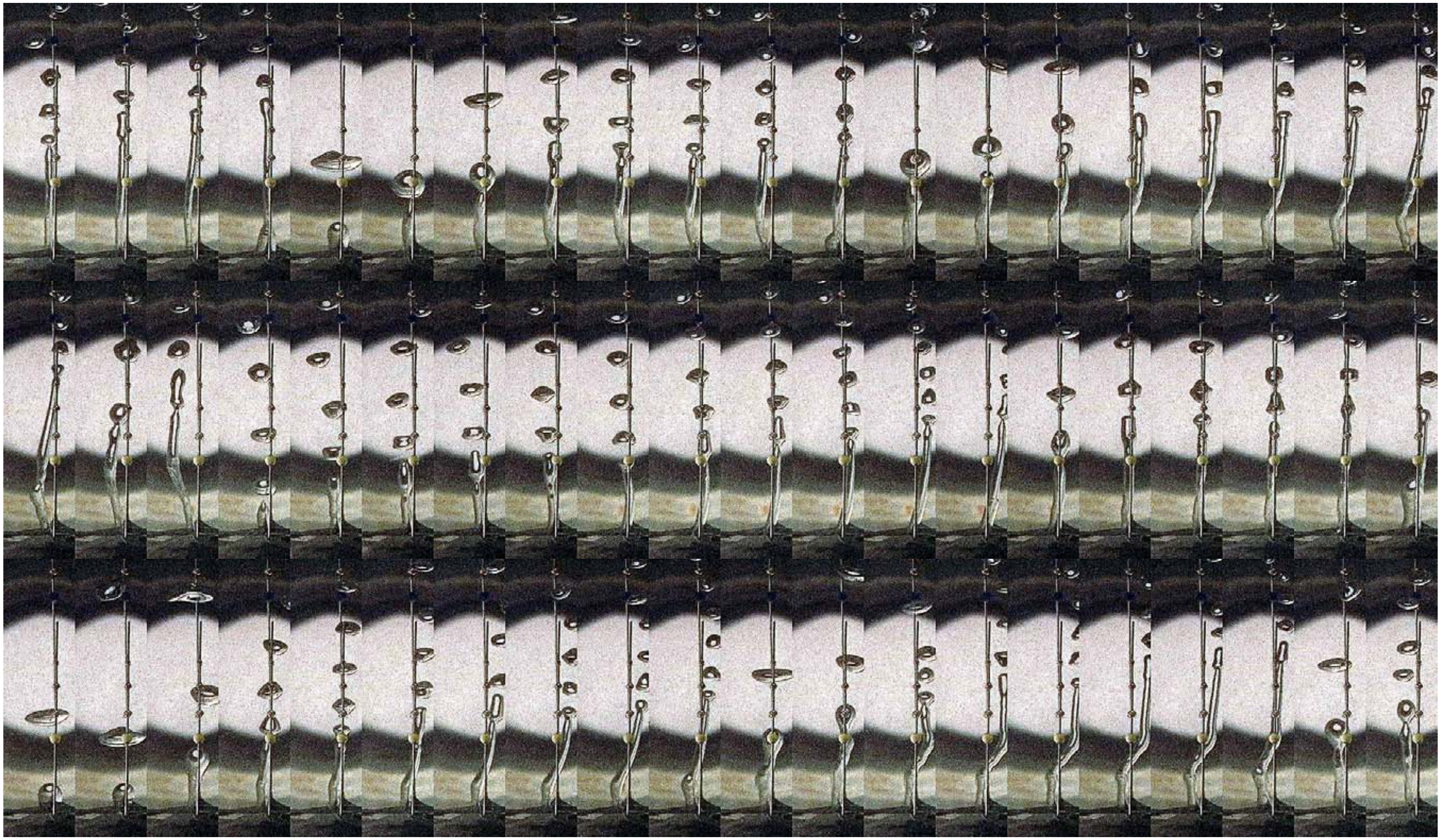

Figure 5.6 Repeating formation of CO_2 thin film hydrate tube for injection from a 5 mm sharp edge orifice. This is the same test run, CDC05WTP52R3, as shown in Figure 5.5 a. Time interval between any two adjacent frames is 1.033 sec.

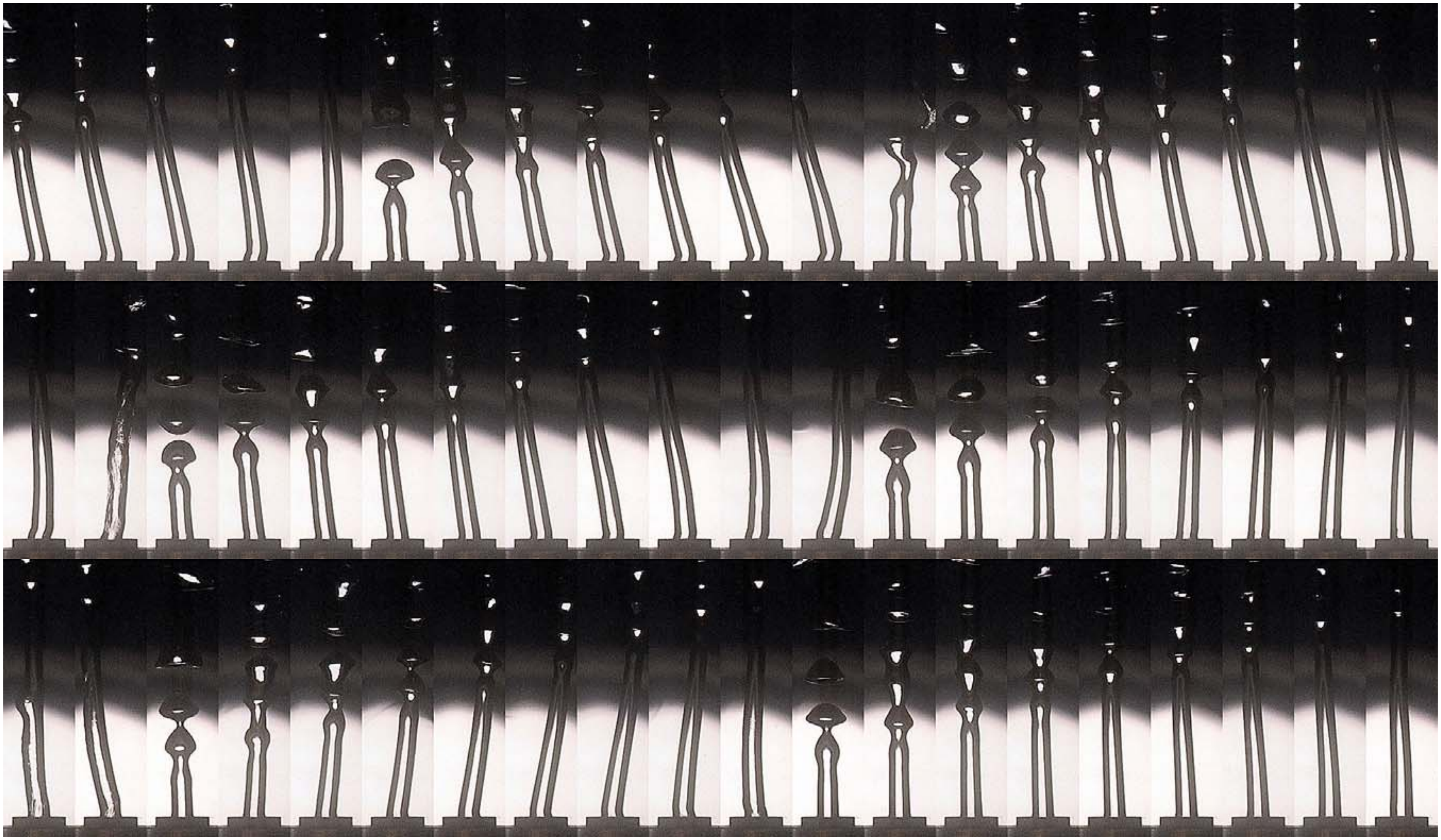

Figure 5.7 Repeating formation of CO_2 thin film hydrate tube for injection from a 5 mm tune orifice. Test run CDT05WTP61R6. Time interval between any two adjacent frames is 2 seconds.

Table 5.2 Injection conditions for the CO_2 thin film hydrate tubes in Figure 5.5.

Thin film hydrate tube in Fig. 5.7	Orifice		Ave. CO_2 Temp [°C]	Ave. CO_2 mass flowrate [kg/min]	Ave. jet velocity [m/s]	Ave. water temp. [°C]	Pressure [bar]
	inside diameter [mm]	shape					
a	5	Sharp	-0.26	0.09	0.087	6.07	52
b	10	Sharp	-2.00	0.30	0.067	13.2	52
c	5	Tube	2.11	0.10	0.094	9.26	61
d	2	Tube	-2.60	<0.10	<0.55	10.74	52

5.3 Hydrate Blockages

For CO_2 ocean sequestration, liquid CO_2 will be transported to the deep ocean via a submerged conduit. It is generally assumed that by the time the CO_2 reaches the injection depth, it will be in thermal equilibrium with the surrounding seawater, typically less than about 5^oC. The seawater-CO_2 system will then be in the hydrate stability regime. Hydrate formation at the injector orifices or upstream in the conduit, should there be ingress of water, could potentially block the flow system. Based on experience in undersea oil and gas operations where methane hydrate blockage can pose major problems, it is anticipated that clearing CO_2 hydrate blockages may be extremely difficult or impossible. During the present CO_2 injection experiments, a few tests were conducted to investigate hydrate blockage phenomena. Also, unplanned blockages occurred spontaneously in several tests. These results have been analyzed and some anecdotal observations are provided in this section.

Figure 5.6 presents video frames from a test where an unexpected severe hydrate blockage of the injector assembly occurred at start-up. The test, conducted at 5.4 MPa, began with low flow rates through a 10 mm sharp edge orifice (C10) in the varicose breakup regime. About two minutes after initiating the flow of CO_2, hydrates formed inside the injector. At that point, the CO_2 temperature was 11.0°C and ambient water temperature was 5.76°C. Hydrate continued to grow on the top of the orifice (Figure 5.8a). When CO_2 flow rate was increased to expel the blockage, liquid CO_2 initially jetted from fissures in the hydrate mass (Figure 5.8b). Total blockage then occurred. Depressurizing the DOS from 5.4 MPa to about 2.7 MPa failed to expel the hydrate blockage inside the orifice. Figures 5.8c and 5.8d show pieces of hydrate debris that were slowly ejected from the nozzle during depressurizing.

In a subsequent test using the stainless steel 10 mm sharp edge orifice (C10) a week later, hydrate blockage occurred again. The CO_2 flow rate, 1.18 kg/min, was higher, corresponding to a jet velocity of about 0.27 m/s. Water temperature was 8.89°C and CO_2 temperature was 3.5°C. Pressure was 5.2 MPa. These conditions fall within the hydrate stability regime. A hydrate blockage of the orifice formed about one minute after flow was initiated. This time, instead of depressurizing, the water inside the DOS was warmed using a heat exchanger. It took about 90 minutes to heat the water to 10.5 °C and expel all the hydrate. In tests conducted using the same

10mm sharp edge orifice where pressure and temperatures were even slightly outside the hydrate stability regime, no blockage occurred.

A small number of experiments were conducted with the objective of examining hydrate fouling of internal passages. Figure 5.9 shows some sample video images of CO_2 flow though a transparent tube nozzle. The clear acrylic tube had an inside diameter of 0.95 cm (3/8 inch). Water at 3^{o}C and 5.6 MPa. was allowed to fill the tube, then cold liquid CO_2 was slowly injected. Conditions fell within the hydrate stability regime. Solid hydrates that formed were easily fractured and expelled when the flow rate was increased. This may be due to the adhesion of the hydrate to the plastic surface. Hirai *et al.* suggest that metal surfaces are more prone to hydrate blockages than plastic and other similar materials.

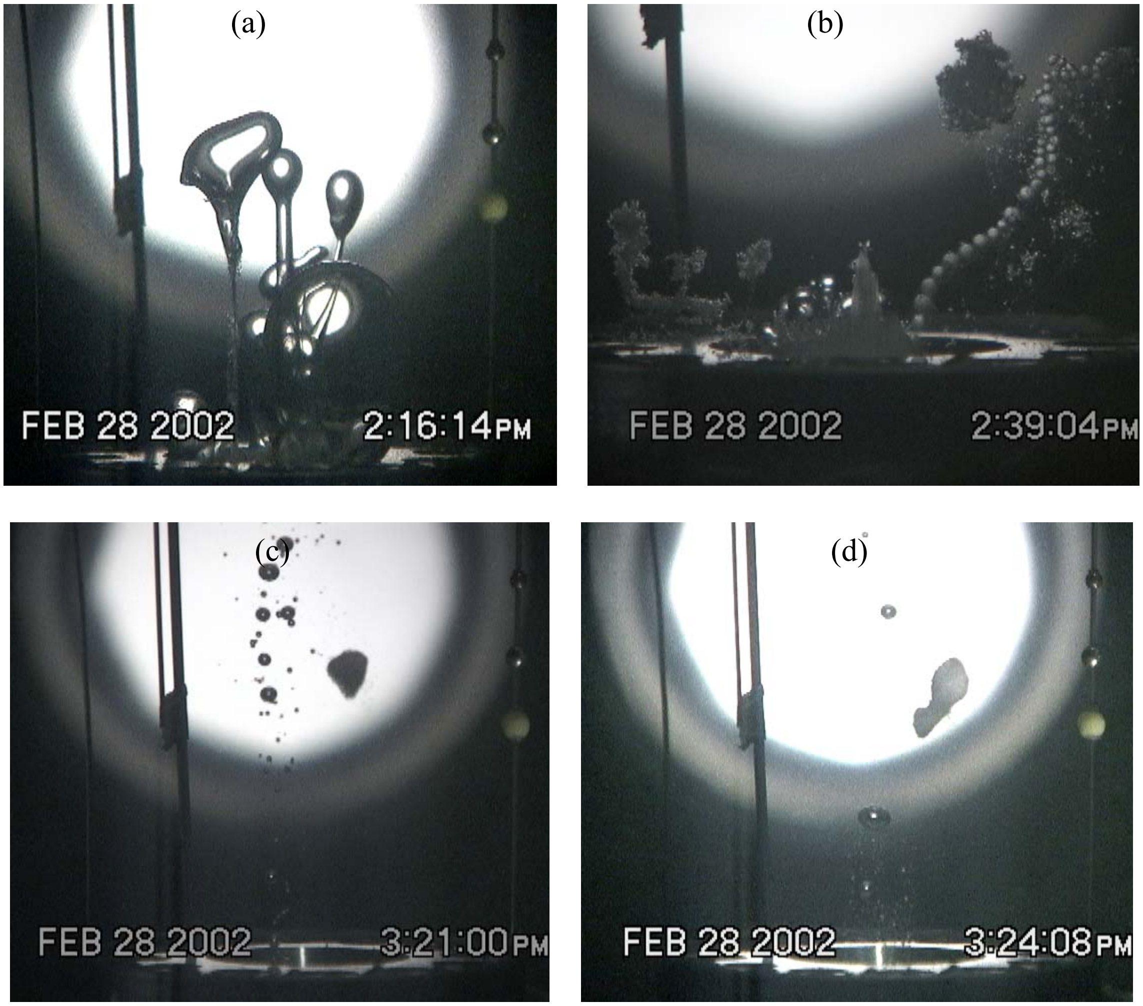

Figure 5.8 Hydrate blockage in the 10 mm sharp edge orifice (C10) for low flow rate CO_2 injection into tap water. (a) Hydrate blockage inside and on the top of the orifice. (b) Restarting at higher flow rate to expel hydrate. (c & d) Pieces of hydrate debris ejected from the inside of the nozzle assembly during depressurization.

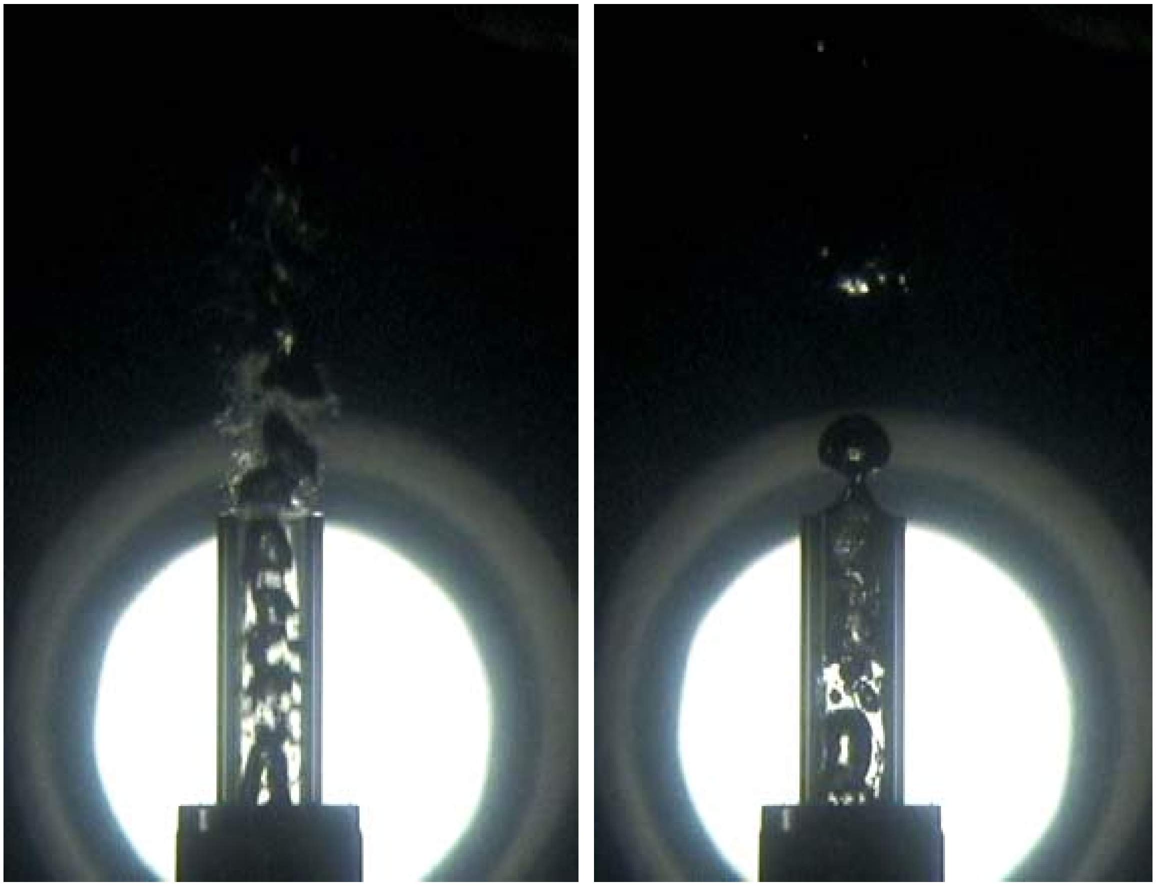

Figure 5.9 Liquid CO_2 and tap water flow through a clear nozzle used to investigate hydrate blockage; pressure = 56 bar; water temperature = 3°C.

5.4 CO_2 Droplet Aggregation

CO_2 droplets covered with hydrate films tend to aggregate (but do not coalesce) once they contact each other following breakup. The video data suggested that aggregated droplets appear to have an enhanced capacity to attract additional droplets than single droplets. To a certain extent, this may simply reflect the larger surface area for contact and "collection" of additional droplets. Eventually, hundreds of droplets may attach to form a large aggregated cluster ball. Figure 5.10 show an example of CO_2 droplet aggregation observed for tests performed under hydrate forming conditions. CO_2 flow rate corresponds to filament breakup regime 3. Here, the droplet density is low. The probability of aggregation of two moving droplets is, therefore, also low. Aggregation in this test occurred when a droplet attached to the steel line of size reference beads near the orifice (Figure 5.10a). This provided a stationary target that subsequent droplets could contact. As time went by, more and more droplets became attached (Figure 5.10b and 5.10c). As flow rate was increased, the droplet cluster became unstable due to the dynamic reaction with the jet. Finally it took off from the steel line (Figure 5.10 d). Figure 5.11 shows huge droplet clusters observed from the 2nd level of DOS viewports located about 70 cm above the orifice. Again, the clusters from when droplets attached to the wires and form stationary collection points.

At higher CO_2 jet velocities in breakup regimes 4 and 5, droplet number density (i.e., droplets per unit volume) is increased significantly. This increases the probability of droplet-droplet contact, especially near the injection orifice where droplet velocities and number densities are of the highest. Numerous droplet aggregation clusters were observed with the tube orifice (Figure 5.12a and 5.12b) at 61 and 52 bar.

CO_2 droplet agglomeration has also been observed in the deep ocean *in situ* by Brewer *et al.* (2000) and in other laboratory studies, (Yamane *et al.,* 2001). Agglomerated droplet cluster may have unusual hydrodynamics and will dissolve more slowly that single droplets. This will influence the effectiveness and environmental impacts of the dissolution method of CO_2 sequestration. The critical factor to avoid droplet agglomeration appears to by reducing droplet concentrations, possibly by careful selection of the jet break up regime and be providing adequate separation between CO_2 injectors if a multiple nozzle array is employed.

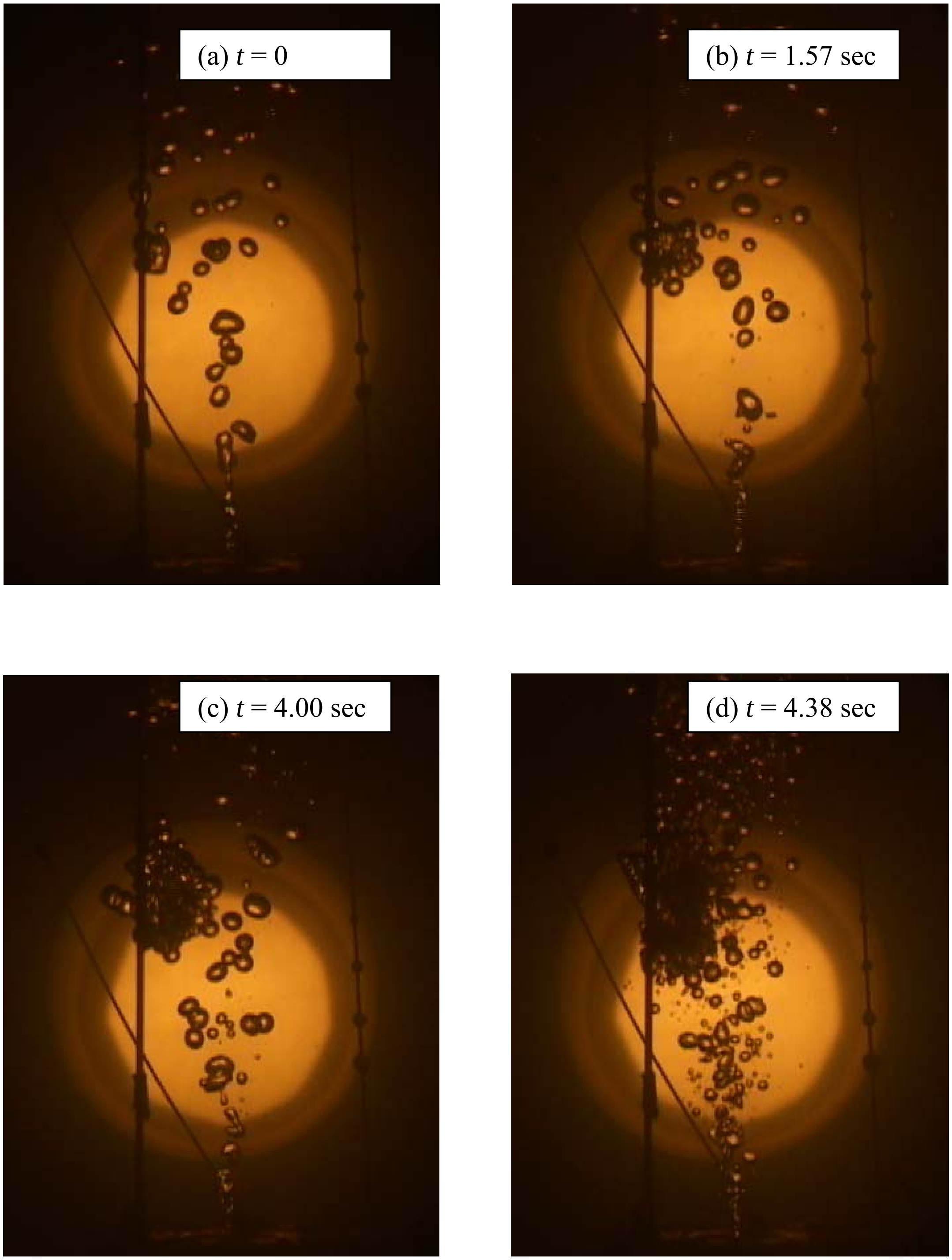

Figure 5.10 CO_2 droplet aggregation. Liquid CO_2 flow rate increases from (a) 0.113 kg/min to (b) and (c) 0.136 kg/min. Flowrate in (d) is 0 .191 kg/min (d). The CO_2 droplet cluster separated from the wire 1 second after frame (d).

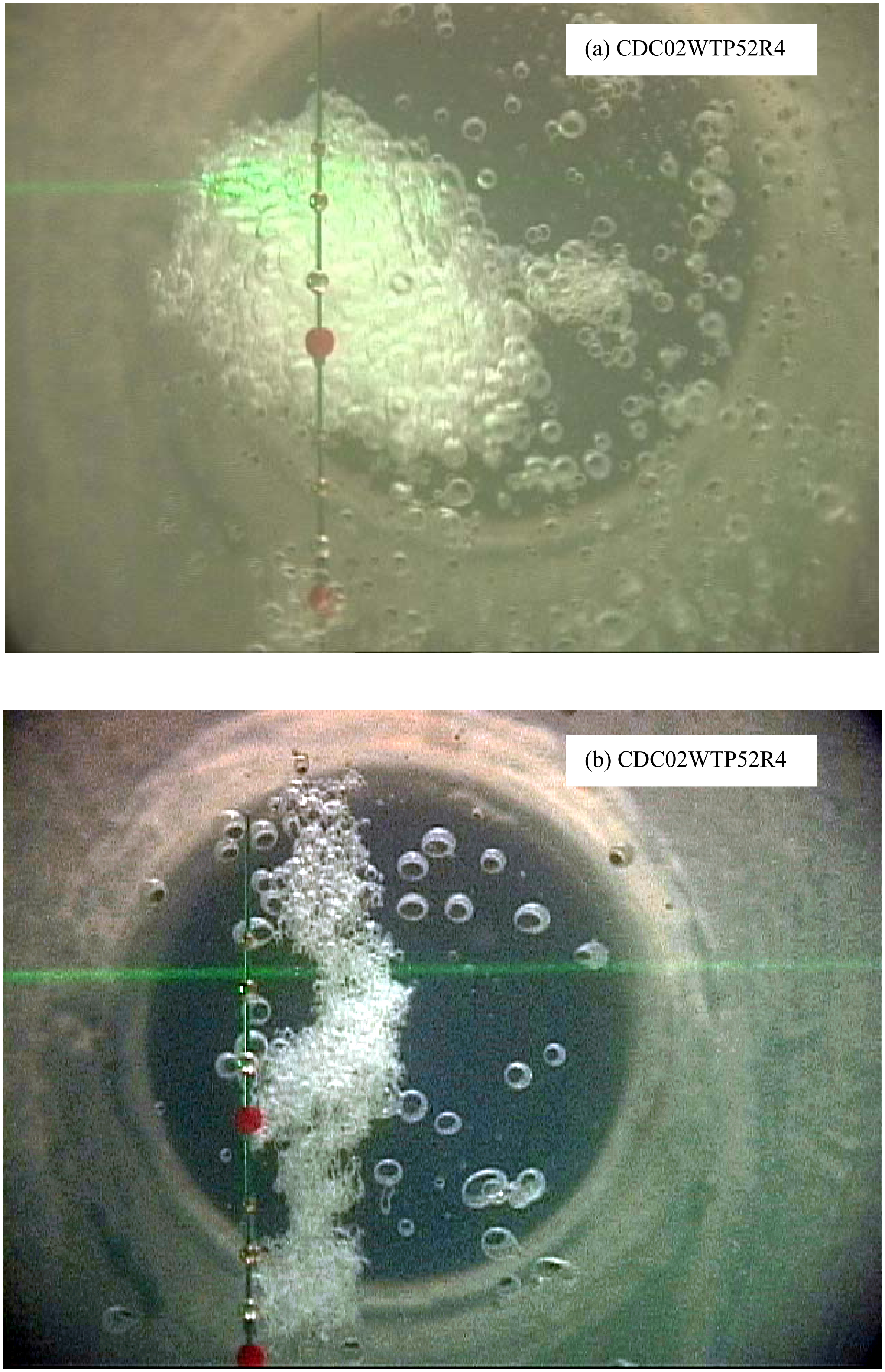

Figure 5.11 Single droplet clusters observed 70 cm above 2mm sharp edge orifice (C02).

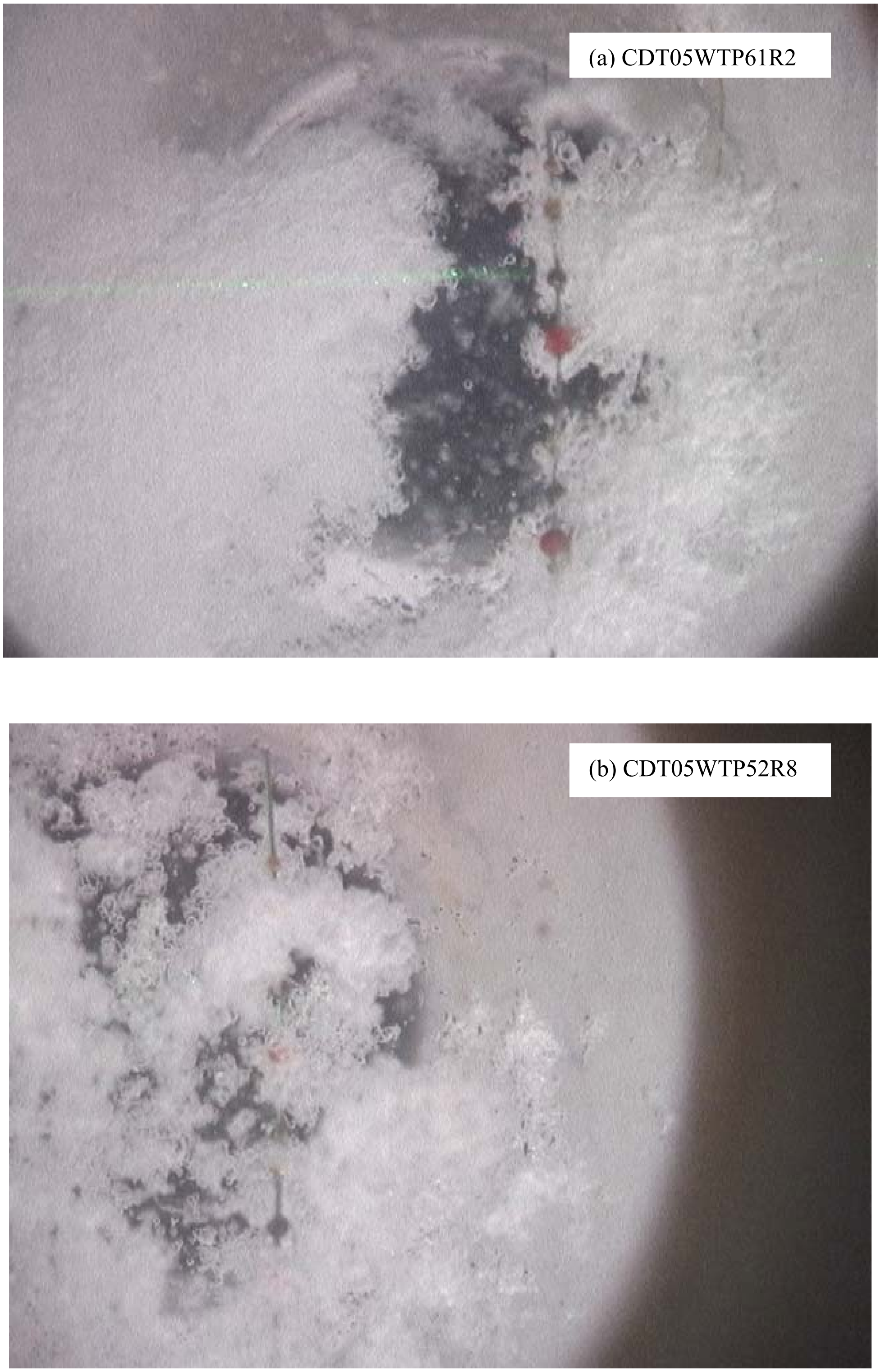

Figure 5.12 CO_2 droplet aggregation observed at (a) Q =2.67 kg/min; T_{co_2}=-3.25°C; T_w=8.13°C, P=61 bar and (b) Q=2.65 kg/min; T_{co_2}=-2.18°C; T_w=9.45°C, P=52 bar.

5.5 Some Hydrate Photos

During the CO_2 injection experiments, we observed many interesting hydrate geometries.b This section provides some photos of those hydrates.

In Figure 5.13 a CO_2 droplet covered with hydrate film formed on the tip of the 2 mm tube orifice when the flow was shut off and CO_2 left in the orifice slowly oozed out. When the flow was suddenly restarted, the jet burst though the top of the CO_2 hydrate film.

CO_2 hydrate with grape-like shapes formed at low flow rates as shown in Figures 5.14 and 5.15. The hydrate film was very thin and elastic. Figure 5.16 is a photo of a tube hydrate.5 The grape and tube types of hydrates were also observed by Aya & Yamane (1992).

CO_2 hydrates that appeared almost fibrous, like a wad of cotton candy, formed when liquid CO_2 flowed around a solid surface placed above the orifice (Figure 5.17). CO_2 temperature = -6.74 °C; water temperature = 10.10°C; CO_2 flow rate = 5.45 kg/min.

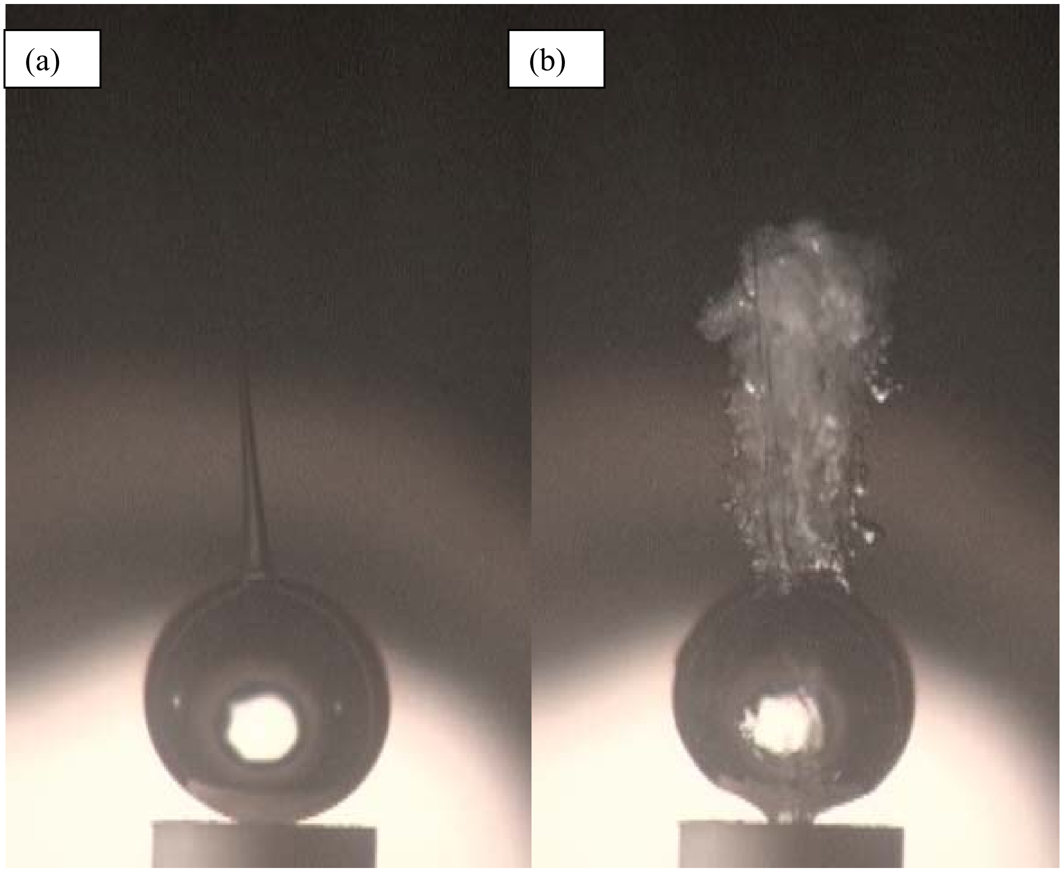

Figure 5.13 (a) CO_2 droplet covered with hydrate film on the tip of the 2 mm tube orifice. (b) When CO_2 flow was restarted, the jet penetrated the top of the CO_2 hydrate film.

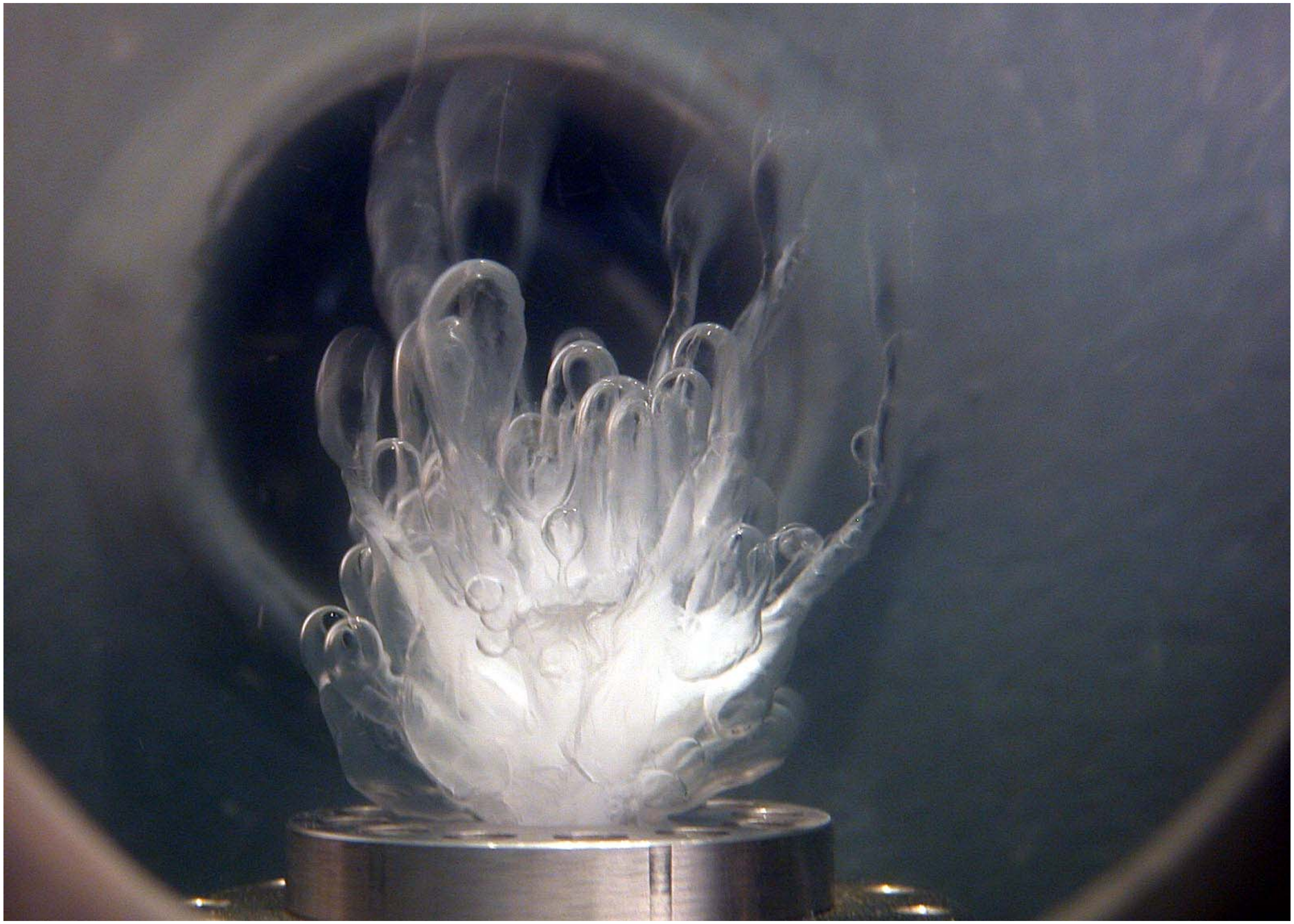

Figure 5.14 Grape type hydrate on the top of the 2 mm sharp edge orifice (C02).

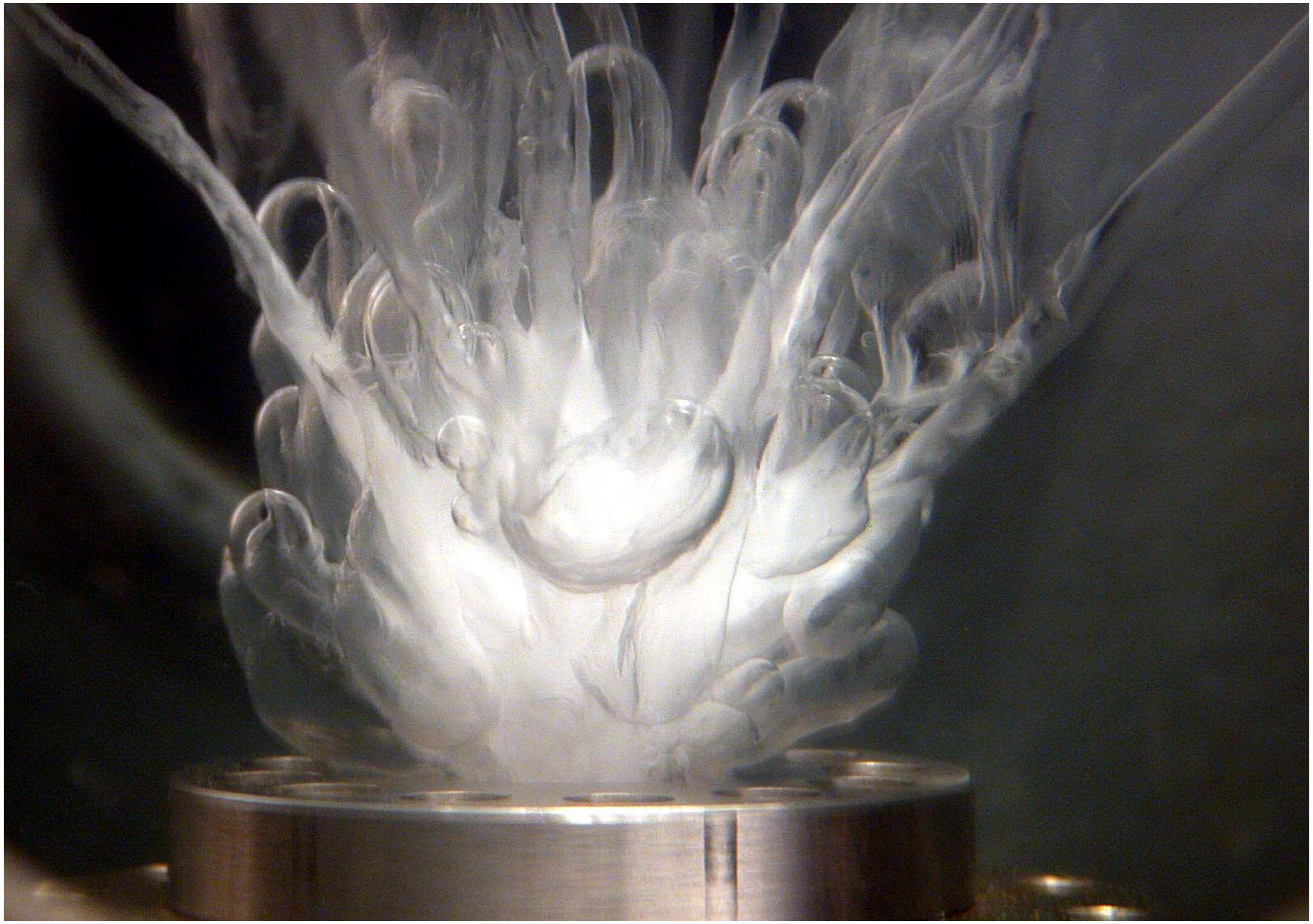

Figure 5.15 Close-up of Grape type hydrate on the top of the 2 mm sharp edge orifice (C02).

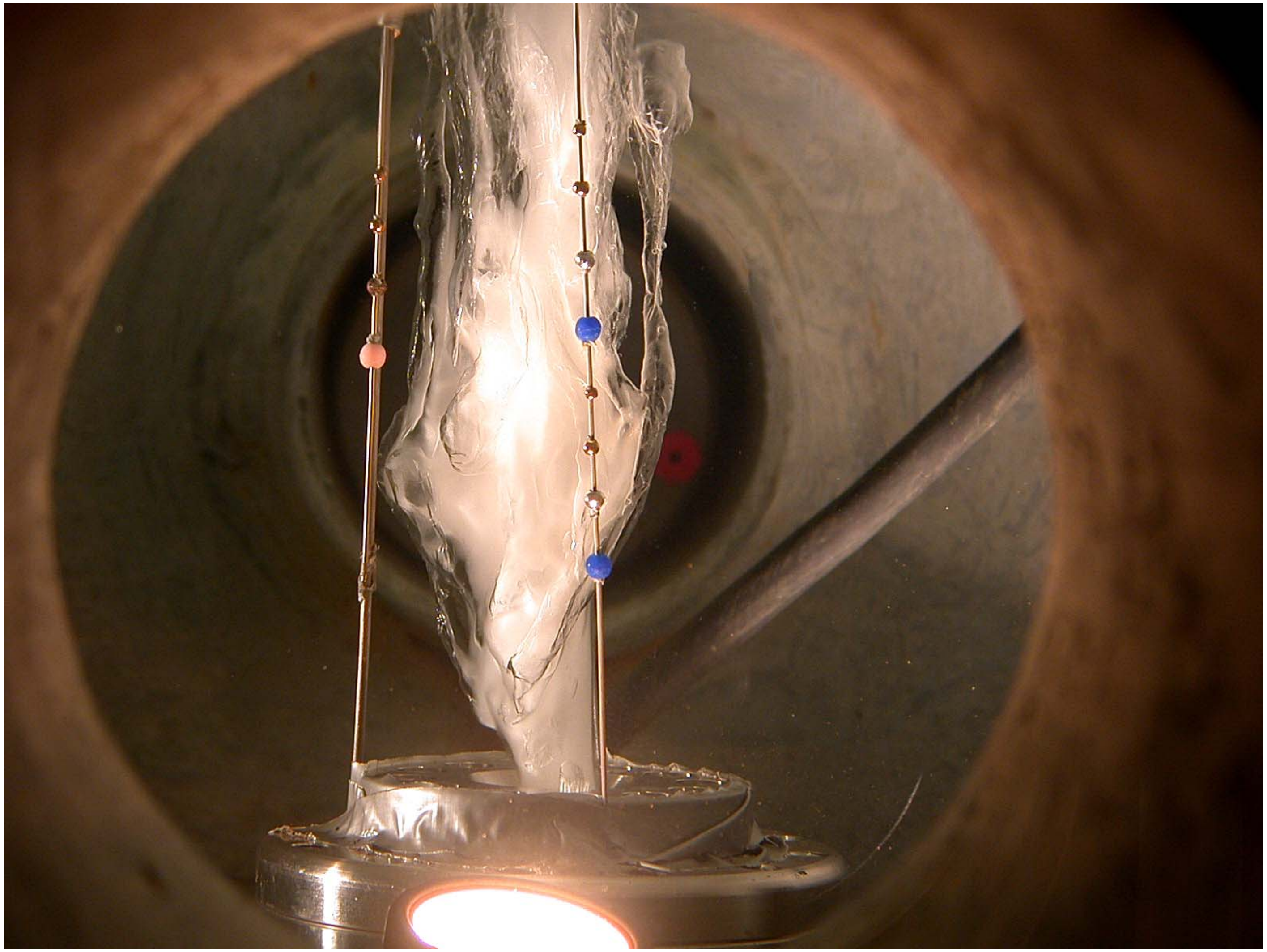

Figure 5.16 Hydrate tube on the top of the 10 mm sharp edge orifice (C10).

Figure 5.17 Cotton type of CO_2 hydrate observed when liquid CO_2 flows around a solid surface

.

5.6 Hydrate Results Summary

Figure 5.18 summarizes the types of CO_2 hydrates observed during liquid CO_2 injection tests corresponding to the different instability regimes. The tests employed a variety of orifice diameters, orifice shapes, water temperatures, liquid CO_2 temperatures, and pressures. The orifice diameter and shape, as well as the pressure are indicated by the alphanumeric code on the right-hand axis as explained in section 3.3.2.

Thin film hydrate tubes are likely to form on the jet surface at low flow rates for most test configurations (i.e., orifice sizes and shapes, and fluid temperatures and pressures) in the varicose break up regime. The characteristic time for instability growth is expected to be long relative to the hydrate formation time in this regime. Surprisingly, hydrate tubes were not clearly evident in the transitional breakup regimes, but thick hydrate tubes did form for some cases (with sub-zero CO_2 temperatures) in the atomization regime. The vertical growth rate of the thick hydrate tube appears to scale with the CO_2 flow rate.

Pre-breakup hydrate formation appears to affect the size distribution of the droplet phase primarily by changing the effective geometry of the jet. When a hydrate tube forms, the interface between the CO_2 and water begins at the end of the tube, which may have a different size and shape opening than the original orifice. Furthermore, flow through the tube will alter the jet inlet velocity distribution, producing more time for boundary layer growth. In the case of thick tubes, hydrate branches will divert some of the CO_2 out of the main jet flow and could produce larger droplets.

As expected, the experimental results suggest that CO_2 droplet concentration is a critical factor that influences agglomeration. High flow rates corresponding to transitional or atomization breakup generate large numbers of droplet in close proximity near the orifice. This enhances the probability of contact and agglomeration. Aggregate droplet clusters were not observed frequently in the varicose or transitional breakup regimes where droplet concentration is relatively low. Droplets aggregated readily on contact, but the hydrate films on their surfaces prevented coalescence.

Severe hydrate blockage occurred in some tests. There was some evidence that support the proposal that certain materials (e.g., steels) are more prone to blockage since hydrate adheres well to them. Tests performed with plastic nozzles resulted in hydrate blockages that were relatively easy to expel.

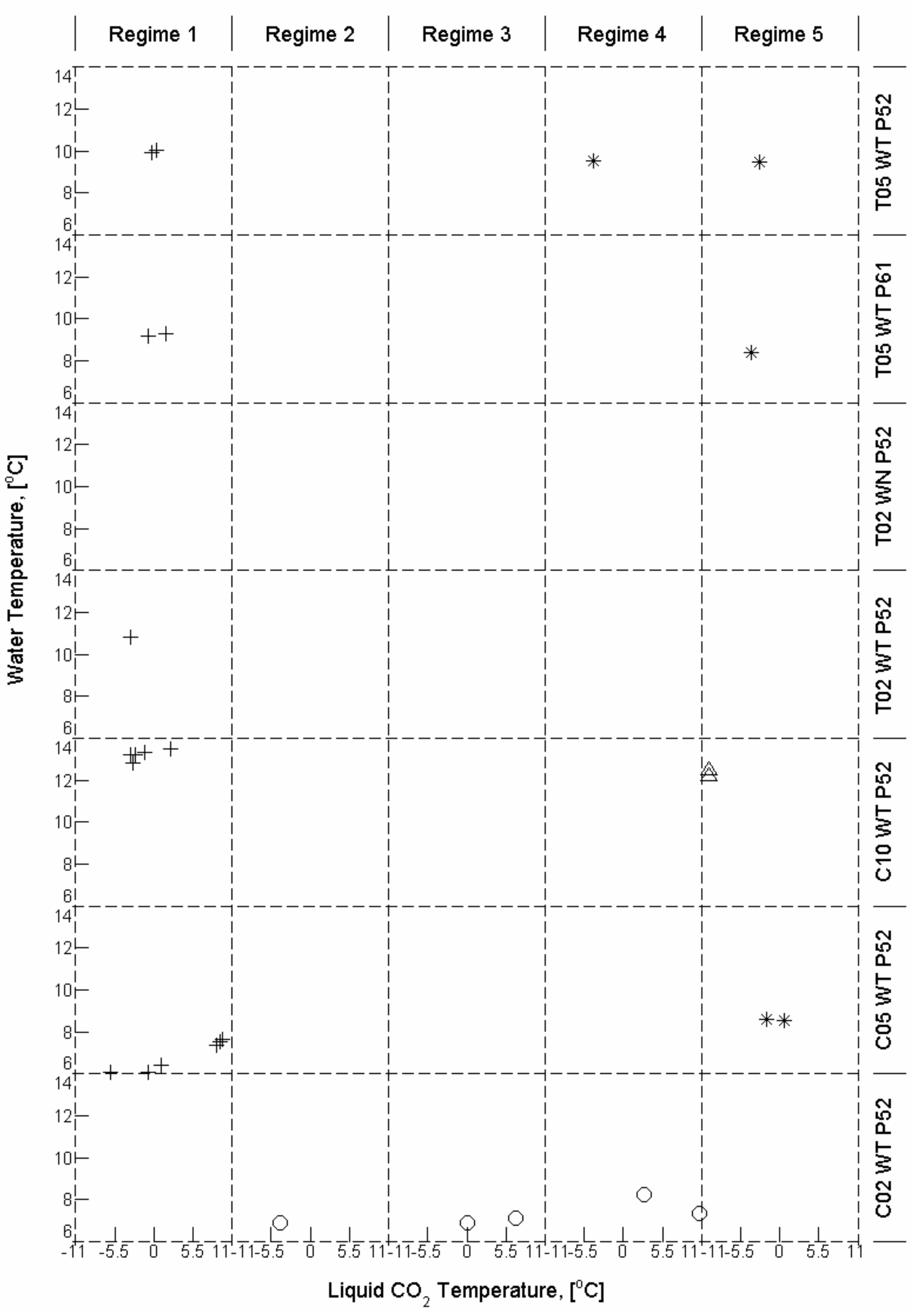

Figure 5.18 Summary of CO_2 hydrates observed in the different breakup regimes. +, thin film hydrate tube. Δ, thick hydrate tube. o, single or several droplet aggregations. *, massive CO_2 droplet aggregations.

6 SUMMARY AND CONCLUSIONS

Laboratory experiments were conducted to identify the mechanisms and characteristics of liquid-liquid jet breakup into droplets under conditions relevant to CO_2 ocean disposal. Jet fluids included liquid CO_2 and silicone fluid, which served as an easily-handled analog to CO_2. For the sake of completeness, we have also included information in this report on other tests conducted with high viscosity oils for an unrelated investigation of deep oil spills (Masutani & Adams, 2000). Including the oils, viscosities of the jet fluids ranged over more than three orders of magnitudes. Emphasis was placed on the largely unstudied class of transitional and turbulent jets, and measurements were conducted at different jet velocities and with various size jet discharge orifices.

The primary objectives of this study were:

- Identify the mechanisms and characteristics of liquid-liquid jet breakup into droplets under conditions relevant to CO_2 ocean disposal; provide data on breakup regimes similar to Reitz and Bracco (1986) that can be applied to the design of injection systems (i.e., injector orifice diameters and flow rates).

- Obtain data on CO_2 droplet size spectra over the entire range of jet instabilities for use with current plume models to estimate dispersion and dissolution of the discharged CO_2.

- Investigate CO_2 hydrate formation under deep ocean conditions to assess flow assurance threats and to understand the influence of this solid phase on droplet formation and dissolution.

The major results and conclusions of this study are summarized below:

1. Five instability regimes were identified by a comprehensive review of the digital video records of the 294 test runs. The five regimes which occur in sequence as liquid-liquid jet disintegration progresses from laminar instability to turbulent atomization are: (1) varicose breakup, where Rayleigh instability dominates and a symmetric surface wave forms and grows, eventually pinching off the jet; (2) sinuous wave breakup, where an asymmetric instability emerges that causes the jet to wave sinuously and generate a polydispersion of droplets; (3) filament core breakup, where the surface of the jet becomes unstable to short wavelength disturbances and disintegrates close to the orifice into fine droplets, while the core of the jet persists as a continuum fluid filament that breaks up further downstream into large droplets; (4) wave atomization, where the breakup location of the jet core filament moves closer to the orifice and the fraction of fine droplets increases; and (5) full atomization.

2. A linear regression to the data yielded relationships for the boundaries between the five instability regimes in dimensionless Ohnesorge Number, *Oh*, and jet Reynolds Number, *Re*, space. The relationships are:

   Boundary 1 between instability regions **1** and **2**:

   $$Oh = 4.9196 \ Re^{-1.0459}$$

   Boundary 2 between instability regions **2** and **3**:

   $$Oh = 9.5979 \ Re^{-1.0255}$$

   Boundary 3 between instability regions **3** and **4**:

   $$Oh = 15.4108 \ Re^{-0.9989}$$

   Boundary 4 between instability regions **4** and **5**:

   $$Oh = 24.9548 \ Re^{-1.0027}$$

3. The exponent for *Re* in the relationships for the instability regime boundaries are all very close to –1. Referring to the definitions of *Re* and *Oh*, this means that the transition between regimes is independent of jet viscosity, and the relationships for the boundaries can be rewritten as *We* ~ constant, where *We* is the Weber number. The critical transitional Weber numbers are the square of the coefficient of *Re* in the relationships for the boundaries, i.e.,

   Boundary 1 between instability regions **1** and **2**:

   $$We \sim 24$$

   Boundary 2 between instability regions **2** and **3**:

   $$We \sim 92$$

   Boundary 3 between instability regions **3** and **4**:

   $$We \sim 237$$

   Boundary 4 between instability regions **4** and **5**:

   $$We \sim 623$$

4. A method was developed to obtain a complete, composite droplet size spectra by combining size data from the PDPA and image analysis. The PDPA was not able to measure droplets larger than about 4 mm. The digital video image analysis could not measure droplets smaller than about 3 mm. The method exploits the overlap between the

two incomplete size spectra and can be applied to similar situations involving different particle size diagnostics.

5. Droplet size spectra was measured for liquid-liquid jet breakup over the full range of instabilities from regime 1 through regime 5. Characteristic average diameters and other statistics were calculated from these spectra. Over the range of conditions examined in this study, jet velocity, orifice size and geometry, and jet fluid viscosity affected droplet size. There appeared to be limited or no difference in spectra obtained for injection into tap water and sea water or for liquid CO_2 tests conducted at 52 and 62 bar.

6. Characteristic diameters decrease steadily with increasing jet velocity (and increasing *We*) in instability regimes 1 through 4, attaining an asymptotic value in regime 5. Orifice diameter appears to influence average droplet size at low *We* in regimes 1 and 2. This effect diminishes as regime 3 is approached and essentially disappears in regimes 4 and 5; the characteristic droplet diameters appeared to be the same for 2 mm, 5 mm, and 10 mm orifices, at the same value of *We*, in these regimes. This may reflect the lack of sensitivity to the transverse length scale (i.e., jet or orifice diameter) of higher order surface instabilities that have been postulated to generate small droplets. Orifice geometry (sharp edge or tube) did not seem to have a significant effect for the very low viscosity liquid CO_2, but did impact droplet size for higher viscosity jet fluids. Larger droplets and a more uniform distribution were produced when silicone fluid was injected from the tube nozzle. Finally, at low *We* in regime 1, jet viscosity seemed to have little effect on mean droplet size. In the transitional breakup regimes, droplet diameters appeared to increase slightly with viscosity.

7. For liquid CO_2 injection under deep ocean conditions, a variety of solid hydrates were observed to form, depending mainly on jet velocity, provided that temperatures and pressures were within the hydrate stability regime. At low CO_2 flow rates, in instability regime 1, thin film hydrate tubes are likely to form on the jet surface. Hydrate tubes were not evident in the transitional breakup regimes 3 and 4, but thick hydrate tubes did form for some cases (with sub-zero CO_2 temperatures) in the atomization regime 5. The streamwise growth rate of the thick hydrate tube appears to scale with CO_2 flow rate.

8. Pre-breakup hydrate formation appears to affect the size distribution of the droplet phase primary by changing the effective geometry of the jet. When a hydrate tube forms, the interface between the CO_2 and water begins at the end of the tube, which may have a different size and shape opening than the original orifice. Furthermore, flow through the tube will alter the jet inlet velocity distribution, producing more time for boundary layer growth. In the case of thick tubes, hydrate branches will divert some of the CO_2 out of the main jet flow and could produce larger droplets.

9. CO_2 droplet concentration was determined to be a critical factor which influences agglomeration. High flow rates corresponding to transitional or atomization breakup generate large numbers of droplet in close proximity near the orifice. This enhances the probability of contact and agglomeration. Aggregate droplet clusters were not observed frequently in the varicose or transitional breakup regimes where droplet concentration is

relatively low. Droplets aggregated readily on contact, but the hydrate films on their surfaces prevented coalescence.

10. Severe hydrate blockage occurred in some tests. There was some evidence that support the proposal by other researchers that certain materials (e.g., steels) are more prone to blockage since hydrates adhere well to them. Tests performed with plastic nozzles resulted in hydrate blockages that were relatively easy to expel.

APPENDIX A EXPERIMENTAL UNCERTAINTIES

This Appendix describes the analyses performed to estimate uncertainties in the calculated values of Reynolds, Weber, and Ohnesorge numbers and the droplet size measurements.

A.1 Uncertainty of *Re, Oh* and *We*

By definition, $Re = f(U, D, \rho, \mu)$; $We = f(U, D, \rho, \sigma)$; and $Oh = f(D, \rho, \mu, \sigma)$. Uncertainties in *Re*, *Oh*, *We* therefore reflect the uncertainty in the values of U, D, ρ, μ, and σ used to calculate these parameters.

Examination of the orifices with a microscope suggests that D agrees with the nominal values to within about ±3%. Although the PDPA has the ability to measure velocity, this requires scattering droplets rather than the continuous jet column that exists before breakup. U was therefore determined using data from the inline flowmeters and the cross sectional area, A, of the discharge orifices:

$$U = \frac{Q}{A} = \frac{4Q}{\pi D^2}$$

where Q is the measured volumetric flowrate. The uncertainty in U can be determined from the uncertainties in Q and D.

Flowrate uncertainties in the present experiment arise from two sources: (1) the measurement device and (2) variations in the flowrate during a test (e.g., due to pumping fluctuations; changes in back pressure, etc.). The crude oil and silicone fluid experiments used the same jet fluid delivery system. The CO_2 experiments required a different delivery system to supply the high pressure, liquid CO_2. Flowrate fluctuations during the crude oil and silicone fluid tests were small and the flowmeters employed were frequently calibrated to minimize instrument error. The liquid CO_2 system, however, was subject to larger flowrate fluctuations during individual tests (as a consequence of the single-action, positive displacement pumps that had to be used) and direct calibration of the flowmeters was not possible, although redundant flowmeters were employed in some tests for comparison. Based on a review of the flowmeter characteristics and flowrate data records, it is estimated that the uncertainties in Q for crude oils, liquid CO_2 and silicone fluids are ± 2%, ±7.5% and ± 4.2%, respectively. Taking the uncertainty in D to be ±3%, the corresponding errors in the calculated U are ± 8% (crude oil), ±13.5% (liquid CO_2) and ± 10.2% (silicone fluid).

The magnitude of the uncertainties in the values of the fluid properties, ρ, μ, and σ, used to calculate *Re*, *We*, and *Oh* varied widely for the three types of jet fluid and are discussed separately.

Silicone Fluids. Properties of the two silicone fluids, GE silicone SF96-20 and Dow Corning 200(R) (ν = 0.65 cs) are well documented by the manufacturers. The principal source of uncertainty was the temperature at which these properties were evaluated from the database. Viscosity was much more sensitive to changes in temperature than ρ or μ. In the present experiments, the temperature records indicate that the maximum variation in silicone fluid temperature during a test run was 0.04 °C. This corresponds to only a 0.1% uncertainty in ν.

Crude Oils. An extensive discussion of the uncertainties in estimated crude oil properties for these experiments is provided in Masutani & Adams (2000). Environment Canada analyzed the four crude oils and determined their densities and viscosities. Interfacial tension, σ, however, was not measured was and had to be estimated from surface tension data for similar oils. A mean value of 25.9 dyne/cm was used to calculate *We* and *Oh* in this study. Based on the range of values reported in the database (21.6 to 30.2 dyne/cm), the uncertainty in σ is believed to be approximately ±17%. This potential error is dwarfed by the uncertainties in dynamic viscosity, μ, related to possible changes in oil composition due to devolatilization. Relationships provided by Environment Canada predict that between 12% (Platform Gail) and 19% (Neptune SPAR) of the oil mass could evaporate in 1 hour at the air temperatures at which the experiments were conducted. Anticipating this problem, oil was pumped from the sealed storage barrels and the oil injection system reservoir was filled and covered to minimize evaporation. In the worst case, evaporation would yield a modest increase in density of around 4%. Dynamic viscosity, however, could change by a factor of 14 for Platform Gail and 4 to7 for the other three oils (Masutani & Adams, 2000).

ρ and μ were estimated by extrapolation from the Environment Canada property data reported at 15°C and 25°C. Differences between temperatures measured with the thermistor in the oil supply line before it enters the water tank and actual temperatures of the oil exiting the orifice also contribute to the experimental uncertainty. A detailed heat transfer analysis was conducted to identify the maximum oil temperature change that could occur between the measurement point and the orifice due to heat transfer to the cooler water in the tank. This analysis predicted a difference of less than 3°C for the worst case of extremely low oil flow rate. The corresponding uncertainties in ρ and μ are insignificant relative to the uncertainties associated with devolatilization.

Liquid CO_2. There is an extensive and accurate database on the properties of pure CO_2 as functions of pressure and temperature. This database was employed to estimate ρ and μ. The effect of contaminants in the liquid CO_2 on jet fluid properties was neglected, since vendor analysis indicated that the level of impurity was very low. CO_2 temperature variations during a test was the primary source of uncertainty in the values of ρ, μ, and σ. The –20°C liquid CO_2 extracted from the refrigerated storage tank is pressurized and passed through heat exchangers to warm it before being injected. Particularly at low flow rates, it was difficult to maintain a constant CO_2 temperature. In the worst case (2mm orifice, low flow rate, long test duration), the temperature of the liquid CO_2 rose by 10°C. This corresponds to an decrease in density of around 1.5% and a decrease in kinematic viscosity of around 19% (the actual uncertainties are about half these values, since properties are evaluated at the time mean temperature during the entire duration of the run). These numbers represent the upper limit of uncertainty, since temperature variations were typically much smaller in other tests. From Uchida (2002), the interfacial tension of liquid CO_2 and pure water at $P = 50$ bar is approximately 28 mN/m at $T = 5$

°C (278K) and 38 mN/m at $T = 15$ °C (288K). For a 3 wt% NaCl solution, interfacial tension increased by about 10% from these values. A value of 30 mN/m was used to calculate *We* and *Oh* for the present liquid CO_2 injection tests. The uncertainty in σ is estimated to be ± 26 %.

Following conventional methods (e.g., Allisy, 1980), the uncertainties in *We*, *Re*, and *Oh* for the three types of jet fluid were calculated using the estimated uncertainties in properties discussed above. The results are summarized in Table A.1.

Table A.1 Estimated uncertainties of *Re*, *Oh* and *We*

			Uncertainty		
		Units	Crude Oils	CO_2	Silicone Fluids
Orifice Diameter D		%	3	3	3
Jet Flow Rate Q	Accuracy	%	1	0.5	1.2
	Fluctuation	%	1	7	3
	Total	%	2	7.5	4.2
Jet Fluid Temperature T		°C	3	10	0.4
Jet Velocity U		%	8	13.5	10.2
Kinematic Viscosity, ν		%	14	10	0.6
Density ρ		%	4	1	1
Surface Tension σ		%	17	26	1
Re		%	19	20.5	7.8
Oh		%	26	25	3.1
We		%	28	45	13.4

A.2 Droplet Size Uncertainties

Individual measurements of droplet size by means of the PDPA or video image analysis are subject to error. In this section, the magnitude of these errors are estimated.

A.2.1 CO_2 Droplet Circularity Analysis

The theory of operation of the PDPA assumes that the measured particles are spherical. Non-spherical droplets result in errors. In order to quantify these errors, it was necessary to estimate the deviations from sphericity of droplets with sizes that fell within the PDPA measurement range in the present experiments. Toward this end, video data from the CO_2 tests (which generally had good image clarity) were analyzed.

Since the video data provide two dimensional projections of the three dimensional droplets, we assume that there is a direct correlation between sphericity (3-D) and circularity (2D). The circular shape parameter, *C* is defined as

$$C = \frac{a}{b}$$

where *a* and *b* are the longest and shortest segments from the centroid of a droplet to its contour (edge) pixels. The shape parameter of a circle is 1. Departures from circularity (and sphericity) increase with increasing *C*.

In the present work, the spatial resolution of the image analysis technique is about 0.19 mm/pixel. It was decided, therefore, to limit the study of circularity to droplets with diameters larger than 3 mm, which would provide good S/N. The circular shape parameter was determined for 3740 different CO_2 droplets. Figure A.1 plots *C* as a function of droplet diameter. As expected, the shape parameter increases with droplet size. Representative images of CO_2 droplets with different shape parameters are provided in Figure A.2. The number inside the image is the individual droplet identifier (between 1 and 3740). The first number in the paranthesis under each image is the shape parameter *C*; the second number is the calculated droplet diameter in mm. The dots in the droplets are their centroids.

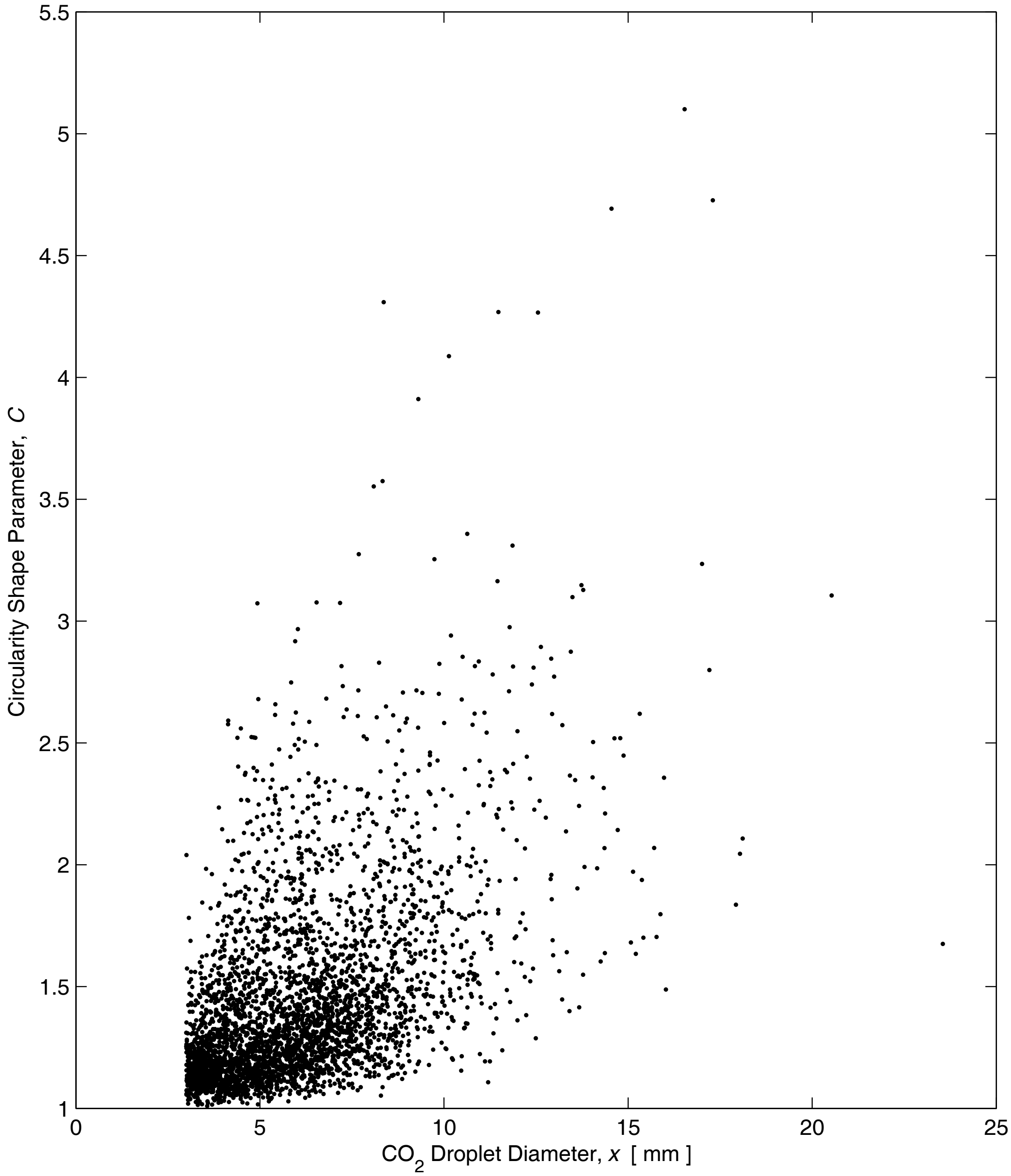

Figure A.1 Circularity shape parameter versus droplet diameter. Data are for 3740 CO_2 droplets measured by image analysis with $x \geq 3$ mm.

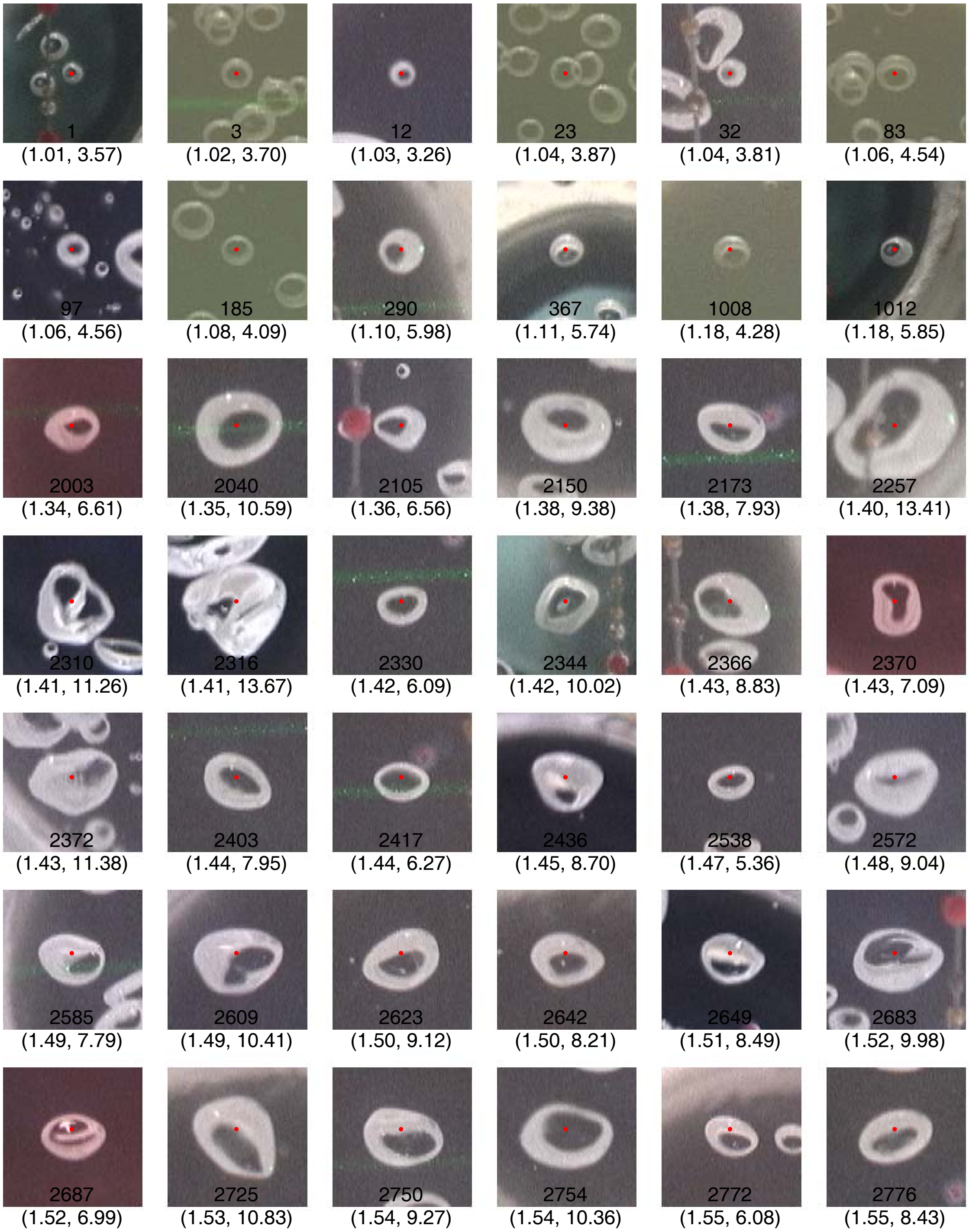
1
(1.01, 3.57)
3
(1.02, 3.70)
12
(1.03, 3.26)
23
(1.04, 3.87)
32
(1.04, 3.81)
83
(1.06, 4.54)
97
(1.06, 4.56)
185
(1.08, 4.09)
290
(1.10, 5.98)
367
(1.11, 5.74)
1008
(1.18, 4.28)
1012
(1.18, 5.85)
2003
(1.34, 6.61)
2040
(1.35, 10.59)
2105
(1.36, 6.56)
2150
(1.38, 9.38)
2173
(1.38, 7.93)
2257
(1.40, 13.41)
2310
(1.41, 11.26)
2316
(1.41, 13.67)
2330
(1.42, 6.09)
2344
(1.42, 10.02)
2366
(1.43, 8.83)
2370
(1.43, 7.09)
2372
(1.43, 11.38)
2403
(1.44, 7.95)
2417
(1.44, 6.27)
2436
(1.45, 8.70)
2538
(1.47, 5.36)
2572
(1.48, 9.04)
2585
(1.49, 7.79)
2609
(1.49, 10.41)
2623
(1.50, 9.12)
2642
(1.50, 8.21)
2649
(1.51, 8.49)
2683
(1.52, 9.98)
2687
(1.52, 6.99)
2725
(1.53, 10.83)
2750
(1.54, 9.27)
2754
(1.54, 10.36)
2772
(1.55, 6.08)
2776
(1.55, 8.43)

(a)

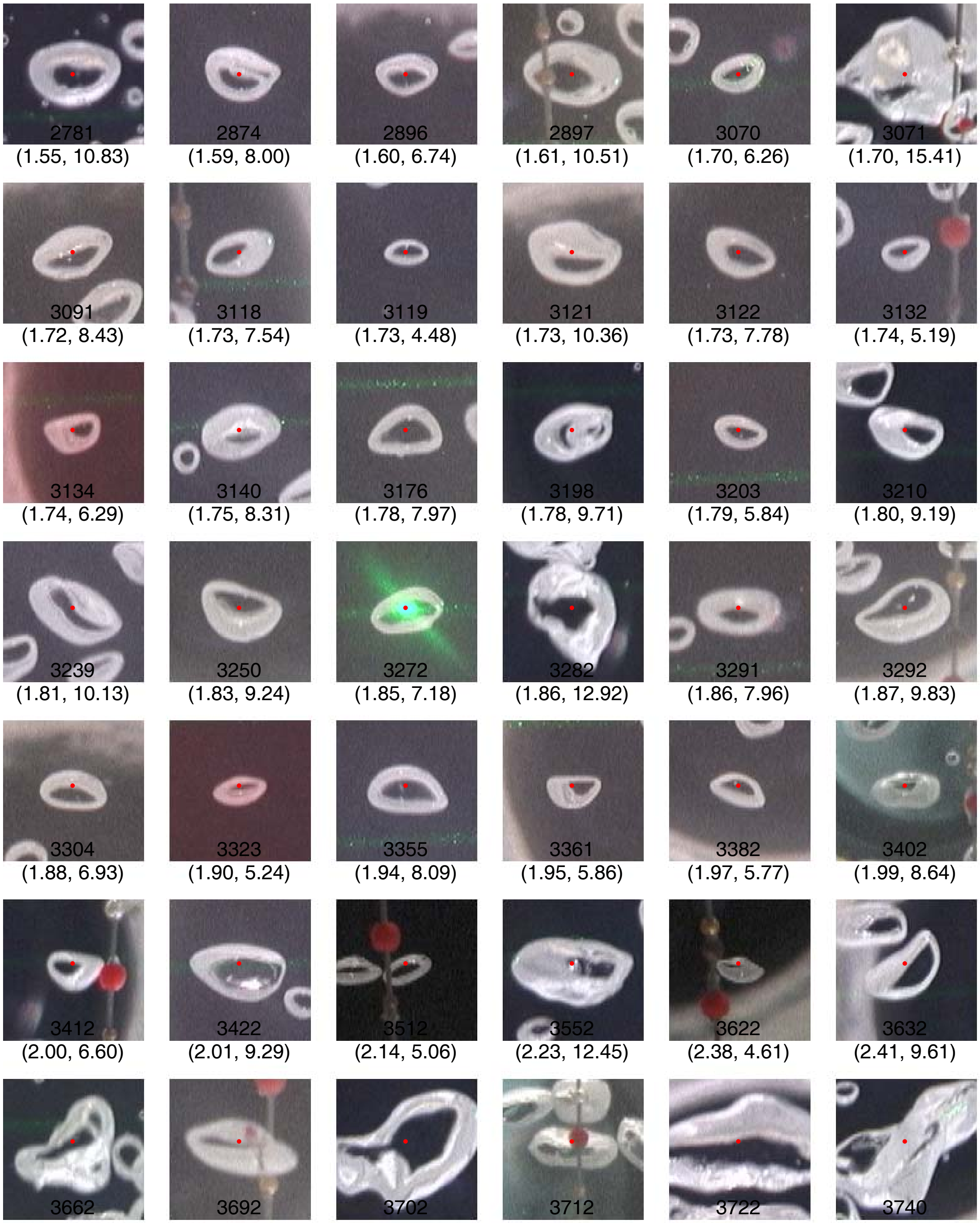

(b)

Figure A.2 Images of CO_2 droplets with different shape parameters. The numbers inside the images are the droplet identifiers. The first number in the parenthesis is the shape parameter C; the second number is the droplet diameter in mm.

A.2.2 PDPA Errors

PDPA bias (i.e., the tendency to detect large droplets of a polydispersion and miss small droplets) precluded application of the instrument to perform measurements of the crude oil. Bias did not appear to be a problem in measurements of the clear silicone fluid and liquid CO_2 (Masutani & Adams, 2000).

The primary source of PDPA error in the present tests is believed to be due to non-spherical droplets. Figure A.3 provides examples of the types of measurement errors that can occur when a non-spherical particle crosses the PDPA optical probe volume.

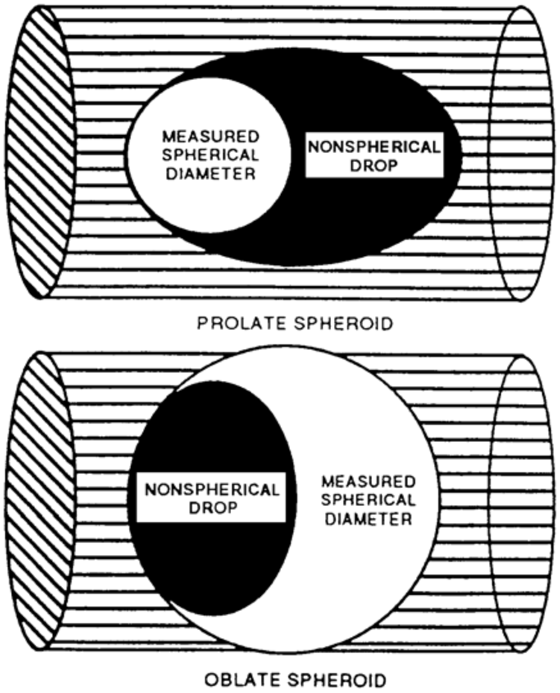

Figure A.3 Examples of the PDPA response to non-spherical droplets (Bachalo, 1994).

As implied in Figure A.3, the Phase Doppler method responds to the radius of curvature of the droplet in the plane of the two incident beams. This idea is depicted further in Figure A.4. The size of an elliptical droplet will be overestimated if its major axis is perpendicular to the PDPA laser fringes and will be underestimated if it is aligned parallel to the fringes. Hence, the measurement error depends on the orientation of the droplet, as well as its shape. It may be argued that if the non-spherical droplets are randomly orientated or oscillating, then the measured average size will adequately represent the equivalent sphere (Bachalo, 1994).

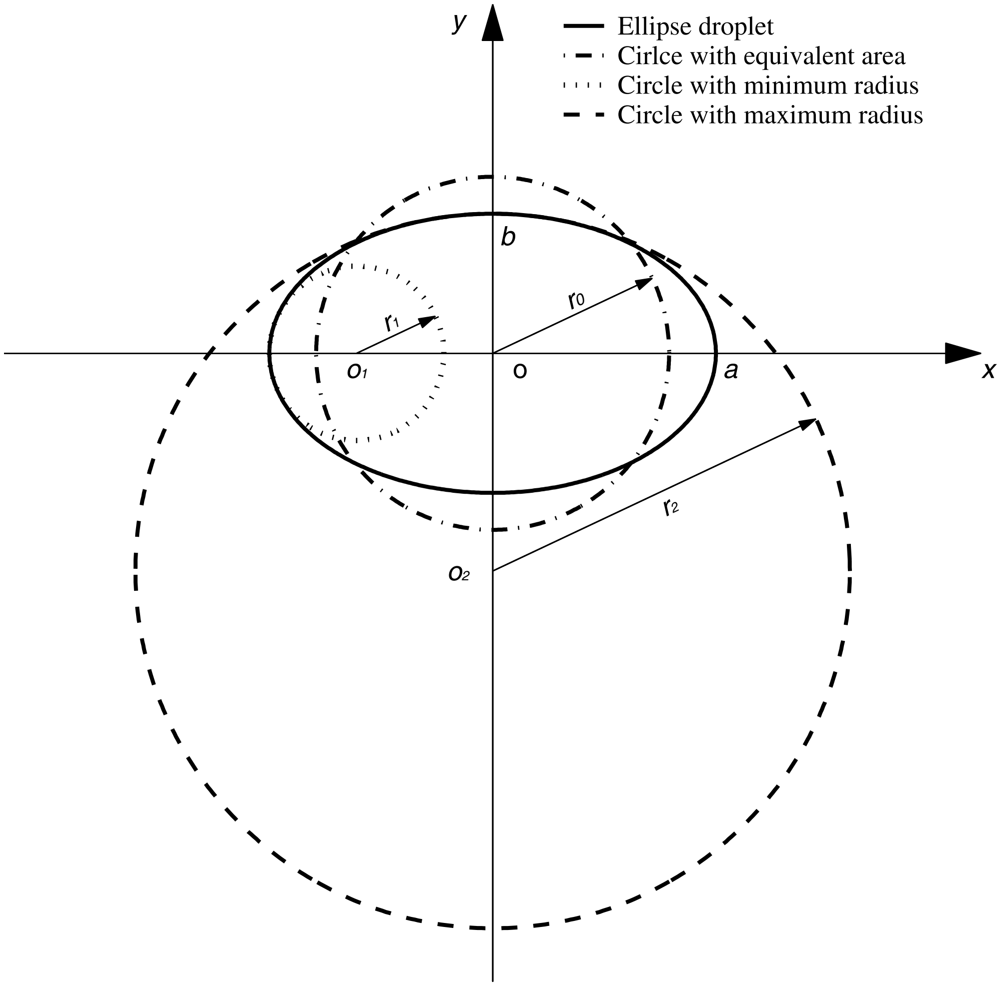

Figure A.4 PDPA measurement uncertainty of an elliptical droplet with a major axis of 2a and a minor axis of 2b depending on whether the PDPA fringes align with x or y. r_0 is the equivalent radius of a circle with the same area as the ellipse (desired result); r_1 and r_2 are the minimum and the maximum radius of curvature of the ellipse and the radii of the droplets erroneously detected by the PDPA.

To estimate the magnitude of the uncertainty associated with non-spherical droplets, we assume elliptical (symmetric) droplets. Adopting the terminology from Figure A.4, the droplets have a major axis of length 2*a* and a minor axis of length 2*b*. The projected area of the droplet is πab. A sphere with the same projected area has a radius:

$$r_0 = \sqrt{ab} \tag{A.1}$$

Assuming that the droplet can be oriented at any angle relative to the laser fringes in the PDPA optical measurement volume, the measured value of *r* can be any value between r_1 and r_1, i.e.,

$$r_1 \leq r \leq r_2$$

where

$$r_1 = b^2 / a; \tag{C.2a}$$

$$r_2 = a^2 / b \tag{C.2b}$$

Using the circularity shape parameter defined in Section A.2.1:

$$C = a/b, \tag{C.3}$$

we obtain

$$a = r_0 C^{1/2}$$

and

$$b = r_0 C^{-1/2}$$

Equations A.2a and A.2b can then be rewritten as

$$r_1 = r_0 C^{-3/2} \tag{C.4a}$$

and

$$r_2 = r_0 C^{3/2} \tag{C.4b}$$

The relative error in the measurement as a function of C is then

$$\varepsilon = \frac{r - r_0}{r_0} = C^{\pm 3/2} - 1 \tag{C.5}$$

Figure A.5 presents ε as a function of the circularity shape parameter *C*. Also included in this figure is a histogram of measured values of *C* for 821 CO_2 droplets with diameters of 3 mm < *x* < 4.08 mm which fall in the PDPA measurement range. This data set is a subset of the ensemble of 3740 droplets that were analyzed in Section A.2.1. In this size range, the mean value of the circularity parameter is 1.23 and the standard deviation is 0.17. For this value of *C*, ε = +36% and –27%. It should be pointed out, however, that, as seen in the histograms provided in Section 4.3, the fraction of droplets with 3 mm < *x* < 4.08mm measured by the PDPA typically is quite small. Furthermore, since the circularity shape parameter decreases for smaller droplets, the relative error calculated above represents an upper bound. If the droplets are indeed randomly oriented, then deviations from sphericity should have a limited effect on the statistical quantities such as characteristic diameters. In the present experiments, however, hydrodynamic forces exerted on large buoyant droplets would tend to flatten them and favor an orientation where the major axis is aligned with the laser fringes, leading to underestimates of droplet size.

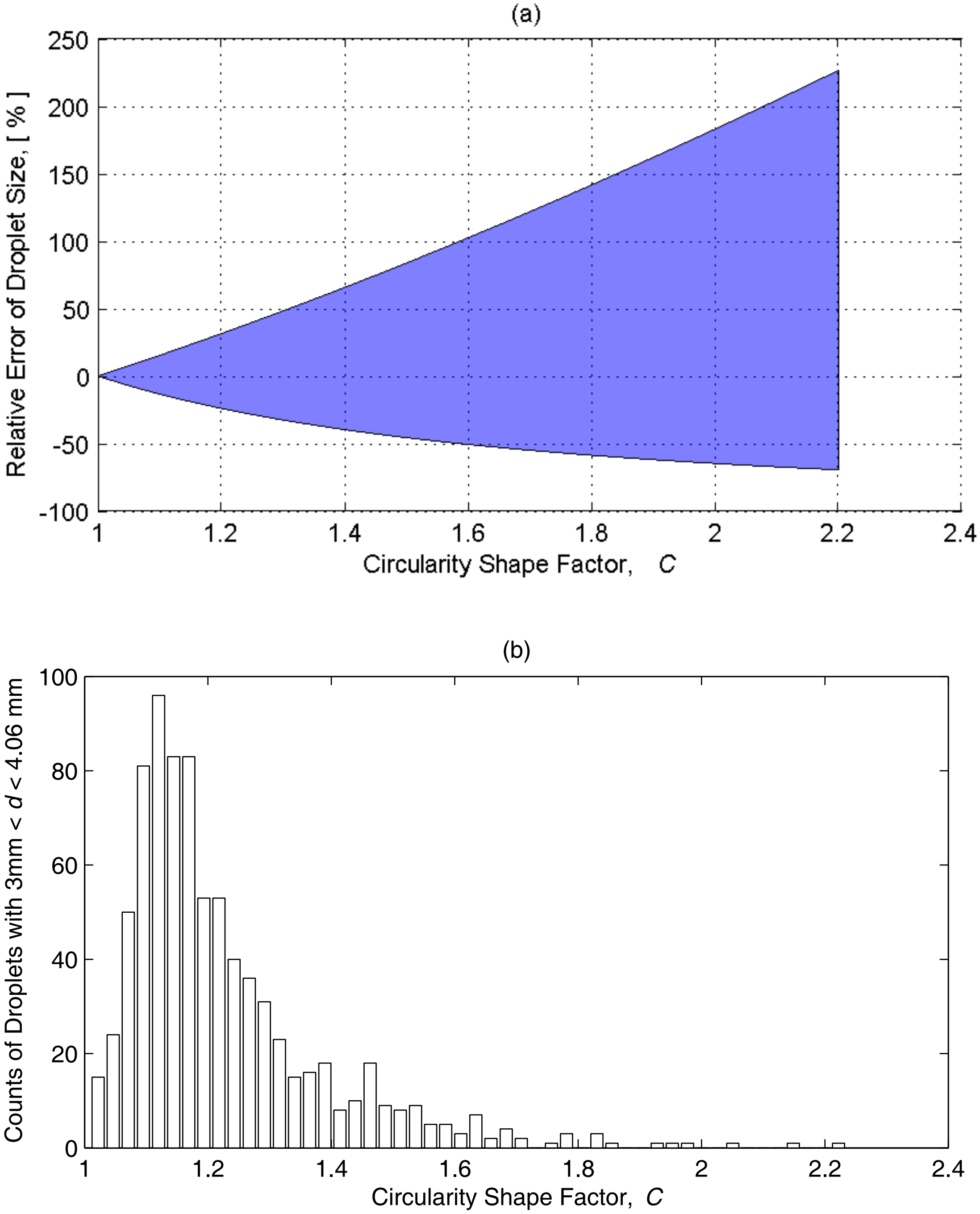

Figure A.5 PDPA measurement uncertainty. (a) Size relative error versus circularity parameterr C. The relative error falls within the darkened band. (b) Histogram of measured shape parameters of 821 CO_2 droplets (3 mm < x < 4.06 mm) that fall within the PDPA measurement range.

A.2.3 Image Analysis Errors

To estimate the uncertainty of the image analysis technique, multiple measurements were performed to determine the size of a reference bead of known diameter. The solid spherical reference bead had a diameter of 3.68 mm. 160 different images of the bead were selected from the digital video records of case CDC10WTP52 (liquid CO_2 injection into tap water from a 10 mm sharp edge orifice at a pressure of 52 bar). Figure A.6 present representative images that were analyzed of the bead during different tests. The dimension of each image is 640 × 480 pixels.

The statistics of the 160 video image analysis measurements are provided in Figure A.7. Figure A.7a is the size histogram of the measured reference bead diameter, which is approximated reasonably well by a normal distribution with mean = 19.92 pixels and standard deviation of 0.60. In Figure A.7b, the relative error of these measurements has a normal distribution with mean = 0 and standard deviation of 0.03. Based on this study, the relative uncertainty of the image analysis technique is estimated to be approximately ± 11% of the measured value of diameter.

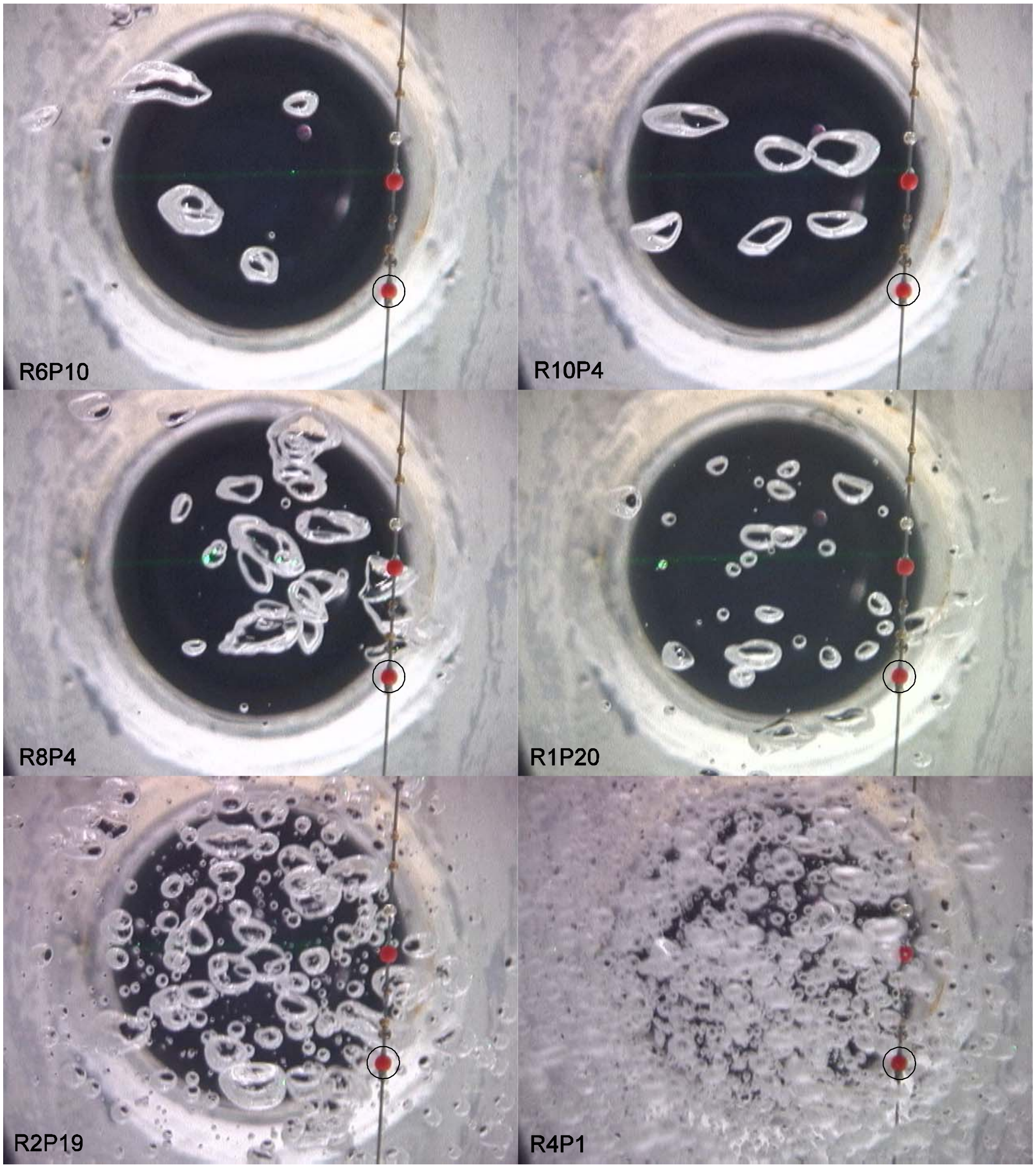

Figure A.6 Video images of the reference bead (circled). Images are for liquid CO_2 injection into tap water through a 10 mm sharp edge orifice (CDC10WTP52). Dimension of each image is 640 × 480 pixels. ”R”+digit is the run number. “P”+digit is the photo number.

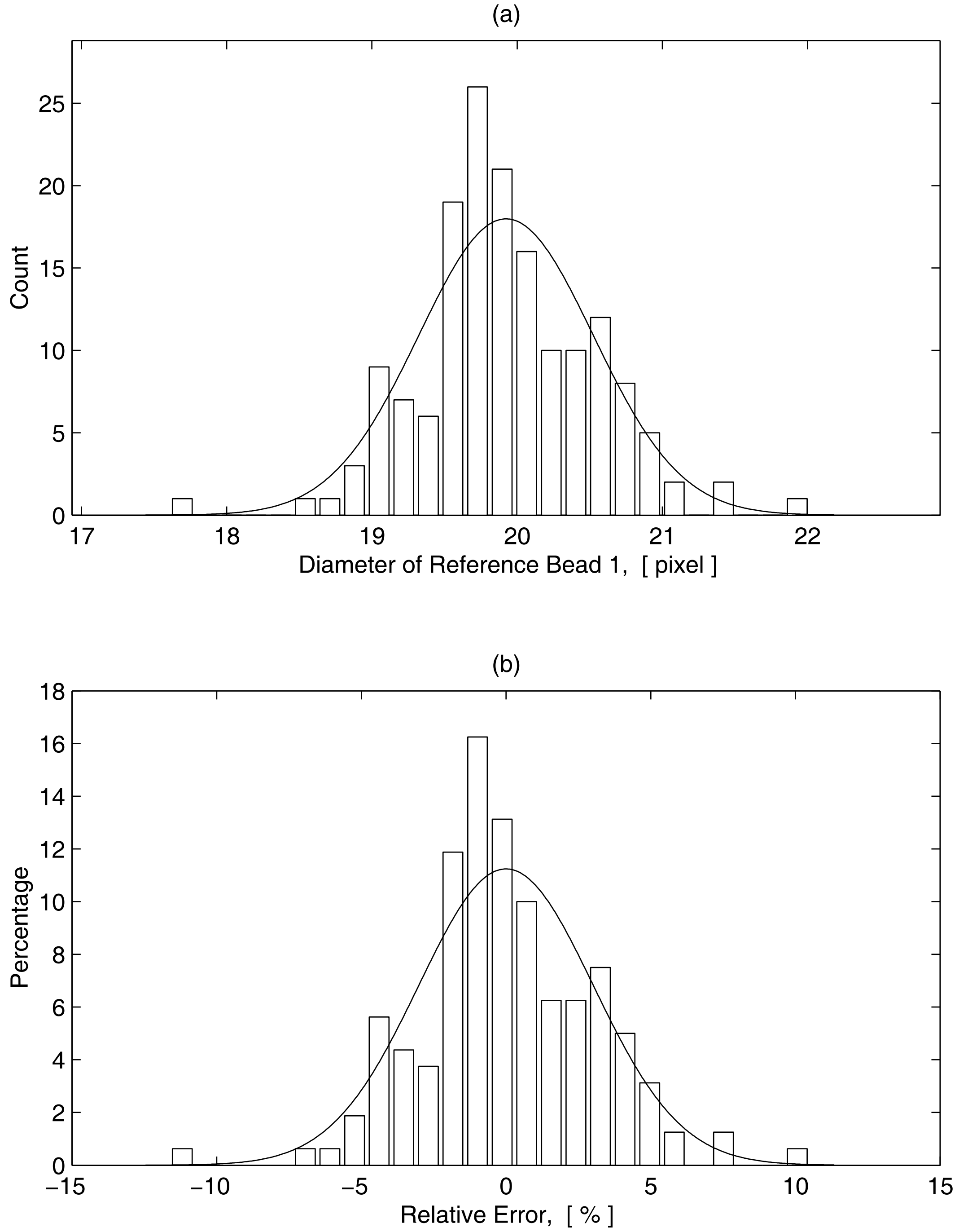

Figure A.7 (a) Size histogram of multiple image analysis measurements of the same reference bead. Solid line is Normal distribution fitted to the histogram with mean of 19.92 pixels and standard deviation of 0.60. (b) Relative error of (a) has a normal distribution with mean of 0 and standard deviation of 0.03.

REFERENCES

Allisy, A. (1980). Some statistical methods used in Metrology. *Proceedings of the International School of Physics "Enrico Fermi," Course LXVIII*, (Milone, A.F. and Giacomo, P., eds.), North-Holland, Amsterdam.

Arai, M. and Amagai, K. (1999). Surface wave transition before breakup on a laminar liquid jet. *In. J. Heat Fluid Flow*, pp. 507-512.

Ashgriz, N. and Mashayekhi, F. (1995). Temporal analysis of capillary jet breakup. *J. Fluid Mech.*, Vol. 291, pp. 163-190.

Auerbach, D. (1996). *Climate change mitigation via ocean disposal of power-plant-generated CO_2: A comprehensive environmental and political analysis*. Master Thesis, Department of Civil and Environmental Engineering, MIT.

Aya I. and Yamane, K. (1992). Stability of Clathrate-hydrate of carbon dioxide in highly pressurized water. *Fundamentals of Phase Change: Freezing, Melting, and Sublimation*, ASME, HTD, Vol. 215, pp. 17-22.

Aya I., Yamane, K. and Nariai, H. (1997). Solubility of CO_2 and density of CO_2 hydrate at 30 MPa. *Energy*, **22**(23), pp. 263-271.

Bachalo, W. D. (1980). Method for measuring the size and velocity of sphere by dual-beam light scatter interferometry. *Appl. Opt.,* **19**(3), pp. 363-370.

Bachalo, W. D. and Houster, M. J. (1984). Phase doppler spray analyzer for simultaneous measurements of drop size and velocity distributions. *Opt. Eng.*, **23**(5).

Bachalo, W. D. (1994). Experimental methods in multiphase flow. *Int. J. Multiphase Flow*, **20**, supplement, pp. 261-295.

Berger, S. A. (1988). Initial-value stability analysis of a liquid jet. *SIAM Journal of Applied Mathematics*, **48**, pp. 973-991.

Bogy, D. B. (1978). Wave propagation and instability of a circular semi-infinite liquid jet harmonically forced at the nozzle. *J. Appl. Mech.,* **45**, 469.

Bozzeo, A. Z., Chen, H.-S., Kass, J.R. and Bardhum, A.J. (1975). The properties of the hydrates of chlorine and carbon dioxide. *Desalination*, **16**, pp.461-466.

Brackbill, J. U., Kothe, D. B. and Zemach, C. (1992). A continuum method for modeling surface tension. *J. Comput. Phys.*, **100**, pp 335.

Brewer, P. G., Peltzer, E. T., Friederich, G., Aya, I. and Yamane, K. (2000). Experiments on the ocean sequestration of fossil fuel CO_2: pH measurements and hydrate formation. *Mar. Chem.*, **72**, pp. 83-93.

Chaudhary, K. C. and Maxworthy, T. (1980). The nonlinear capillary instability of a liquid jet. Part 2: Experiments on jet behavior before droplet formation. *J. Fluid Mech.*, **96**, pp. 275-297.

Chen, H.-S. (1972). *Res. Develop. Frog.* Report No. 830. Office of Saline Water, U.S. Dept. of Interior, Washington, D.C.

Das, T. K. (1997). Prediction of jet breakup length in liquid-liquid system using the Rayleigh-Tomotika analysis. *Atomization Sprays*, **7**, pp. 549-559.

Donnelly, R. J. and Glaberson, W. (1966). Experiment on capillary instability of a liquid jet. *Proc. Royal Soc. London*, *Ser. A*, **290**, pp.547-556.

Eggers, J. and Dupont, T. F. (1994). Drop formation in a one-dimensional approximation of the Navier-Storkes equations. *J. Fluid Mech.*, **262**, pp.205.

Grant, R. P. and Middleman, S. (1966). Newtonian jet instability. *AIChE. J.*, **12**(4), pp. 669-678.

Green, A. E. (1976). On the non-linear behavior of fluid jets. *Int. J. Eng. Sci.*, **14**, 49-63.

Goedde, E. F. and Yuen, M. C. (1970). Experiments on liquid jet instability. *J. Fluid Mech.*, **40**, pp. 495-511.

Hayworth, C. B. and Treybal, R. E. (1950). Droplet formation in two-liquid-phase systems. *Ind. Eng. Chem. Res.,* **42**(6), pp. 1174-1181.

Haenlein, A. (1931). Disintegration of a liquid jet. Forschung, 2, 139, NACA TN659(1932).

Hirai, S., Okazaki, K., Tabe, Y. Hijikata, K. and Mori, Y. (1997). Dissolution rate of liquid CO_2 in pressurized water flows and the effect of clathrate films. *Energy*, **22**(23), pp. 285-293.

Homma, S., Koga, J., Matsumoto, S. and Trggvason, G. (2000). Numerical investigation of a laminar jet breakup into drops in liquid-liquid system. *The 8th International Conference on Liquid Atomization and Spray System*, Pasadena, CA, USA.

Kitamura, Y. and Takahashi, T. (1986). Stability of jets in liquid-liquid systems, Chapter 19. *Encyclopedia of Fluid Mechanics*, Vol. 2, (N.P. Cheremisinoff, ed.), Gulf Publishing Company, Houston, TX.

Kowalewski, T. A. (1996). On the separation of droplets from a liquid jet. *Fluid Dynamics Research*, **19**, pp. 121-145.

Kumar, A. and Hartland, S. (1996). Unified correlation for the prediction of drop size in liquid-liquid exaction columns. *Ind. Eng. Chem. Res.*, **35**, pp. 2682-2695.

Kumar, A. and Hartland, S. (1984). Correlation for drop size in liquid-liquid spray columns. *Chem. Eng. Commun.*, **31**, pp. 193-207.

Lafrance, P. (1975). Non-linear breakup of a laminar liquid jet. *Phys. Fluids*, **18**, pp. 428.

Lefebvre, A. H. (1989). *Atomization and Sprays*. Hemisphere Publishing Corporation.

Lieb, S. J. and Goldstein, M.L. (1986). Convective and absolute instability of a viscous liquid jet. *Phys. Fluids*, **29**(4), 952-954.

Lin, S.P. (2003). *Breakup of Liquid Sheets and Jets*. Cambridge University Press.

Longmire, E. K., Norman, T. L. and Gefroh, D. L. (2001). Dynamics of pinch-off in liquid/liquid jets with surface tension. *Int. J. Multiphase Flow*, **27**, pp. 1735-1752.

Mansour, N. N and Lundgren, T. S. (1990). Satellite formation in capillary jet breakup. *Phys. Fluids*, **2**(7), pp. 1141-1144.

Mashayekhi, F. (1994). *Numerical study of capillary and thermocapillary jets and drops*. Ph.D. Dissertation, Department of Mechanical and Aerospace Engineering, State University of New York at Buffalo.

Mashayek, F. and Ashgriz, N. (1995). Advection of axisymmetric interfaces by the volume-of-the-fluid method. *Int. J. Numer. Methods Fluid*, **20**(12), pp.1337.

Masutani, S.M. and Adams, E.E. (2000). *Experimental study of multi-phase plumes with application to deep ocean oil spills*. Final Report to U.S. Dept. of the Interior, Mineral Management Service, Contract No. 1435-01-98-CT-30946.

Meister, B. J. and Scheele, G. F. (1969). Drop formation from cylindrical jets in immiscible liquid system. *AIChE J.*, **15**, pp. 700-706.

Milosevic, I. N. and Longmire, E. K. (2002). Pinch-off modes and satellite formation in liquid/liquid jet systems. *Int. J. Multiphase Flow*, **28**, pp. 1853-1869.

Nishikawa, N., Ishibashi, M., Ohta, H., Akutsu, N., Tajika, M., Sugitani, T. Hiraoka, R., Kimuro, H., and Shiota, T. (1995). Stability of liquid CO_2 spheres covered with clathrate film when exposed to environment simulating the deep sea. *Energy Convers. Manage.*, **36**, pp.489-492.

Ohnesorge, W. (1936). Formation of drops by nozzles and the breakup of liquid jets. *Z.A.M.M.* **16**, pp. 355.

Papageorgiou, D., and Orellana, O. (1998). Study of cylindrical jet breakup using one-dimensional approximations of the Euler equations. *SIAM Journal of Applied Mathematics*, **59**(1), pp. 286-317.

Pimbley, W.T. and Lee, H.C. (1977). Satellite droplet formation in a liquid jet. *IBM J. Res. Dev*., **21**, pp.21-30.

Rayleigh, L. (1878). Instability of Jets. *Philos. Mag*, Nov, pp. 5-13.

Rayleigh, L. (1879). On the instability of jets. *Proc. London Math. Soc.*, **10**, pp. 4-13.

Rayleigh, L. (1892). On the instability of a cylinder of viscous liquid under capillary force. *Philos. Mag*. S.5. **34**(207), pp 145-154.

Reitz, R. D. (1978). *Atomization and other breakup regimes of a liquid jet*. Ph.D. Thesis, Princeton University.

Reitz, R. D. and Bracco, F. V. (1986). Mechanism of breakup of round liquid jets. *Encyclopedia of Fluid Mechanics,* Vol. 3 (N.P. Cheremisinoff, ed.), Gulf Publishing Company, Houston, TX.

Richards, J. R., Neris, A. N., and Lenhoff, A. M. (1993). Steady laminar flow of liquid-liquid jets at high Renolds numbers. *Phys. Fluids A,* **5**(7), pp.1703-1717.

Richards, J. R., Lenhoff, A. M. and Beris, A. N. (1994). Dynamic breakup of liquid-liquid jets. *Phys. Fluid*s, **6**(8), pp. 1640-2655.

Richards, J. R., Beris, A. N., and Lenhoff, A. M. (1995). Drop formation in liquid-Liquid system before and after jetting. *Phys. Fluid*s, **7**(11), pp. 2617-2630.

Schulkes (1993). Dynamics of liquid jet revisited. *J. Fluid Mech*., **250**, pp. 635-650.

Shokoohi, F. and Elord, H. G. (1987). Numerical investigation of the disintegration of liquid jets. *J. Comput. Phys.,* **71**, pp. 324-342.

Skelland, A. H. P. and Walker, P. G. (1989). The effect of surface active agents on jet breakup in liquid-liquid systems. *Can. J. Chem. Eng*., **67**, pp.762-770.

Teng, H. (1994). Laminar instability of cylindrical liquid jets. Ph.D. dissertation, Department of Mechanical Engineering, University of Hawaii.

Teng, H., Kinoshita, C. M. and Masutani, S. M. (1995). Prediction of droplet size from the breakup of cylindrical liquid jets. *Int. J. Multiphase Flow*., **21**(1), pp.129-136.

Teng, H., Masutani, S. M., and Kinoshita, C. M. (1995). Nonlinear analysis of flow in post-dryout. *Heat Transfer*. pp.150-157.

Teng, H., Masutani, S. M., Kinoshita, C. M. and Nihous G. C. (1996). The effect of hydrate formation on CO_2 jet instability. *Prepr. Pap., American Chem. Soc. Div. Fuel Chem.*, **41**(6), pp. 1447-1451.

Teng, H. and Yamasaki, A. (1999). Hydrate formation on surface of buoyant liquid CO_2 drops in a counterflow water tunnel. *Energy Fuels*, **13**, pp. 624-628.

Tjahjadi, M., Stone, H. A., and Ottino, J. M. (1992). Satellite and subsatellite formation in capillary breakup. *J. Fluid Mech*., **243**, pp. 297-317.

Tomotika, S. (1935). On the stability of a cylindrical thread of a viscous liquid surrounded by another viscous fluid. *Proc. Roy. Soc., Ser. A*, **150**, 322.

Tomotika, S. (1936). Breakup of a drop of viscous liquid immersed in another viscous fluid which is extending at a uniform rate. *Proc. Roy Soc*., *Ser. A*, **153**, 302.

Torpey, P.A. (1989) A non linear theory for describing the propagation of disturbances on a capillary jet. *Phys. Fluids A*, (1), pp. 661-671.

Tyler, E. (1933). Instability of liquid jets. *Philos. Mag.*, Vol. 16, pp.504-518.

Uchida, T., Ebinuma, T. and Narita, H. (2000). Laboratory studies on the formation and dissociation processes of CO_2-hydrate crystals-measurements of interfacial tension between CO_2 and water. OCEANS 2000, Honolulu, Hawaii.

Wadesley, M.W.(1995). Thermodynamics of multi-phase equilibria in the CO_2-seawater system. *Direct Ocean Disposal of Carbon Dioxide*. Ed. Hanada, N. and Ohsumi, T., TERRAPUB, Tokyo.

Wong, C. S. and Hirai, S. (1997). *Ocean Storage of Carbon Dioxide: A Review of Oceanic Carbonate and CO_2 Hydrate Chemistry*. IEA Greenhouse Gas R & D Programme Report.

Weber, C. (1931). On the breakup of a liquid jet. *Z.A.M.P.*, **11**, pp. 136-141.

Yamane, K., Tang, L., Masutani, S.M., Kojima, R and Aya, I. (2001). Numerical simulation of agglomeration of CO_2 droplets with hydrate film. *The Eleventh International Offshore and Polar Engineering Conference*, Stavanger, Norway.

Yuen, M.C. (1968). Nonlinear capillary instability of a liquid jet. *J. Fluid Mech.*, **33**, pp. 151-163.